CHARACTERIZING PHOTON AND NEUTRON RESPONSES IN CDMS DETECTORS USING REAL AND SIMULATED CF-252 DATA

A Dissertation

by

JOSHUA DANIEL WINCHELL

Submitted to the Graduate and Professional School of
Texas A&M University
in partial fulfillment of the requirements for the degree of

DOCTOR OF PHILOSOPHY

Chair of Committee,	David Toback
Committee Members,	Bhaskar Dutta
	Ricardo Eusebi
	Mahmoud El-Halwagi
Head of Department,	Grigory Rogachev

December 2023

Major Subject: Physics

ABSTRACT

The SuperCDMS collaboration is searching for dark matter via direct detection of WIMPs. We want to better understand how our detectors respond to both WIMP events and other interactions to help us analyze previously-taken data and also prepare for the next experiment. We focus on the Californium-252 calibration source used in the real experiment, as the neutrons it releases will produce signals similar to those caused by WIMPs; by comparing real Cf-252 data and data produced in our simulation framework, we can trace the physical processes that produce the features we see in the output of the detectors. We find that the initial stages of the simulation are consistent with real Cf-252 behavior and have reasonable detector responses, but we also identify potential improvements to make simulations more realistic. Further, using simulations we identify several measurement complications that might be taken into account to improve analyses for real data.

ACKNOWLEDGMENTS

I have been fortunate to be a part of Prof. David Toback's research group. Prof. Toback has always been level-headed and ready to help despite always being busy to a degree that would have made others cranky and out-of-touch. Senior and previous group members Jon Wilson, Jorge Morales, and Richard Lawrence taught me a lot of the things I had to do to produce this dissertation and they put up with a lot of questions of varying relevance. Likewise Michael Kelsey, who built and maintains a major segment of our simulation chain, has always been willing to provide guidance on both high and low-level computing topics, which have always been some combination of useful and/or fun.

CONTRIBUTORS AND FUNDING SOURCES

Contributors

This work was supported by a thesis (or) dissertation committee consisting of Professors David Toback [advisor], Bhaskar Dutta, and Ricardo Eusebi of the Department of Physics and Astronomy and the Mitchell Institute for Fundamental Phsyics and Astronomy and Professor Mahmoud El-Halwagi of the Department of Chemical Engineering.

Portions of this research were conducted with the advanced computing resources provided by Texas A&M High Performance Research Computing.

All work conducted for the dissertation was completed by the student under the advisement of Prof. David Toback of the Department of Physics and Astronomy, in collaboration with the members of the SuperCDMS experiment.

Funding Sources

This work was funded primarily via a research grant from the U.S. Department of Energy (DOE) to the SuperCDMS collaboration and also was supported by funding from the Mitchell Institute for Fundamental Physics and Astronomy for work on the Brazos computing cluster, teaching assistantships from Texas A&M University, and research assistanships from the same.

TABLE OF CONTENTS

Page

LIST OF FIGURES

FIGURE Page

LIST OF TABLES

1. INTRODUCTION

There is significant evidence that the universe contains a large amount of matter that cannot be seen directly. Based on its effects on the movement of celestial objects and the large-scale structures seen in the universe, this "dark matter" is thought to comprise about five times as much of the universe as "normal" (baryonic) matter does[1]. However, efforts to detect dark matter itself have so far not succeeded; its minimal interactivity with normal matter means that while its effects can be observed on large scales (i.e. galactic scales and beyond), actually catching a glimpse of it here on Earth would be extremely difficult. It need not be impossible, though–it may just be that we need experiments that are extremely precise and well-understood.

In this thesis we discuss how simulations help us better-understand one such precise experiment, the Cryogenic Dark Matter Search, or CDMS[2, 3]. CDMS does direct-detection searches for particulate dark matter using detectors that can sense extremely small interactions for which precise analysis is needed to fully understand what is being detected. With simulations, we hope to improve such analyses and, in so doing, improve the experiment's overall sensitivity as well.

In this first chapter we provide an overview of what we are doing and why. Section 1.1 describes, briefly, our reasoning for searching for dark matter in the first place and how we go about searching for particulate dark matter specifically. Section 1.2 describes how CDMS joins the search and the aspects of the experiment we focus on in this work–namely the CDMS detectors' response to known particles with specific energies from radioactive calibration sources. Section 1.3 introduces CDMS simulations and our goals here, and section 1.4, finally, describes the layout of the rest of this thesis.

1.1 Motivation For Dark Matter Searches

The natural question to ask at the start is: why are we bothering to look for dark matter in the first place? What first made us think that there is something unseen that needs to be found? In simplest terms, the answer is that we observe objects in space moving in unexpected ways: we expect the motion of celestial objects to be dominated by the gravitational force exerted on them by the visible mass around them–but the mass we see is not enough to account for the motion we see[1].

Early signs of this problem were reported by Zwicky in 1933[6], when he published observations of the Coma cluster; in his study he observed the cluster's constituent galaxies moving at speeds higher than expected based on the expected gravitational interactions from visible matter. This was later seen on smaller scales as well: Rubin and Ford[7] observed that stars orbit around galactic centers notably faster than they "should" (the left side of Fig. 1.1 shows this same conclusion from a more recent study). Such observations have since been confirmed, repeated, and expanded upon by others (see e.g. Ref. [5] for a good overview). So if astronomical objects are experiencing a greater gravitational pull than they should be experiencing from the observed quantities of matter around them, there are two potential explanations[2]: either we need to update our description of gravity, or there is more matter out there that we just aren't seeing.

Both options are subjects of current research, but the work in this thesis is done in pursuit the second option: looking for unseen–i.e. "dark"– matter, specifically in the form of particles. Good evidence for this option is given by the Bullet Cluster, shown on the right side of 1.1, which has gravitational effects more easily explained by dark matter particles than by modifications to gravity (see the figure caption for more detail). Here we will proceed by assuming the simplest case wherein this dark matter is comprised of a single type of individual particle[3]. The following sections describe what kind of particle might comprise dark matter and how we hope to make our first direct observations of it[4].

---

[1] In slightly more complex terms, the most basic and well-tested forms of General Relativity and the Standard Model of particle physics do not predict the observed phenomena[4, 5].

[2] It's possible for both explanations to be relevant at once, but currently that introduces more complexity than utility, so we'll consider this to be an either/or case.

[3] As opposed to large, conglomerate objects like dwarf stars or black holes–which have been largely ruled-out[10, 11]; wave dark matter[12]; or dark matter composed of multiple types of particles[13].

[4] For more thorough overviews of these subjects, refer to Refs. [4, 5, 14]

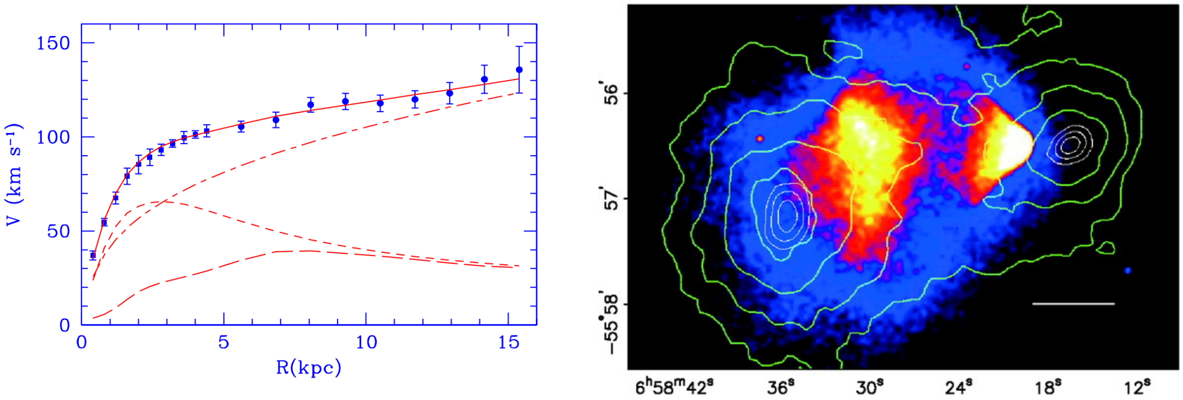

Figure 1.1: This figure shows two notable observations suggesting the existence of dark matter and provides motivation for searching to see if it is particle in nature. On the left is a plot of the measured orbital velocity of stars as a function of their distance from the galactic center (blue points) in galaxy M33, along with the expected contributions from the gravity of three groups of matter (red lines); from Ref. [8]. The expected contributions from mass of the visible stellar and gaseous matter in the galaxy are shown by the short-dashed and long-dashed lines, respectively; these together do not adequately describe the data. Including a contribution from a spherical dark matter "halo" (dash-dotted line) however, produces a final best-fit line (solid) that matches observations well. The figure on the right shows a separate set of data suggesting the particle nature of dark matter from the collision of two galaxy clusters known together as the Bullet Cluster. The image shows the Bullet Cluster as observed via X-rays (blue/red/yellow areas) and gravitational lensing (green contours), which indicate the amount of atomic mass and gravitational mass, respectively. As the galaxies of the clusters collide, their normal, atomic matter heats up and emits X-rays; the two brightest patches in the image represent the highest-intensity of X-rays, and so the greatest concentration of atomic matter. Gravitational lensing measurements, however, detect the highest concentrations of mass at different locations than the X-ray peaks (that is, the green contours are not centered on the bright X-ray patches). This suggests that most of the matter present in the cluster is something other than normal, visible matter–i.e. some sort of "dark" matter particles that did not interact or slow down during the collision. Image from Ref. [9]

1.1.1 Potential Dark Matter Candidates

With the assumption that there exists some as-yet unobserved new particle in the universe, how we go about finding and identifying this "dark matter" particle will depend on what, exactly, it is. Here we discuss the characteristics it must have, provide a brief overview of what kinds of particles satisfy these criteria, and explain why we we choose to focus on our preferred candidate: weakly-interacting massive particles, or "WIMPs". We will largely follow Ref. [5] for this discussion.

The expected properties of particle dark matter are as follows:

- It is, firstly, "dark": i.e. it cannot be directly seen because it doesn't interact electromagnetically and emit or reflect light–meaning that it must be electrically neutral.
- It likely has mass, given that we're inferring it from its gravitational effect on other objects in space.
- It is "cold," meaning it moved non-relativistically (i.e relatively slowly) in the early universe (and now). This model of dark matter–as opposed to the faster "warm" or "hot" models–best explains the large-scale structure (e.g. clumping of normal matter) seen in the universe [15, 16, 17].
- It must be stable given how it affected the universe early on (large-scale structure again) and continues to affect present-day objects[18, 19].

These characteristics limit what kinds of particles we consider. Dark matter is, firstly, not likely to be "normal", baryonic matter belonging to the Standard Model of particle physics (hereafter "SM"). This is because dark matter doesn't have charge and is likely stable, which means the only SM particles (or small conglomerate objects) it could be are a) neutral atoms in objects that don't emit light, or b) neutrinos; neither of these have the abundances in the universe necessary to be dark matter, however. So we have to consider non-SM particles such as axions, light gravitinos, sterile neutrinos, and WIMPs. Discussion of each of these is beyond the scope of this work; see e.g. Refs. [4, 5, 15] for more a more thorough look. Here we focus only on our preferred candidate, "WIMPS".

In short, WIMPs are good dark matter candidates because they are a relatively simple, single-particle option that would solve or account for more than just the few otherwise-unexplained astronomical considerations we've mentioned so far. Of particular note is the "WIMP miracle" in modern cosmology: if there was a new (i.e. currently undiscovered) single type of particle that interacted with itself at a rate similar to those of weakly-interacting SM particles (e.g. the W and Z bosons), after the Big Bang such particles would have naturally settled into a density in the universe that is consistent with the density we measure for dark matter[5][5, 17]. This cosmological coincidence provides guidance for estimates of how often and by what mechanisms we might expect to be able to detect WIMPs with a given search method in an experiment.

1.1.2 Search Methods

With some ideas for what we might be looking for, we now discuss how we might go about detecting something that has so far not been detected. If we assume dark matter directly interacts with more easily-observable SM particles, which detection approach ultimately works will depend on what, exactly that interaction is (though each of the approaches we discuss here are sensitive to a range of interaction possibilities beyond those they focus on). The WIMP suggested in the previous section, per the name, is expected to interact weakly–that is, via the weak nuclear interaction–with SM nuclei; if WIMPs are their own antiparticle as well, then they might also pair-produce and annihilate from/to SM particles. These possible interactions suggest three approaches to detection, as illustrated in Figs 1.2 and 1.3: creation, indirect detection, and direct detection.

For the first method, we could simply attempt to create some dark matter ourselves (reading

---

[5] To elaborate, we can estimate the density of dark matter in the universe by studying the Cosmic Microwave Background (or "CMB")–photons from early in the universe's life that only just now reach us; fluctuations in the distribution of these photons tell us how matter (dark and otherwise) was distributed in the early universe[1, 20]. Assuming the simplest case in which dark matter is a single kind of particle that is its own antiparticle, its density determined from the CMB is closely related to its self-interaction rate (and its mass). If it interacts with itself too frequently/rarely, it would have annihilated too much/little in the early universe and left smaller/larger effects in the CMB than those we observe[20]. The interaction rate in the middle of the extremes that would match our observations happens to be similar to that of the W and Z bosons, the mediators of the weak force.

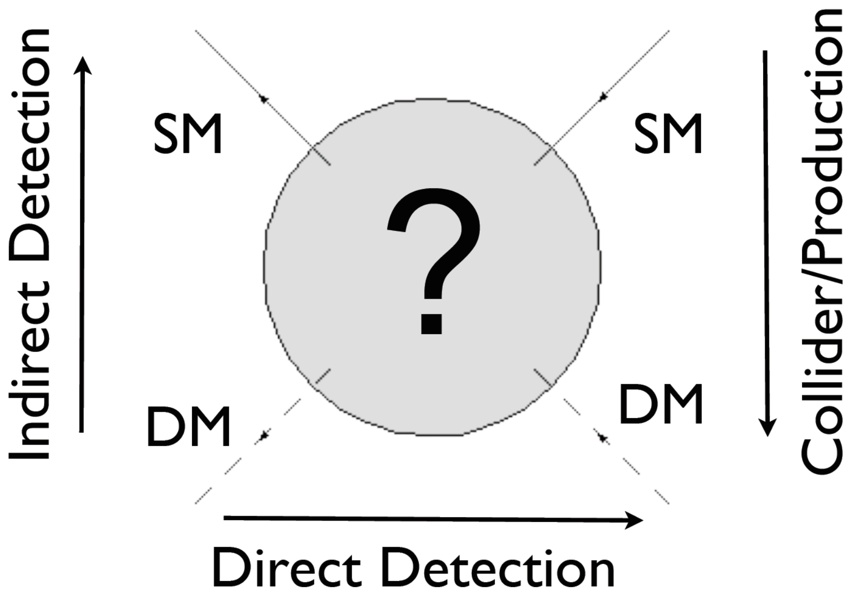

Figure 1.2: This figure shows a simplified Feynman diagram of three potential ways dark matter ("DM") might interact with standard model ("SM") particles and the corresponding approaches to detecting particle dark matter (Fig. 1.3 shows these in slightly more detail). Each approach is represented by an arrow indicating the flow of time. The options are 1) inferring it ("indirectly") by observing its annihilation daughters, 2) producing it in a collider with Standard Model ("SM") particles (and again watching for its daughters), and 3) watching for it directly interacting with SM particles (the focus for this thesis).

Fig. 1.2 such that time flows from top to bottom, and shown in the top row of Fig. 1.3). This could mean colliding SM particles with enough energy to pair-produce dark matter particles or creating heavier particles that can decay into dark matter, for example. In both of these cases, though, we'd have to "observe" this production of dark matter by either its SM byproducts or subsequent interactions[21]. Collider production, broadly, has the advantage of being sensitive to more potential dark matter candidates in a single experiment than other methods.

The second option for dark matter detection is indirect detection (reading Fig. 1.2 from bottom to top, and shown in the middle row of Fig. 1.3), in which we search for particles in space with high energies characteristic of dark matter annihilating with itself (assuming it's its own antiparticle). Generally this means looking for annihilation products coming from gravity wells in which dark matter likely accumulates–e.g. looking for characteristic photons from the galactic core, or looking

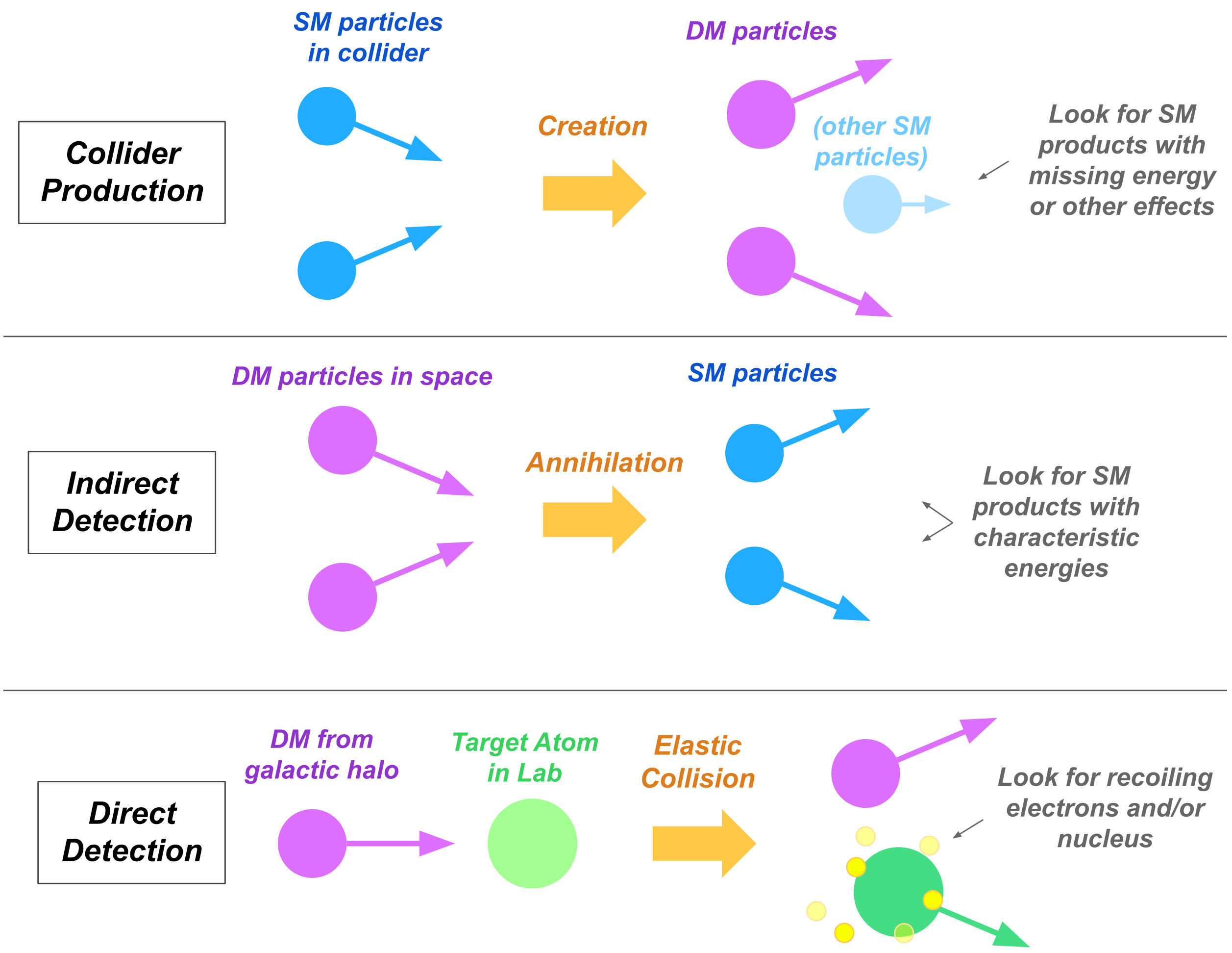

Figure 1.3: This figure illustrates the underlying physical processes (in simplified forms) of the three general approaches to detecting dark matter ("DM") particles (Fig. 1.2 shows these in a more succinct, if more abstract Feynman diagram). Top row: In collider production of dark matter, SM particles are collided with high enough energies to either produce dark matter directly or produce something more massive that can decay to dark matter. In either case, the dark matter must be inferred by the energy missing from other, observable, SM particles produced in the collisions. Middle row: Indirect detection generally watches gravity wells in space (or possibly the Earth's core), looking for SM particles with energies characteristic of dark matter annihilating with itself. Bottom row: Direct detection looks for interactions between dark matter particles from the Milky Way and SM particles–specifically the atoms in ultra-sensitive detectors. Measuring the energy of a recoiling nucleus and/or the freed charges (depending on the exact dark matter interaction model) tells us about the particle (perhaps a WIMP) that hit it.

for neutrinos from the cores of the Sun or the Earth. Charged particles in cosmic rays may also reflect local–if not concentrated–dark matter annihilation[4, 22].

The third option is direct detection (reading Fig. 1.2 horizontally, and shown in the the bottom row of Fig. 1.3, as well as the left side of Fig. 1.4), in which we try to observe a dark matter particle scattering off an SM particle by using ultra-sensitive–and often underground–detectors. Dark matter is expected to form a continuous "halo" in and around galaxies (based on the rotation curves of galaxies)[8], so in theory there are plenty of dark matter particles from the Milky Way passing through the Earth, ready to interact if we set out detectors for them; a dark matter particle could bounce off one of the atoms in a detector and we'd identify it by measuring the energy of the atom as it recoiled from "nothing." This is the method we focus on here–specifically, looking for WIMPs interacting (weakly) with the nuclei of atoms.

1.2 SuperCDMS Direct Detection Experiments

The SuperCDMS (Super Cryogenic Dark Matter Search) collaboration uses direct-detection methods to search for dark matter, specifically searching for low-mass (sub-10GeV) dark matter[6]. There have been several iterations of the main SuperCDMS experiment, starting with CDMS-I at Stanford University[23], moving to the Soudan mine in Minnesota for CDMS-II and SuperCDMS[24, 25], and currently being set up to run at SNOLAB in Ontario in 2024[26]. In this section we will discuss the central physics principles underlying all of these iterations, begin our focus on the Soudan experiment in particular, and introduce the radioactive calibration sources used at Soudan to help identify particle interactions in dark matter search data.

Central to most variants of the CDMS experiment (there are alternate operation modes we won't cover here[27]) is distinguishing between two ways that particles–of any kind–can interact in our detectors: electron recoils and nuclear recoils, which are illustrated in Fig. 1.4 and will be described in further depth in chapter 3. The significance of these two recoil types is that WIMPs would interact as nuclear recoils (hereafter "NRs") while most everything else would cause electron

---

[6] We will maintain our focus on WIMPs here, but the experiment is sensitive to other potential dark matter candidates as well.

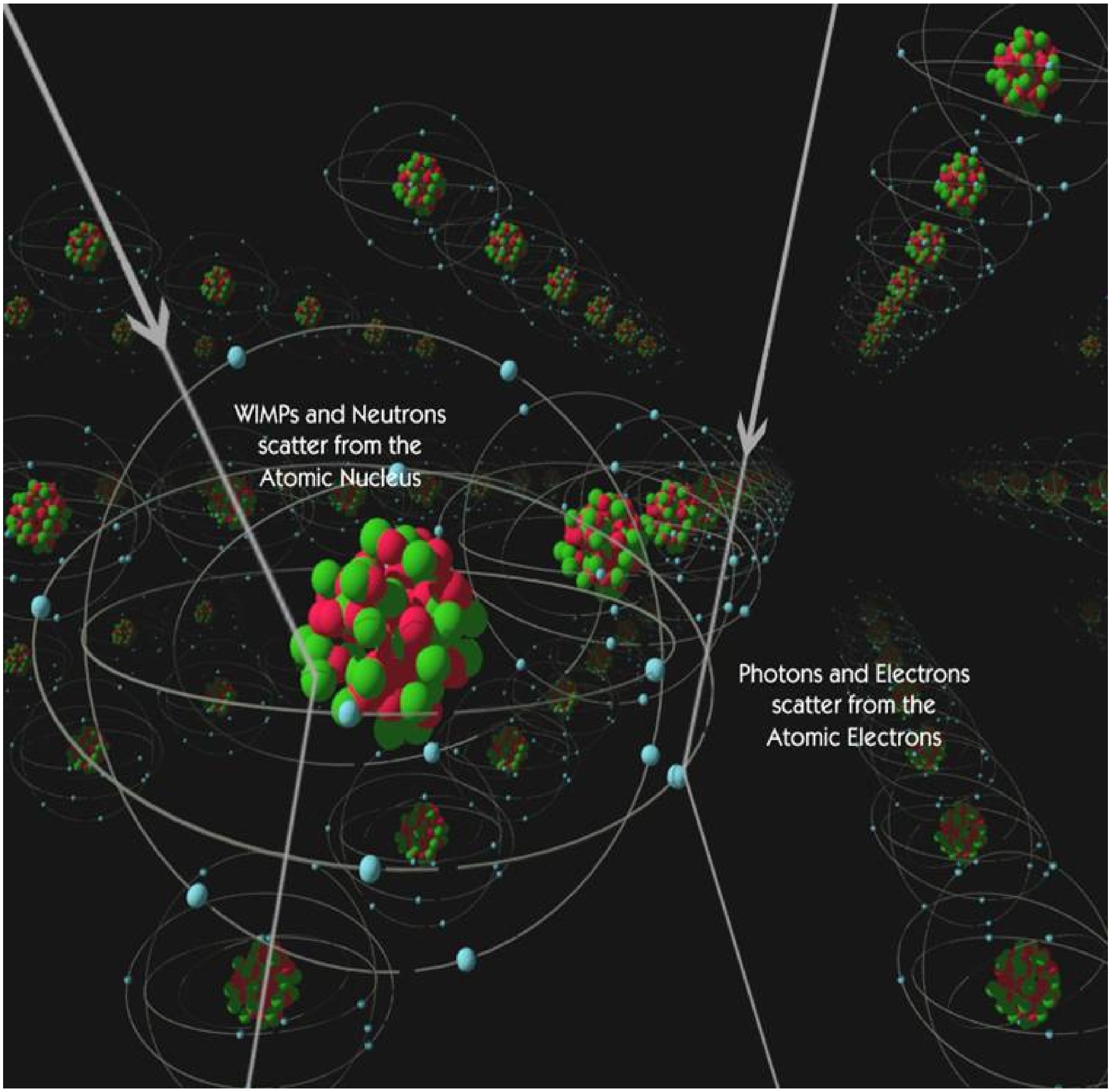

Figure 1.4: This figure shows two interactions of different types between incoming particles and an atom that is part of a larger crystal lattice (as in a detector in a direct-detection experiment). We show this because differentiating between these two interaction types is important for identifying dark matter in direct detection. The track/arrow on the left represents uncharged, massive particles like WIMPs or neutrons interacting with the atom's nucleus; these are called "nuclear recoils" (or hereafter "NRs" for brevity). The track on the right shows photons or charged particles interacting with the atom's outer electrons; these are "electron recoils" ("ERs"). The CDMS experiment is designed to identify dark matter by distinguishing an NR signal (from e.g. a WIMP) from an ER background (noise or other interactions from other sources).

recoils ("ERs")[7]; anything else causing NRs that might be confused for WIMPs are, ideally, either blocked by the rock overburden and apparatus shielding or accounted-for in analysis–though these methods aren't perfect (we will discuss these more in the next three chapters).

1.2.1 The Experiment at Soudan

SuperCDMS at Soudan was an upgrade to the prior CDMS II experiment, using the same apparatus (the "cryostat") in the same location in Soudan Mine, but with new detectors[28]. Chapter 2 will provide more details on the apparatus as a whole; chapter 3 will further describe the inner workings of the detectors–one of which is shown here in Fig. 1.5. The Soudan experiment was operated between 2011 and 2015 [27], during which there were multiple analyses and detector modes used; Fig. 1.6 illustrates several of these, associating them with particular sensitivity ranges–i.e. ranges of possible dark matter particle masses.

Here we focus on some of the methods used in the "Low-Threshold" ("LT") analysis, which specifically searched for low-energy interactions between WIMPs and nuclei in the detectors. The LT analysis used data taken between October 2012 and June 2013, resulting in a total WIMP-search exposure of 577 kg-days [28]. Results are shown in Fig. 1.7, which shows distinct behaviors for ERs and NRs in terms of ionization (or charge) energy and phonon energy (vibration in the detector); these types of measured energies will be explained further in Chapters 2 and 3. Note that this thesis is not about this particular LT data; we will, however, be using some of the same analysis methods to study those same ER and NR behaviors.

1.2.2 Soudan Calibration Sources

In this thesis we will be focusing not on the WIMP-search data itself, but on data–real and simulated–from two radioactive calibration sources used at Soudan: Barium-133 and Californium-252 (hereafter abbreviated "Ba-133" and "Cf-252"). We do this as part of a long-term effort to better understand the detectors to improve their sensitivity and help guide data analysis. In the ex-

---

[7] Note that one difference between the CDMS experiment and the simple direct-detection schema shown in Fig. 1.3 is that the "target nuclei" are at fixed lattice points in detector crystals, and they don't really move much. ERs and NRs are differentiated by the way the imparted recoil energy is propagated away from the nucleus.

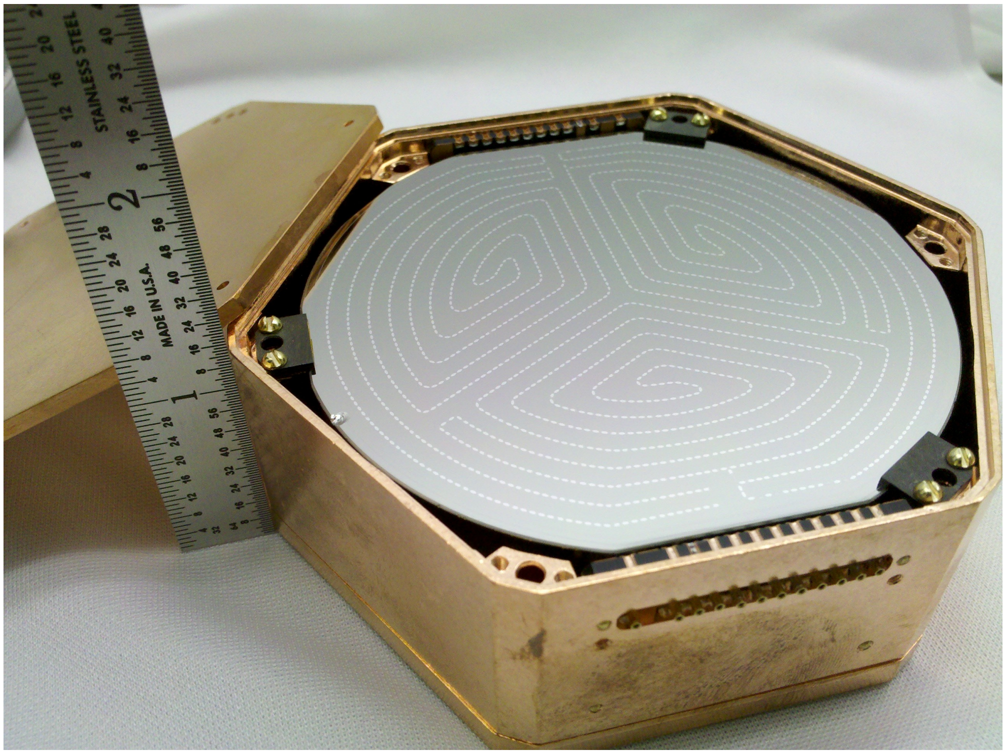

Figure 1.5: This figure shows one of the detectors (in its copper housing) used by the CDMS Collaboration for data-taking in the Soudan Mine experiment. We show it to provide a sense of scale and foreshadow details of the apparatus that we'll describe later. On the faces of the detector are lines of sensors for both phonons and charges; collecting both will allow us to distinguish between interactions due to massive particles (e.g. potential dark matter candidates) and interactions due to noise or backgrounds.

periment, Ba-133 and Cf-252 sources were occasionally placed near the detectors, emitting particles providing ERs and NRs with known behaviors, allowing us to both identify particular energies from the detector readout and see what WIMP-like events should look like. Here we summarize their basic use; more complete descriptions will be given in Chapter 5.

As Ba-133 decays, it emits photons which cause ERs when they hit the detectors. This photon spectrum has several standout energies between 300 and 400 keV–most notably at 356 keV–that are easily recognizable in the detector readout. These allow us to calibrate the energies reported by the detector–in addition to giving us a sense of how ERs generally should appear in the results.

Californium-252 (Cf-252) has multiple decay modes and products (including photons that cause ERs), but most significant are the neutrons it emits in spontaneous fission, which provide

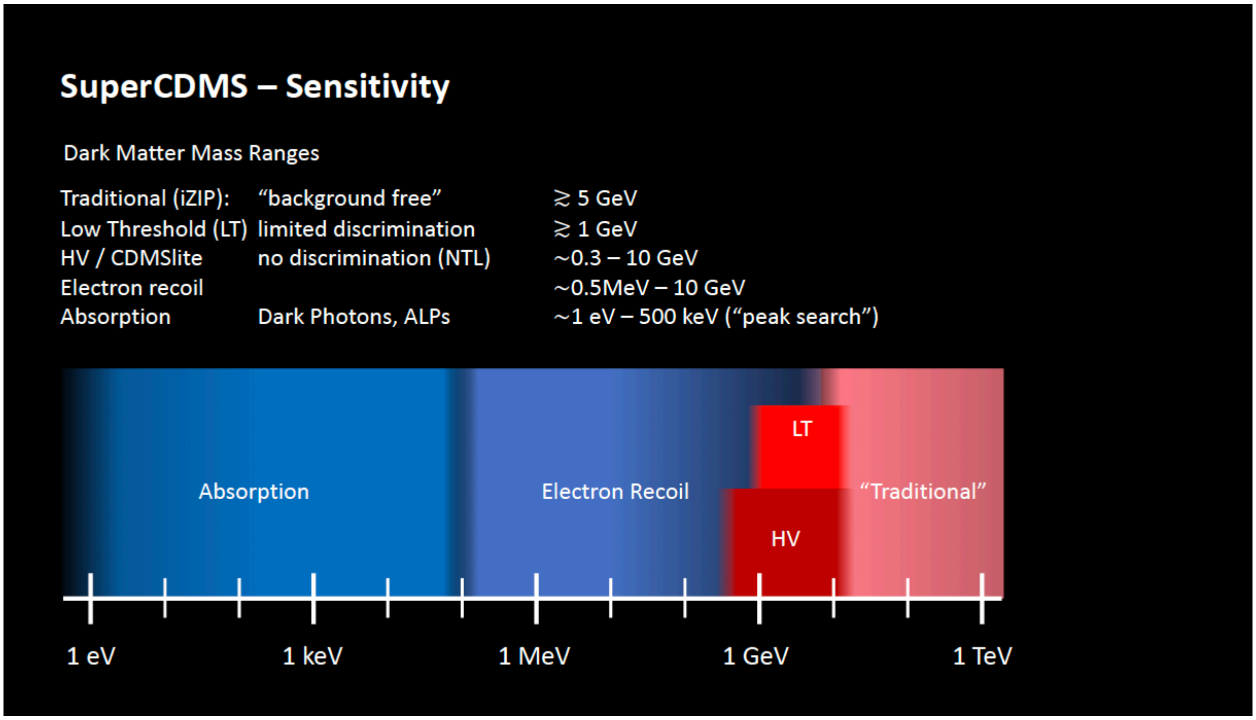

SuperCDMS – Sensitivity

Dark Matter Mass Ranges

Traditional (iZIP):	“background free”	≳ 5 GeV
Low Threshold (LT)	limited discrimination	≳ 1 GeV
HV / CDMSlite	no discrimination (NTL)	~0.3 – 10 GeV
Electron recoil		~0.5MeV – 10 GeV
Absorption	Dark Photons, ALPs	~1 eV – 500 keV (“peak search”)

Figure 1.6: This diagram shows the different types of analyses done in the CDMS experiment and the potential dark matter masses each would be sensitive to. The work presented in this thesis focuses on the "traditional" and "low-threshold" (or "LT") ranges, which cover dark matter candidates with masses between 1 and 10 GeV.

example NRs in the detector. These NRs demonstrate what WIMP interactions–also NRs–would look like in the data. Calibration with Cf-252 was done only every few months.

Fig. 1.8 shows data from these two calibration sources that we’re going to be studying. The left side is comparable to Fig. 1.7; the right side shows the same data in a form that more clearly distinguished between ERs and NRs. While these plots do show identifiable trends for each recoil type, we want to make sure we understand the events around them that less clearly follow those trends; as we will show, some are in fact mismeasurements that we want to remove for WIMP-search data while others are well-measured but complicated events we want to be able to distinguish from WIMP-like events.

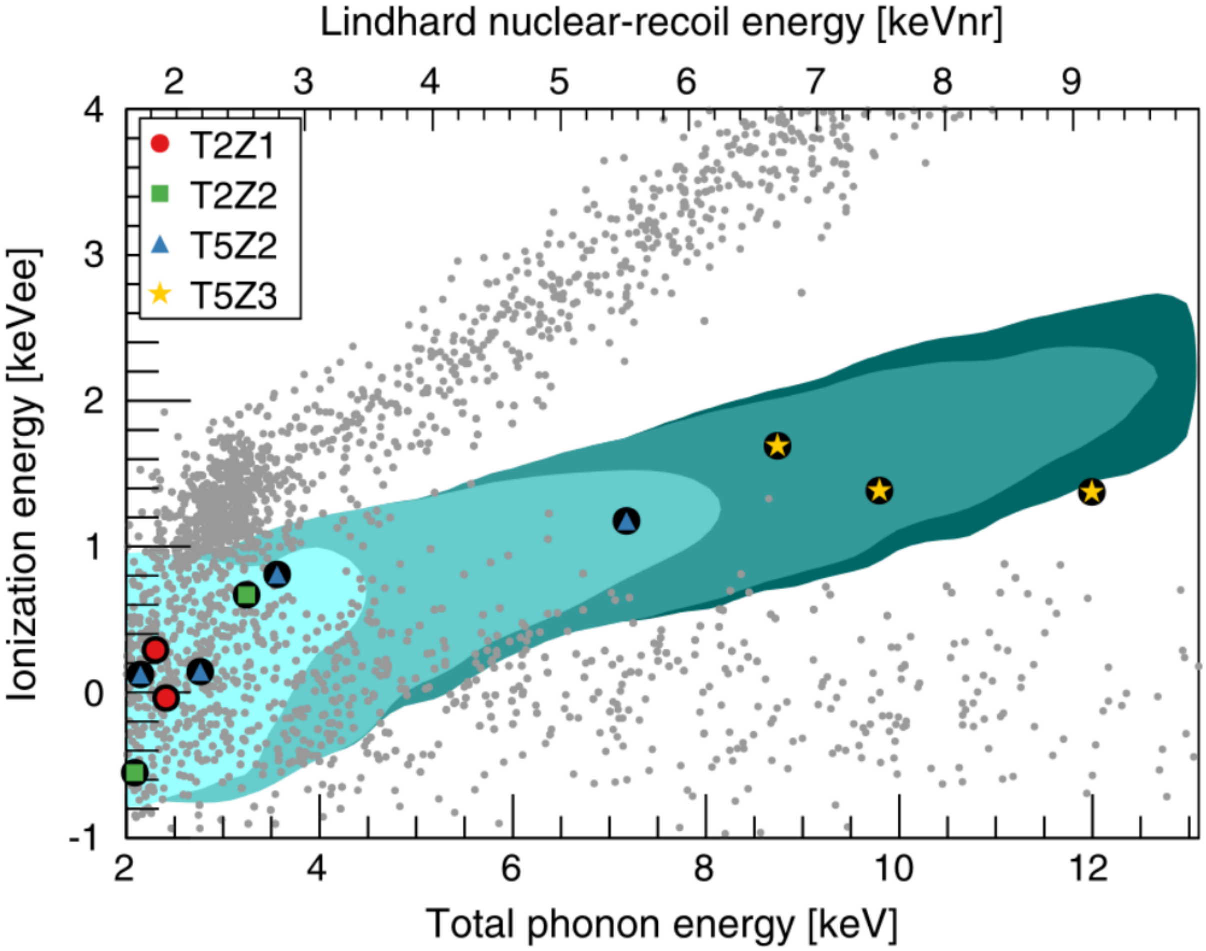

Figure 1.7: This figure shows charge and phonon energy measurements for the "low-threshold" WIMP-search analysis of the Soudan experiment, from which we can see the different behavior between ERs and NRs (see chapter 3 for more); from Ref. [28]. The y-axis represents measured ionization (i.e. charge) energies and the x-axis measured phonon energies; in this plane we identify three collections of events. Most importantly, the upper, angled band of grey dots is comprised of ERs while the colored region at a shallower angle is where NRs should appear. The events along the bottom, meanwhile, are due to a particular form of mismeasurement along the edges of the detectors; these are understood, but not particularly useful to identifying dark matter, so we won't discuss them much. The black circles with shapes in them (corresponding to specific detectors, whose names are shown in the legend) represent what were potential dark matter signals (see how they are all in the NR region) but these were determined to be consistent with backgrounds.

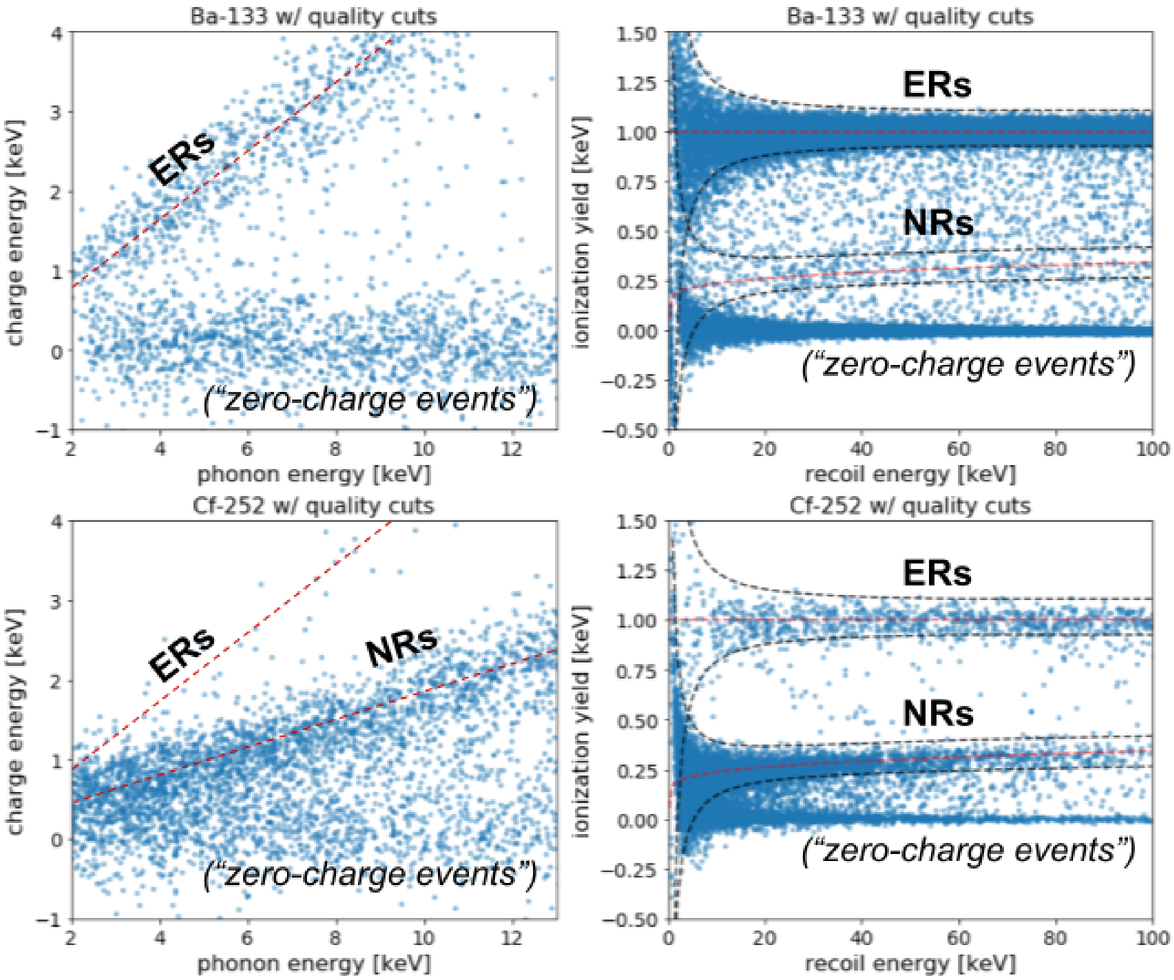

Figure 1.8: This figure shows two different representations of charge and phonon energy measurements for two calibration datasets from the Soudan experiment–one for each calibration source–which are used to identify the behaviors for ERs and NRs that we expected to see in Fig. 1.7. These events were collected when either Ba-133 or Cf-252–not both at once–calibration sources were placed near the detectors (unlike in the previous figure, where none of the events are purposefully introduced). The top row shows event from photons emitted by Ba-133, which cause only ERs; the bottom row shows events from Cf-252, which involves both photons (more ERs) and also neutrons, which will cause NRs–which are more like the expected WIMP signals. The left two plots show charge vs. phonon energies–to compare with Fig. 1.7– while the right two plots show ionization yields vs. recoil energy, a variation we'll be using more often in this thesis, since it more plainly shows the differences between ERs and NRs. The dashed red lines show the expected yields while the black lines in the right two plots mark two standard deviations from those expectations; from these we see that the data does show the expected ER and NR behaviors, but there are also events between and below those main bands to account for; we'll find that some are mismeasurements while others are well-measured but complicated. Note that some mismeasurements have been removed here already via "quality cuts," some of which will be described in Chapter 4.

1.3 Simulating Data Collection with Calibration Sources to Study Detector Interactions and Inform Experiment Analyses

To better understand real data we turn to simulations, in which we can trace individual particles, energies, recoils, etc. throughout the apparatus and detectors. This allows us to (eventually) determine what physical processes contribute to the final observed data points–something we cannot do for real data. In other words, while simulations don't match real data we can learn about what physics we haven't considered, and once our simulations match real data we can learn about the latter by studying the former. The full CDMS simulation chain is illustrated in Fig. 1.9. We provide a brief overview of these simulations and our use of them here, but we will go into more detail in later chapters.

There are three main stages in the simulation chain: SourceSim, DetectorSim, and Reconstruction. SourceSim, built on Geant4[29, 30, 31], models incoming particles (from calibration sources, contaminants, WIMPs, etc.) and their interactions in the apparatus, including energy deposits in the detectors. DetectorSim–also partly built on Geant4 but with additional condensed matter physics processes included[32]–models the detector response and readout due to SourceSim's energy deposits; it also adds realistic noise and formats the simulated data to match the form that real "raw" data would have in the experiment. This means the final stage, Reconstruction, can be applied to simulated data the same way it is to real data; in this stage raw data is converted from detector electronics signals back to meaningful physics quantities ("reconstructed" or "measured" data).

After Reconstruction, simulated data is directly comparable to real data. If those reconstructed results match, it is evidence that we've understood the behavior of the real detectors. The plan, then, is to simulate our best understanding of the physics (of the calibration sources in particular), validating simulation stages as we go, to see if that best understanding–after undergoing the same processing as real data–produces results that look like real data. That, then, provides a jumping-off point for creating more precise analysis cuts and background estimated for real data that could help pick out dark matter signals from non-dark-matter backgrounds. Fig. 1.10 illustrates this plan.

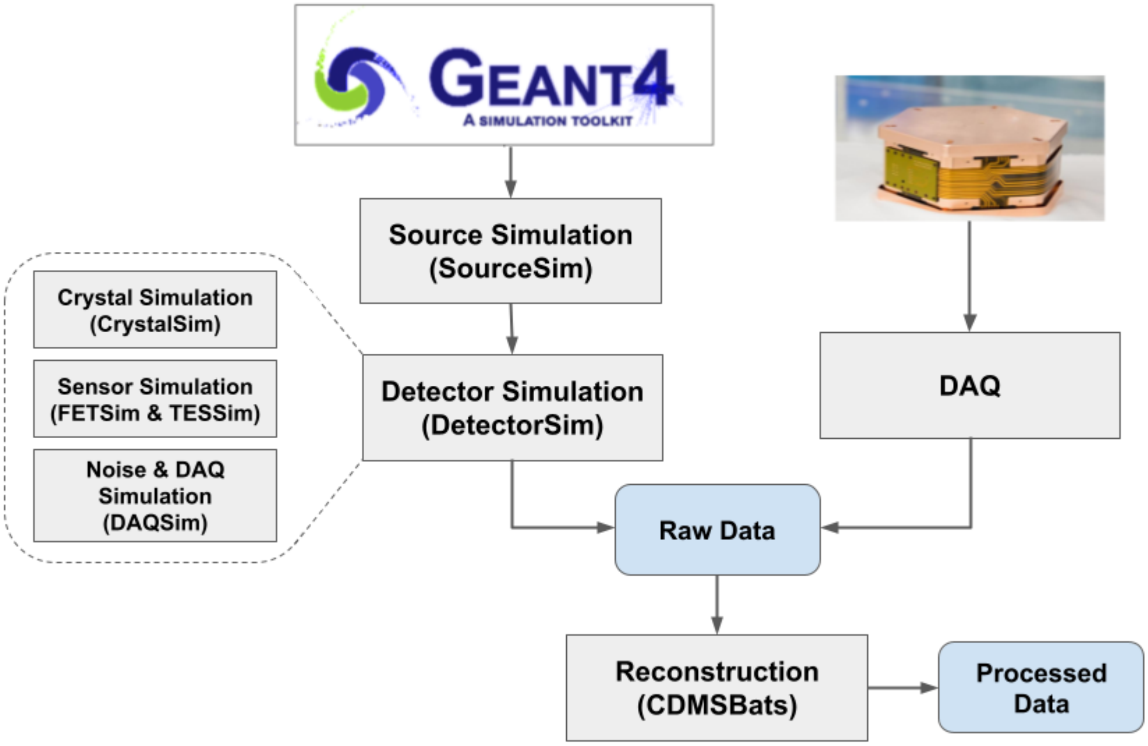

Figure 1.9: This figure shows the workflow used for simulations and how it parallels real data-taking and processing. The upper-left branch shows the steps of the simulation while the upper-right shows the corresponding components of the real experiment; both are fed into the same reconstruction code at the bottom. For simulations, we can validate the output of each stage individually and even check the behavior of individual events. At the end, we can evaluate the simulations' overall performance by comparing its reconstructed results to those for real data. If the results match, we have grounds to study the behavior of simulated ERs and NRs to learn about real ERs and NRs (in all our data–be it the calibration sources we focus on here or real WIMP-search data).

1.4 Overview of the Thesis

In this thesis we will provide details on the CDMS Soudan experiment and describe how our simulation results give us increased understanding of the real experimental results. We proceed as follows:

- Chapters 2-5 describe the real experiment and physics:
    - Chapter 2 describes the experiment itself–the basics of the hardware and the physics of particles (dark matter or otherwise) entering the apparatus and depositing energy in

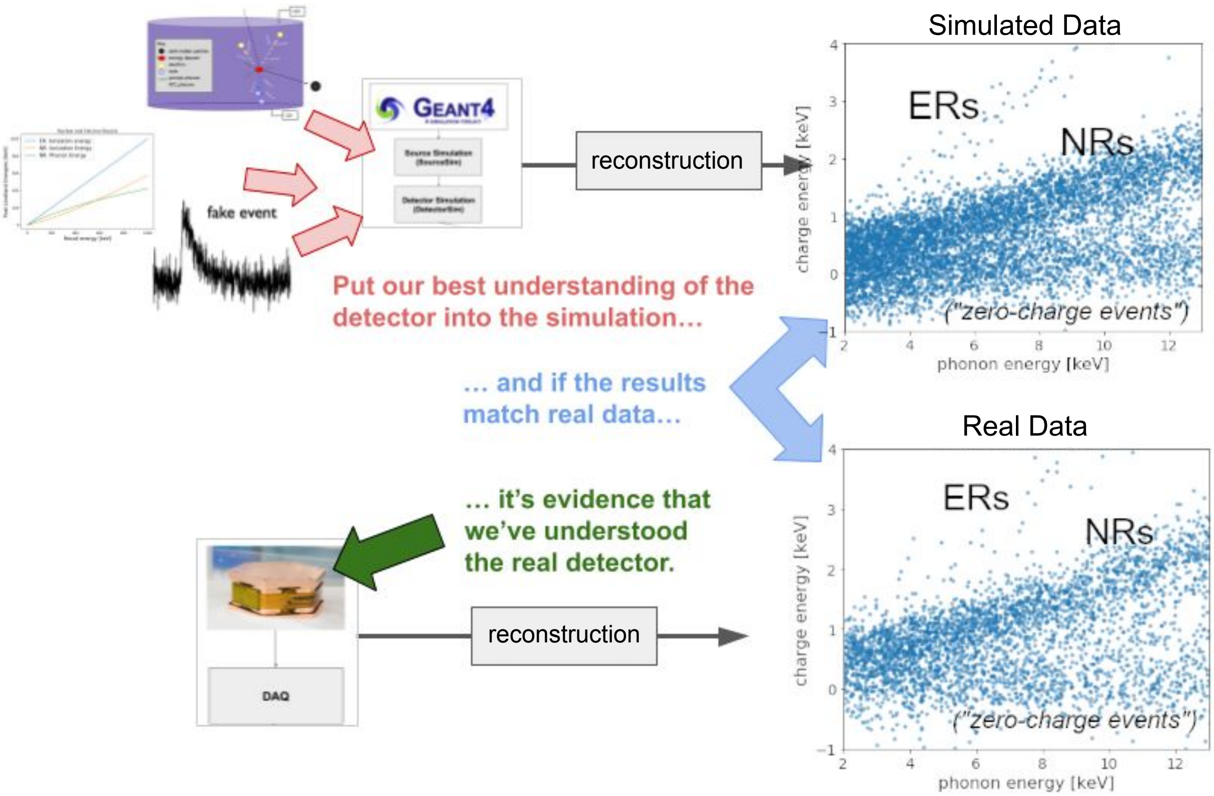

Figure 1.10: This figure shows a flowchart that illustrates the approach this thesis takes to validate that simulated results are generally consistent with real data–and in so doing, learn about the behavior of real detectors. The specifics of the upper-left images will be discussed later.

detectors.

  - Chapter 3 describes how the deposited energies propagate through the detector crystal and produce a signal upon collection.
  - Chapter 4 describes how the detector readout is reconstructed to tell us about the physics of the event.
  - Chapter 5 describes the physics of the Ba-133 and Cf-252 calibration sources and the energy distributions expected from them.

- Chapters 6-9 covers our simulations–how they are set up and what we simulate:
  - Chapter 6 provides a more in-depth description of the simulation workflow shown in Fig. 1.9 and introduces the specific samples analyzed here.

  - Chapter 7 validates the behavior of the Ba-133 and Cf-252 calibration sources in SourceSim by checking particle energies and rates as they travel from the sources to the detectors.
  - Chapter 8 covers samples in the Detector Monte Carlo (DMC), which simulates deposited energies propagating through the detectors and their resulting signals.
  - Chapter 9 covers the final, reconstructed results of the simulation.
- Chapter 10 compares the final simulation output for Ba-133 and Cf-252 to real data from the Soudan Experiment.
- Chapter 11 summarizes and concludes.

2. CDMS SOUDAN EXPERIMENT DESCRIPTION

As with any direct-detection experiment, the key issue CDMS needs to solve is how to pick out a tiny and rare dark-matter interaction ("signal") from a sea of normal, SM-particle interactions (known, along with electronics noise, as "backgrounds"). CDMS's approach to this, in short, is setting out extremely sensitive, extremely shielded detectors in hopes of excluding everything but DM interactions. In this chapter we describe the iteration of this experiment run at Soudan mine (shown in Fig. 2.1). After defining terms and relevant particles in section 2.1, section 2.2 will cover the apparatus itself, how it is meant to detect DM, how it mitigates backgrounds, and which backgrounds will still be seen; section 2.3 will discuss Ba-133 and Cf-252–two radioactive particle sources introduced purposefully for calibration and understanding detector response; and section 2.4 will discuss how all of the signals and backgrounds may be impacted by the apparatus. The next chapter will discuss what happens to those energies in the detectors themselves.

2.1 Terminology and Particles

Before proceeding, we first define several terms for clarity. These will be particularly useful when discussing simulations later, but we start with them now for consistency across discussions. We first describe several general concepts:

- "Primary particles, or "primaries", are whatever particles begin a sequence leading to energy deposition and readout in the detector. This could be an external particle entering the apparatus or a particle emitted from a decaying nucleus in the experiment. A WIMP, a photon emitted from the Ba-133 calibration source, or a neutron emitted from the Cf-252 source are examples of primaries.

- A "hit" is an energy deposit or interaction in the detector that produces a measurable energy. A single incoming particle can cause multiple hits across multiple experimental components or within a single detector; that particle may also leave without depositing all of its energy in hits.

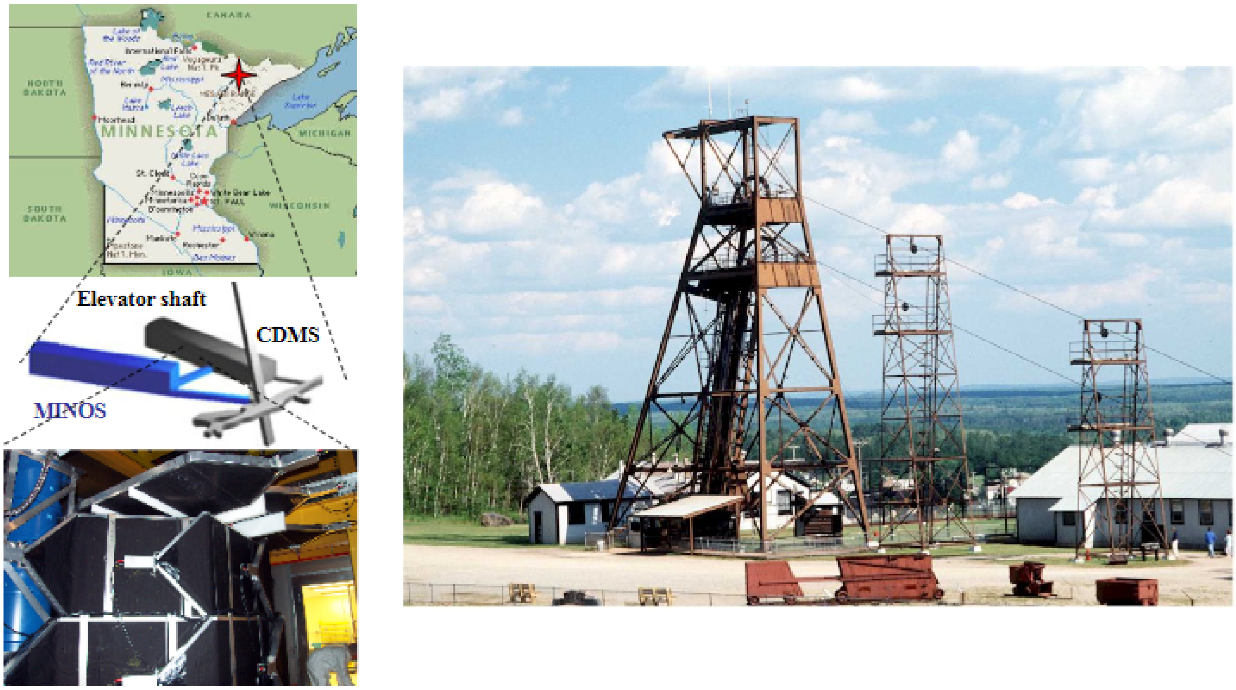

Figure 2.1: This image shows the location of the Soudan mine, its layout, and the CDMS experiment's location. The underground location provides a good deal of shielding from cosmic rays that might contribute to backgrounds. Excerpt from Ref. [33].

- The "readout time window" (or just "readout window") is the time span over which a detector reports on its collections of hits. Ideally it could report each hit individually, but our detectors cannot do this; if multiple hits occur within the readout window, their energies are all reported essentially in sum.

- An "event" encompasses a group of hits (or possibly just one) occurring close together in space (i.e. in a detector) and time that, ideally, are all related by a single parent primary.

  - In **real** data, events are simply identified as every hit occurring within the readout time window. Since specific particles can't be identified individually, these events might include multiple hits ("multi-hit events") and subsequent particles, which can easily cause mismeasurements and misidentified event sources[1].

---

[1] The most extreme of these being "pileup events" in which hits due to completely unrelated primaries occur together. These tend to be separated in time enough (though still within the readout window) that we can identify and remove them from consideration later.

  - In **simulated** data, events are associated with specific primaries and simulated individually, meaning all of their hits can be identified and collected perfectly[2].

- We sometimes refer to particular energies as "lines" or "peaks" when they occur so often that they stand out visually in finely-binned histograms. Ba-133 emits a large number of photons at 356 keV, for example, and we look for the "356 keV line" when looking at the energy distributions for Ba-133 calibrations.

- "Signal" refers to the events, hits, and/or energies that we want to see in our data. This could mean particular energies from Ba-133 (the aforementioned 356 keV line, for example) or Cf-252 during their respective calibration runs; otherwise it generally refers to WIMPs.

- "Backgrounds" are unwanted contributions in the data. This can be noise (from the experiment's electronics), external particles (besides WIMPs) that fly in to deposit energy (from outer space ["cosmogenics"], from radioactive contaminants in the mine ["radiogenics"], etc), or unwanted particles in the apparatus itself (e.g. contaminants that settled on the detectors during fabrication–further radiogenics). Most of the apparatus is meant to block external backgrounds.

- By "energy loss" we refer to any transfer of energy such that our final energy measurements are reduced from what they would be in an ideal world. In other words, it's the difference between an "expected" energy and an "observed" energy, where the latter is lower than the former. More broadly we would consider mismeasurments as a whole, but effectively all mismeasurements in this experiment involve energy reductions–not increases–hence our use of "loss." Our use of the term will also include cases where an expected energy is not produced in the first place–not just cases in which existing energies are reduced. Energy losses

---

[2] One caveat here being the case of a single primary exciting a nucleus that would then decay some time later. Hits caused by the primary and its immediate daughters could be significantly separated in time from hits due to the nuclear de-excitation. Our simulations could either identify all the hits as a single event (since they are all from the same primary) or identify them as two or more separate events (since they are separated in time and would be interpreted as separate events in real data).

are a concern because they cause us to mismeasure real energies and potentially misidentify the particles involved.

- CDMS had several "running modes" or "data-taking modes"–specific setups and purposes for discrete periods of data-collection time. These included:
    - "WIMP-search" mode: looking for dark matter interactions when there were minimal interactions from other sources (i.e. minimal backgrounds).
    - Two (separate) "calibration modes," one for each of the two calibration sources discussed in section 2.3.
    - A "randoms" mode where data is taken randomly–with or without calibration sources nearby–to evaluate backgrounds or electronics noise levels[34, 35].

Lastly we include a brief word about the particles relevant to the experiment. We can loosely group these into particles relevant *outside* the detectors (which are more relevant to this chapter) and particles more relevant to energy transfer *inside* the detectors (discussed more in the next chapter).

- Outside the detector we consider (non-WIMP) particles that might cause energy deposits:
    - Alpha particles ("alphas") are helium-4 nuclei: that is, two protons and two neutrons. These are relatively large and easily blocked because they interact very readily.
    - Beta particles ("betas") can be either electrons or positrons. These tend to be easily blocked, but also easily created as other particles interact.
    - Gamma rays ("gammas") are photons with relatively high energies (over 100 keV) generally emitted from nuclear processes. Many of these will reach the detectors.
    - X-rays are photons with relatively low energies that are emitted due to atomic processes. These are generally blocked.
    - Muons are similar to but more rare than electrons. These are often produced by particles entering Earth's atmosphere from space; most are blocked in the experiment.

- Inside the detectors we focus on the particles carrying the energies shown in Figs. 1.7 and Fig 1.8:
    - "Charges" in this context refer to either electrons or "holes" in the detector crystal lattice; these two carry "ionizing energy" (or just "charge energy"). In the detector, an energy deposit may knock out electrons (one or more) from their atoms (or "ionize" them), leaving behind "holes" in the lattice (i.e. in the orbitals the electrons were in) that can themselves be treated as particles; both the electrons and the holes can then travel independently through the detector (the holes "moving" as other electrons move to fill them and leave more holes behind) and eventually "recombine" (re-associate with atoms) in the lattice. These electrons and holes are not themselves the energy we measure, but since a known ionizing energy (specific to the given crystal composition) was required to free each pair of them in the first place, by measuring the number of charges collected by the sensors at the detector faces we can estimate that original energy.
    - "Phonons" are simply quantized vibrations in the nuclei of the detector's crystal lattice. Such quantized energies/vibrations move through the detector like neutrally-charged particles. These carry "non-ionizing energy" (or "phonon energy").

We will talk more about the particles inside the detector in the next chapter.

2.2 Apparatus

Fig. 2.2 illustrates the full apparatus used in the Soudan experiment. As WIMPs are expected to interact rarely and weakly with the detectors, the several shielding layers surrounding them are important for removing backgrounds that would interact easily and obscure such rare, faint WIMP signal events. Section 2.2.1 will describe the outer shielding layers of this setup and the unwanted backgrounds they are meant to mitigate. Section 2.2.2 then will briefly describe the detectors in the middle of the apparatus (inside the cryostat); the next chapter will cover how the detectors actually respond to energy deposits in more detail. For more about the apparatus, see Refs. [35, 36].

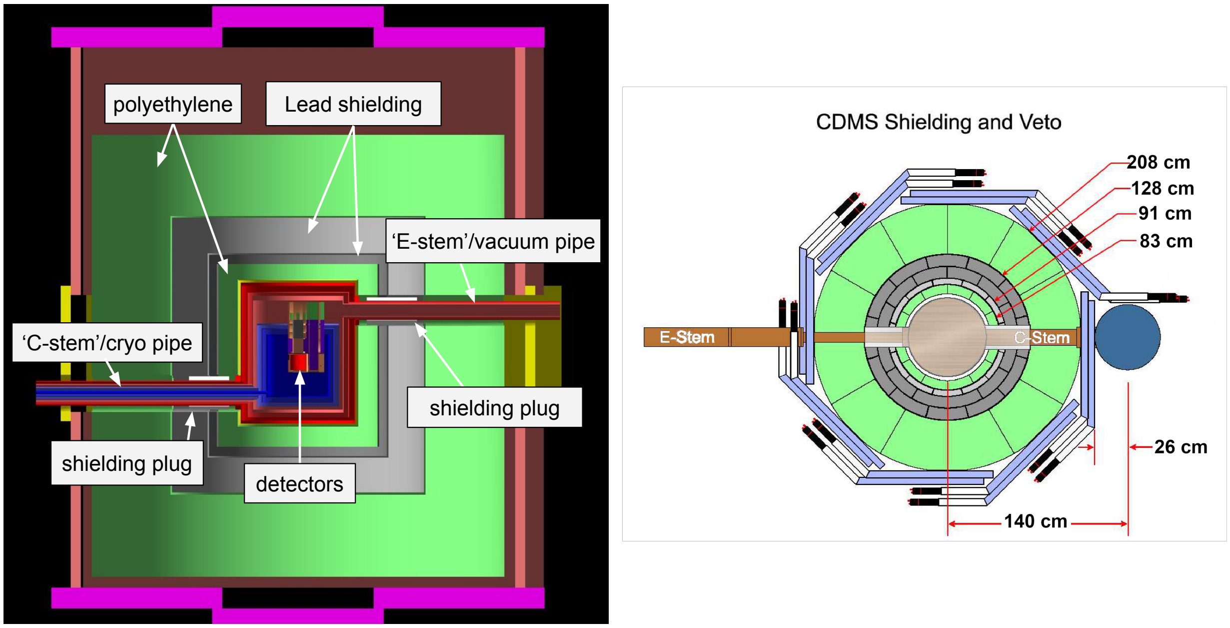

Figure 2.2: This figure shows two views of the apparatus used at Soudan and its components, including the detectors in the middle and the two access pipes on opposite sides. At left is a side view and at right is a top-down view. The detectors, in the very middle, are kept at microKelvin temperatures by the cryostat (the red and blue rectangle in the left image), which also provides some shielding from backgrounds. Outside that are larger, more dedicated shielding layers to reduce backgrounds of various kinds. For example, the polyethylene (green) slows down neutrons while the lead (grey) blocks photons. The overlapping veto panels, visible in the right image, allows us to identify external events that aren't blocked by the shielding. The "E-stem" and "C-stem" pipes provide connections to the electronics and cryogenics, respectively, but also allow calibration sources to be placed closer to the detectors–past some of the shielding.

2.2.1 Shielding and Associated Backgrounds

Here we describe the shielding layers of the apparatus and the cosmogenic and radiogenic backgrounds they are meant to mitigate (note before we proceed that none of them will be 100%-effective); in the next chapter we will discuss additional backgrounds due to mismeasured events. In other words, this section covers sources of events that are entirely unwanted and can (or can't) be blocked with hardware, while the next chapter will address ways in which events that *are* wanted may be poorly-measured (though unwanted events will also be affected in some of the same ways).

2.2.1.1 Apparatus Hardware

The outermost shielding layers are meant to reduce backgrounds from muons produced in cosmic rays. One could say the very first level of "shielding" is actually provided by the Earth's crust, which blocks muons produced in cosmic rays[37]; the experiment's location in Soudan mine–2341ft, or 713m below ground–puts it under an amount of rock equivalent to 2090m of water, which reduces the muon flux by a factor of about 50,000[36]. Muons that do manage to pass through the rock and reach the experiment itself are handled by the outermost layer of shielding proper: a set of "veto" panels, which record when external particles (muon or otherwise) have entered from outside the experiment. Flagged by the veto panels, such events due to external particles can then be excluded from WIMP-search analyses (WIMPs would also enter the experiment from outside, but they would interact too rarely to show up both in the veto panels and the detectors themselves).

The next few layers of shielding within the veto panels are meant to block neutrons and photons–which could be created by muon interactions or local radioactivity. First is a 40cm layer of polyethylene, which moderates neutrons (i.e. slows them down and reduces their energies). Inside that is a two-part layer of lead–18cm of modern lead and then 4.5cm of ancient, low-activity lead; these block photons–the inner, more inert layer blocking radiation from the outer layer. Within this is another 10cm of polyethylene to block neutrons–again from radioactivity in the lead (or interactions with other particles in the lead)[35, 36].

In the middle, finally, is the cryostat, which has multiple components we will not describe in detail. Overall, though, they contribute a few centimeters of copper, which blocks alpha and beta particles[36].

There are two major but necessary holes in the shielding layers described above:

- The electronics pipe (or "E-stem") is where the cables connecting the detectors' readout electronics to the external Data AcQuisition–or "DAQ"– system run.
- The cryogenics pipe ("C-stem") connects to the dilution refrigerator that keeps the detectors at operating temperatures. The refrigerator has to be outside the shielding both because it is noisy (in terms of electronics) and because it is not free of radioactive contaminants[35].

While on the one hand these pipes are gaps in our defenses, so to speak, they do have additional utility beyond the functions noted above: they provide locations for us to place calibration sources close to the detectors, as will be described in section 2.3.

2.2.1.2 Caveats and Summary of Backgrounds

We note that while neutrinos are expected to frequently pass through the apparatus, they have such low energies and interaction rates that they can be neglected in this iteration of the experiment–no additional shielding required. More sensitive detectors in the near future will have to deal with these neutrino backgrounds, however [38].

The remaining sources of backgrounds cannot be blocked by shielding: radioactive contaminants in and around the detectors. The most problematic source is contamination by Pb-210, which is a product of the decay chain of radon, which settles in and on detector components during fabrication and assembly. Pb-210 has a half-life of over 22 years, meaning it and its daughters will be consistent sources of gammas, betas, and even alphas–which may cause problematic NR events. Somewhat less worrisome are activations (nuclei becoming excited) in the detectors themselves, as zinc, gallium, and germanium isotopes produced due to either cosmogenics or neutron calibrations (described in the next section) gradually de-excite. These are fairly well-understood energies and CDMS constructed a model for these backgrounds to deal with them during analysis[28].

Cosmogenic Backgrounds		
Background Source	Recoil Type	Mitigation Method
Photons and charged particles ("Compton background")	ER	Mostly shielded; otherwise discriminated as different than NRs during analysis
Muons	ER	Shielded or vetoed
Neutrons	NR	Shielded; rates studied via simulation
Neutrinos	NR	Neglected, as their energies and interaction rates are too small for Soudan

Contaminants In or Near Detectors		
Background Source	Recoil Type	Mitigation Method
Ge Activation	ER	Accounted-for in analysis
Pb implantation	NR	Accounted-for in analysis

Table 2.1: This table lists backgrounds or other events we'll have to account for when trying to identify WIMPs in data, including the relevant recoil type (ER or NR) and how CDMS deals with them. We include this primarily for completeness in our description of the apparatus/experimental setup; we won't discuss these further, though these could also be studied in simulations. For further information, see Ref. [34], (the source of this table).

We've now discussed all the outer, shielding layers of the apparatus and the backgrounds that motivate them. In the next section we'll move to the the very center of the apparatus to discuss the detectors. For now we conclude with table 2.1, summarizing the backgrounds the detectors may have to deal with.

2.2.2 iZIP Detectors

The detectors, located in the center of the apparatus and arranged as shown in Fig. 2.3, are called "iZIPs": interleaved Z-sensitive Ionization and Phonon [detectors]. There were 15 of these detectors total, each a cylindrical germanium (hereafter "Ge") substrate comparable in size and shape to a hockey puck–except for a few flat sides cut into the outer edges–and weighing 0.6kg. The cryostat kept the detectors at milliKelvin temperatures for normal operation (further explanation in the next chapter). We provide a brief description of the detectors here; see Refs. [35, 39] for more detail.

On the top and bottom of each detector were arrays of charge and phonon sensors, as shown in Fig. 2.4. These consisted of lines of electrodes to collect charges and transition-edge-sensors ("TES"s) to collect phonons (note the TESs are actually part of larger components called "QETs", which will be described in the next chapter). The detectors are operated with an overall voltage difference (or "voltage bias," hereafter V_{bias}) of 4V between the faces, implemented by holding the charge electrodes at ± 2 V while the interleaved TESs are grounded. These interleaved voltages create an electric field in the detectors that is mostly uniform in the middle, but more complex near the faces. We will discuss the purpose and implications for this in the next chapter.

The particular iZIP variant used for the SuperCDMS Soudan experiment, the iZIP5, organizes the sensors into eight phonon channels and four charge channels, which are split evenly between the top and bottom detector faces; Fig. 2.4, again, shows how these channels are arranged. Because these channels can be read out individually, we are able to do a rough estimate for the location of events in the detector, based on which channels measure the most energy. Though this positioning information isn't very precise, it does give us some ability to judge the likelihood of events being well-measured (see section 3.2.4).

2.3 Calibration with Ba-133 and Cf-252

We've so far mentioned the dark matter events we want to see and the non-dark-matter events we don't want to see (during WIMP-search running modes, at least); now we discuss two sources of non-dark-matter events that are purposefully introduced: the calibration sources Ba-133 and Cf-252. Chapter 5 will discuss the physics of these sources in more detail, but here we describe their basic purpose and usage in the experiment.

As mentioned in the previous chapter, these two sources have useful, known behaviors–be they particular energies or recoil types–that allow us to calibrate the detector output and determine how both WIMP-like events and non-WIMP-like events should appear in our data:

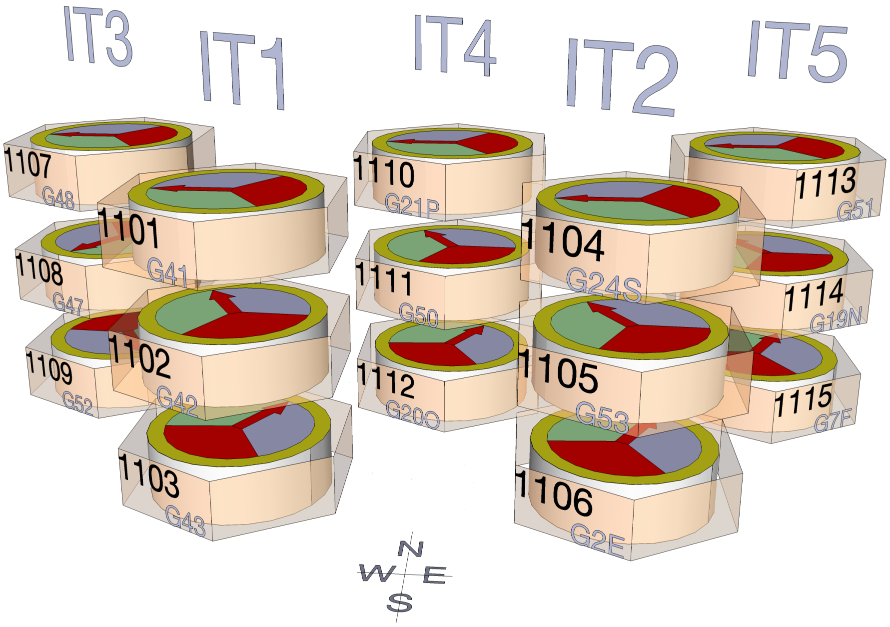

Figure 2.3: This figure shows the layout of the 15 detectors used at Soudan, which were organized into five "towers" of three detectors each in the middle of the cryostat, as shown in Fig 2.2. This is shown because even though we'll be focusing on single detectors here, the presence of other detectors affects the readings of those adjacent (e.g. by blocking incoming particles or contributing electronics noise). The towers were arranged asymmetrically, as shown, and located near one another in the center of the apparatus. The labels in this figure represent three sets of hardware and analysis names, but as we will be focusing only on individual detectors, we won't use these labels.

- Ba-133 is very useful for calibration of charge and phonon energies. It primarily emits photons[3]–causing only ERs–and its 356 keV photon line in particular is easily-identified in data.

- Cf-252, given energy calibration from Ba-133, is useful for demonstrating WIMP-like and non-WIMP-like events. It emits multiple particles, including both neutrons and photons, so it causes both ERs and NRs, signaling to us how well they can be distinguished. Additionally, the neutrons may also convert Ge-70 atoms in the detectors into Ge-71, which emits an identifiable 10.36 keV line (with a half-life 11.43 days) that can be used to supplement or

---

[3] It emits electrons and neutrinos as well, but these won't cause signals in the detectors.

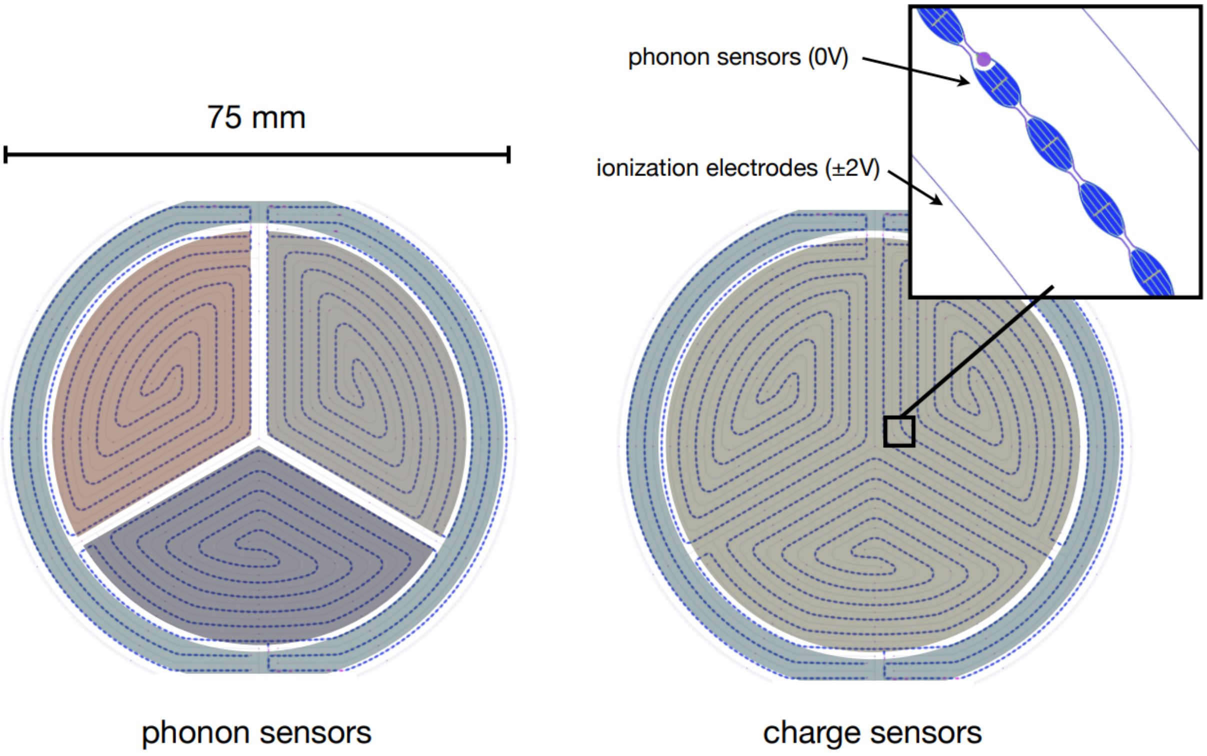

Figure 2.4: This figure shows both the charge and phonon sensor layouts on the iZIP5 detector faces. The bumpy blue lines are the phonon sensors–which are visible as well in Fig 1.5–while the thinner charge sensors are in-between those. The colored regions on the left indicate the distinct phonon sensor groupings and those on the right show charge sensor groupings. Having distinct readouts for each of these regions gives us both energy and position information. Note that both sides of the detectors have these divisions (so there are eight total phonon sensor groupings and four total charge sensor groupings). Note also that the sensors themselves are shown in both images, though only the QETs (phonon sensors) are visually apparent. Taken from Ref. [35].

replace the Ba-133 energy calibration[25, 27]; we refer to this as "germanium activation."

Fig. 2.5 shows the two locations where the calibration sources could be placed in the apparatus–along the cryogenics and electronics pipes, up against the shielding plugs; note that both locations were not necessarily used at the same time. Ba-133 sources were inserted into the apparatus several times a week–usually into both locations at the same time, though there were several single-source runs as well. A single Cf-252 source was used only every few months[25] to reduce the germanium activation backgrounds. Note that during the times that these sources were inserted (and for some time after Cf-252, due to Ge-71 activation) no events were considered as potential

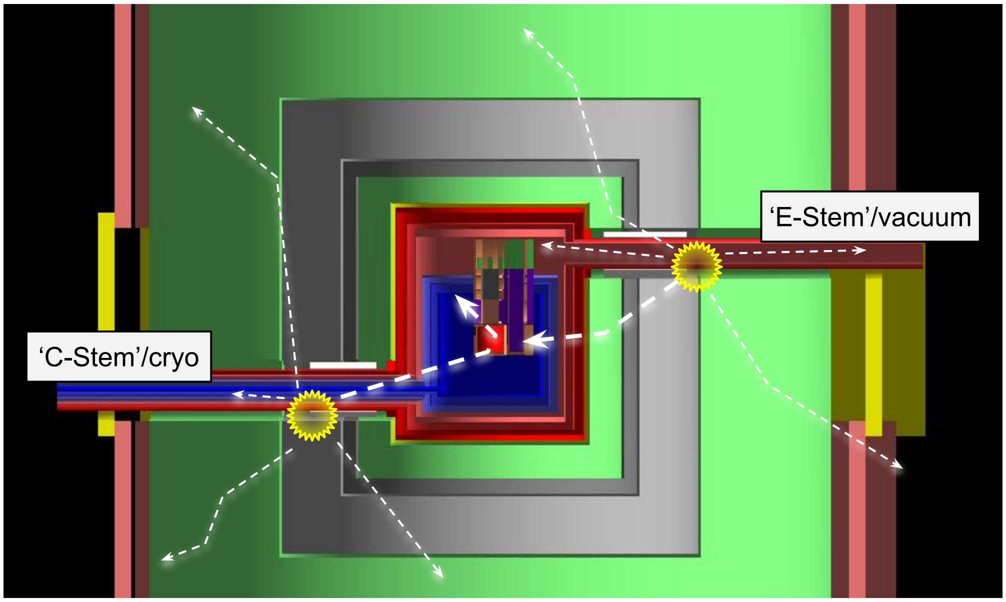

Figure 2.5: This figure is the same as the left image in Fig 2.2 but highlights only the locations where the Ba-133 and Cf-252 sources can be during calibration data-taking runs and shows some example particle paths. We show this because these two sources provide the data we'll focus on in this thesis. Wafers of a given source were occasionally placed in one or both of the electronics ("E-Stem" or "vacuum") pipe or cryogenics ("C-Stem" or "cryo") pipe, up against the shielding plug–locations marked with yellow sunbursts in the figure. Decay particles would be emitted isotropically from those locations, with only a relatively small proportion of them bouncing their way to the detectors in the middle (the myriad possible bounces along the way not shown). For future reference, note that chapter 7 will involve simulations with C-Stem sources while subsequent chapters will have E-Stem sources.

WIMP candidates; that is, WIMP-search times and calibration times were mutually exclusive.

2.4 Energy Losses in the Apparatus

To summarize, broadly, the experimental setup is such that we expect three sources of energy deposits: the searched-for dark-matter signals, the unwanted contaminant backgrounds, and the purposefully-introduced calibration source particles (when the sources are inserted). The final consideration at this point is how much measureable energy the particles from each of these sources actually deposit, as much of that energy will not make it all the way through the apparatus to the detectors–i.e. it is "lost" along the way.

This is, of course, the purpose of the shielding surrounding the detectors: it is meant to stop unwanted backgrounds from depositing energies in the detectors. However, while it isn't expected to affect the rarely-interacting WIMPs, the shielding does also moderate the energies of primary particles we look for from the calibration sources; as shown in Fig. 2.5, even being inserted into the two access tubes does not provide particles from the calibration sources a direct path to the detectors.

During calibration runs, photons and neutrons emitted from the sources in the E-stem and C-stem pipes will often scatter off other components in the apparatus–losing energy each time–before finally reaching the detectors we actually want to calibrate. Further, the detectors block one another: if we consider only a single detector (as we will for simulations in the following chapters), its energy spectrum will be reduced simply because some of that energy was likely deposited in an adjacent detector as well.

These considerations mean that, even ignoring the inner workings of the detector themselves, we should expect some non-unity efficiency in our energy collection (that is, the ratio of observed to true/original energy is less than 1). That means, for example, that photons emitted from the Ba-133 source with 356 keV won't necessarily deposit 356 keV in the detectors–nor will the corresponding peak in the data have perfect resolution (i.e. there will be variations), even if the detectors themselves somehow had perfect resolution. Hence, in part, the need for calibration in the first place–and our interest in using simulations to better understand exactly how energies propagate to and through the detectors. In the next chapter we will discuss physical processes that further complicate our data and motivate our simulation work here.

3. DETECTOR PHYSICS

The previous chapter described the experimental setup and the particles and energies that could reach the detectors. In this chapter we discuss how the iZIP5s react to those particles and energies– i.e. the physics that happens within the detectors themselves and what kind of output the detectors give us. The next chapter will round out our description of the experiment by describing the reconstruction and analysis done on that detector output.

Here we will cover what happens during energy depositions (in section 3.1), how those energies propagate to the sensors as charges and phonons (and new phonons created along the way–in section 3.2), and how the sensors react to those charges and phonons (section 3.3). Fig. 3.1 shows a cartoon of these processes in a detector. Each of these processes have their own mechanisms of energy loss, which we will discuss at the end of each section and then summarize at the end of the chapter. Note that the descriptions given here are somewhat brief. For more complete discussions, see Ref. [17] for the phonon system, Ref. [40] for charges, and Ref. [39] for a look at both across the CDMSII and SuperCDMS experiments.

Throughout this chapter keep in mind our goal: we want to collect all the charges and phonons produced by hits in the detectors, use their energies to determine the recoil energy and ionization yield of each event, and from that infer what kind of particle hit the detector in the first place. If we do not collect all the charges and phonons, then, we might mismeasure the relevant energies and misidentify the particles involved.

3.1 Energy Deposition In the Crystal

As suggested by the name, iZIPs are able to measure both ionization and phonon energies in the detector crystals. As noted previously, being able to collect both is important for identifying what kind of particle could have caused a given energy deposition. In this section we describe the relationship between the initial recoil energies of hits, and the resulting charge and phonon energies released into the detector. Section 3.1.1 describes how individual ERs and NRs split up

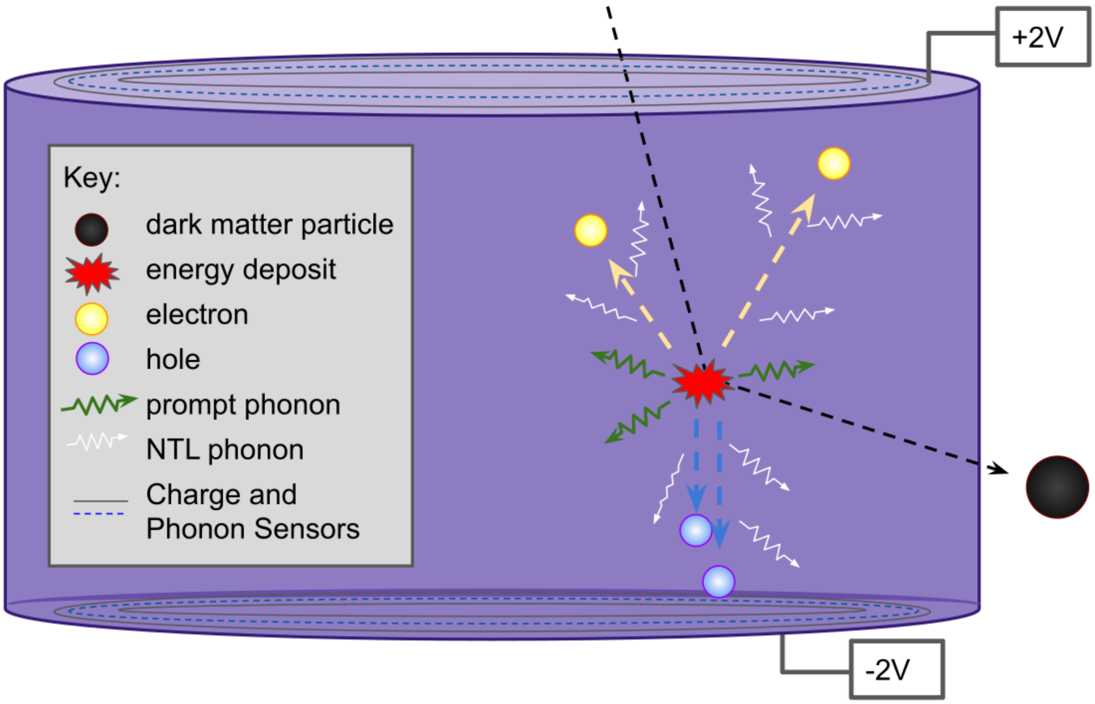

Figure 3.1: This figure shows a cartoon of a dark matter particle depositing energy in an iZIP detector and the particles we collect for readout and measurement. Here the dark matter particle enters from the top, interacts only once (as expected) and leaves the volume. The initial deposit creates both prompt phonons and electron-hole pairs that drift apart (electrons following valleys) and emit NTL phonons on their way to to the detector faces, where they are collected by the interleaved charge and phonon sensors

their energies during hits, section 3.1.2 describes events containing both ERs and NRs together, and section 3.1.3 addresses potential energy losses. Note that here we only discuss what happens in the initial hits; section 3.2 will address where the charges and phonons go from there.

Beginning with an initial hit, the total recoil energy E_{recoil} imparted to the detector by an external particle is distributed between ionizing and non-ionizing energies at the point of impact:

$$E_{recoil} = E_Q + E_{Ph,primary} \tag{3.1}$$

where E_Q represents charge energy and $E_{Ph,primary}$ represents only the phonon energies created in the original hit; there are other contributions to phonon energy that we will discuss later in this chapter. We can estimate the number of electron-hole pairs created (N_{eh}) by dividing the total charge energy by the single-charge-pair ionization energy in low-temperature germanium, 2.96eV [41], (E_{eh}):

$$N_{eh} = \frac{E_Q}{E_{eh}}. \tag{3.2}$$

The number of charge pairs is quantized, of course; any leftover energy contributes to the kinetic energy of the freed charges. However, the above equation only provides an average; the exact number of charge pairs created for events of a given recoil energy is subject to variations known as "Fano fluctuations" or "Fano noise"[42]; outside of very low-energy events, though, such fluctuations will not be significant to us.

The amount of energy that goes into each of the charge and phonon systems is described by the "ionization yield"–or just "yield" for short–which is the ratio of ionizing energy to recoil energy. We will refer to the true value of this as the "expected Yield", Y_{Exp}, given by:

$$Y_{Exp} = \frac{E_Q}{E_{recoil}}. \tag{3.3}$$

3.1.1 Electron and Nuclear Recoils, Charge Liberation and Lattice Vibrations, and the Lindhard Model and Yields

The yield is important to the CDMS experiment because it is different between ERs and NRs. This is because different particles interacting with the crystal lattice typically distribute their energy differently:

- Photons and electrons (or other charged particles) cause electron recoils: they interact with the electrons surrounding the nuclei in the detector crystals, ionizing them and creating electron-hole pairs that can drift to and be picked up by the sensors on the faces of the detectors (these drifting charges will also create phonons along the way via Neganov-Trofimov-Luke (or simply "NTL" or "Luke") gain[43]; see section 3.2.2). Any interaction with the nuclei themselves is negligible.

- WIMPs and neutrons (electrically-neutral particles) instead cause nuclear recoils: they bounce off the nuclei of the lattice, both causing the nuclei to recoil and also shaking off some electrons. The energy deposited in this case will be split among freed charges and phonons according to a yield described by the Lindhard Model [44] (see below).

The expected yield can be calculated for individual hits of known energies. Because ERs only *ionize* atoms when they hit, their *ionization yield* is just unity. The energy from an NR, meanwhile, is split up between ionization and phonon creation; this partitioning and the resulting yield is described quantitatively by the Lindhard model[44]:

$$Y_{Exp} = \begin{cases} 1 & ERs \\ Y_{Lindhard} & NRs. \end{cases} \tag{3.4}$$

$$Y_{Lindhard} = \frac{k * g(\epsilon_L)}{1 + k * g(\epsilon_L)} \tag{3.5}$$

where $Y_{Lindhard}$ is the "Lindhard Yield"[1], k is the electronic stopping (i.e. a measure of how much energy a particle loses per unit length), ϵ_L is a rescaled/dimensionless form of the recoil energy, and the function $g(\epsilon_L)$ is determined semi-empirically[2]. Establishing these equations and quantities is beyond the scope of this work; refer to Ref. [44] for the original derivation, Ref. [45] for application to dark matter direct detection, and chapter 3 of Ref. [39] for a less thoroughly-technical description. For now, note simply that $Y_{Lindhard}$ rises with recoil energy. Figure 3.2 shows the expected yields and corresponding ionization and phonon energies for ERs and NRs.

Note, however, that in the real experiment we are working backwards: with the energies we measure, we calculate the yield and infer what happened in the original hit. This is important because we can't pick out individual ERs and NRs if there are multiple hits in the same detector within a given readout window (that is, within the same event). The next section will discuss the

---

[1] Note that for brevity we may use the term "Lindhard Yield" to refer to both the ER and NR yields at the same time, though the term, strictly, only applies to NRs.

[2] In these quantities I use the subscript in ϵ_L to signify this is Lindhard's ϵ. In chapter 8 I will be using the ϵ character for unrelated quantities.

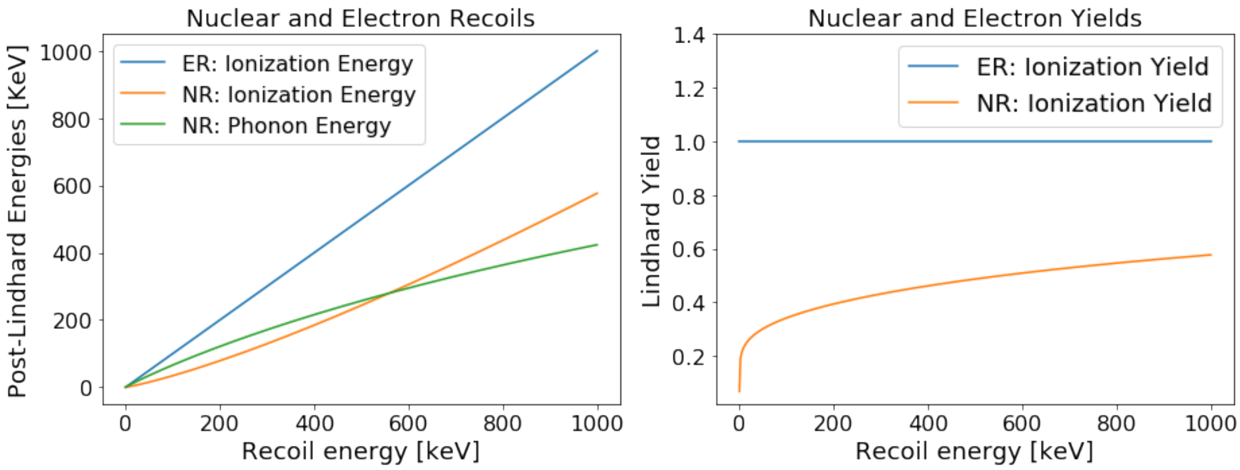

Figure 3.2: This figure shows two depictions of how energy is divided between charge liberation and phonon creation for ER and NR interactions according to the Lindhard model. The different behaviors seen here allow us to distinguish between the two recoil types, as was seen in Fig 1.8. As shown in the left image, ERs only impart ionizing energy, meaning they only liberate charge pairs. NRs, meanwhile, split their energy between ionizing energy and non-ionizing energy, meaning they also create lattice vibrations, or "phonons", that propagate through the detector crystal. Importantly, the fraction of ionizing (and non-ionizing) energy in NRs is not constant–as it is for ERs–and does not scale linearly with recoil energy. This is shown in the plot to the right, which shows the expected ionization yield as defined in 3.4 for ERs and NRs: while that for ERs always equals one, the NR Lindhard Yield is a function of recoil energy.

various combinations of recoils that we have to deal with in real data.

3.1.2 Single- and Multiple-Interaction Events and Associated Yields

ERs and NRs–as lone, individual hits–are the two fundamental types of particle-atom interactions in play, but not every event–which may consist of multiple hits or incident particles–can be classified as simply one or the other. Our calibration sources, for instance, will emit multiple photons or neutrons at once–and these may knock out further particles on the way to the detectors–meaning there can be multiple ERs and/or NRs that occur in quick succession (i.e. within the readout time window, such that they look like a single hit) in a given detector.

As will be seen later in our simulation results, events with mixtures of ER/NR interactions do still follow some broad patterns we may be able to pick out in data. For now, we identify the following energy deposition patterns:

- Simple nuclear recoil: a single neutral particle scatters off a single lattice nucleus, depositing detectable energy and causing no other effects–i.e. a single, identifiable NR. Illustrated in Fig. 3.3.

- Electron recoil: photons or charged particles interact with atoms to deposit energy. In theory this could be as simple as, e.g., a photon that is absorbed and an electron that is released, but more likely there would be several interactions close together that we treat as one (which is valid since they all have yields of 1). Illustrated in Fig. 3.3

- Quasielastic: a neutron scatters off a nucleus and continues on, but also leaves the nucleus in an excited state; the nucleus then de-excites soon after, emitting photons and/or electrons. Illustrated in Fig. 3.4

- Neutron Capture: similar to quasielastic but the neutron does not leave; it is captured by the nucleus, which again de-excites soon after, emitting photons or electrons. Illustrated in Fig. 3.4

- Inelastic[3]: a neutron strikes a nucleus hard enough to knock out something big–such as another nucleon. There may also be de-excitation photons and electrons. Illustrated in Fig. 3.4

- Multi-nuclear-recoils: For our purposes, we identify this category as multiple simple nuclear recoils (in the sense defined above) caused by either a single neutron bouncing multiple times or multiple neutrons bouncing off multiple nuclei. These multiple bounces could cause any combination of the previous effects, but we will identify such an event with those specific other cases. Illustrated in Fig. 3.5.

- Mixed events: Events in which an electron/photon and a neutron deposit energies in such quick succession that we cannot identify them as separate events in our results. This could easily be caused by, for example, a neutron scattering quasielastically in one detector and

---

[3] The previous two categories may also be described as "inelastic"; here we use the term to mean "other inelastic"

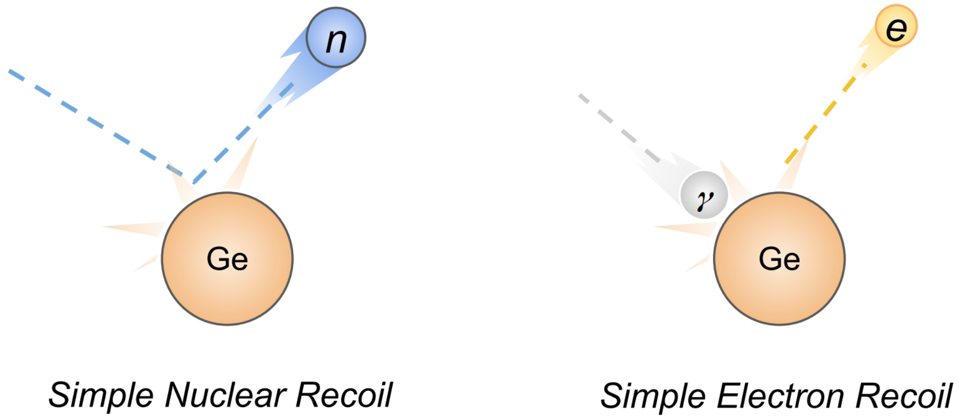

Figure 3.3: This figure shows the two simplest recoil types we expect to occur in our detectors, which will be the most easily-identified types of events in our data, as the energies we observe from them will adhere very closely to expectations from the Lindhard model. In a simple nuclear recoil, a neutron bounces off a (Ge-71) nucleus, transferring energy with no further effects. In a single electron recoil, either photons or charged particles interact with an atom, causing it to become excited or ionized, possibly emitting further photons or charged particles. Not shown here (or in the following two figures) are the phonons or charges created per the Lindhard model.

both it and the subsequent de-excitation particles from the nucleus it hit all depositing energy together in an adjacent detector. Illustrated in Fig. 3.5.

Keep in mind that for recoil patterns involving multiple hits, each hit has its own yield, charges, and phonons–but since in real detectors we collect the resulting energies all at once, we likely won't be able to distinguish each hit individually (like we will in simulations); instead we will have some conglomerate, "measured" energies and yields representing all the hits together.

It should be emphasized that the Lindhard Yield rises with recoil energy (as was shown in Fig. 3.2). This will be significant in the case of Multi-NRs, because it means that a neutron that scatters twice will always have a lower measured yield than a neutron that deposits the same total recoil energy in a single hit.

3.1.3 Energy Losses in Detector Hits

Particles that hit the detectors don't necessarily deposit all their energy–that is, the recoil energy E_{recoil} may be less than the incident energy (which itself may have already suffered from the energy

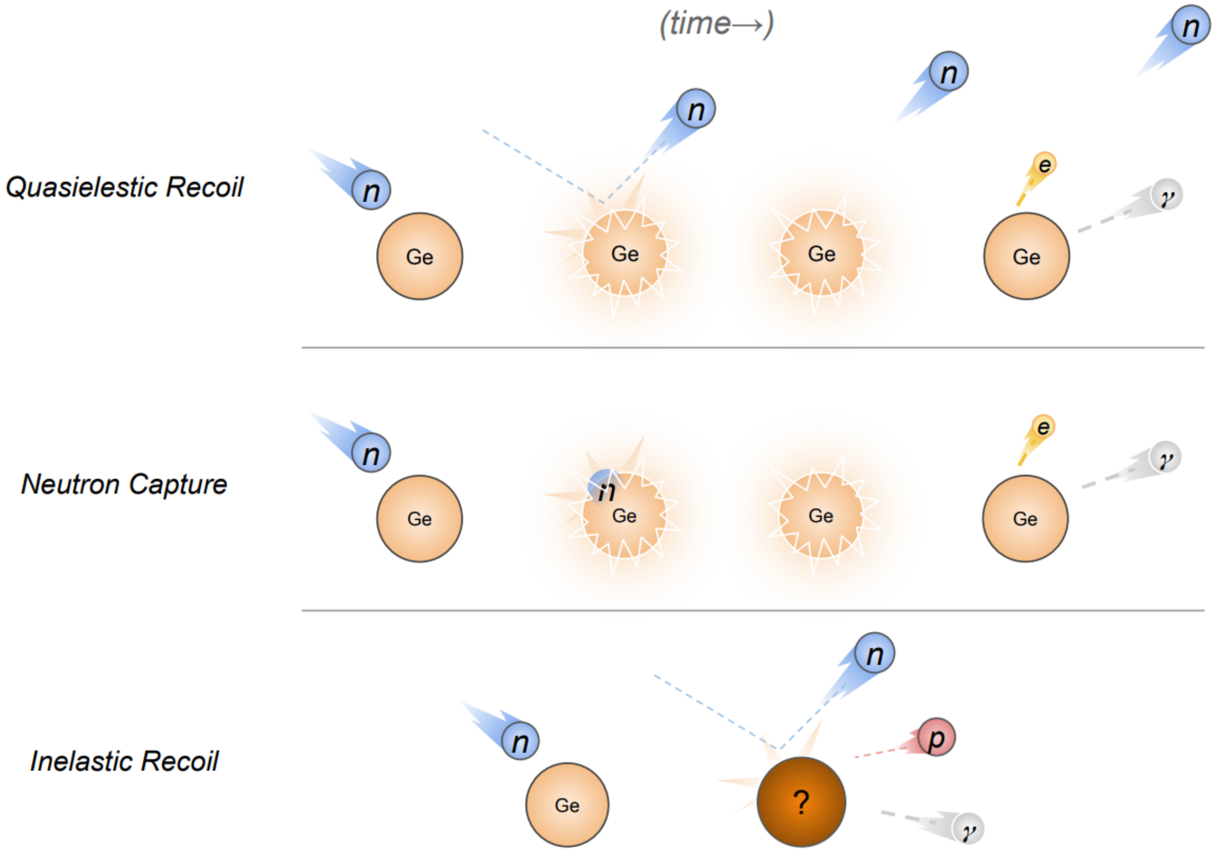

Figure 3.4: This figure shows three more complicated recoil types in which neutron interactions can create multiple outgoing particles. These types of interactions will be more difficult to interpret in our data because their overall yields will fall somewhere between those for simple ERs and NRs, since they will have aspects of both. Note that these might all be called "inelastic" collisions on the grounds that they have more particles leaving than entering, but we reserve that term for just the last, least-specific case. Quasielastic recoils, shown at the top here, are like simple nuclear recoils, but have more particles emitted due to an excited nucleus. Neutron captures–middle– are similar, but the neutron does not leave. Inelastic recoils–bottom– involve other heavy particles besides the neutron being emitted.

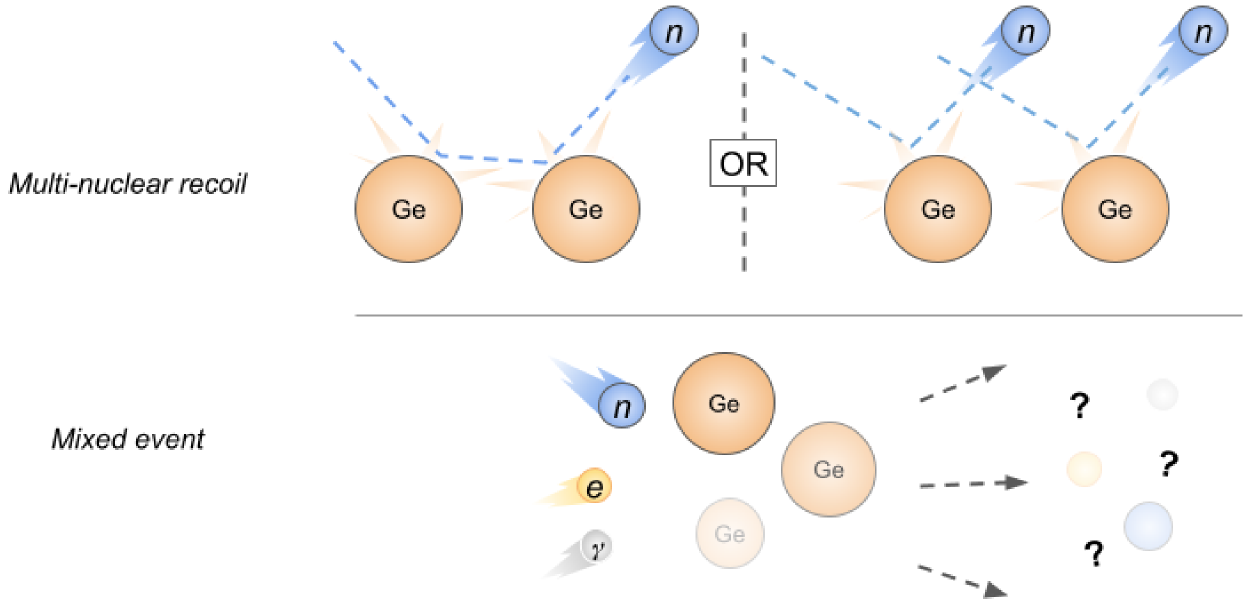

Figure 3.5: This figure shows the two recoil types that will be the most difficult to interpret, as they will involve multiple incident or target particles. The top half shows multi-nuclear recoils, where either a neutron interacts multiple times or multiple neutrons interact within a single event's readout time. Both variants will have measured yields that are different than that from a simple NR, due to the Lindhard yield changing non-linearly with energy. Shown at the bottom is a mixed event, which is just a grab bag: some complicated array of particles come in and any number of things could come back out (i.e. some combination of the previous recoil types).

losses discussed in section 2.4). Where a lower-energy neutron may be absorbed entirely, for example, a higher-energy neutron may only skim off detector nuclei, leaving only a small amount of energy. Similarly photons, via Compton scattering[46], may deposit full energy in a head-on collision with an atom but might also strike at an angle, leaving the detector with only a small amount of energy transferred.[4]

3.2 Motion of Charges and Phonons in the Detector Crystal

In this section we cover what happens in the crystal after the initial energy deposits, but before any of the energy has reached the readout circuits. Here we describe the motion of charges and phonons in a crystal lattice generally (section 3.2.1), how an applied voltage additionally splits up the charges and creates more phonons (section 3.2.2), and the potential ways energy might be lost through these processes (section 3.2.4).

3.2.1 Motion of Electrons, Holes, and Phonons in a Lattice

Every event will have some number of electrons, holes, and phonons that we collect to measure the original recoil energy and determine recoil type. Here we describe the different ways each kind of "particle" traverses the detector crystal. We do not cover all the relevant solid-state and semiconductor physics here; see Appendix A for some additional explanation or Refs. [40, 47, 48] for more thorough descriptions.

We start with charges. In the germanium CDMS detectors, the motion of electrons traveling to one face is different than that of holes traveling to the other[49] (they travel to different faces due to an applied electric field, described in the next subsection). Electrons prefer to travel along energetically-favorable "valleys" determined by the crystal lattice, occasionally jumping between them; these favored directions in a Ge-71 crystal are shown in Fig. 3.6. Holes, meanwhile, travel ballistically–not favoring any particular direction. Groups of electrons end up spreading out more than groups of holes, then, as was illustrated in Fig. 3.1.

Phonons also favor certain directions determined by the structure of the crystal lattice they are

---

[4] Fano fluctuations also mean we might get slightly less–or more–energy, but these are small effects.

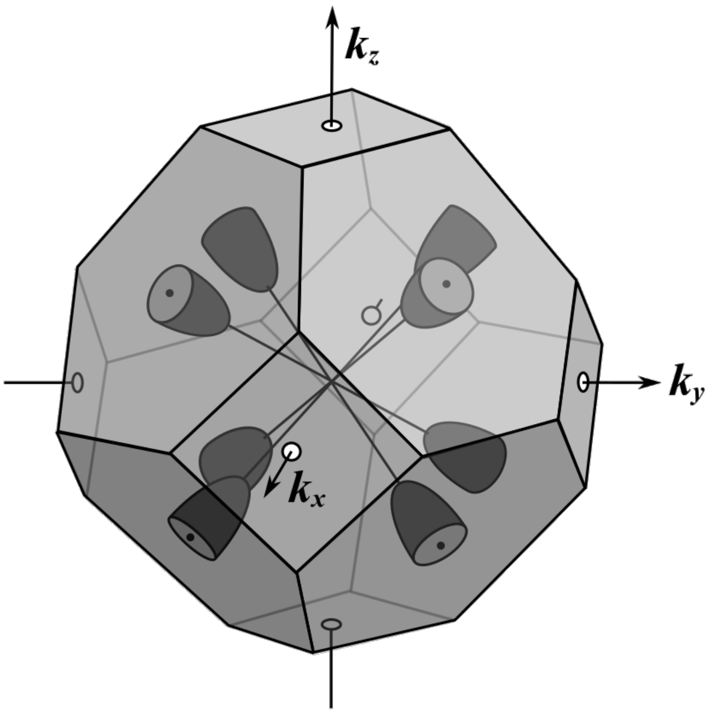

Figure 3.6: This figure shows a unit of a Ge-71 crystal and the preferred directions for electrons to travel in it (all shown in momentum-space–or "k-space", hence the axis labels). The Ge-71 crystal makes electrons favor the eight indicated diagonals; the iZIP's applied electric fields cause the electrons to favor the four upper diagonals while holes travel downwards. Holes do not favor the directions indicated for electrons; for details see appendix A. From Ref. [50].

in[51], though these are not the same as the valleys favored by charges. However, prompt phonons will very quickly split into new, lower-energy phonons (they "down-convert" via "anharmonic decay") or scatter off impurities (other isotopes) in the crystal[35]; such processes occur quickly enough that the phonons can be treated as being emitted isotropically from the original interaction point [52].

3.2.2 Effects of the Voltage Bias on Charge Motion and Phonon Creation

In addition to crystal physics, the populations of charges and phonons inside the detectors are also affected by an applied electric field (though the specific effects are different for each), shown in Fig. 3.7. Here we cover how this field affects the motion of charges, how it varies in different detector regions, and how it leads to more phonons being created.

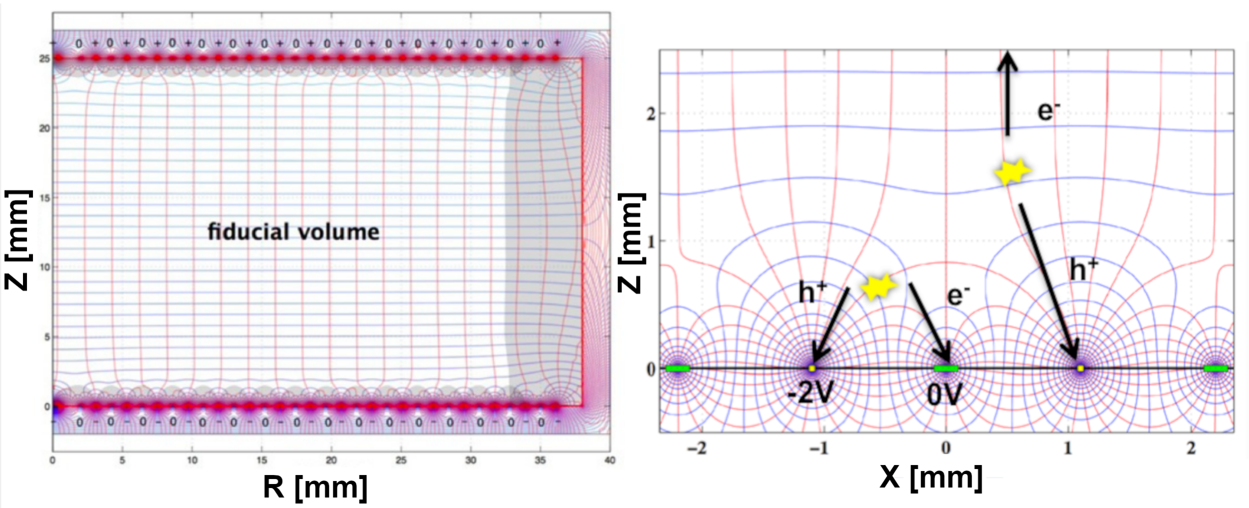

Figure 3.7: This figure shows two side views–one full and one zoomed-in–of an iZIP5, showing the electrodes, QET traces, and the resulting electric field lines they create. These fields determine how freed charges move through the crystal. The top electrodes are held at +2V, the bottom electrodes at -2V, and the QETs are grounded. The image on the left shows the full detector volume, in which resulting electric field is largely uniform in the bulk of the detector, but becomes uneven near the edges, changing rapidly near the electrodes in particular. The central, uniform region roughly marks out a "fiducial volume" in which events are expected to be well-measured. The image on the right shows a zoom-in of the "scalloped" electric field near the bottom of the detector, with example events. Electrons (e^-) and holes (h^+) created closer to the center of the detector will be split up and collected on separate sides–hopefully on the electrodes– while all the charge carriers from events close to the faces will be collected together. Original figure from Ref. [17].

Once electrons are freed from atoms in a hit, both types of charges are accelerated towards the detector faces due to the previously-mentioned 4V difference between them. This generally splits up charges such that electrons are collected at the top and holes are collected at the bottom–in theory giving us redundant charge measurements.

The motion of charges is complicated slightly–by design (and beyond the previous crystal considerations)–by the "interleaved" aspect of the iZIP sensors; this helps mitigate certain mismeasurements. Recall that the electrodes that collect the charges are kept at ± 2 V on each face, and these are interleaved with the grounded phonon sensors. This leaves a (mostly) uniform electric field in the bulk of the detector, but also creates a "scalloped" electric field at the detector faces. This is done purposefully to reduce the effects of "face events," in which hits occur very close to the detector faces. The problem with such events is that electrons and holes created near the faces may get stuck at the surfaces[5] and recombine with the lattice immediately, without traveling any significant distance–canceling each other out and causing us to lose charge signal. This was a significant problem for previous detectors, but the iZIP5's interleaved design and scalloped fields help mitigate this; the scalloped fields near the faces pull apart more of those charge pairs–but both are collected on the same detector side while the opposite side gets nothing. While this recovers some signal for one side, more importantly it creates a charge measurement asymmetry between the sides, indicating to us which events are edge events that should probably be excluded from analysis. Fig 3.7 illustrates these electrodes, fields, and charges. See Refs. [39, 40] for more details on these detector design considerations. Note also, lastly, that the electric field near the detector sidewalls is not quite as intricately-crafted as the field near the faces, since there are no sensors on the sidewalls; for the motion of charges in this high-R region, all bets are off and most events will likely be mismeasured.

The motion of charges in the electric field, further, will produce phonons [43]–this is in addition to the prompt phonons created in the initial recoil. In essence, the electrons and holes are accelerated by the electric field on the one hand, but decelerated by the interactions with the crystal lattice (e.g. NTL emission) on the other[6]. The energy transferred from the charges to the lattice in these interactions will then continue to propagate through the crystal as "NTL phonons" (named after the three authors who first described the effect). These propagate more or less as a cone radiating out from the trajectory of the charges. We can estimate the total energy of these secondary phonons based on the number of charges and the voltage bias:

$$E_{Ph,NTL} = N_{eh} * e * V_{bias} = E_Q * \frac{eV_{bias}}{E_{eh}} \tag{3.6}$$

where e is the electron charge and we have substituted in equation 3.2. In principle this should

---

[5] Though the electric field mostly drifts them in particular directions, there are small elements of "random-walk" in the motion of charges that can get them to the detector edges if they're close enough.

[6] The accelerating and decelerating forces (which become stronger with charge speed) balance out relatively quickly, so the charges settle at a sort of "terminal velocity"[52].

be independent of the Z-location of the original hit since any distance not covered by one of the electrons or the holes will be covered by the other–but there are several ways that a given charge may not traverse the full voltage drop (as will be discussed in section 3.2.4) and so not emit all the NTL phonons expected (which will be a form of energy loss).

3.2.3 Recombination Phonons and the Total Expected Phonon Energy

We now consider one final source of phonons, which is due to the *charge* system. As charges recombine to the lattice (at the electrodes or otherwise), they release energy–the same energy that was required to split up the charge pairs in the initial recoil[7], E_Q in equation 3.2–in the form of phonons; as such, we refer to these as "recombination phonons"[17, 39]. Because of this, all the original recoil energy makes it way back into the phonon system–either from the prompt phonons in the first place or from the charges returning their energy at recombination; NTL phonons add additional energy on top of this.

To summarize all the phonon energies we'll see, then: we will be collecting the primary phonons (in the case of NRs), the secondary/NTL phonons created as charges drift through the crystal, and the recombination phonons created when charges recombine with the lattice[51]. The recombination phonons–whose energies come from the originally-freed charges–can be combined with the primary phonons to sum to the original recoil energy:

$$\begin{aligned} E_{Ph} &= E_{Ph,primary} + E_{Ph,NTL} + E_{Ph,recombination} && (3.7) \\ &= E_{recoil} + E_{Ph,NTL} && (3.8) \end{aligned}$$

(compare eq. 3.1). Eq. 3.8 describes the final phonon energies we expect to read out. We will later

---

[7] Technically, it might be slightly less. Any leftover energy from the original hit that wasn't enough to split up another charge pair would have gone into charge velocities and subsequent NTL phonons instead of being recovered in recombination phonons. This amount would be small, though, and doesn't change the overall phonon energies anyways.

use a variant of this obtained by using equations 3.3 and 3.6:

$$E_{Ph} = E_{recoil} + E_Q * \frac{eV_{bias}}{E_{eh}} \tag{3.9}$$

$$= E_{recoil} * (1 + Y_{Exp} * \frac{eV_{bias}}{E_{eh}}). \tag{3.10}$$

3.2.4 Energy Losses in the Crystal

There are several mechanisms by which the energy of charges and phonons traversing the detector crystal might be lost. The three main processes by which charge energy is lost might broadly be described as "charges stopping in the wrong places"–but more precisely we'll call them "impurity charge trapping", "sidewall events", and "face events" (the latter two of these together we'll call "edge events" as they are due to interactions at the edges of the detectors, either horizontally or vertically). The phonon system will also lose some energy due to the above processes (and other, more subtle processes not covered here). We'll discuss each of these briefly here.

The first three charge loss mechanisms we have in mind are illustrated in illustrated in Fig. 3.8; they each involve charges that do not make it to the detector faces they are expected to. (These might all be referred-to as "charge-trapping", but we will reserve that term for the first item):

- Impurity charge trapping, which refers to electrons and/or holes becoming stuck in imperfections in the Ge-71 crystal [53, 54][8].

- Sidewall events, which have energy deposits at high radii, where charges (usually the electrons) travel sideways enough to land on–and potentially stick to–the sidewalls of the detectors. As there are no sensors on those edges, we lose those energies.

- Face events, introduced in the previous subsection, involve hits very close to the top or bottom edges of the detector, where electrons and holes might get stuck on the surfaces and recombine too quickly, reducing our charge measurements. As described previously, the

---

[8] In addition to their energy being lost to measurement, these stuck charges can accumulate over time and worsen the detectors' overall charge collection; to combat this, every so often during/between data collection runs the detectors would be grounded and exposed to LED lights to warm up and free trapped charges [35].

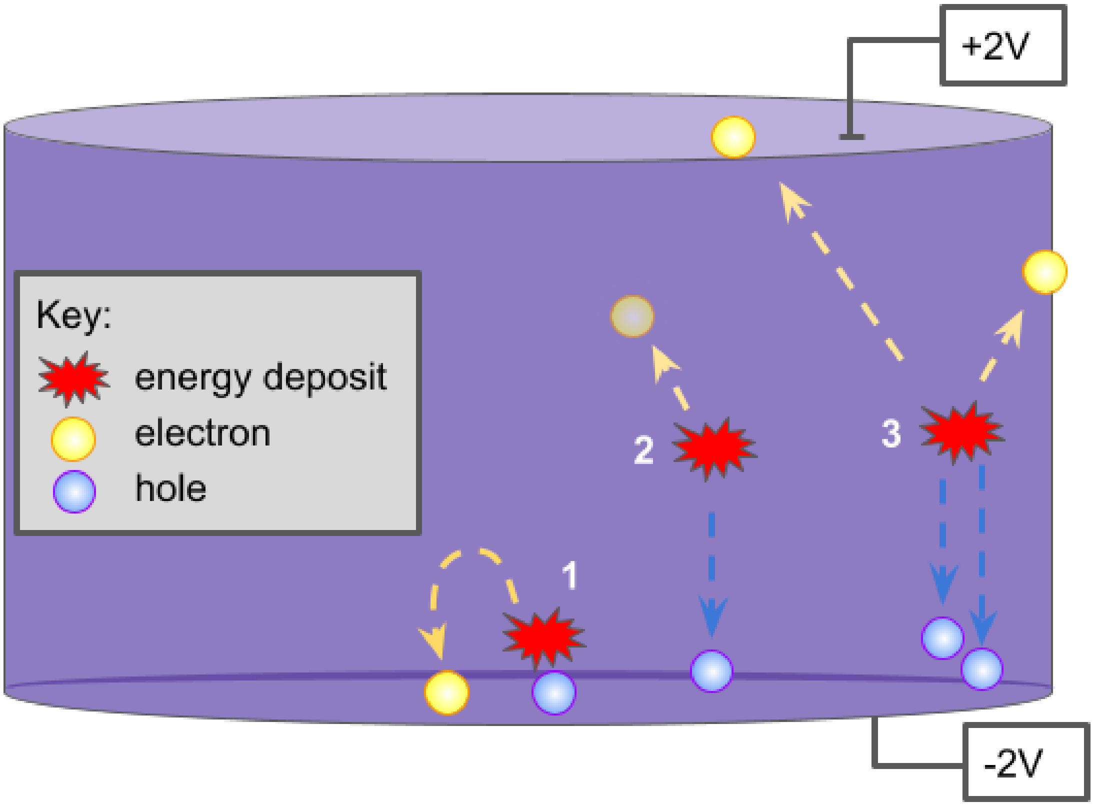

Figure 3.8: This figure shows a cartoon of three example interactions that would be poorly-measured due to charges not reaching the detector faces they are expected to. Energy deposit 1 shows a face event: as seen in Fig. 3.7, the electric field due to the interleaved electrodes and QET lines can capture both electrons and holes if a hit occurs close to a detector face. Energy deposit 2 shows "impurity charge trapping": defects in the crystal can catch charges before they reach the sensors. Energy deposit 3 shows a "sidewall event": hits at high radii can free charges that travel to the sidewall and get trapped. This is more common for electrons, which spread out further horizontally due to the valleys, but holes can do this as well.

interleaved electrode design helps mitigate/identify these as shown in Fig. 3.7.

A separate issue–and one that we will devote significant time to in future chapters–is illustrated in Figs 3.9 and 3.10. Even if charges reach the detector faces we expect them to, it's possible for them to "miss" the sensors they should be collected on. This happens most often for events located above or below bends in the electrodes (along the lines shown in Fig. 3.9) and more often for holes than electrons (though these details are currently only identifiable in simulations). We note two things:

- The red-dashed lines marked on Fig. 3.9 represent the highest density of bends in the iZIP5 electrodes. As there is slightly greater separation between the electrodes where they bend, the electric fields they create are slightly weaker.
- Because holes do not interact with the lattice as much as electrons do, they reach higher energies [47] and spread out less than electrons (as in Fig. 3.10).

This means that charges–holes in particular–may speed through the detector's scalloped electric fields at the faces and land off-electrode. As will be described in section 3.3.1, then, this means they do not induce the full charge signals they should. We will refer to these as "off-electrode" effects in reference to the behavior of the charges, but these affect phonons as well.

Energy losses in the phonon system have some overlap with the above charge mismeasurements, but the exact mechanisms are different. We note the two mechanisms most important for us here; refer to chapter 5 of Ref. [17] for more detail. Phonons generally just keep bouncing until all of them are absorbed (by the sensors or otherwise), but we may lose some of their expected energies if they are not created in the first place or become undetectable:

- Recall that charges being accelerated through the detector emit NTL phonons. This means that charges that are lost early via the mechanisms described above won't emit all the NTL phonons they would have if they'd reached the detector faces and traversed the full voltage bias; in other words, the V_{bias} term in equation 3.10 will be an overestimate.

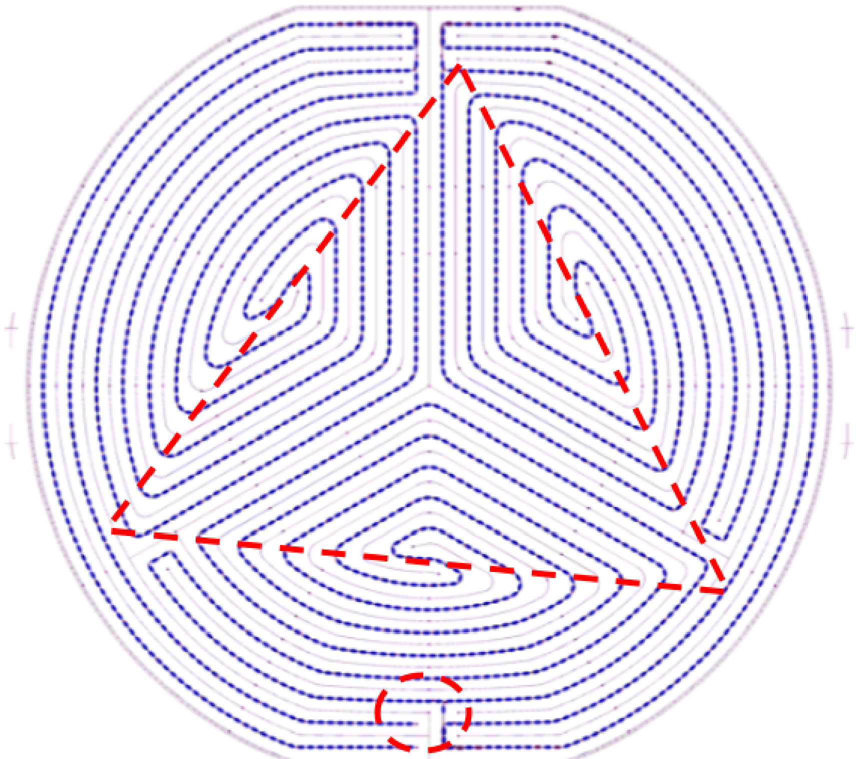

Figure 3.9: This figure shows the iZIP sensor layout (the blue lines are the TESs and the thinner lines in-between those are the charge-collection electrodes), but we've overlaid red dashed lines to indicate where charge mismeasurements are more likely. The marked paths have the highest concentration of electrode bends, where, on the iZIP5, the electrodes are slightly further apart from one another than usual; this in turn results in slightly weaker electric fields, which may not be able to direct all charges onto the electrodes. Per Fig 3.11, then, we expect there to be more mismeasurements than usual along these lines, though the position resolution of the real detector is not good enough to validate this prediction precisely.

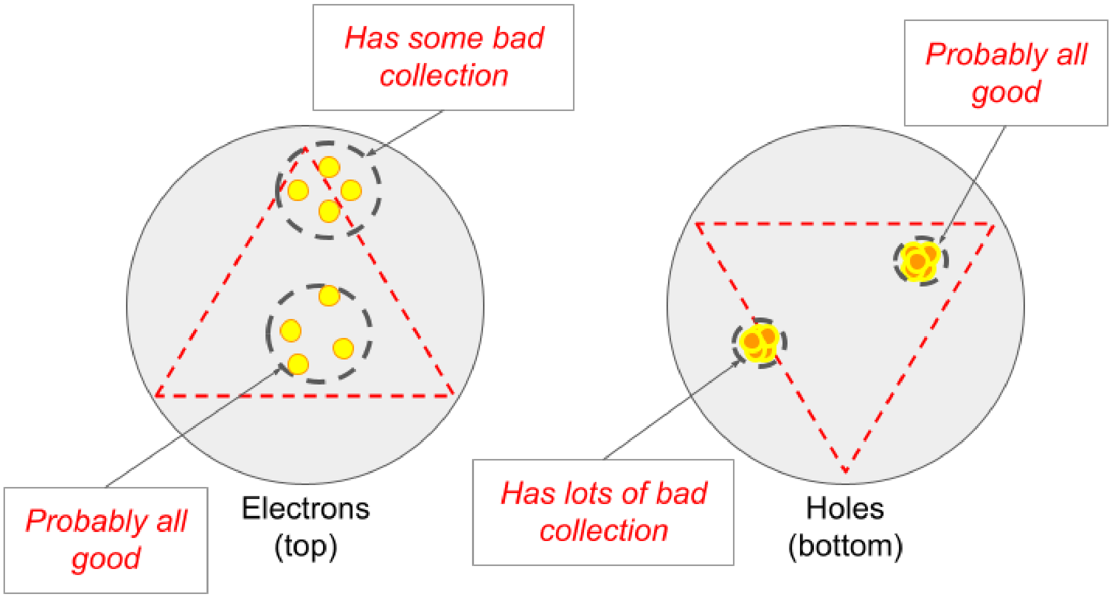

Figure 3.10: This figure shows a cartoon of electrons and holes when they are collected on the detector faces, highlighting the differences in how they each spread out. We show it because this difference in spread means the two kinds of charges are affected by the triangle of electrode bends differently. Left: electrons spread out due to valleys (refer to Figs 3.1 and 3.6), meaning in a cluster of electrons from a given hit, a relatively small portion of them will strike near the electrode bends and have an elevated chance of mismeasurement. Right: Holes do not spread out very much, meaning a given cluster is more likely to miss the electrode bends than a cluster of electrons, but when they *do* hit, it will be all together, which could dramatically cut the collected energy.

- Phonons that bounce around long enough may downconvert to such low energies that they can't be detected by the QETs[9]. Their energy (heat) is gradually pulled out of the detector by the cryostat. Ref. [17] estimates this to lose about 6% or less of the phonon energy.

3.3 Reading out Energies from the Detectors

Charges and phonons are collected on interleaved electrodes and TES lines, respectively, as was shown in Fig. 2.4. Here we provide more detail on how these particles are collected and where energy might be lost along the way. Section 3.3.1, first, describes how the charges are read out. Section 3.3.2 covers how the phonons–from all sources–are read out. Section 3.3.3, lastly, describes the ways energy could be mismeasured during these processes.

---

[9] For our purposes, this is "thermalization" even if the given phonon still has more energy than the thermal bath.

As noted previously, we won't be describing the collection circuits in detail; for more complete descriptions, refer to Ref. [17] for the phonon system and Ref. [40] for charge system. For sake of terminology, though, we note that the charge circuits involve field-effect transistor (FET) amplifiers, so for simplicity and symmetry, we refer to "FETs" and "TESs" for charge and phonon collection, respectively–even though the FETs themselves are not the components that measure charge energies in the way that TESs themselves measure phonon energies.

3.3.1 Charge Collection and Readout

Here we describe how charges are "collected" in the FET circuits, leading to our charge signals. As we'll describe, "collection" doesn't actually involve charges being moved into the electrodes.

Recall, firstly, that charges are collected on (or rather sensed by) bending lines of electrodes grouped into four charge channels, as was shown in Fig. 2.4–an inner channel and an outer channel for each side. The charge collection descriptions in the following paragraphs apply to each channel; what is gained by having multiple channels is some amount of position estimation. If the outer charge channels measure higher energies than the inner channels, for example, it means that there was likely an edge event–which are often mismeasured and so may be removed from analysis.

As for the charge energy measurement mechanism itself: though we use the term "charge collection," a signal does not necessitate charges actually being captured exactly on the iZIP5 electrodes; a charge at a distance can still induce a signal. The Shockley-Ramo Theorem [55, 56] provides a way to describe the contribution from any given charge at any location based on its magnitude and local electric field. This is illustrated in Fig. 3.11 and described below.

To apply the Shockley-Ramo Theorem to an array of electrodes and charges, first choose a single electrode, consider it to be at unit potential, and the others at ground; call the resulting field the "Ramo field," ϕ_{Ramo}. Then, for charged particle i, the induced charge, $Q_{ind,i}$ on the electrode is simply the product of the particle's charge q_i and the value of the Ramo field at its location r_i:

$$Q_{ind,i} = q_i \cdot \phi_{Ramo,i}(r_i) \tag{3.11}$$

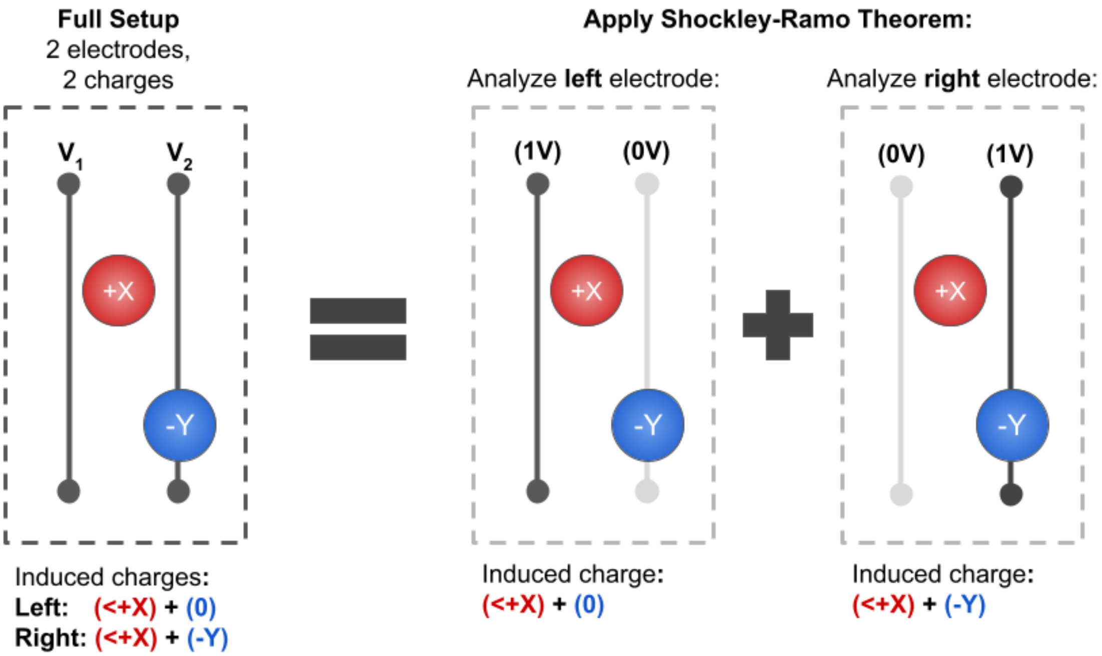

Figure 3.11: This figure shows an example event in which two charges are detected by two electrodes, demonstrating the use of the Shockley-Ramo Theorem to determine induced charge. The two electrodes–the vertical lines–have arbitrary voltages V_1 and V_2 and the two particles–red and blue– have arbitrary charges +X and -Y; the +X charge is absorbed between the electrodes and the -Y charge lands directly on the electrode to the right. It is determined that the red, +X charge is mismeasured and the blue, -Y charge is well-measured as follows. Per the Shockley-Ramo Theorem, we analyze each electrode individually, setting the given electrode to unitary potential and grounding the rest, which establishes the "Ramo field". Then for each particle, its charge multiplied by the Ramo field value at its location equals the induced charge on the analyzed electrode. As shown in the middle box, doing this for the left electrode shows it has an induced charge less than +X from the red particle (which is at distance) and no induced charge from the blue particle (which is grounded). The far-right box shows that the right electrode, meanwhile, again has only some induced charge due to the red particle but full induced charge from the blue. In total, then, the red charge is mismeasured on both electrodes and the blue charge is well-measured on one. We call the red charge "mismeasured" because in the experiment we use the output of the electrodes to estimate the original charge (the reverse of the above process), meaning, in this case, we'd assume a well-measured charge less than +X, as opposed to a +X that landed off-electrode.

and the total measured charge on the given electrode is just the sum of this product over all charges:

$$Q_{ind} = \sum_{i} q_i \phi_{Ramo,i}(r_i) \tag{3.12}$$

This can then simply be repeated for each electrode in turn.

Note that this description of charge collection provides a simple way to describe the charge mismeasurements covered in the section 3.2.4:

- Edge charge trapping and impurity charge trapping: in both cases, the particle is stuck somewhere where there are no electrodes, meaning the Ramo fields will all be near zero–and so the induced charges and final signals will be as well.
- Face events: if an electron and hole are created within the scalloped electric fields near the faces, one may be collected on the expected electrode and be measured correctly, but the other will be caught by the grounded TES lines, meaning no induced charge on the electrodes that "should have" collected it.

In a perfect detector where all the charges land exactly on the electrodes, $\phi_{Ramo,i}(r_i)$ would always equal 1.

3.3.2 Phonon Collection and Readout

Now we describe the hardware that collects phonon energies (in brief; see Ref. [17] for more detail). The detector faces have arrays of superconducting tungsten wires with aluminum fins to collect phonons; as with the charge channels, there are several groupings of sensors per detector side to provide some position information. As illustrated in Fig. 3.12, when a phonon deposits energy in the aluminum, it breaks Cooper pairs into quasiparticles that are then guided into the tungsten wires[10] that are being held right at the transition between superconducting and normal-conducting states (these are the transition-edge sensors–TESs–proper; the combined fin-and-TES arrangement is referred to as a QET, or quasiparticle-assisted electrothermal-feedback TES). The

---

[10] Phonons may also interact with and heat up the tungsten directly, but this is less common.

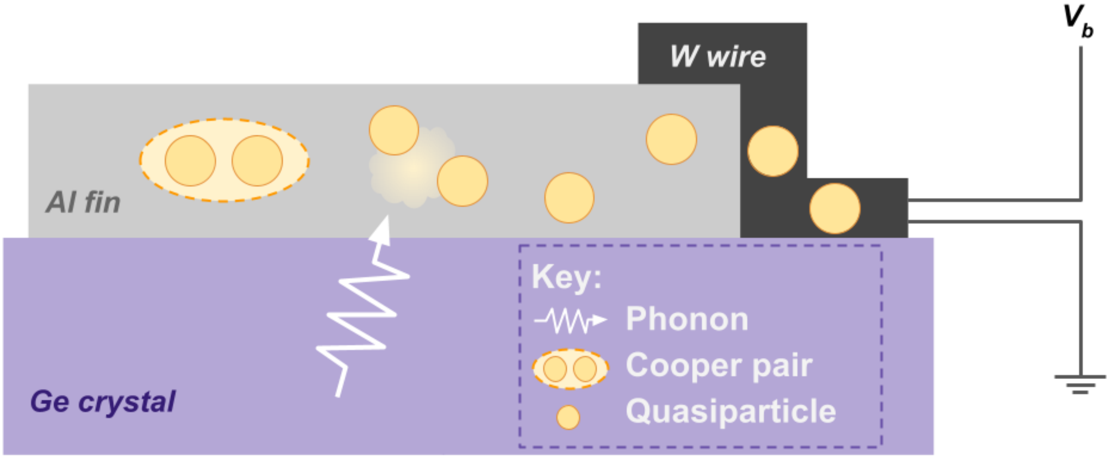

Figure 3.12: This figure shows a cross-section of a single QET on an detector face and how it converts phonon energy to a current in the readout circuitry. Phonons from the germanium (Ge) crystal are typically collected in the aluminum (Al) fin and break up Cooper pairs into quasiparticles. The quasiparticles are then guided into the superconducting tungsten (W) wire, which heats up and provides a signal, as described in Fig. 3.13.

energy gathered in the tungsten increases its temperature which, because the tungsten is operated right at its superconducting transition point, causes a relatively large change in its resistance, which is observed by a change in the current run through the sensors (and amplified with superconducting quantum interference devices, or SQUIDs); this is shown in Fig. 3.13.

Note that the tungsten is essentially operated with a constant voltage across it, which helps stabilize it around the superconducting critical temperature. The basics of this stabilization can be seen with just Ohms law (V=IR). With fixed voltage:

- A rise in resistance results in a smaller current, which produces less heat, which moves the system back to lower resistivity.
- Conversely, should the resistance drop, the current will increase and create more heat, which will push the resistance back up to its original value.

3.3.3 Energy Losses in Collected Energy Measurement

There are several ways for energies to be poorly-measured at the readout stage, but we do not cover them at length here because–looking ahead–we do not currently simulate many of these

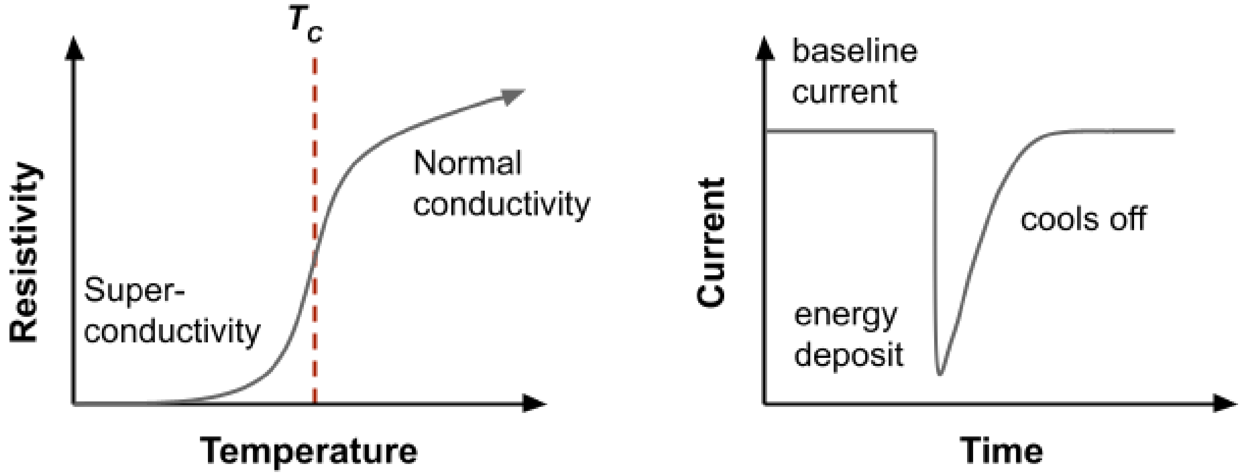

Figure 3.13: This figure shows the qualitative behavior of a superconductor's resistivity around its critical temperature (T_C) and how this affects the current running through the QETs as a function of time in the experiment. We show this because the transition between normal conductivity and superconductivity is central to the operation of a "transition edge" sensor (e.g. our iZIP phonon sensors). As shown on the left, by keeping the superconductor just at its critical temperature, any energy deposit causing even a small temperature change (i.e. vibrations, or phonons) will cause a drastic change in resistivity, in turn causing a noticeable change in the current running through the device, as shown on the right, which is then amplified to signal an energy deposit.

effects. See chapter 5 of Ref. [17] for more detail about phonon mismeasurements and chapter 6 of Ref. [34] for more about charge mismeasurements.

We note, firstly, some reasons that phonon energies that traverse the detector are not fully read-out by the QETs/TESs:

- The detectors have components other than the aluminum and tungsten QET components where the phonons could be absorbed. If phonons land on apparatus infrastructure like the detector holding clamps, for example, their energy is lost.
- The QETs, recall, are aluminum and tungsten components atop germanium crystals. That is, there are several materials and interfaces between them that quasiparticles must navigate– and it's possible they might get stuck in those interfaces, for example, in which case that energy is lost. Heat flowing from the QETs back into the germanium is also generally lost.

Some mismeasurements are more due to limitations in the hardware than the specifics of charges or phonons[34]:

- In very high-energy events, the readout circuits might become overloaded, or "saturated"[17], and their output will no longer scale with energy until the energy dissipates (on the right side of Fig. 3.13, saturation would mean the bottom of the trough would flatten out for some time).
- The sensors do not know what created the phonons and charges they collect; if two hits happen in quick succession, then, the sensors will happily read out the summed energies of both together as an erroneously-energetic[11] "single hit". The more extreme case would be multiple unrelated primaries–that "should" be separate events–causing hits at the same time, in which case the whole "event" (called a "pileup" event) might appear anomalously energetic.
- The readout channels interact with one another capacitively, meaning a current in one will induce a slight current in another.
- Glitches and low-frequency noise broadly refer to short-duration and long-duration changes in the observed readout that are not necessarily explained (though probably due to non-detector electronics), but are often easily identified in the output[35].

While events with such measurements issues can't be prevented entirely, they tend to be easily accounted-for.

3.4 Final Detector Output and Summary of Important Mismeasurements and Mitigation Methods

At this point we've traced incoming energies all the way through the detectors. The DAQ system reports the results to us as "raw data," which consists of many circuit pulses like those shown in Fig. 3.14, which just shows a single event in one FET channel and one TES channel (real raw data has multiple channels of each and many, many more events!). In the next chapter we will

---

[11] These will more so be misclassifications than energy "losses" in that sense.

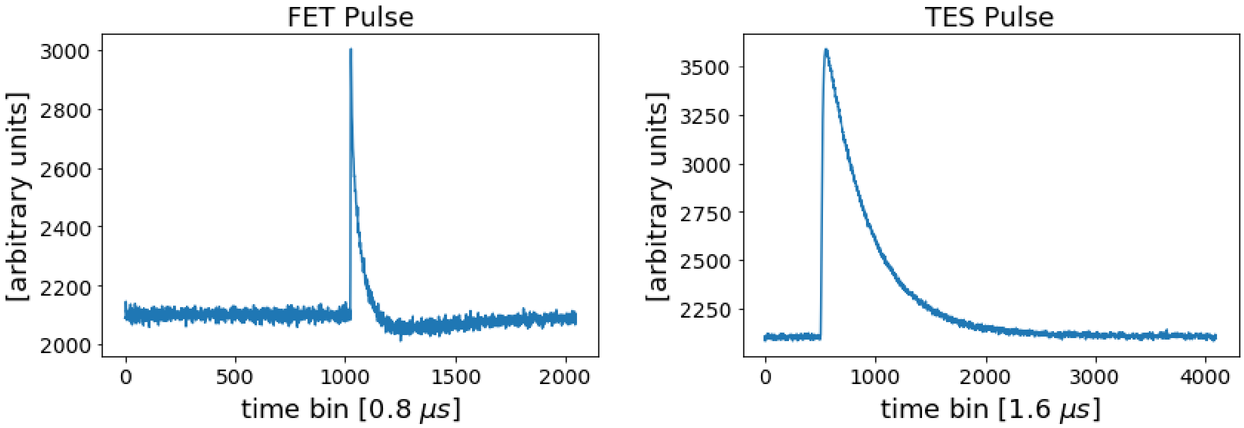

Figure 3.14: This figure shows examples of the detector output we'd see when energy is deposited; charge readout is on the left and phonon output is on the right. We show it because these pulse shapes are how we reconstruct the original energies. Both plots show noise-only segments on the edges and the pulses/signals of interest in the middle. Left: Readout of the sort we'd see for a charge being collected in an FET circuit. The current running through the electrodes (y-axis, in arbitrary units) experiences a spike when charges are collected. Right: Readout of phonons being collected on a TES circuit. This pulse is actually flipped vertically; as per Fig 3.13, collecting photons causes an increase in the resistivity of the circuit, meaning the current decreases and then gradually returns to normal as the remaining phonons are absorbed and the system cools down.

describe how the Reconstruction stage analyzes pulses like these to determine what happened in each event.

We first conclude this chapter, though, by reviewing the most significant causes of mismeasurement (or the appearance thereof) that would affect the pulses in Fig. 3.14 (these are mismeasurements due to physics in the detectors; Reconstruction and analysis will have their own limitations due to software and mathematical details); we keep these particular pathologies in mind because we'll want to distinguish them from events that are simply complicated–like those in section 3.1.2. Below we describe the main mismeasurements we'll have in mind going forward[12] and how they might be mitigated (see Table 3.1 for a summary):

- Electronics noise is ever-present (that's the "fuzziness" throughout the pulses in Fig. 3.14) and cannot be predicted precisely; on the other hand, it can be understood and quanti-

---

[12] Note that we're leaving off impurity charge trapping. This is not currently simulated, so we will not be studying it here.

fied generally (as will be described in the next chapter) and usually only contributes small effects/energies–generally just increasing our energy resolutions slightly. Usually, then, it's only a particular problem for very low-energy events, though particularly large noise fluctuations may erroneously be read out as real, small events themselves. Those extreme cases aside, noise can be handled generally by requiring minimum energies for events.

- "Sidewall events" involve energy deposits at high radii in the detectors where the ionized charges propagate to the vertical edges of the crystal and get stuck there. Not only do we lose the energies of these charges, we also lose some phonon energy, as those charges that get stuck on the sidewalls don't emit all the NTL phonons they would have as they traveled to the detector faces. The effects of these events can be mitigated in analysis by removing any events that have significant energies collected in the outer charge channels.

- "Face events" involve energy deposits close to the top or bottom faces of the detectors, in which some of the ionized electron-hole pairs might just recombine immediately, essentially canceling out in one electrode instead of creating signals in two opposing electrodes. This is particularly bad because reduced ionization signals could make non-NR events look like NRs. These events are mitigated by the scalloped electric fields in the detector, which help split up some of the electrons and holes, but cause them to be collected on the same side. This restores some signal on one side, but also causes asymmetric charge measurements between the sides, signaling to us that this was an edge event that can be removed from the analysis.

- "Off-electrode events" mostly involve hits aligned vertically with bends in the iZIP5 electrodes. As the electric fields near the electrode bends will be weaker than usual, more charges than usual may speed through the field and land off-electrode, where they do not induce a full signal (per the Shockley-Ramo Theorem) or create all the NTL phonons they should. As the effect is stronger for holes, this will cause a skew to lower energies for the bottom-side charge channels in particular (complicated further by a dependence on hit location, as we will see), though the association to electrode bends are currently only identifiable in simulations. Otherwise these are somewhat mitigated by removing events with asymmetric charge measurements, as is done for face events. Note that all events are likely subject to off-electrode *effects*, as the energies we work with create large numbers of charges; off-electrode *events* are just those that are the most obviously mismeasured due to such effects.

- "Semi-fiducial" events haven't been discussed yet and are specific to multi-hit events. These are events that have some hits near the center of the detector (the "fiducial volume") and some hits near the edges. In these cases, the inner hits may be well-measured while the outer hits are poorly-measured–for any of the reasons described above–meaning the event as a whole is mismeasured. Events like these can be somewhat handled with the same methods as those above, but if the poorly-measured hits are symmetrically mismeasured (or small enough compared to the well-measured hits) the whole event may appear as a well-measured but lower-energy (or lower-yield) event. Note that here we discuss only multi-hit events within a single detector; events with hits across multiple detectors are more easily identified and dealt with.

Note that none of our mitigation methods for these potential mismeasurements are absolute; we can only identify trends in well-measured events and try to exclude events that don't clearly follow them. But further complicating all of this, there is the matter of events that only *appear* to be mismeasured; in a perfect world we'd only see plain ERs and NRs, but in reality we will have to watch for the recoil types listed in section 3.1.2, which will not be easily interpreted in our data even if they are well-measured. Simulations will help us better-understand problems or complications like these and how we might improve the methods we use to distinguish between normal events, complicated events that only look mismeasured, and events that actually are mismeasured. We will discuss these further in chapters 4, 8, and 9.

Mismeasurement Type	Problem	Mitigation Method
Noise	Somewhat unpredictable (though broadly generalizable) electronics effects cause fluctuations in all measurements.	Require real events to have a minimum energy–informed by how far noise extends when no real sources of events are present.
Sidewall Events	Charges freed in interactions at high radii in the detector can drift to the sides and get stuck. In this case, some charges never reach the FET sensors at the faces and don't emit all the NTL phonons they would normally (see deposit 2 of Fig 3.8).	Require that events do not deposit significant energies in the outer charge channels.
Face events	Charges freed in interactions near the top or bottom of the detector, where the electric field is nonuniform, may get trapped on the "wrong" side (see deposit 1 of Fig 3.8)	Require events to have similar amounts of charge collected ("symmetric" charge measurements) on each side, which is most likely to happen for hits occurring in the center of the detector, where the electric field is uniform.
"Off-electrode" events	Charges may speed through the electric fields near the detector faces and land off-electrode, where they do not induce a full signal (see Fig 3.11). Some NTL phonons are missing as well.	Require symmetric charge measurements, as above.
"Semi-fiducial" events	Events with multiple hits where some energy is deposited near the center of the detector but some energy is also deposited near edges, where it is mismeasured. If some hits are well-measured but others are mismeasured, the event as a whole is mismeasured.	Require symmetric and non-outer-channel measurements, as above.

Table 3.1: This table summarizes the primary causes of mismeasurements, how they may be mitigated, and additional notes. Note that none of the mitigation methods are absolute–we can only identify trends in well-measured events and try to exclude events that don't clearly follow those trends. Simulations help us better understand these trends and problems and how we might improve our mitigation methods. More details on the problems, mitigation methods, and potential improvements are given in chapters 4, 8, and 9.

4. EVENT RECONSTRUCTION AND ANALYSIS

Chapter 2 covered incoming particles depositing energy in the detectors and chapter 3 covered how those energies propagate through and are read out from the detectors. In this chapter we discuss the final step: using the output of the detector electronics to "reconstruct" the physics of the original energy deposits. The reconstructed energies will still need some cleanup before the main analysis begins, so in this chapter we will also discuss calibration and data selection for identifying well-measured events.

4.1 Event Reconstruction

Once we have raw data from the detectors[1], we can process it through the standard CDMS event reconstruction software known as "CDMSBats." The raw data is in the form of pulses–jumps in otherwise flat currents (except for noise) being run through each sensor channel, as was shown in Fig. 3.14; though these pulses vary in size, they tend to have the same basic shape across all well-measured events. The main goals here, then, are:

- Determine what energies are represented by the varying sizes of these pulses/jumps
- Account for noise in the pulses, which will be frequency-dependent
- Quantify how confident we are in each given measurement.

In this section we summarize how these are accomplished with an algorithm known an "optimal filter"–here covering its basic implementation in reconstruction, the outputs it gives us for analyzing what happened in each event as a whole, and some of the quantities we calculate from them.

4.1.1 Pulse Reconstruction With the Optimal Filter

The basic function[2] of our "Optimal Filter" (or "OF") is illustrated in Fig. 4.1. In short, we begin with the assumptions that the real pulses from DAQSim all have the same basic shape and

---

[1] There is more DAQ hardware and software between the detectors and the reconstruction software–as was shown on the right branch of Fig. 1.9–but we won't describe such circuitry here. Refer to section 3.4 of Ref. [57].

[2] The full reconstruction code has many more complications we will not cover here.

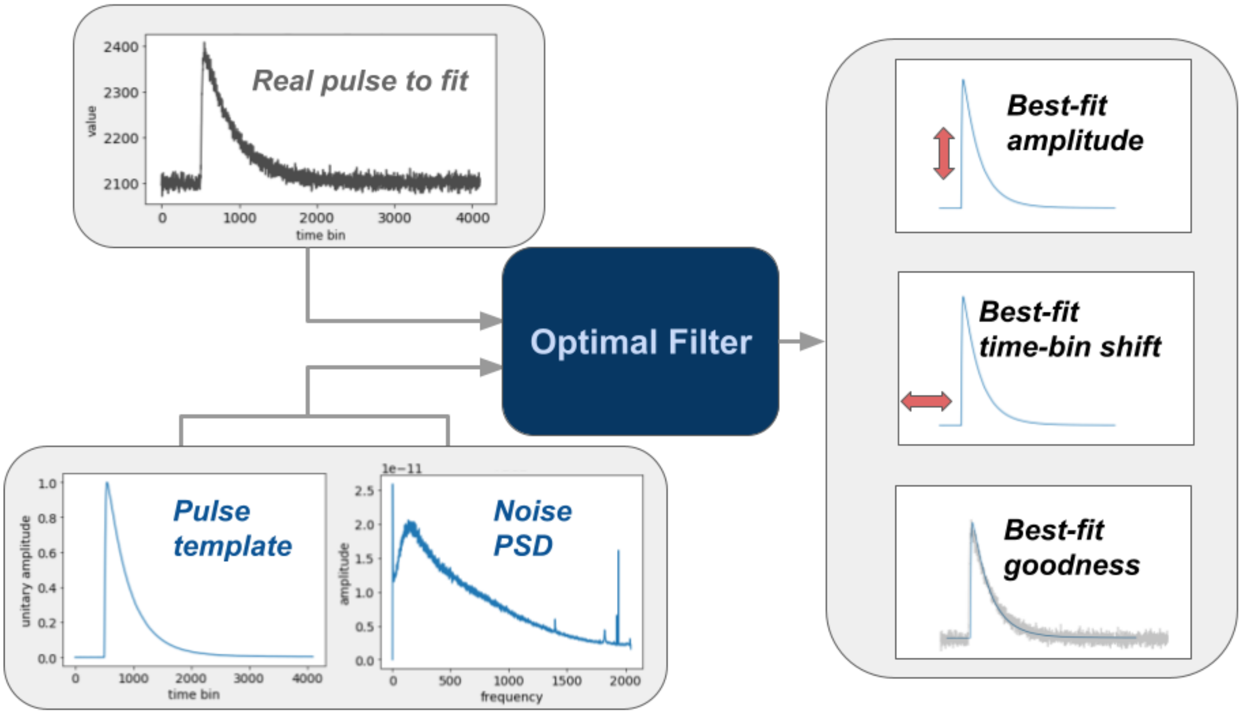

Figure 4.1: This figure shows an overview of "event reconstruction", in which pulse readout from the detectors is turned into energy measurements and other physically-meaningful quantities. The central algorithm, called an "optimal filter," takes a real pulse and tries to fit it using a provided pulse template and a power spectral density function representing noise. It returns the amplitude and time offset that minimizes the differences between the real pulse and its fit–this difference quantified as a chi-squared value.

that any variations from those expected shapes are due to frequency-dependent electronics noise. In more technical language, the OF, rescales that basic pulse shape (a "pulse template") until it matches (via χ^2 minimization) real data pulses, prioritizing frequencies (characterized by a "Power Spectral Density" function, or "PSD") with minimal noise; based on how much rescaling was done and the final χ^2, this provides an estimate of the pulse's original energy, its timing, and a measure of how reliable these estimates themselves are. We provide only a brief overview of the OF's inputs and implementation here; a more complete description can be found in Appendix B of Ref. [58].

To set the stage, we begin by modeling a real pulse $v(t)$ as the sum of a scaled template pulse

$s(t)$ and noise $n(t)$ in both time and frequency space:

$$v(t) = As(t) + n(t) \tag{4.1}$$

$$\tilde{v}(f) = A\tilde{s}(f) + \tilde{n}(f) \tag{4.2}$$

where A is an amplitude to be estimated (proportional to the energy of the pulse) and the tildes mark Fourier-transformed quantities (since we are working with finite, digitized data, these are discrete Fourier transforms implemented as Fast Fourier Transforms in the reconstruction software). We work with Fourier-transformed quantities in frequency space because noise in the experiment is largely repetitive–and it is more apparent at some frequencies than others. Such noise, then, can be described/accounted-for more easily by independent frequencies in frequency space than by times that are related to other times in time space.

4.1.1.1 Constructing Pulse Templates and Characterizing Noise

We now describe the two inputs that provide the OF with what a real pulse "should" look like: pulse templates describing the overall shape and noise PSDs describing deviations from it. Looking ahead, note that these inputs are created using real data, but we can use them for reconstruction of both real and simulated data.

Template pulses are created for each detector and channel by normalizing and averaging the pulses from a set of events known to be well-measured. For charge channels we also create "crosstalk" templates to account for capacitative interactions between the inner and outer channels. All non-pathological pulses have the same basic shape, though, so these two sets of pulse templates for each channel can be used to reconstruct all events.

Meanwhile, we describe noise in terms of its power as a function of frequency–the "PSD" (labeled in Fig. 4.1). If the noise as a function of time is given by $n(t)$ (and its Fourier transform by $\tilde{n}(f)$), the PSD function $J(f)$ can be constructed as:

$$J(f) = \lim_{T\to\infty} \frac{1}{2T} |\tilde{n}(f)|^2 \tag{4.3}$$

or, in the case of discrete binning:

$$J(f_p) = 2T|\tilde{n}_p|^2 \tag{4.4}$$

$$J(f) =< J(f_p) > \tag{4.5}$$

where T is the sampling time and p is the bin number for the discrete case. Both forms are essentially a measure of the variance in the noise as a function of frequency[3].

4.1.1.2 Optimal Filter Implementation

With templates for the pulses and PSDs for the noise, we can now try to reconstruct real pulses/events to determine their energy, timing, etc. We do this by minimizing the difference in frequency space between a real pulse and our parameterized model of it. We can quantify this initially with a χ^2 constructed as follows:

$$\chi^2(A) = \int_{-\infty}^{\infty} df \frac{|\tilde{v}(f) - A\tilde{s}(f)|^2}{J(f)}. \tag{4.6}$$

In English, the OF could use the above equation to look for the energy (derived from A) that minimizes the difference between the real pulse and the reconstructed pulse (numerator)–with greater weight assigned to frequencies with less noise (denominator). This is not quite the form we use, however.

We introduce two changes to better match our goals: first, we make it a discrete sum (as we are working with digitized bins) and second, we introduce a time dependency in the template term (since we don't know exactly when energy arrived in a given readout segment) via a complex phase factor:

$$\chi^2(A, t) = \sum_n \frac{|\tilde{v}(f) - Ae^{-i2\pi ft}\tilde{s}(f)|^2}{J(f)}. \tag{4.7}$$

There is an additional modification to this calculation in the CDMS "non-stationary optimal filter" that handles additional noise variations but this is beyond the scope of this thesis. Refer to Ref.

---

[3] The discrete form could just be given as $J(f) =< \tilde{n}^2(f) >$[36]; that is, the most important part about J(f) is that it's the average of the Fourier-transformed noise variance. Including $2T$ helps with units–making the result V^2/Hz.

[17] for details.

Reconstruction requires more than simply applying equation 4.7 (and the relevant template and PSD) to each channel individually: there are inter-channel effects to consider as well. Firstly, the pulses should occur in adjacent channels at essentially the same time, constraining t. Secondly, there is the matter of crosstalk between channels again, which would turn equation 4.1 into a matrix expression (where $s(t)$ becomes a 2x2 matrix with normal and crosstalk templates) linking the inner and outer channels. The relevant math expands quickly and is not a focus of this work, so refer to Appendix A of Ref. [36] for more.

4.1.2 Outputs and Measured Yields

Reconstruction in CDMSBats produces many output quantities for energies, timing, quality flags, individual channel measurements, channel aggregates, and so on–on top of which we perform additional calculations of our own. Specifically, we usually combine results from multiple channels to form full, event-level quantities; we note the quantities $qimean$ (mean of the inner charge channel energies) and $ptNF$ (total collected phonon energies from the Non-stationary OF) in particular, as we will most often be using them as our reconstructed charge and phonon energies, respectively. Table 4.1 summarizes some of the quantities we will be using–including both reconstructed quantities from CDMSBats and some simulation-specific quantities from earlier stages that are useful for tracking what the reconstructed quantities were actually trying to reconstruct.

Two important calculated quantities to note are what we'll call the "measured yield" and the "measured recoil energy" (though we may also use the word "reconstructed" instead of "measured" for each), denoted below as Y and E_{RR}, respectively. Since for real data we can't determine the true, individual-hit-specific Lindhard yield, we estimate it for full events (a conglomerate of hits) based on our collected energies as follows. First, we can rearrange 3.8 to estimate the original

Notation	Description
$-OF$ or $-NF$	Indicates quantities constructed from the optimal filter or the more elaborate "Nonstationary optimal Filter"
i or o	Refers to the inner (i) or outer (o) charge channels
1 or 2	Refers to the top (1) or bottom (2) side of the detector

Quantity Name	Description	Units	In Real or Simulated Data?
$ptNF$	Measured phonon total ('pt') energy	keV (energy)	Both
$q * \#OF$ (*=i,o, or sum #=1,2, or mean)	Measured charge energies for the inner channels, outer channels, or both (the sum) and detector side 1, 2, or the mean of the two	keV (energy)	Both
R_{hit}, Z_{hit}	R and Z coordinates for energy depositions in the cylindrical detectors (Z=0 in the middle of the detector)	mm or m (spatial coordinates)	Simulation only
$PhononE$	Total phonon energy collected in TESSim	eV or keV (energy)	Simulation only
$ChargeQ$	Total number of charge units collected in FETSim (though we generally convert to energy)	e (electron charge)	Simulation only
$[channel]sat$	For the given charge or phonon channel, the number of time bins in which the pulse exceeds a fixed "saturation" threshold in the sensors.	(raw count)	Both

Table 4.1: This table lists for many of the variables used in the text for brevity. The upper section of the table explains some notation common across multiple variables while the lower section lists specific variables we'll be using.

recoil energy–this estimate being E_{RR}:

$$E_{RR} = E_{Ph} - E_{Ph,NTL} \tag{4.8}$$

$$= E_{Ph} - (E_Q * \frac{e * V_{bias}}{\epsilon_{eh}}) \tag{4.9}$$

where we have substituted in equation 3.6. Then, combining this with equation 3.3, we have:

$$Y = \frac{E_Q}{E_{RR}} \tag{4.10}$$

$$= \frac{E_Q}{E_{Ph} - (E_Q * \frac{e*V_{bias}}{\epsilon_{eh}})} \tag{4.11}$$

where E_Q and E_{Ph} are usually $qimean$ and $ptNF$–but may be other variants depending on analysis needs.

We've now reached the end of the real-data path of Fig. 1.9 (the path beginning in the top-right): we've covered the physics of the experiment, the detector readouts, and the main analysis algorithm. However, we still don't have our final results; we still need to calibrate the output data and select for well-measured events.

4.2 Calibration Sources

Though at this point data-taking and event reconstruction are done, we don't yet have the "final" energies we'd use for analysis. The energy losses discussed in previous chapters and the uncertainties involved in the OF mean our resulting energies will need some correction to be identified with the "true" energies they should reflect (that is, the energies of the original deposited energy–in turn identified with certain primary energies). As mentioned previously, we use Ba-133 as a photon source–providing relatively-easily-identifiable energies that we can use to calibrate our reconstructed energies; neutrons from Cf-252 can then be used to check how the detectors respond to NRs. We describe these in turn in this section.

4.2.1 Calibrating Energy Measurements with Photons from Ba-133

Ba-133, as mentioned previously, emits several identifiable photon energies, most notably one at 356 keV. After reconstructing events taken while the Ba-133 source was in the apparatus, we can find that 356 keV peak in the data (after quality cuts, described below) to determine how to match up the uncalibrated data (which both suffers from the previously-mentioned energy losses and also is in arbitrary readout-electronics units) to real energies (e.g. units of keV); this can generally be done for each channel with a simple multiplicative factor. The width of the resulting peak can also be used to estimate the experiment's energy resolution.

4.2.2 Comparing ER and NR Events With Photons and Neutrons From Cf-252

Following Ref. [34], we can think of Cf-252 as having three main uses. In this section we will cover its use in distinguishing ERs and NRs, providing example non-WIMP NRs, and doing additional energy calibration

WIMPs, recall, will cause NRs, which can be distinguished from ERs using the measured yield. To test how well the detectors identify NRs, then, we cause some ourselves using neutrons from the Cf-252 source. Since the neutrons themselves will knock out photons and charged particles on their way through the apparatus, with this source we will have both ERs and NRs and the opportunity to see how well they can be distinguished after reconstruction (in visual terms, they help determine the bounds for the ER and NR bands in Figs. 1.7 and 1.8).

While these neutrons are similar to WIMPs in that they cause NRs, they are also different in that they will reach energies much higher than those considered in the experiment (as will be shown in Chapter 5) and also often interact multiple times in the detectors (Chapters 7 and 8). So in addition to helping distinguish between ERs and NRs (per the previous paragraph), they also can be used to study potential WIMP-like backgrounds (that is, events in the NR band caused by particles other than WIMPs).

As mentioned in Chapter 2, neutrons (from Cf-252 or otherwise) can also excite Ge-71 atoms in the detectors and lead to another identifiable photon energy peak around 10 keV that can be used for calibration along with the peaks from Ba-133 (though we will not be using this germanium peak in our studies).

4.3 Identifying Events of Interest

Mitigating noise and backgrounds will require significant effort since the hoped-for WIMP signals will likely have very low energies and occur very rarely. Here we describe how we try to cut the data down to well-measured events (hopefully with identifiable recoil types); given that conditions within the detectors are not all equal and isotropic (per Figs. 3.6 and 3.7) we will try to select for well-measured events by proxy by selecting for the specific detector regions (i.e. the middle) where such events are most likely. The main cuts we describe here are summarized in Table 4.2.

4.3.1 Event Selection Criteria

The various Soudan analyses used many different event-selection criteria (hereafter "cuts") in various combinations, but we will gloss over most of the complexities here. Ref. [25] provides a very concise description and extra detail can be found in Refs. [35] and [59]; here we will strike a middle ground, focusing mostly on just the few cuts we are interested in for use with our simulated events–with some mention of real-data cuts since we will be comparing simulations to real data later. Refer back to Table. 3.1 for some of the measurement problems motivating these cuts.

The cuts we use most often in this thesis are:

- Soudan "quality cuts": these mostly address real-world problems that won't be relevant in simulations. These cover problems associated with certain time periods of the experiment (e.g. high external noise, temperature shifts, potential interference from other experiments, etc.) or pulse-specific problems (e.g. unusual pulse shaped caused by glitches or hardware failures).

- Saturation cut: this is a pulse-specific check that can be used for both real and simulated data. This checks that the pulse shapes do not abruptly level-off, which would indicate that the sensors have become saturated and aren't responding fully to higher energies.

Cut Name	Cut Variable and Condition/Threshold	Applies to Real or Simulation Data?
Soudan "quality cuts"	(Various)	Real only
Charge Symmetry	$qi1OF \approx qi2OF$ (energy-dependent)	Both
Charge Fiducial	$qo[1/2]OF$ look like noise (over 1 keV in our simulations; over 2σ from noise mean for real data)	Both
Minimum Energy	$qimean > 3keV$	Both
SimFiducial	$\|Z_{hit}\|$ < 12.7mm $R_{hit,top}$ < 0.034 $R_{hit,bot}$ < 0.025	Simulation only
LT Fiducial	(Combination of the above two charge cuts and the minimum energy cut)	Both, but primarily simulation (real data has other general quality cuts)
Saturation	$(channel)sat = 0$ for all channels	Both

Table 4.2: This table lists the data-selection cuts used here to identify well-measured events. See text for descriptions. Note that the second column shows the criteria for events to *not* be removed. See Refs. [27, 28, 35] for more background on the Soudan quality cuts and others.

- Minimum energy cut: though CDMS is pushing towards lower energy sensitivities, we set a low-energy cutoff for Soudan data here where the signal-to-noise ratio is just too low to draw meaningful conclusions.

- Inner-charge cut: this cut is designed to remove "edge events" by rejecting events with significant energy readings (i.e. readings inconsistent with mere noise) in the outer charge channels. This cut is illustrated on the left side of Fig. 4.2.

- Charge symmetry cut: this is designed to remove "face events" by rejecting events where the two side of the detector read out dissimilar charge energies. Such readout asymmetries would indicate hits near detector faces, where too many electrons and holes were collected on the same side (by design, as described in section 3.2.2). This cut is illustrated on the right side of Fig. 4.2.

We note that in a real WIMP-search there would be additional physics-based cuts to remove events that aren't WIMP-like. These would include cuts to exclude ERs and multi-hit events, for example. We will apply such cuts briefly to study specific subsets of events in later chapters, but we will not be applying them as a rule.

4.3.2 Well-Measured Events and Fiducial Volumes

We describe here two more conglomerate cuts that we will be using frequently later. Recall Fig. 3.7 showed a "fiducial volume" in the center of the detector, where the electric fields were the most uniform. We want to be able to identify events that occurred in this region, as such events will have the fewest mismeasurements (while events outside this region could be well-measured, but aren't reliably so, due to edge effects). While this is fairly easily-done in simulations (which record exact hit locations) real data requires some inference and cut combinations.

The two "fiducial region" cuts we will be using in this thesis are:

- "SimFiducial": this is defined by exact radial and height cutoffs and is simulations-specific. Because we know exact event coordinates in simulated data, we can specifically identify

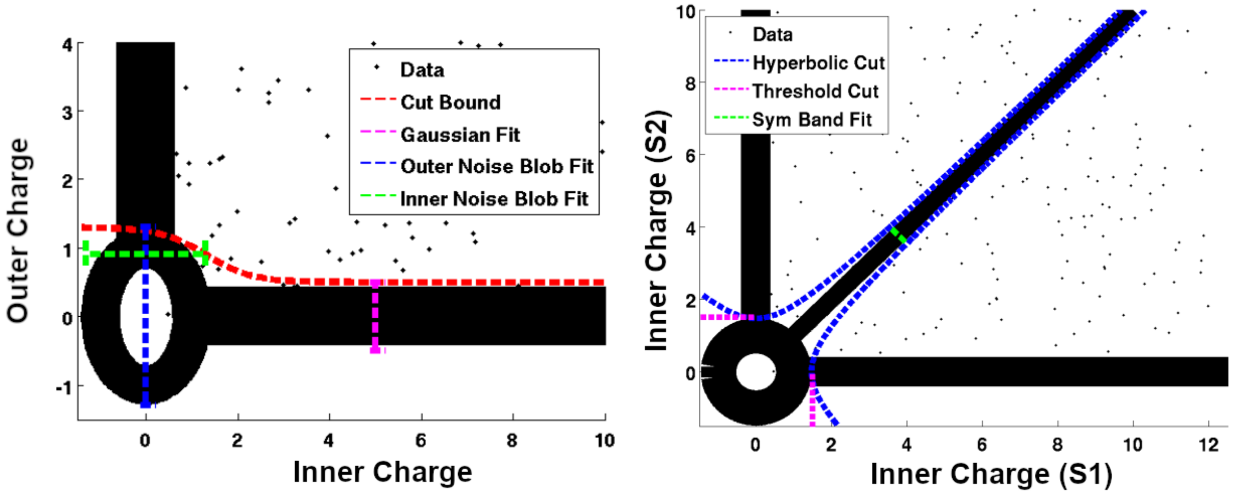

Figure 4.2: This figure shows the qualitative construction of the charge fiducial and symmetry cuts (see Table 4.2), which help identify well-measured events based on the energies deposited in the inner and outer charge channels. Note that the behavior of both changes slightly at low energies to accommodate low-energy noise (the "noise blob"). Left: the charge fiducial cut is meant to remove edge effects by rejecting events that have anything more than noise in the outer charge channels. Broadly, this is done by removing events beyond 2σ from the mean of the baseline noise. More specifically, Gaussian fits are applied to the noise blob and to normal noise to find their 2σ ranges (shown by the blue and magenta lines) and the values between them are interpolated using a sigmoid function (red line; the width of its transition is informed by another Gaussian fit shown in green). Right: the charge symmetry cut removes events that are too close to the detector faces by requiring that the measurements from sides 1 and 2 are similar. In the plot, it passes everything between the blue hyperbolas at high energies and between the magenta lines around the noise blob. Figure taken from Ref. [35]. See also Ref. [28]

what detector volume has actually has reliably well-measured events and limit analysis to events in that volume. This will be described in chapter 8.

- "LT Fiducial": this is inspired by the LT Analysis[28] and is comprised of cuts that can be applied to real data, as it requires only quantities that would be provided by the reconstruction code. While this cannot be an exact spatial cut, it should mostly select events in a region similar to SimFiducial. The specific cuts used for this are the "minimum energy," "charge symmetry," and "inner-charge" cuts. This will be further described in chapter 9.

SimFiducial will be useful for validating the performance of earlier stages of our simulation chain. LT Fiducial will be useful for comparing real and simulated data–and hopefully will match SimFiducial results.

We have now finished our overview of the experiment: Ch. 2 described the basic hardware and the particles we expect to deal with, Ch. 3 described the behavior of the detectors, and this chapter described how we analyze the detector output. In the next chapter we go into more detail about the calibration sources we are introducing into this system; after that we will transition to how it is all simulated.

5. PHYSICS OF CALIBRATION SOURCES

As described previously, Ba-133 is a photon source with easily-identifiable energies that we can use to calibrate the detector output. Cf-252, meanwhile, is a neutron source (though it also produces other particles) which we can use to check how NR interactions in the detector are reconstructed. For the Soudan experiment, we periodically inserted wafers of these sources into the cryogenics and electronics stems to expose the detectors to photons and neutrons and collect calibration data. In this chapter we describe more thoroughly the physics of these sources and the particles and associated energies we expect to see from them in the data–concluding with a brief look at actual calibration data from Soudan.

5.1 Physics of Ba-133 Decays

The Ba-133 source will cause only ERs in the detectors, as it emits photons and electrons as it decays (it also emits neutrinos, but these will not measureably affect anything else). We briefly summarize the decay process and associated energies–illustrated in Fig. 5.1–below, but more information can be found in Ref. [60].

Ba-133 has a half-life of 10.5 years, decaying via electron capture to Cesium-133 (Cs-133). The first step is the capture itself, in which a proton combines with an inner-shell electron, turning into a neutron and a neutrino (which escapes the system):

$$p + e \rightarrow n + \nu_e.$$

We now have a Cs nucleus and two sources of outgoing energy:

- The first source is the electron system of the atom, which now has a hole in an inner orbital that needs to be filled. As electrons in the atom's orbitals reorganize to fill the hole, the system will release energy either by emitting X-rays or by kicking out other electrons from outlying shells (called "Auger electrons"[61, 62]). There are many possible patterns

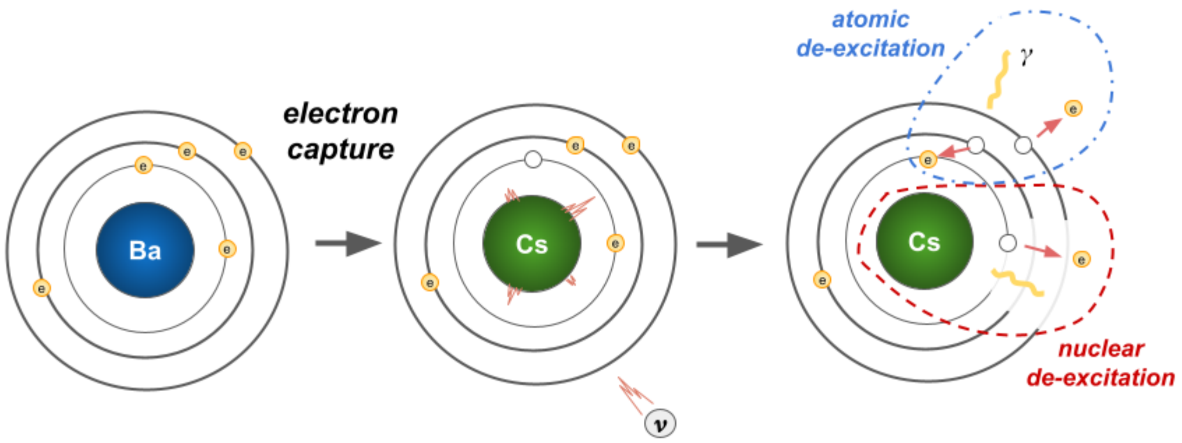

Figure 5.1: This figure shows a cartoon of a Ba-133 electron-capture decay, with subsequent de-excitations and the expected decay particles. We show this because this decay method releases particular energies we can identify for use in calibration or simulation validation. In the initial decay, an electron and a proton combine to form a neutron and an electron neutrino (which exits the system and our consideration). After this, both the nucleus and the atom as a whole will be in some combination of excited states. The nucleus can de-excite by emitting gammas and internal conversion electrons while the atom's outer electrons can de-excite by emitting X-rays or Auger electrons.

the electrons may go through as they de-excite, so we will not check their specific output energies.

- The second source is the nucleus, which is left in one of four excited states after the electron capture (shown in Fig. 5.2). We will be most interested in the gammas emitted as the nucleus de-excites; there are fewer than 10 unique energies emitted (shown by the vertical arrows in Fig. 5.2), and the highest of them are easily identified in data.

Fig. 5.3 shows the primary photon spectrum emitted from the decay–both the electronic X-rays and the nuclear gamma rays. Energy losses due to interactions as the photons move between the source and the detector will smear out the peaks significantly, but the three highest-energy gammas at 303, 356, and 384 keV will still be apparent enough that we can use them for energy calibrations (the 356 keV peak in particular).

Fortunately, Cs-133 does not further decay, meaning there are no additional spectra or other changes over time to be accounted-for. The next calibration source, Cf-252, will not be so simple.

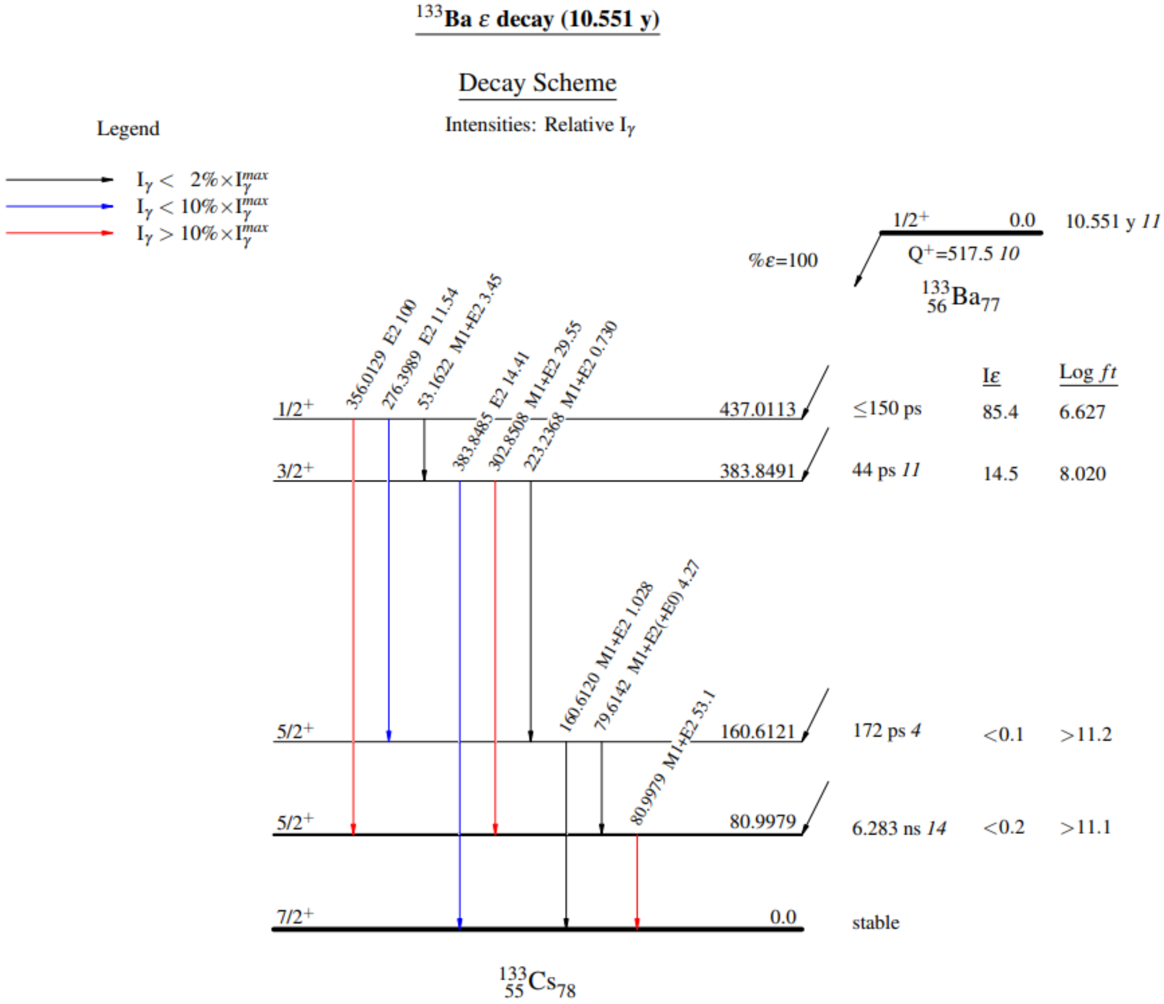

Figure 5.2: This figure shows the electron-capture decay scheme for Ba-133, including the energy levels of the daughter nucleus and the emitted energies and rates of subsequent de-excitations. The vertical lines represent the photon (gamma) energies emitted as the nucleus de-excites after neutron capture; the gammas with 303, 356, and 384 keV are generally visible in Ba-133 data and help us determine what calibrations are needed to convert detector output to final measurements. Note that these decays may release X-rays as the electrons outside the nucleus re-settle, but these are not shown here. Even if they are created, they are blocked and do not reach the detectors. For completeness, though, we can check their original energies in simulations, as seen in the next figure. From Ref. [60].

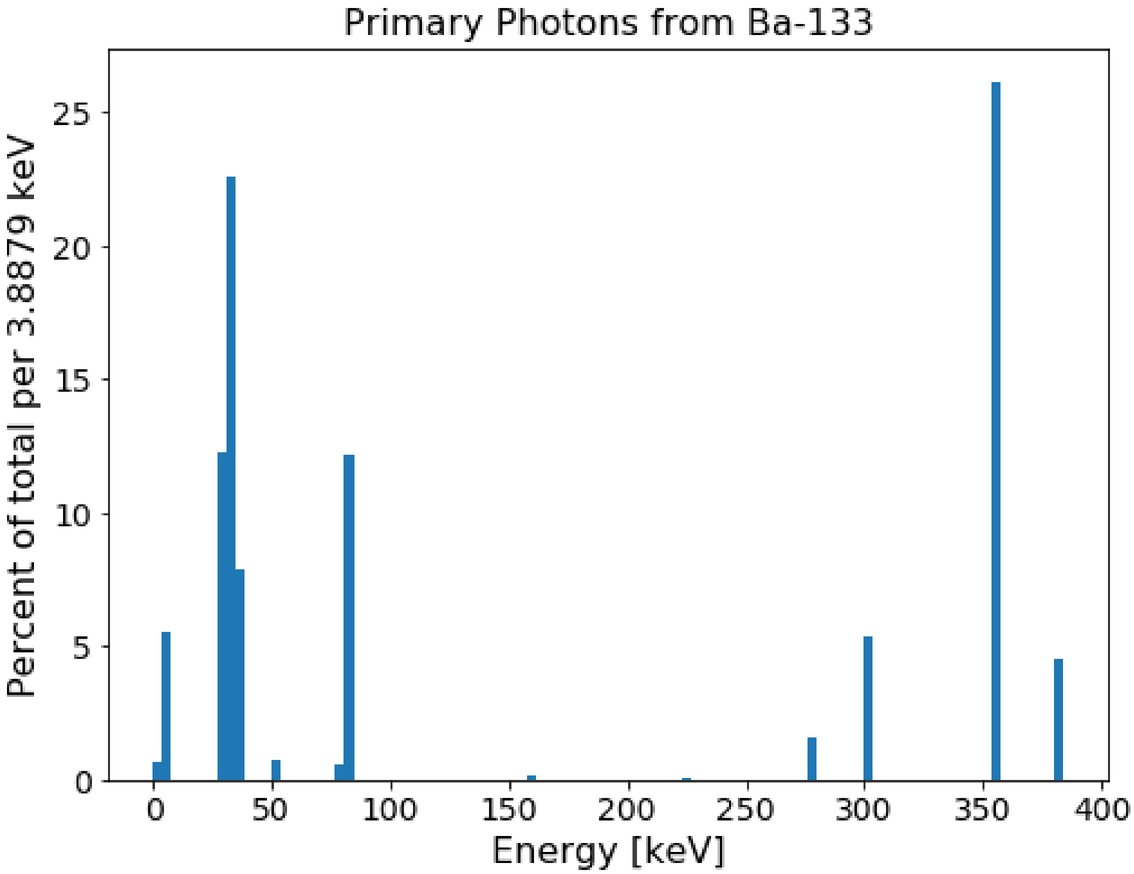

Figure 5.3: This figure shows the full expected photon spectrum emitted from Ba-133's decay to Cs-133 (the data in this plot created by our simulation chain). The high-energy peaks towards the right are the gammas that were shown in Fig 5.2; the lowest energies towards the left are X-rays. We expect to see these gamma peaks in our final detector output, but the X-rays will have been blocked.

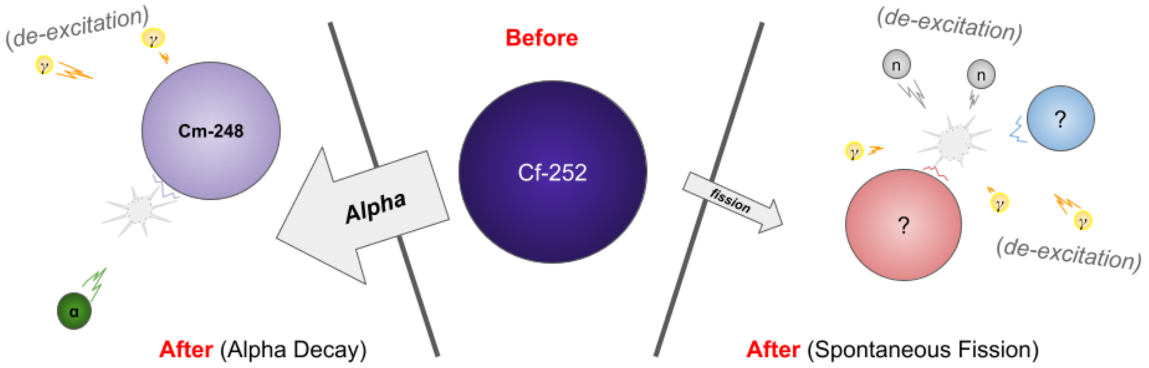

Figure 5.4: This figure shows Cf-252's two decay patterns and immediate products. On the left is shown the most common decay, alpha decay. This produces photons and an alpha that will most likely be reabsorbed before it exits the source capsule (i.e. it is never seen by the detectors). At right is shown spontaneous fission, which is less common but more important, as it's where we get our calibration neutrons.

5.2 Physics of Cf-252 Decay

Cf-252 is commonly used as a neutron source, and, as mentioned previously, for CDMS this means it can provide examples of NRs to demonstrate how well WIMP-like recoils can be distinguished from other recoils. The complete Cf-252 decay chain contains much more than just our neutrons, however, and a full description of the possibilities is far beyond the scope of this work; the interested reader should refer to the National Nuclear Data Center's Chart of Nuclides and ENSDF databases[63] as a starting point for more information. Here we will only briefly describe Cf-252's two decay options, what we expect to see from them, and how they may change over time. We'll be keeping particular track of how they might affect the neutron spectrum we're interested in.

Cf-252 has a half-life of about 2.6 years, meaning it will be reasonably active over the course of our few-years-long experiments (the Cf-252 itself, that is; its decay daughters will have their own [half-]lives after the initial decay). The original nucleus can undergo either alpha decay (96.91% of the time) or spontaneous fission (3.09%), though the latter is our primary focus, for reasons described below.

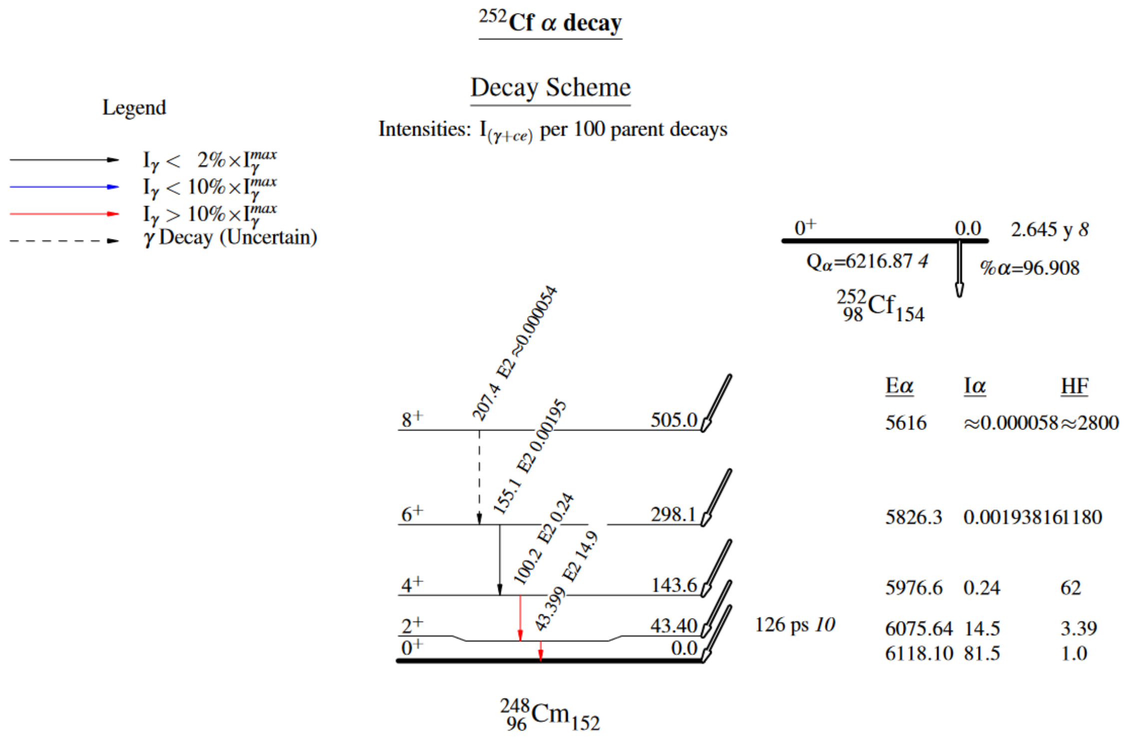

Figure 5.5: This figure shows the alpha decay scheme for Cf-252, including the energy levels of the daughter nucleus and the emitted energies and rates of subsequent de-excitations. We show these for completeness; we're more interested in the fission neutrons, but the alpha decays can be another check that our simulation is working. From Ref. [64].

5.2.1 Alpha decay

In alpha decay, the Cf-252 nucleus splits into an alpha particle and a Cm-248 nucleus. Most often the Cm nucleus will be in the ground state, but excited states are possible and correspond to smaller energies in the outgoing alpha particle; these excited states will also emit X-rays and/or electrons as they relax to the ground state. Fig. 5.5 shows the nuclear levels and energies involved in the original decay.

The Cm-248 nucleus can further decay (and its full decay chain is extensive) but it has a half-life of over 340,000 years, which makes its daughters largely ignorable for CDMS purposes. There are a few possible spontaneous fission events in the chain that could produce confounding neutrons, but even if the relevant parent nuclei are produced on our timescale, those spontaneous fissions are unlikely options for the decay of those nuclei.

So on our time scale we ultimately only expect the original alpha particle and possibly some deexcitation X-rays and electrons from the alpha-decay chain. But we don't expect any of these to actually reach our detectors, as they will all be blocked by the various layers of shielding. The bulky alpha particle in particular won't even make it out of the source capsule itself.

5.2.2 Spontaneous Fission

The spontaneous fission decay chain is of more interest to us, as its where we get our neutrons–which will not be entirely blocked in the way that the alpha-decay products are. Fission can produce a range of daughter nuclei (illustrated nicely in Ref. [63]'s Chart of Nuclides) and associated neutrons and photons (plus whatever else the likely-excited fission fragments subsequently emit), and we describe the expected output as a statistical distribution of energies instead of the specific steps shown for alpha decays.

There exist multiple quantitative models of the prompt neutron emission spectrum[1], but no single model satisfactorily matches all real data, though they all have the same basic shape: a peak around 1 MeV with a tail out to higher energies. The two models we will mention here are Mannharts corrected Maxwellian spectrum [66] and Froehners Watt spectrum[67], the latter shown in Fig. 5.6. Note, again, that these are statistical–not describing a single "one true" fission event. Fission events are messy and can involve myriad combinations of variously-sized and variously-excited fission fragments emitting various combinations of neutrons; the models we use describe a conglomerate result over many events (see Ref. [68]'s Appendix E for numerical calculations).

On the one hand, the neutron spectrum has no specific energies for us to use in calibration; on the other hand, with calibration already handled by Ba-133, it is handy that Cf-252 provides example NRs for a broad range of energies, covering reasonable WIMP recoil energies and beyond.

Fission photons, as with neutrons, are described statistically, though these will be less important for us; they have, in fact, generally been less important for others as well, such that there is no

---

[1] There may also be some "delayed" neutrons emitted from the fission fragments up to some seconds later, but these are relatively rare[65].

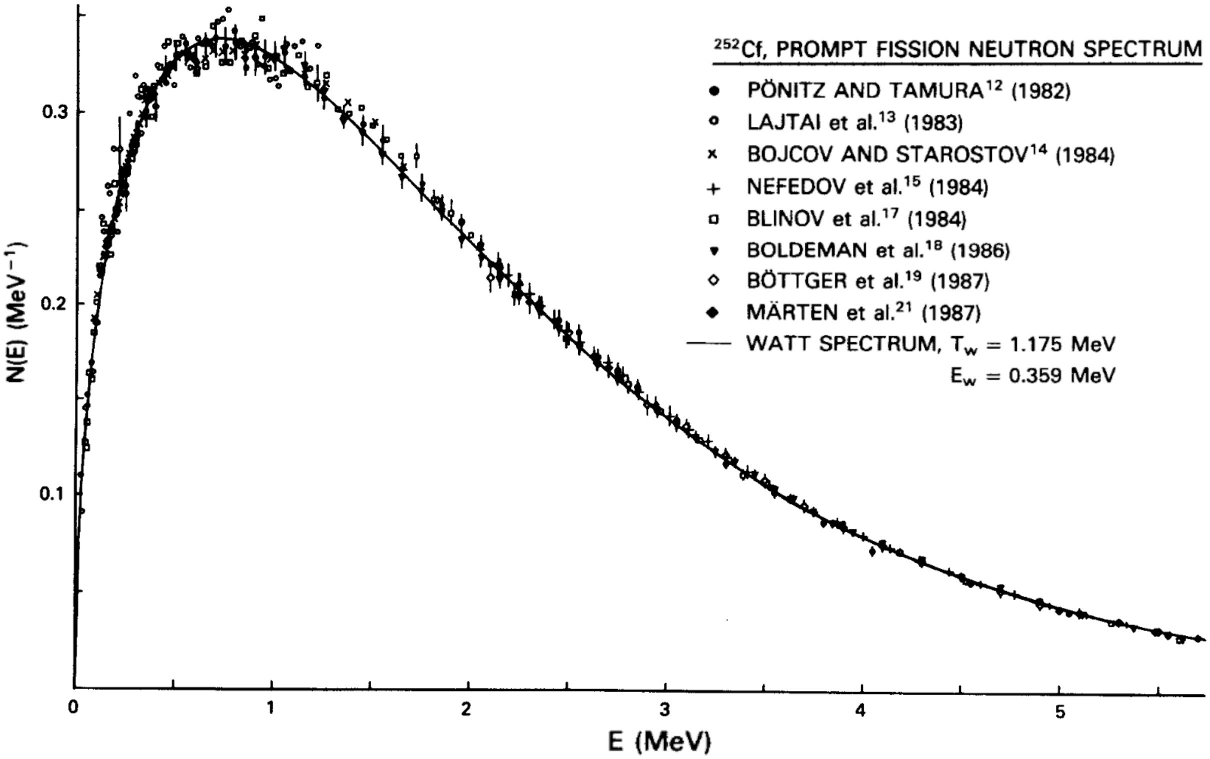

Figure 5.6: This figure shows the rate that neutrons are emitted as a function of their energy from the spontaneous fission of Cf-252, along with a fit using a Watt spectrum model; taken from Ref. [67]. Note that there are multiple models used for this neutron spectrum other than the Watt spectrum (our simulations can also use a variant of a Maxwellian distribution, for example) but they all have the same qualitative features: a maximum around 0.7 MeV and a long tail towards higher energies.

widely-used, dedicated model for fission photons. It has been observed that the Cf-252 prompt fission photon spectrum is similar to that for neutron-induced fission of U-235 [69], and so models for the former spectrum are generally just based on the latter.

The fragments from Cf-252 will further decay, which complicates any description of what the full output spectrum from Cf-252 will be, though we can generalize. The fission fragments will most often be neutron-rich nuclei that undergo beta(-) decay [70] to produce more electrons and photons. These exact spectra will change over time, as described in the next section, but since we are not making use of their specific energies this is not too worrisome for our work. Further, the neutron spectrum–our primary interest here–is unaffected by beta decays.

5.2.3 Evolution of a Cf-252 source and Summary

As described in the previous two sections, Cf-252 decays into nuclei that can decay further. Since we are only interested in the "prompt" neutron spectrum of our physical Cf-252 source, one could worry about how it is affected by the buildup of these radioactive daughter nuclei, as illustrated in Fig. 5.8. This is largely a matter of change due to spontaneous fission daughters, since the alpha decays Cm-248 nucleus has such a long half-life, as noted previously.

Per the previous section, we expect the fission fragments to most often undergo beta(-) decay, so changes over time will mostly be in the electron and photon spectra. See Refs. [70] and [71] for more in-depth descriptions of changes in an aging Cf-252 source's spectra (including changes due to contaminants).

To summarize, Cf-252 does much more than emit the fission neutrons we use in the experiment; a realistic "Cf-252 source" will even build up other elements and associated spectra that differ from our prompt spectra. However, the prompt neutron fission spectrum is essentially unaffected by these considerations, and since that is our focus, we won't much consider the other spectra.

5.3 Soudan Calibration Sources

Now that we've described the behavior of the calibration sources, we address how they were used in the Soudan experiment and their results.

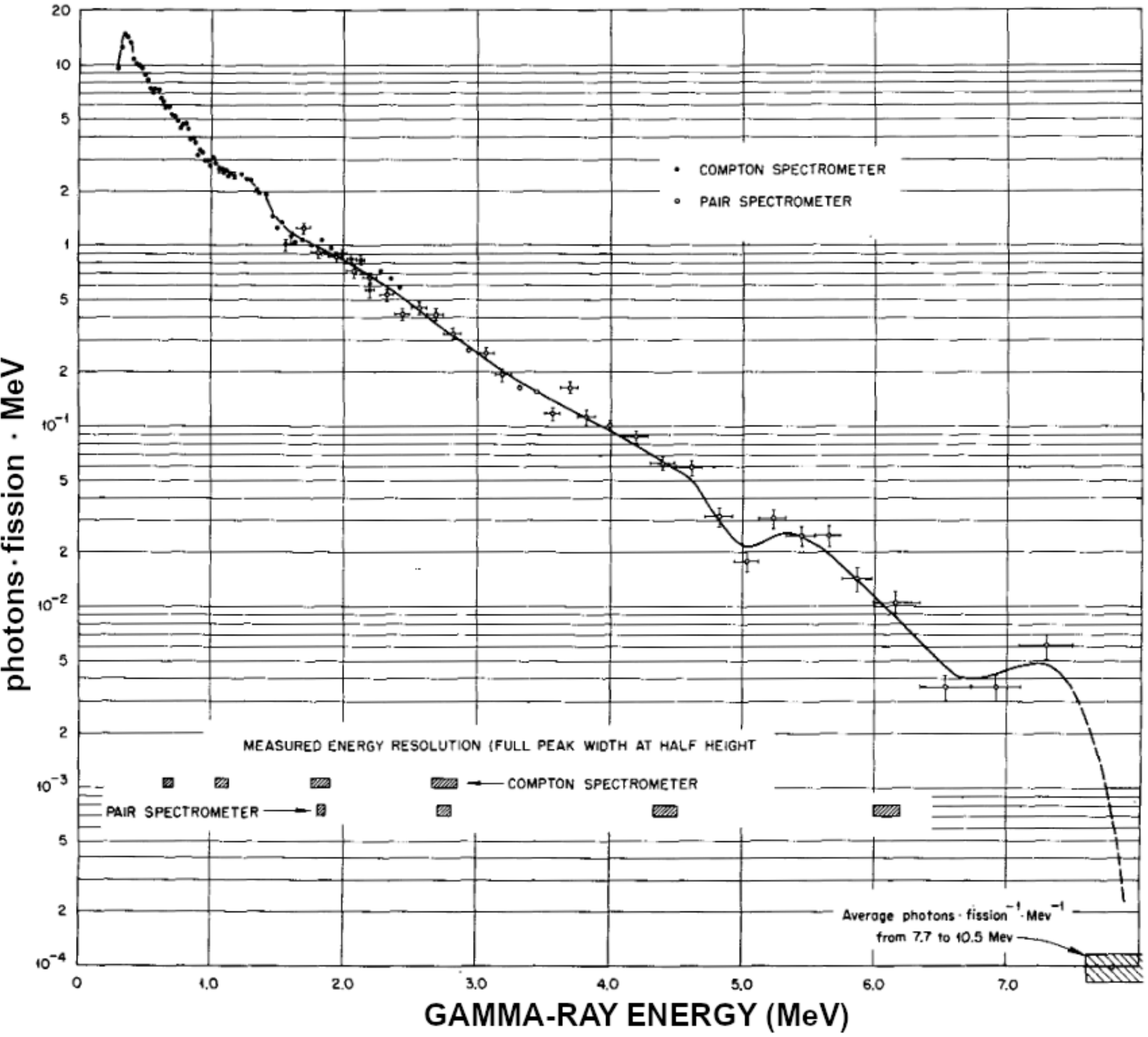

Figure 5.7: This figure shows the rate that photons are emitted as a function of their energy from the neutron-induced fission of U-235, from Ref. [69]. Geant4 uses this data to simulate the photons released in Cf-252 fission because the U-235 photon spectrum is comparable to and more thoroughly-studied than that for Cf-252.

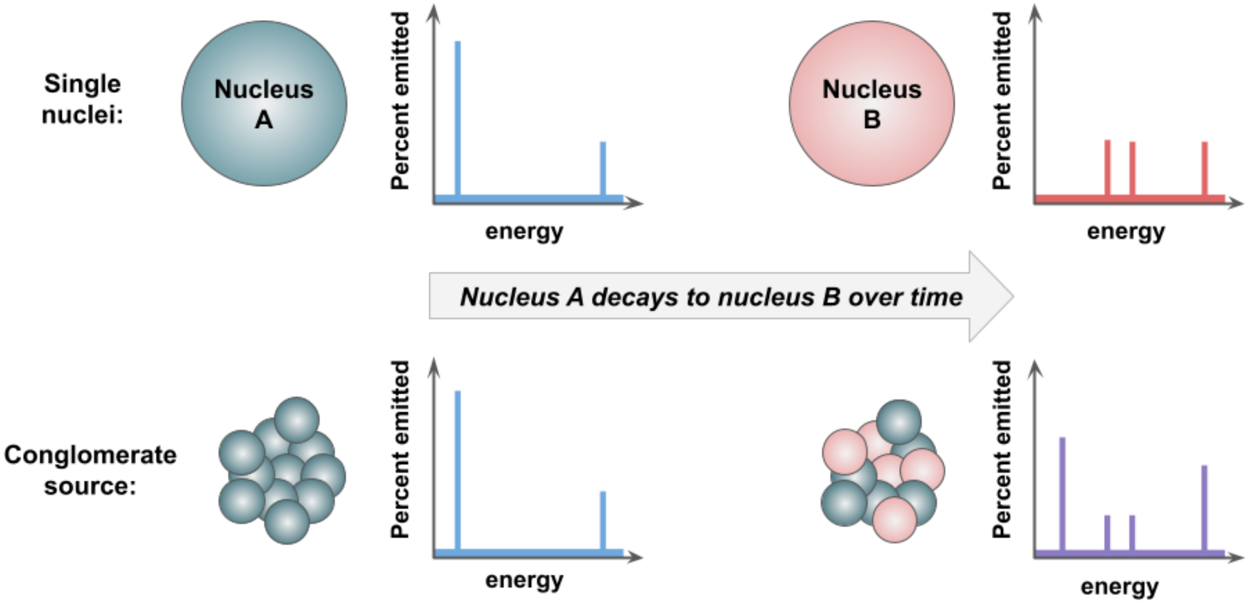

Figure 5.8: This figure illustrates how a source that evolves over time releases a different energy spectrum as it changes. Though it does not much impact the neutron spectrum we are interested in, this process will cause some divergence between real and simulated Cf-252 data because the former evolves in this manner while the latter, as currently implemented, does not. For the simplified case in this figure, consider two arbitrary, hypothetical nuclei, A and B (top). Say we are interested in the energies emitted as nucleus A decays to B, but B itself decays further, emitting other spectra/products. A physical source capsule consisting entirely of nucleus A, emitting the spectrum we're interested in (bottom-left), will accumulate nucleus B over time, changing the observed spectrum along the way (bottom-right).

5.3.1 Experimental Configuration

As mentioned previously, Ba-133 and Cf-252 sources were periodically inserted into the cryogenics or electronics pipes in the apparatus (as was shown in Fig. 2.5) so their decay products could more easily reach the detectors. For Ba-133 there were usually two sources inserted at once–one in each pipe, once or twice a day–for a total of about 15 hrs each week [35]. A single Cf-252 source, meanwhile, was introduced only every few months (to minimize backgrounds from germanium activations, as noted in section 2.3). Note that Ba-133 and Cf-252 calibrations did not overlap[2].

In this study, we do not use all the data taken for calibration sources at Soudan. We focus, firstly, on the subset of data taken near the LT Analysis period, as we are using data-selection cuts inspired by this analysis (as noted in chapter 4). We cut down further from there, secondly, to match the specific experimental setup that we simulated for chapter 8 and beyond: single calibration sources in the electronics pipe. Our simulations can handle more than this (and are ever-improving, in addition), but they can be very computationally intensive and the output files can take up a lot of disk space–so with multiple simulations to analyze, we made some limiting choices.

5.3.2 Results

Fig. 5.9 shows energies measured in a single detector across one Cf-252 and 13 Ba-133 data-taking runs at Soudan. These look different than Figs. 5.3 and 5.6, as expected due to the energy loss mechanisms described in chapters 2 and 3. We will analyze these results further in later chapters–with simulation data for comparison–but for now, we note:

- The Ba-133 data shows the 356 keV peak clearly (and smaller 303 and 384 keV peaks are visible as well), which is the main data point needed for calibration (note that the peaks are currently low; we will be doing some calibration ourselves). Otherwise we see that many events have Compton-scattered out of the expected peaks to lower energies (i.e. the photons left without depositing their full energy–most around $356/2 = 178$ keV).

---

[2] Except once when the Ba-133 holder broke off inside the apparatus and wasn't removed until after Cf-252 calibration.

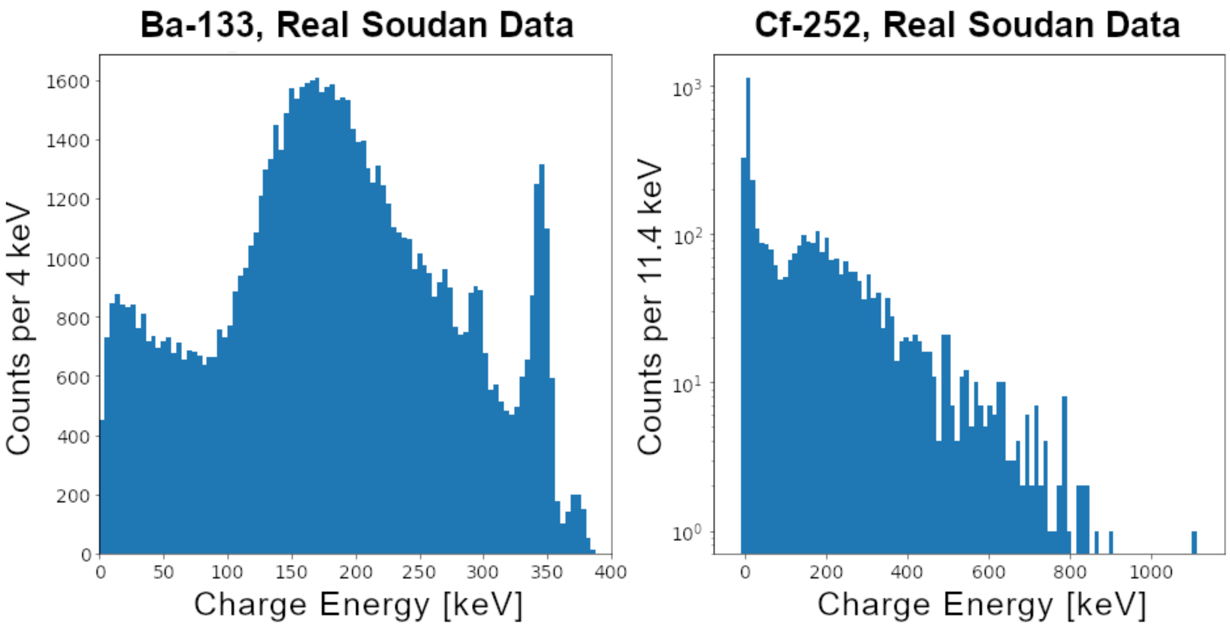

Figure 5.9: This figure shows the measured charge energy distributions from a set of Ba-133 and Cf-252 calibration source runs at Soudan. Note that here we've used qimean as our measurement of the charge energy (refer to Table 4.1). Left: the Ba-133 spectrum has a prominent peak around 356 keV that we use for calibration (the peaks near 303 and 384 keV may be used as well; these were all visible in Fig 5.3). Many photons, though, will have lost energy interacting with other apparatus components and many, further, won't deposit their full energies when they hit, both factors resulting in lower energies in the detector–most notably the Compton peak just below 200 keV. Right: Cf-252 emits neutrons that can be used to study NR interactions, but their deposited energies don't have as many identifiable features as those for Ba-133. Here we mostly see events depositing low energies after bouncing through many detector components between the source capsule and the detector.

- The Cf-252 spectrum doesn't have features as obvious as those in Ba-133 (though we'll make use of the peak around 200 keV in chapter 10), but we see that all energies have been shifted much lower (nearly all the events are below 1 MeV, the expected peak value). This is reasonable, as high-energy neutrons can easily bounce through multiple materials and only deposit a fraction of their original energy in the detector.

Fig. 5.10 shows the same data as Fig. 5.9, but in terms of the reconstructed yields as a function of recoil energy. Here we see Ba-133's ER events with yields clustered around 1–as is expected for photons–and Cf-252 with both ER events at 1 and NR events following the Lindhard yield.

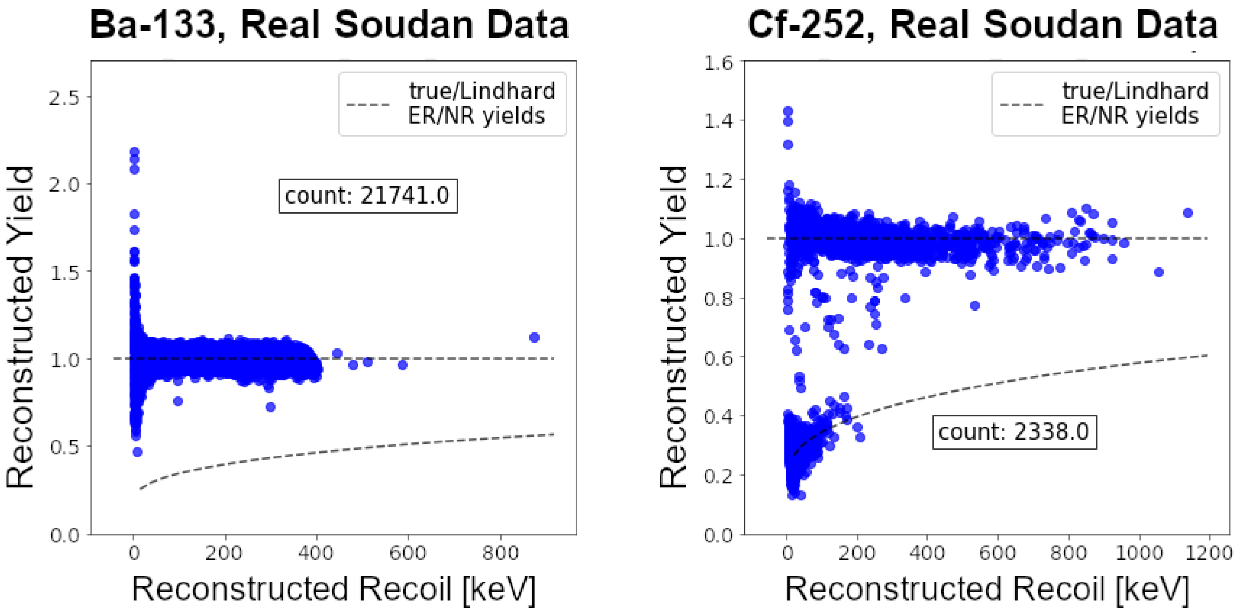

Figure 5.10: This figure shows the same data as Fig. 5.9, now plotted as the reconstructed or calculated yield as a function of measured recoil energy. The distinct behaviors of photon (ER) and neutron (NR) events are clearly visible here. Both the yields and recoil energies are calculated from the reconstructed charge energies (like those shown in Fig 5.9) and phonon energies (specifically qimean and ptNF; refer to Table 4.1). The distinction between the upper ER band of events and the lower NR band in the Cf-252 data (right) is our ultimate interest, as WIMP-like events are expected to show up in the NR band (note that the x and y scales are different between these two plots; the ER bands are centered around yields of 1 for both). In subsequent chapters we will study what factors and processes affect the shapes of these bands in simulations and what we can learn about this real data from them.

While there is a visible distinction between ERs and NRs, we also see events deviating from those expected behaviors and blurring the boundaries–such events likely being either mismeasured or multi-hit, as was covered in Chapter 3; we'll be studying these in simulations going forward.

We've now described all the real physics involved in the experiment–including the sources we're studying and the apparatus they propagate through. The remainder of this thesis will cover how well our understanding of these physical details has been implemented in simulations, how well those simulations match the real data shown here, and what we can learn about the events blurring the lines between ERs and NRs.

6. SIMULATION INFRASTRUCTURE AND VALIDATION PLAN

The previous chapters described the real Soudan experiment and the data we got from it. We now move to simulations of the experiment. Monte Carlo methods/simulations have played a significant role in previous experiments (including major discoveries like the top quark[72] or the Higgs boson[73]) by, e.g., helping to understand detector responses, determine background rates[25], and optimize analyses–and we continue to use and expand our simulation tools to both analyze previous data and prepare for the next experiment. In this chapter we'll describe the steps/stages of the full simulation chain and introduce the groups of datasets we'll use in our studies.

6.1 Simulation Overview and Goals

As shown in Fig. 6.1, the full simulation chain models what is done by real detectors and the data acquisition system and ends–as real data collection does–with event reconstruction. Simulated data ultimately produces the same "raw" format as real data and can be run through our standard CDMS reconstruction and analysis code CDMSBats with minimal effort.

We identify three main theoretical divisions of the simulation chain: SourceSim, DetectorSim, and Reconstruction–though the actual code is not neatly divided into those categories (and the third step, Reconstruction, is not specific to simulations).

- SourceSim models the creation of primary particles and their propagation through the experimental apparatus–the end result being energy deposits in the detectors (and related information like timing, particle type, energy, and location).

- DetectorSim models charges and phonons–created by SourceSim's hits–propagating through (and interacting with) the detector crystals and the resulting readouts from the detector sensors and the DAQ.

- Reconstruction is the same process described previously for real data in chapter 4–where the

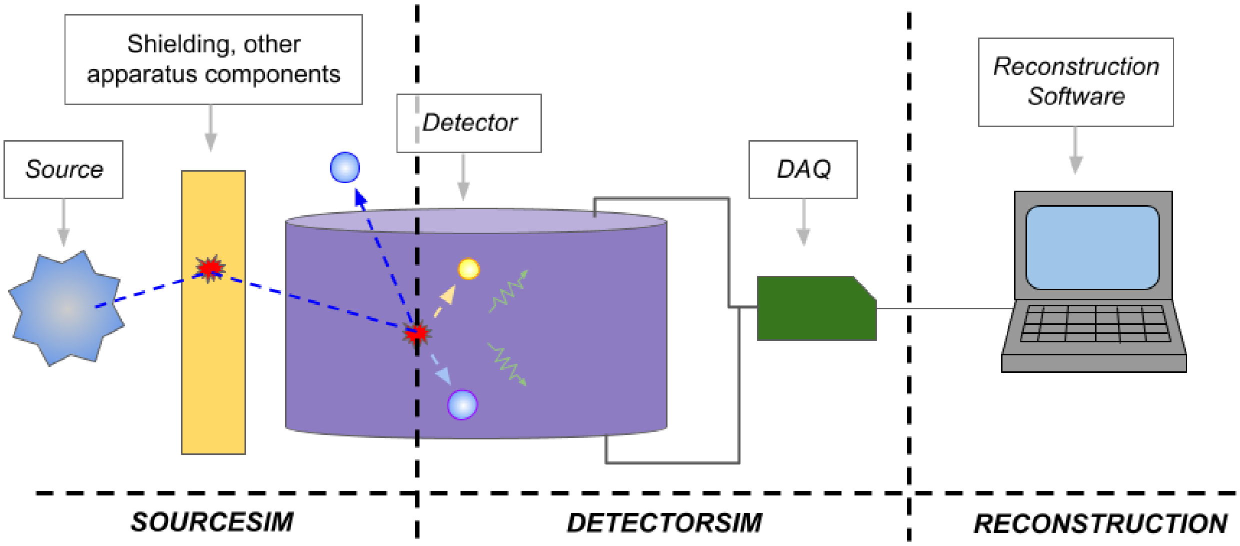

Figure 6.1: This figure shows a more detailed version of the simulation workflow in Fig. 1.9, now mapping the simulation stages to the corresponding physical components. We show this to provide a general idea of what each stage will be handling. There will be more physics to validate towards the left and more mathematics and tuning to validate towards the right.

detector output is converted into useful physics quantities.

That is, these three divisions generally correspond to the content of chapters 2, 3 and 4–and will be recapitulated for simulations in the following three chapters.

6.2 SourceSim: Modeling Particles Traversing the Apparatus and Depositing Energy

"SourceSim" covers the source (of primaries) we want to simulate (be it WIMPS, photons or neutrons from calibration sources, contaminants whose rates we want to verify, etc.), the energy depositions within the detector volumes it leads to, and everything in-between. This includes particles that have multiple interactions throughout the full apparatus and particles that don't interact at all–though in practice we don't usually store such information unless we mean to validate the behavior of the source itself (as we will in the next chapter).

The code handling this stage, built by CDMS, is named "SuperSim" and is built on Geant4 [74], a toolkit for simulating particles interacting with/passing through matter[1]. SuperSim itself

---

[1] Note that while Geant4 (and so SourceSim) uses Monte Carlo (or "MC") methods for simulations, we usually reserve that terminology for the Detector Monte Carlo (or "DMC") in the next simulation stage, DetectorSim. In other

handles the geometry and materials of CDMS hardware (shielding, detectors, etc.) and the sources (WIMPs, calibration sources, etc.). The final product, then, allows us to specify particles of interest, simulate them scattering through detector components, and see what energies they deposit in particular volumes.

At the end of the SourceSim stage, the data is in the form of exact energies and locations in the simulated volumes (and related information, including particle types and timestamps). The hits that are left in detector volumes get passed off to the next stage, DetectorSim.

6.3 DetectorSim: Modeling Energy Propagation and Readout in the Detector

SourceSim gave us particular energies and interaction types at particular locations. Next, DetectorSim models the detectors response to those energies/interactions at those locations and the DAQs response to the detectors. We identify four sections within this stage: CrystalSim, TESSim, FETSim, and DAQSim, the first three being components of the Detector Monte Carlo, or "DMC". Fig. 6.2 illustrates the components of DetectorSim and the processes they simulate.

6.3.1 The Detector Monte Carlo

The current DMC is implemented as part of SuperSim (alongside SourceSim; both the DMC and SourceSim are Geant4-based Monte Carlo simulations). A single SuperSim job, then, can start with a primary particle and end with pulses similar to those output by the real detector–though at this stage the pulses will be ideal, noiseless, and in units only used by the sensors themselves; the next stage, DAQSim, will make them more reaslistic. Before that, though, we discuss the three divisions of the DMC: CrystalSim, TESSim, and FETSim.

CrystalSim is the actual Monte Carlo segment of the DMC. As described previously, ERs and NRs in the detector produce charges and phonons in a particular ratio described by the "yield" (equation 3.3), which depends on both the type of particle depositing energy and how much energy it deposited. Given that information from SourceSim, CrystalSim models the resulting charges and phonons traveling to the detector faces and getting collected (or possibly getting stuck elsewhere);

---

words, there are two separate DMC stages, but for sake of distinguishing them (and CDMS historical reasons) we usually only refer to the second stage as our MC simulation.

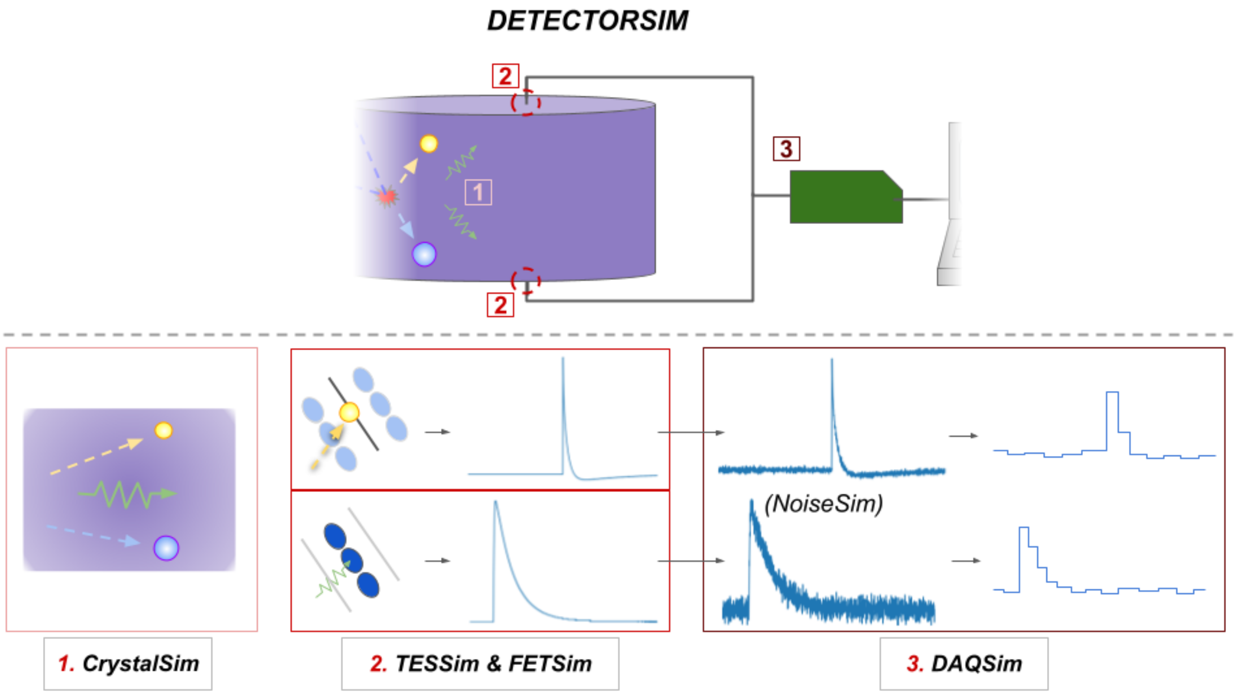

Figure 6.2: This figure shows more detail for the DetectorSim components of Fig 6.1, the cartoons at bottom representing the processes each stage models. CrystalSim simulates charges and phonons moving through the lattice from the original energy deposition to the detector edges. FETSim reads the amount of charge collected on the FET circuits and outputs the corresponding charge pulse. TESSim likewise converts phonon energies into raw phonon pulses. The pulses at this point are "too perfect", and are made more realistic in DAQSim, which adds noise (optionally), rescales to the units used in the real DAQ system, and digitizes the pulses (the scaling and digitization in this figure is greatly exaggerated for illustration.)

this includes processes along the way like NTL phonon emission and phonons reflecting off surfaces. CrystalSim is built on G4CMP, a software package that does Condensed Matter Physics in the Geant4 framework [32].

TESSim[2] takes the total phonon energy collected at the detector faces and produces the corresponding pulse that a TES would have produced. This can be done either by solving differential equations describing heat and electricity in the TESs or by scaling up pulse templates (like those described in chapter 4) using the collected energy; the results shown in this work use the latter option, though we are transitioning to the ODEs for future work. TESSim is able to simulate

---

[2] Note that TESSim and FETSim can be done concurrently. One does not have to precede the other in the same way that the DMC precedes them both.

"saturation" in the sensors as well–leveling off the pulses when the physical hardware would have absorbed too much energy.

FETSim (named in parallel to TESSim, though the FETs themselves are not what absorb energies form the crystal) takes the collected charges and produces a pulse like that that would be experienced by the real experiments electronics. As with FETSim, this can be done either by solving differential equations or scaling template pulses (as with TESSim, we've used the latter[3] here but are moving to the former). The Shockley-Ramo theorem (described in chapter 3) is applied in this stage to determine how much charge is sensed by the electrodes–and the resulting changes in current that will ultimately provide the measured energies.

6.3.2 DAQSim: Pulse Scaling and Noise Addition

DAQSim is the first distinct code after SuperSim[4]. It takes three main steps to convert the simulated pulses of prior stages into the raw data format used in the real experiment.

First, it scales and digitizes the pulses (individually–that is, channel-by-channel for both the FETSim and TESSim output) to be in units of "ADC" counts (that is, Analog-to-Digital-Converter units, which are related to the setup of DAQ hardware). Unfortunately, while the previous simulation stages can give us exact physical units, we must simulate the real DAQs unavoidable digitization and unit-agnostic electrical signals. These ADC units will be converted back into physical units by the reconstruction software operating as normal.

Second, DAQSim simulates noise, which has two aspects:

- DAQSim can directly add noise to the otherwise-perfect pulses from TESSim and FETSim, as illustrated in Fig. 6.3. This is done with PSDs of real noise taken from actual Soudan data, which we use to add small (and frequency-relevant) variations into the ADC counts in each time bin of our pulses[5]. We are able, optionally, to skip this step for simulations, which is useful for validating the performance of each stage–and understanding specific contributions

---

[3] Which has templates for both normal pulses and crosstalk pulses, corresponding to those mentioned in section 4.1.1.1.

[4] To clarify, the code "SuperSim" did both SourceSim and part of DetectorSim.

[5] There are multiple ways noise can be added, but we simply introduce some jitter into the PSD's frequency amplitudes, transform it back to time space, and add the result to our pulses.

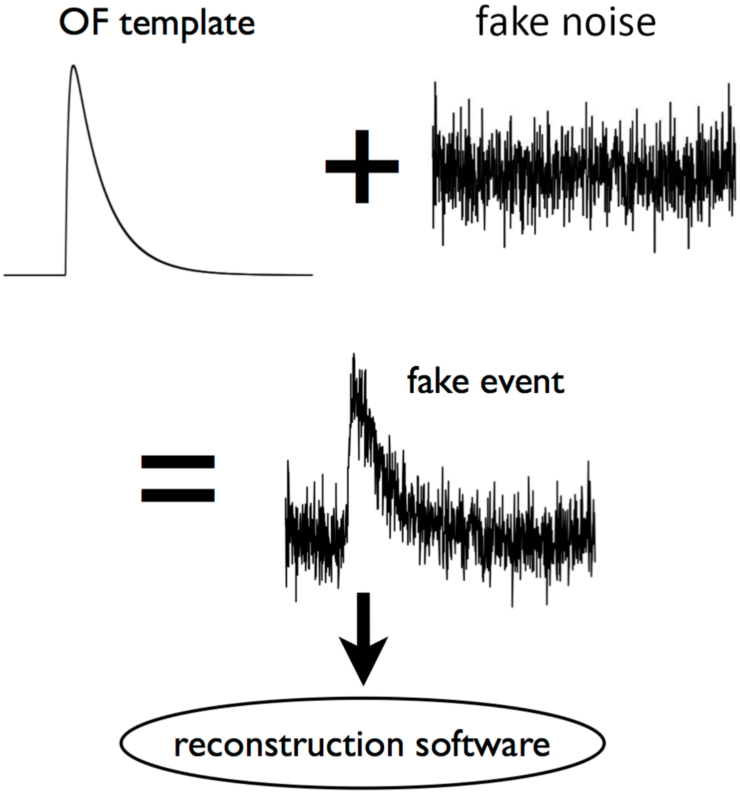

Figure 6.3: This figure shows a generic example of adding noise to a pulse, as performed in the DAQSim segment of DetectorSim. The DMC provides an idealized pulse based on a given event's collected energies; noise can be represented as a PSD or an actual, signal-less pulse from real data. The final simulated pulses combine these two and pass the result on to the normal reconstruction software used for real pulses.

to energy resolutions or mismeasurements.

- DAQSim creates a separate set–or "dump"–of noise-only events. In the real experiment, there were several sets of events recorded when nothing of interest was expected to be happening; that is, the DAQ was purposely set to randomly read out "nothing" from the detectors in order to give us a sort of baseline. These "randoms" let us check how noise by itself would be contributing to the rest of the data (they are used to construct our PSDs). While real data had three variants of these taken at different times for each run ("pre-run randoms", "post-run randoms", and "in-run randoms"), for simulations–where uncontrollable, changing environmental effects are less an issue–we just have DAQSim create a single noise dump.

Lastly, DAQSim writes out the final pulses and noise in the same binary format used in the real experiment. Recall that the output of the SourceSim stage was exact energies at exact locations. By the end of DetectorSim, we now instead have pulses (in ADC units that say more about the real-world electronics tuning than the physics we're simulating) associated with each of the four charge and eight phonon channels. This is a loss of information from SourceSim–but remember in real data we dont have the information SourceSim provides (if we did, the next stage, Reconstruction, wouldn't be necessary). We want to process simulated data just like real data, so we put it in the same format and analyze it the same way.

6.4 Reconstruction: Processing Simulated Data Like Real Data

The end result of DetectorSim (i.e. the output from DAQSim) is simulated data formatted exactly like real raw data from a DAQ. This means we can feed this simulated data directly into CDMSBats for event reconstruction just like we would real data–using the same OF algorithms and getting the same measurables out[6]. The benefit of simulation is that when we see interesting output from Reconstruction, we can look back at the same event(s) in SourceSim to see what physical processes may have contributed or in DetectorSim to check for readout problems (e.g. strange pulse shapes). Now that we've reached this endpoint, where real and simulated data are

---

[6] Though there will likely be calibration differences. We can either calibrate simulated data in a similar manner to real data or explore new methods.

comparable and simulations can be double-checked, we can introduce the samples we'll be using in our studies.

6.5 Samples Used In This Thesis

We use three sets of samples in the following chapters:

- Chapter 7 will have two SourceSim-only samples: in-depth looks at the source simulations for Ba-133 and Cf-252, in which we'll validate that the sources themselves are modeled appropriately and create accurate energy deposits in the detectors.

- Chapters 8, 9, and 10 will share a larger set of simulated samples for which we'll trace results through the full simulation chain. These will be summarized in more detail at the beginning of chapter 8. These will include a set of idealized, artificial ER and NR samples as well as Ba-133 and Cf-252 samples again, though these are different from the chapter 7 samples.

- Chapter 10 will also involve real data taken from the Soudan experiment–that is, the real Ba-133 and Cf-252 data shown at the end of Chapter 5–for comparison with simulations.

With these, we hope to establish that our simulations are internally consistent, that they match real data well, and so can be used to better-understand details of real data that cannot be studied directly themselves.

7. SOURCESIM RESULTS: VALIDATING SIMULATIONS OF CALIBRATION SOURCES AND DETECTOR ENERGY DEPOSITIONS

In this chapter we validate the performance of SourceSim using simulations of our two calibration sources. For each, we simulate single sources in the cryogenics[1] pipe and track the emission and interaction rates and energies of particles as they are created, travel through the apparatus, and deposit energy in a single detector.

7.1 Behavior of Simulated Ba-133

We begin with Ba-133. First we will check the energies emitted from the source itself (agnostic to the rest of the experimental setup). Then we will check the energies that reach and are actually deposited in the detectors; as described in Chapter 5, we will be looking for several high-energy peaks used for energy calibration and a significant Compton peak in the deposited energies.

7.1.1 Primary Particle Energies Released in Decays

To validate the output of the source itself (i.e. the "primaries"), we'll check both the total energies emitted in each decay (which tells us if the expected nuclear and atomic excitations occur at the correct rates) and the individual gamma energies that could be used in calibration. There are other decay products we might check as well, but they are less useful/interesting.

There are many combinations of specific photons and electrons that could be emitted–depending on the precise way the atom de-excites–but the total energy of all particles emitted has relatively few options, determined by the nuclear excitation level and electron capture shell. There are four main nuclear excitation levels that will contribute the most energy to a given decay, and electronic excitations will cause relatively small variations from there. The results shown in Fig. 7.1 and Table 7.1 match these expectations to within 0.1%, showing four large energy groupings with consistent, smaller deviations for each.

Here we also validate the emitted gamma spectrum, as it has relatively few possibilities and

---

[1] Note the following chapters will all switch to the electronics pipe.

Nuclear Excitation Level	Capture Shell	Expected Energy [keV]	Simulated Energy [keV]	Expected Rate [%]	Simulated Rate [%]
Level 1	M1	82.2	82.2 ± 3.2	<0.0072	0.0068
	L1	86.7	86.7 ± 1.7	<0.026	0.025
	K	117.0	117.0 ± 0.9	<0.17	0.166
Level 2	M1	161.8	161.8 ± 8.5	<0.0037	0.0036
	L1	166.3	166.3 ± 4.6	<0.013	0.0129
	K	196.6	196.6 ± 2.2	<0.083	0.0835
Level 3	M2	384.9	384.9 ± 7.9	0.0246	0.0235
	M1	385.0	385.0 ± 1.4	0.726	0.728
	L2	389.2	389.2 ± 4.6	0.0763	0.0724
	L1	389.5	389.5 ± 0.8	2.468	2.461
	K	419.8	419.8 ± 0.4	11.20	11.18
Level 4	M2	438.1	438.1 ± 3.0	0.217	0.208
	M1	438.2	438.2 ± 0.5	6.42	6.411
	L2	442.4	442.4 ± 1.8	0.643	0.617
	L1	442.7	442.7 ± 0.3	20.8	20.77
	K	473.0	473.0 ± 0.2	57.3	57.23

Table 7.1: Counterpart to Fig. 7.1. This table lists the total energies and associated rates (as a percent of the total number of events) expected and observed in a Ba-133 simulation of 10 million events. These "total" energies here include everything emitted in a Ba-133 decay (i.e. everything illustrated in Fig. 5.1 except the neutrino). The four possible nuclear excitation levels contribute the most to the overall energies, but the atomic shells that electrons are captured from are significant enough to be distinguished within each set of decays from a given nuclear level. Note that the "Simulated Energy" for each level/capture shell is an average, as the peaks in Fig. 7.1 have some variation within 100 eV (due to Geant4 leaving some energy with the original nucleus instead of the decay products shown here[74]), and its quoted uncertainty is only statistical. The largest energy difference between expectation and simulation is only 6 eV, for the Level 1, M1 shell decay. The largest difference in rate is about 0.1%, for Level 4, K shell decays. The uncertainties for the simulated rates are only statistical and are no larger than 0.02%.

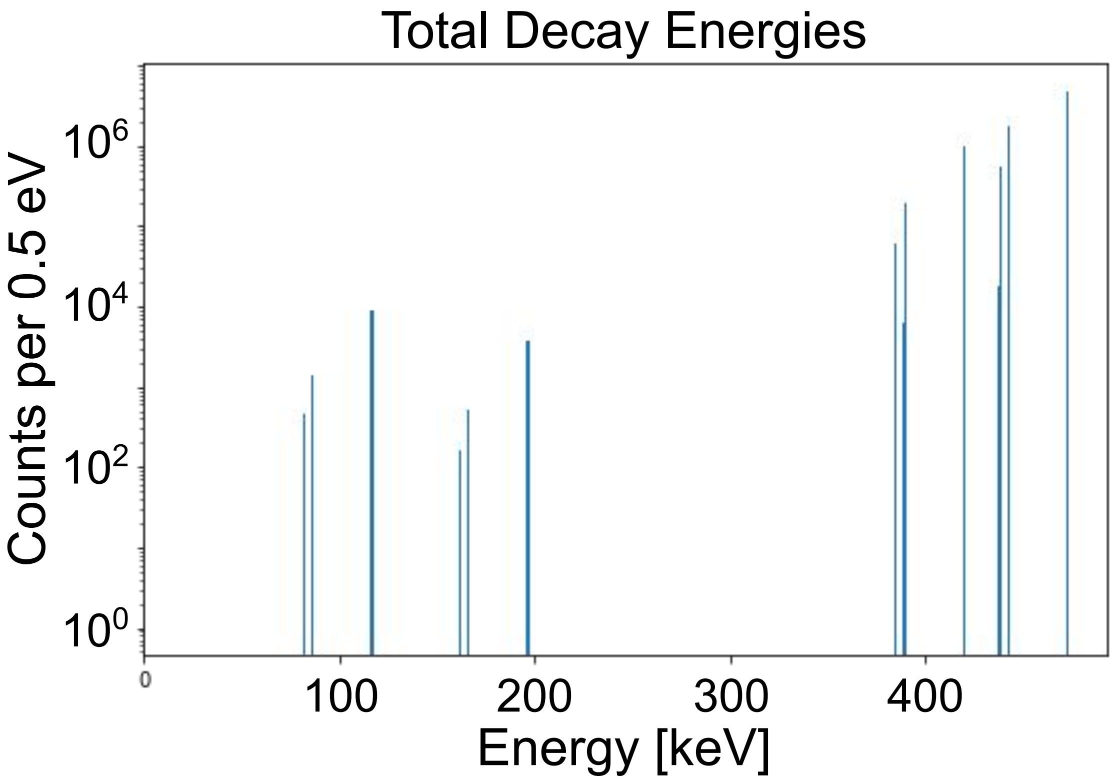

Figure 7.1: This figure shows the total energy released in each decay event for our Ba-133 simulation (this data is also shown in Table 7.1). Each entry in this histogram is the sum of all particle energies in an event together–photons and electrons; Fig 5.3, for comparison, shows only individual photons. These energy sums are convenient for validating the simulation's performance, because while there is a large number of individual electrons and photons that could be emitted, there is only a small number of total energies they should sum to. As expected, we observe four big groupings of three or four lines each–the four big groupings representing the four possible nuclear excitation levels after the electron capture and the three or four lines within each of those representing the possible shells from which the electron was captured (the most clear distinctions being between the K, L, and M shells as a whole, but with some fine detail between subshells outside K).

it is specific gamma energies we look for in the data. These results are shown in Table 7.2, and we again see good match with expectations–the largest energy discrepancy being 0.3 eV and the largest discrepancy in emission rate being 0.4%–both quite acceptable. Most important to us are the three highest-energy gammas, and they each are simulated with appropriate energies and rates.

We do not check the specific electron and X-ray energies as they are either too numerous or too unimportant for our goals; those coming directly out of the source will generally not reach the detectors anyways. As we have validated both the energy totals and the gammas, however, the

Gamma	Expected Energy [keV]	Simulated Energy [keV]	Expected Fraction [%]	Simulated Fraction [%]
$\gamma(4 \to 3)$	$53.1622 \pm (6E - 4)$	53.1623	1.58 ± 0.04	1.609
$\gamma(2 \to 1)$	$79.6142 \pm (12E - 4)$	79.6143	1.95 ± 0.06	1.947
$\gamma(1 \to 0)$	$80.9979 \pm (11E - 4)$	80.9978	24.3 ± 0.4	24.57
$\gamma(2 \to 0)$	$160.6120 \pm (16E - 4)$	160.6118	0.471 ± 0.007	0.467
$\gamma(3 \to 2)$	$223.2368 \pm (13E - 4)$	223.2368	0.335 ± 0.004	0.336
$\gamma(4 \to 2)$	$276.3989 \pm (12E - 4)$	276.3988	5.29 ± 0.07	5.257
$\gamma(3 \to 1)$	$302.8508 \pm (5E - 4)$	302.8508	13.6 ± 0.2	13.64
$\gamma(4 \to 1)$	$356.0129 \pm (7E - 4)$	356.0128	45.9 ± 0.2	45.52
$\gamma(3 \to 0)$	$383.8485 \pm (12E - 4)$	383.8488	6.61 ± 0.08	6.663

Table 7.2: This table lists the intensities (fraction of all gammas, as a percent) and energies (in ascending order) of gammas emitted by the Ba-133–both the expected values from ENSDF and the observed values in the simulation. The parentheticals in the leftmost column indicate which two nuclear energy levels are involved. For the simulation data, the energy uncertainties are negligible and the intensity uncertainties are all just statistical and less than 0.01%. The largest energy difference is 0.3 eV (for the highest-energy gamma) and the largest intensity difference is 0.4% (for the highest-intensity gamma).

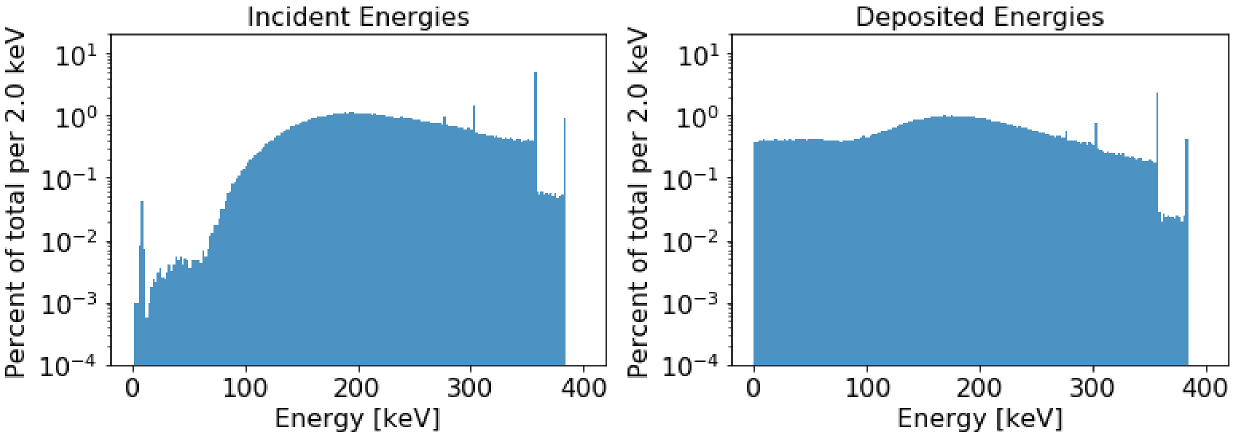

Figure 7.2: This figure shows what becomes of the energies previously in shown for Ba-133's photons in Fig. 5.3–both their kinetic energy as they enter the detector (left) and the energy they finally deposit in the crystal (right). The peaks at high energies have consistent values, which makes them useful for calibration and important benchmarks for the simulation. Left: Note that, due to Compton scattering, the incident energy spectrum is already a continuum instead of discrete peaks before particles ever reach the detector. Right: The deposited energy spectrum has an even stronger trend to lower energies because many particles will skim off of atoms and leave the detector without depositing all their energy.

contributions from electrons and X-rays must also be reasonable overall.

7.1.2 Particle Energies Incident on and Deposited in the Detector

We now move to study the energies of particles after they have propagated through the cryostat to the detectors (recall the distance shown in Fig. 2.5). We'll check both the energies as they enter the detector volume ("incident energies") and also the energies actually deposited into the detector ("recoil" energies). While these distributions should look similar, the deposited energies will have more low-energy events, as many incident particles will deposit only a fraction of their total energies and then leave the volume.

Fig. 7.2 shows the incident and deposited energies for a single detector; compare to the primary gamma spectrum first shown in Fig. 5.3. Most importantly, the high-energy gamma lines are still apparent, above the many events where some energy is lost to Compton scattering; that the peaks themselves have not been shifted to different energies means we are justified in using them as landmarks for energy calibration. This is essentially all we needed to see from Ba-133.

7.2 Behavior of Simulated Cf-252

The full decay behavior of Cf-252, as described in Chapter 5, is extensive, and our simulations do not model every aspect of it–but then much of it is not useful to the experiment, as we will discuss. Here we will check on both the alpha decay and spontaneous fission implementations for completeness, but keep in mind that we're ultimately just interested in the prompt neutron spectrum from fission. Section 7.2.2 will comment specifically on some of the shortcomings of those implementations, which are further described in Appendix B.

As we did for Ba-133, we'll then look at energies out of the source itself, energies incident on the detector, and the energies actually deposited. The Cf-252 data has more complexity than that for Ba-133, though; we'll briefly address both changes to the source over time and, in the next section, the complicated recoil types possible for this source.

7.2.1 Decay Modes in the Simulation

Recall that Cf-252 can decay either via alpha decay or by spontaneous fission. Geant4 does not (or did not, at the time these studies were done) simulate fission daughter nuclei directly, and since the complete alpha decay chain may include other fissions, neither Cf-252 decay chain is completely simulated. In this section we provide a brief overview of how the two overarching decay modes are implemented in simulations and how they are relevant to the results we're looking for.

7.2.1.1 Alpha Decay Implementation

Alpha decays themselves are fairly straightforward to model: simply produce the relevant particles and energies at the rates shown in Figure 5.5. SourceSim can also model subsequent decays from the products, but, again, since the rest of the chain is stuck behind Cm-248s long half-life, the later products are largely irrelevant (future simulations may even implement a time cut to turn off such late-occurring events in the first place).

For simulations in later chapters, we will not even bother with Cf-252's alpha decays at all. Since alpha decays occur about 97% of the time, they are a huge source of uninteresting events (if they show up in the detectors at all) when we only want to study fission neutrons in our samples.

7.2.1.2 Spontaneous Fission Implementation

Our implementation of Geant4 uses a fission model from Lawrence Livermore National Lab [75] to produce individual events based on the average overall outgoing spectra of neutrons and gammas; that is, we are going to be dealing with statistical distributions of those particles–not tracking the specific mechanisms that produce a given single neutron from a specific relaxing fission fragment, say. The specific fission fragments are not produced, in fact, which means we do miss some of the particles they would emit as they decay further.

The energies of outgoing neutrons are drawn from one of three models: a "corrected" Maxwell Spectrum by W. Mannhart[66], a Watt spectrum by F.H. Froehner[67] , and the Los Alamos Model by Madland and Nix[76]. In this chapter we will primarily use Mannhart's corrected Maxwellian, with a few comparisons to the Watt spectrum (which is easier to understand visually).

For gamma energies, LLNL constructed a piecewise function:

$$N(E) = \begin{cases} 38.13(E-0.085)e^{1.648E} & E \leq 0.3MeV \\ 26.8e^{-2.30E} & 0.3 \leq E \leq 1.0MeV \\ 8.0e^{-1.10E} & 1.0 \leq E \leq 8.0MeV \end{cases} \cdot \tag{7.1}$$

This is actually a fit to U-235 data (from Ref. [69]), which, as noted before, is quite similar to that of Cf-252, but better-measured.

7.2.2 Cf-252 Simulation Caveats

As noted, the Cf-252 simulation is missing some pieces–aspects of the simulation that affect the outgoing spectra. Here we briefly summarize them and why they are not major concerns for us; further information can be found in Appendix B.

The first notable shortcoming is the absence of fission fragments. After the initial Cf-252 fission (or possible fissions late in the alpha decay chain), the two daughter nuclei are likely in excited states and will emit further energies. These generally neutron-rich daughters, however, will mostly undergo beta(-) decays (as will their own daughters in turn) that emit no further neutrons (other than relatively small amounts of delayed neutrons some seconds afterward[65]), so our prompt neutron spectrum is essentially unaffected.

A second shortcoming is the age of the source and the timing of decays (i.e. when the emitted spectra change). The real Cf-252 source used at Soudan had already been decaying when it was used for data-taking–meaning it already had daughter nuclei emitting different spectra than their parent. The simulated Cf-252, on the other hand, is only Cf-252: we did not start the simulation with daughter nuclei present and the simulation does not create them. Once again, though, this does little to change the outgoing *neutron* spectrum; the *photon* spectrum will differ between the real source and the simulated source due to these timing issues, but we're not trying to match those up at this time.

In short, then, we are only interested in the fission neutrons and those are not significantly affected by the simulation shortcomings covered here. Other spectra may change, but we are not looking for specific energies from them–as we were for Ba-133–so even if they are not consistent with the real source, they provide example events at energies within our range of interest, which is useful; since we are more generally interested in studying the detector response instead of Cf-252 itself, neutrons would be useful in the same way even if they were affected in the way that the other spectra are.

7.2.3 Particle Energies: Out of the Source Capsule and Incident on the Detector

Here we check the Cf-252 source's outgoing particle spectra and the timing of when particles reach the detector. Again, we will be most interested in the neutrons, but for simulation validation purposes we can check that the other particles behave reasonably as well.

Fig 7.3 shows that the prompt fission neutron spectrum from the Cf-252 simulation matches the expectation given by a Watt spectrum[2]. Fission photons and alpha-decay products are also emitted

---

[2] The simulation here is actually matching a corrected Maxwellian, but the data for that spectrum combines multiple data sets and bins them unevenly, making for visually-unintuitive results.

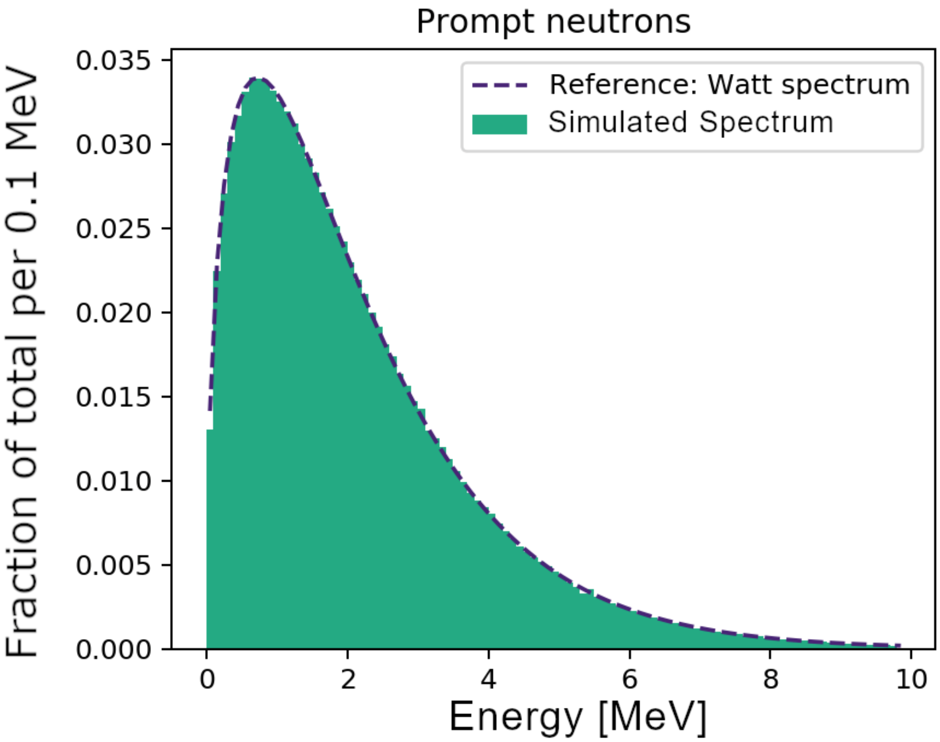

Figure 7.3: This figure shows a comparison between the simulation's outgoing neutron spectrum from fission of Cf-252 and the expected Watt spectrum (compare Fig. 5.6). We show this to check that the simulation matches expectation well, which it does.

at the expected energies and rates, but they are not our focus here (see Appendix B for those).

Fig. 7.4 shows when particles enter the detector, in which we identify three divisions. In the first, "prompt" section before one second, the fission neutrons reach the detector, along with whatever other particles they knock out along the way. Next, between one second and ten years there are more electrons, positrons, and photons–i.e. only particles that cause ERs–that are created in de-excitations of the detector crystals after the initial volley of neutrons excited them. Lastly, particles that enter the detector after ten years are essentially all from the alpha decay chain and are not interesting to us–both because of their timing and because they all, again, only cause ERs.

Fig. 7.4 also shows that neutrons that took longer to reach the detector enter it with lower energies. This is a simple check on the simulation's performance: it makes good physical sense that neutrons that spent time bouncing off other components on the way to the detectors have less

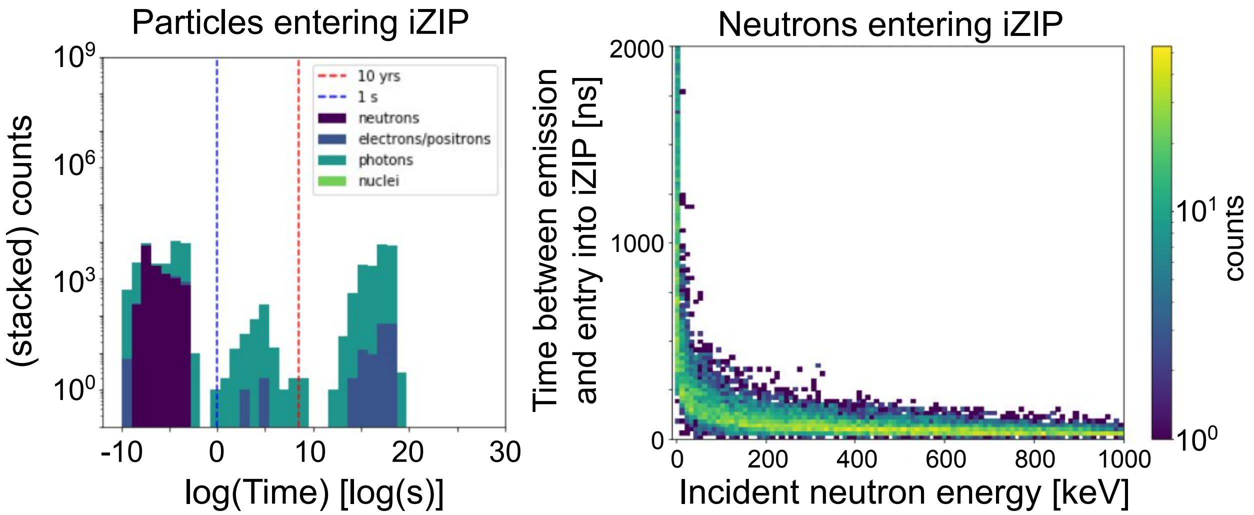

Figure 7.4: This figure shows the energies and times when particles from the Cf-252 source (or particles they create) enter the detector volume, with particular attention on our calibration neutrons. Note that the times for each event are given relative to when the original decay occurred. Left: Times when particles enter the given iZIP's volume, with distinct regions for prompt particles, particles from Ge-71 de-excitations, and later alpha decays. Right: Neutron incidence times vs energy; as expected, neutrons that took longer to reach the detector (because they were bouncing off other components) show up with less energy (lost in previous bounces).

energy when they arrive (since it was lost in those previous bounces).

7.2.4 Energies Deposited in the Detector

Lastly we check on the particles that actually deposit energy in the detector. Fig. 7.5 again shows timing information, now broken down by recoil type–here identified by the set of particles entering the detector within the detector's readout time window (described at the start of chapter 2): if only neutrons enter the volume, the event is an NR; if only photons or charges enter the volume, then it's an ER; and combinations of neutrons and other particles will simply be "mixed" events for now (we will go into more detail later in this chapter). As expected, the deposited energy timing is similar to what was shown in Fig. 7.4, with essentially three divisions dominated by prompt neutrons, Ge-71 de-activations, and late alpha-decay-chain particles. Since we're only interested in the prompt neutrons, for both the rest of this chapter and the rest of this thesis we will exclude

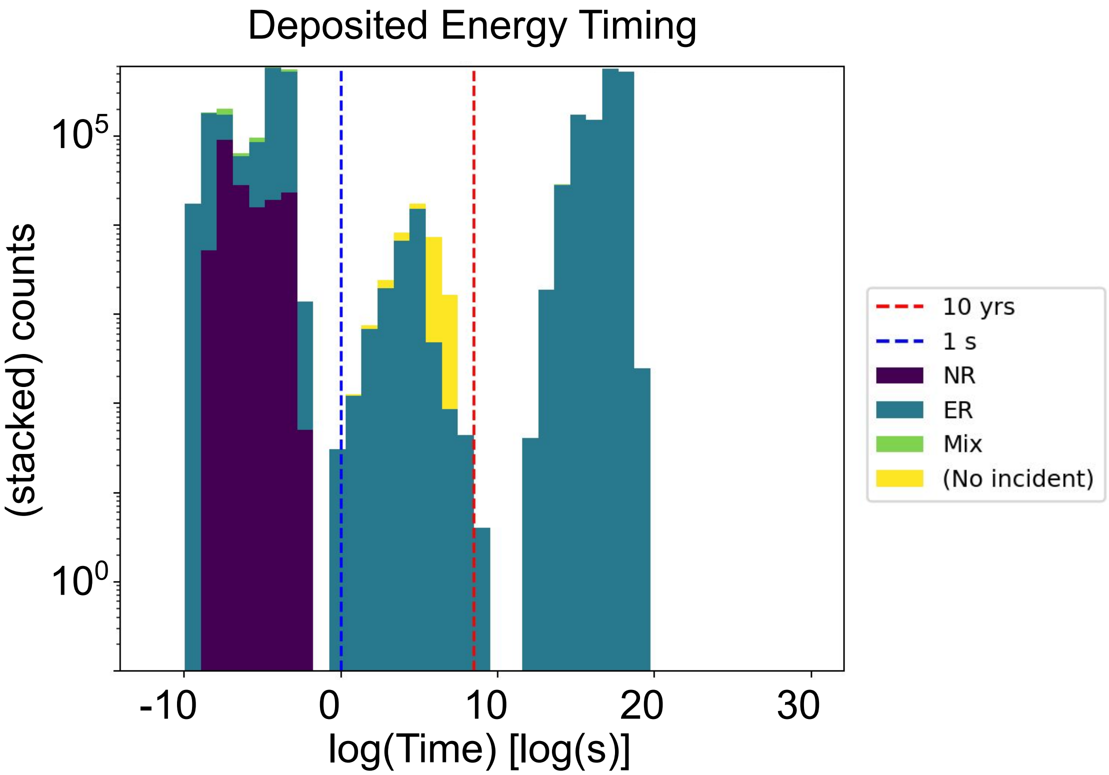

Figure 7.5: This figure is like the left side of Fig 7.4, but shows when energies from the source are actually deposited in the detector–here broken down by recoil type. Note that here we've identified recoil types based on all the particles entering within the iZIP5 readout window since in real data we can't separate hits occurring close together–hence the "Mix" and "No Incident" categories in this figure. Neutrons–our primary interest for Cf– only show up in the "prompt" section again, since they are currently only produced in the initial fission event. There are several depositions with no incident particle in the middle section due to Ge-71 de-excitations in the detector itself.

everything past one second[3].

Fig 7.6 shows–for everything before one second after the initial simulated decays–the fractions of ERs, NRs, and mixed events as a function of energy, in which we see that NRs dominate at the lowest energies while ERs dominate at higher energies. This is reasonable since the neutrons likely bounce around a lot before reaching the detectors–not only losing energy themselves, but likely transferring it to photons and electrons along the way (by exciting nuclei that subsequently release these other particles, that is).

---

[3] The Ge-71 activations in the middle are relevant to the experiment, but we study those in separate, dedicated simulations not covered here.

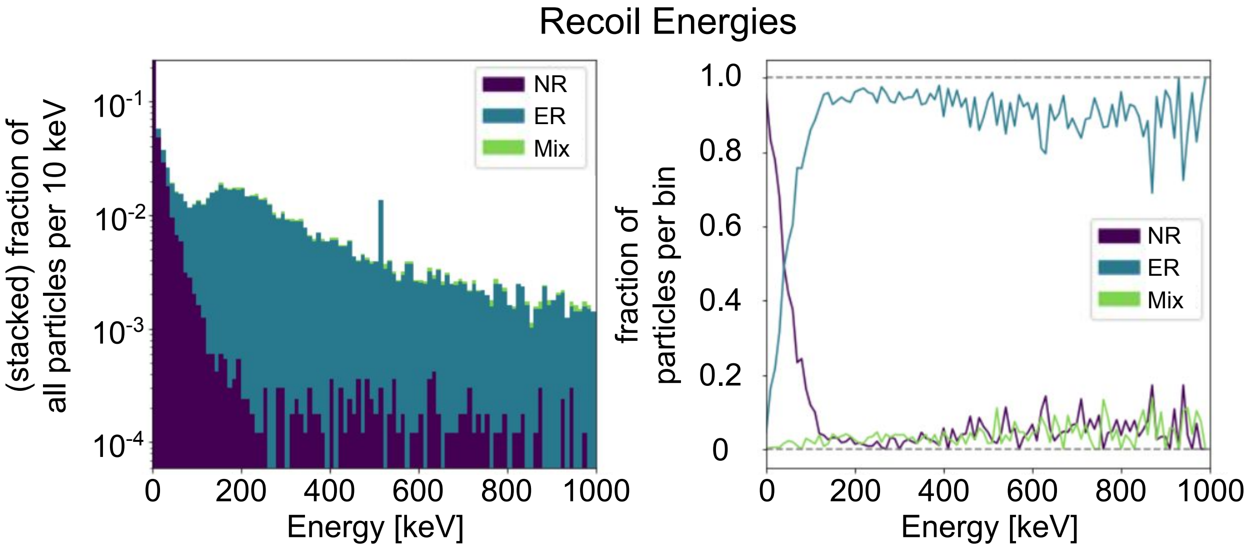

Figure 7.6: This figure shows two comparisons of the proportions of ERs, NRs, and mixed events as functions of deposited energy in our Cf-252 simulation. For each, the left plot shows the fraction of all recoils and the right plot shows the fraction within each energy bin. We note that NRs (purple) dominate at low energies since neutrons usually lose much of their energy bouncing around the full apparatus before they reach the detector. Otherwise ERs (blue)–due to photons and electrons freed in most interactions–dominate at higher energies. There is also a small, relatively constant fraction of hard-to-identify mixed events (green) throughout. Note that the new, thin ER peak at 511 keV in the left plot is due to electron/positron annihilation (neutrons captured in the copper housing of the detectors can create Cu-64, which emits positrons).

Largely constant across all energies is an undercurrent of mixed events, which are typically due to neutron bounces as well. A neutron that transfers some of its energy to photons/electrons in one detector may very well enter another detector alongside those electrons/photons. This results in multi-hit, mixed-recoil events that are difficult to untangle in simulations and would show up as some kind of mix in real data.

We've now seen everything we wanted to see in the SourceSim data itself: the primaries of our samples match expectations, their propagation through the detectors is reasonable, and the final deposited energies are also reasonable. This SourceSim output, then, is ready to be sent to the DMC, but first–for the rest of this chapter–we are going to look more closely at the recoil patterns involved in our energy deposits.

7.3 Looking Ahead: Cf-252 Energy Depositions and Associated Yields

We now extend our use of the Cf-252 sample somewhat to get an early look at what we should expect in the final data. The Lindhard model, which determines how deposited energies are distributed into ionizing and non-ionizing energies (refer back to Ch. 3), is normally handled by the DMC–the next stage in the simulation, and for future samples we will let that proceed as normal. But here we manually apply the Lindhard model (using eq. 3.5) to our Cf-252 SourceSim results to check what sorts of yields we should see based only on the energy deposits themselves (i.e. before detector effects).

7.3.1 Overall Features

Fig. 7.7 shows the ionization energies and recoil energies for the energy deposits shown in Fig. 7.6 (recall this is only deposits before one second and each "event" can include multiple incident particles if they enter in quick succession). We see trends similar to those expected from the Lindhard model (Fig. 3.2) and observed in real data (Fig 1.8). Specifically, there is an upper line of ERs with a slope of unity and a curve of NRs towards the bottom.

Compared to the simple Lindhard Yields shown in Fig. 3.2, though, we already (that is, before the majority of the simulation chain) see deviations from those plain ER and NR lines. The NR "line" here appears imprecise, the ER line has small offshoots branching off of it (one visible starting near an ionization energy of 50 keV and a more faint one near 15 keV), and there are many events between and below the ER and NR lines that look like noise/mismeasurements–even though they actually are all from Cf-252 decays in this simulation. Since these effects are not due to noise or detector effects, we take a closer look at how energies were deposited for each event.

7.3.2 Recoil Type Distributions

We gain some insight into the features of Fig. 7.7 by breaking the events down by recoil type (refer to the full list in section 3.1.2; recall, again, that these "events" are more than just single-particle ERs and NRs). Fig. 7.8 shows this for both ionization energy and ionization yield as a function of recoil energy for each event. Table 7.3 summarizes how often each recoil type occurs

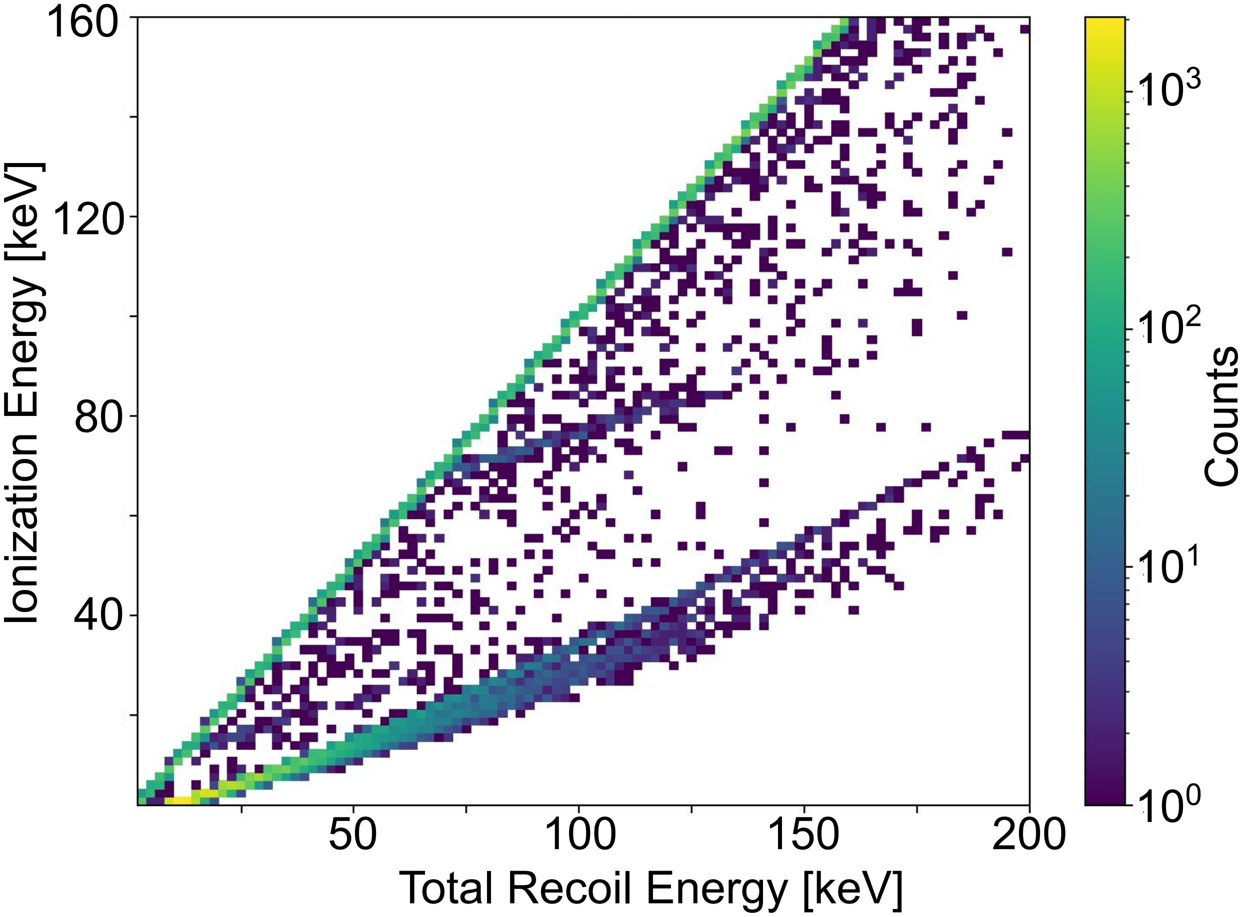

Figure 7.7: This figure shows simulated Cf-252's ionizing energies vs. recoil energies as a heat plot, for comparison with the expected Lindhard Yield in Fig 3.2. We see that the majority of events are normal ERs with Lindhard yield equal to 1 (hence the straight line with slope 1) and normal NRs on a slight curve towards the bottom–as expected. In between those and below the NR band are the various more-complicated recoil types involving multiple bounces and combinations or ERs and NRs. Overall, the shapes here look very similar to Soudan calibration results, as shown in Fig 1.8, though there are no zero-charge events here because that is a detector effect which would occur later in the simulation chain.

Deposition Type	Fraction of depositions [%]	Amount more than 1% away from ER and NR bands [%]
ER	65.53	0
Simple NR	17.00	0
Multi-NR	12.02	97.33 ± 0.64
Quasielastic	1.48	88.16 ± 1.73
nCapture	1.03	19.68 ± 0.98
Inelastic	0.06	97.32 ± 9.32
Mixed	2.89	37.85 ± 0.81
Other	0.0005	0

Table 7.3: This table shows the fraction of all depositions by recoil type in the Cf-252 simulation. The vast majority are simple ERs and NRs, in which all the deposited energies are very close to the amounts expected. The next most common recoil type is the Multi-NR, which almost entirely looks like "too-low" simple NRs in Fig 7.8. The remaining recoil types also have significant, though varying, proportions outside the expected ER and NR bands.

and the proportion of each that is distinct (more than 1% away) from the main ER and NR bands. We next take a closer look at each recoil type.

7.3.2.1 Normal ERs and NRs

ERs are relatively straightforward no matter how many hits are involved because they all have the same Lindhard yield. NRs, though, can be more complicated, so we first identify the simplest case wherein a single neutron scatters from a nucleus without any other particles being created. In Fig. 7.8, these two simplest categories appear exactly where the Lindhard model predicts them, with no deviations. Note that this is true only for this earliest simulation stage; later stages will make even these simple ER and NRs identifiable only within some resolution (due to detector effects, electronics noise, etc.).

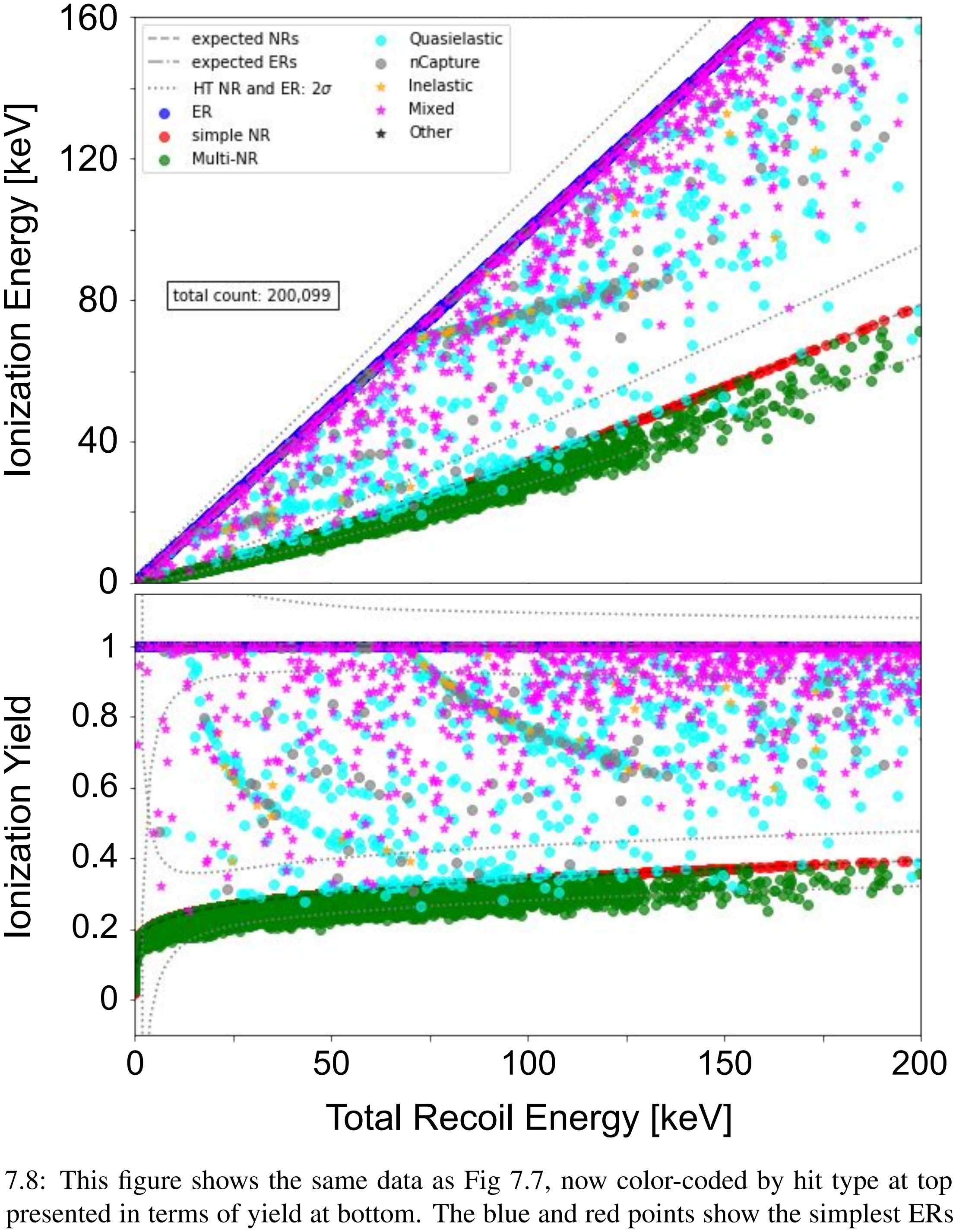

Figure 7.8: This figure shows the same data as Fig 7.7, now color-coded by hit type at top and further presented in terms of yield at bottom. The blue and red points show the simplest ERs and NRs, and in-between are the several compound recoils involving both ER and NR aspects. The lowest, green points show NRs involving multiple hits, which show up low due to nonlinearities in the Lindhard model. All the more complicated recoils, even when well-measured, could be confused with mismeasured simple ER and NR events. The lower plot is essentially the same as the upper plot, but the y-axis is divided by the recoil energy.

7.3.2.2 Multi-NRs

Because the Lindhard yield for NRs depends on the magnitude of the energy deposited, neutrons that scatter multiple times or multiple neutrons that scatter together (assuming no other particles are created for the the purposes of this category) will not result in the same phonon energy as a single neutron with a single scatter. For example, in our Ge-71 detectors, the ionization energy of a 50 keV NR is about 15 keV while that of a 100 keV NR is about 34 keV. So if there are two 50 keV NRs that happen in quick succession such that they look like a single energy deposit, we would see a 100 keV recoil that is "missing" 4 keV in ionization energy. Hence in Fig. 7.8 all the Multi-NRs show up no higher than the normal NRs.

7.3.2.3 Quasielastics, Neutron Captures, and Inelastics

In the case where a neutron (or neutrons) excite a nucleus, there are several possible outcomes in which some combination of nucleons, electrons, and photons are released. This means the observed ionization yield will likely be somewhere between the ER and NR lines (though below the NR line is possible as well, as was described previously for multi-NRs).

Most common among these are "quasielastic" recoils, which make up much of the middle section of Fig. 7.8, though they trend more closely towards the ER line–as do the neutron captures and other inelastic recoils. Most interestingly, though, they appear to cluster somewhat along particular offshoots deviating from the main ER line. This is because most of these energies are due to particles emitted from the nuclei as they de-excite after the incident neutron excited them–meaning we should be seeing energies corresponding to particular nuclear excited states. The two branches visible in Fig. 7.8, for instance, correspond to the 13.28 and 68.75 keV excited states of Ge-73 (see where they branch off from the ER line in the upper plot); there are even more outside the plot range, corresponding to four different isotopes of germanium. Since this is a simulation, we were able to verify that we were seeing energies from these nuclear excited states by artificially adding back in the energies of particles that escaped the detectors in each event; we won't discuss this much more, but see Fig. 7.9 for details.

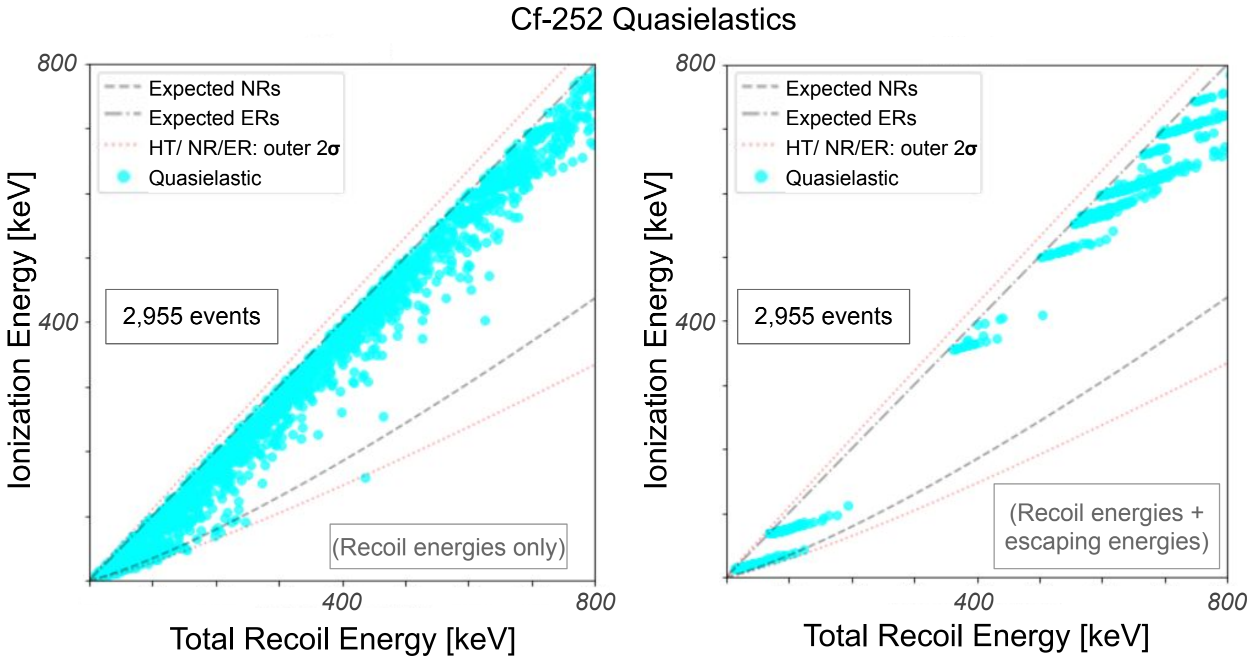

Figure 7.9: This figure illustrates the combined ER/NR nature of quasielastic events. The left plot shows the same quasieleastic events as Fig. 7.8, but zoomed-out to show higher energies. The right plot shows these same events, but with the energies of all photons and charges escaping the detector added back in to each event artificially. Including these escaping energies causes the events to collapse down to particular nuclear energy levels of the various germanium isotopes in our detectors (the lowest two at 13.28 keV and 68.75 keV being from Ge-73, for example)–branching off the ERs to run parallel to the NRs. This is what we expect from quasielastics: some NR-like behavior due to the original neutron interaction, but also ER-like behavior from photons or charges emitted from excited nuclei. These results apply to neutron capture and inelastic events as well, though those have been omitted here for visual clarity.

7.3.2.4 Mixed-Incident Events

The most complicated case is when there are multiple particle types entering the detector and depositing energy in quick succession (which need not be uncommon, since, again, a neutron could have knocked out several other particles along the way to the given detector). It's difficult to identify particular patterns here, but we note that these tend to be more ER-like than NR-like, as could be expected from the energy distributions in Fig. 7.6. There are a few that manage to look like NRs, though.

7.4 Takeaways

To summarize, Ba-133 is important for calibrating the energy responses of our detectors and Cf-252 is important both for providing WIMP-like events and–for this study–for providing a wide range of possible recoil patterns. We've seen now that our calibration source simulations model the real sources well: that their output spectra are accurate, their deposited energies are sensible, and that the resulting yield distributions are already starting to look like expectations and real data.

We see, though, that complicated recoil patterns–which can't be precisely identified in real data–will introduce complications to our measurements even before accounting for detector and reconstruction effects. That is, we lose some of the distinctions between ERs and NRs from nearly the very beginning due to events that appear mismeasured but aren't. Here in simulations, though, we can at least identify some of the physical causes for these events.

In the following chapters we will run new samples all the way through the full simulation chain and see both how well we are able to keep track of our recoil types through each stage and how well the results match real data.

8. DETECTORSIM RESULTS

In the previous chapter we traced simulated primary particles from their external source to where they deposit energies in the detectors. Now, given those particle types, energies, and hit locations, how do the detectors respond? That is: how well are the deposited energies measured, what might go wrong along the way, where in the detectors do those issues occur, and how can we account for them? In this chapter we want to study:

- What proportion of the charge and phonon energies released in each hit are actually collected by the sensors–and how this proportion depends on hit location and total energy,
- What processes negatively affect the amount of energy detected and how we might identify and correct for them,
- What regions of the detector correlate with the largest fraction of energy detected per event (i.e. reliable, or "fiducial" regions, where events are generally well-measured),
- How precisely a given energy can be measured in the detector output (i.e. the energy resolution),
- What calibrations are needed to convert the energies detected in fiducial regions into best-estimates of the true energies.
- What yields we should expect based on the charge and phonon energies we see.

We will be addressing these issues using five different simulated samples, described in the following section. The next chapter will follow these five samples (and the items listed above) the rest of the way through the simulation chain–through reconstruction.

8.1 Introductory Information

Some introductory information will be useful to speed up the main discussion in this chapter. Section 8.1.1 introduces the terms, methods, and samples we will be using through this and the following chapters. Section 8.1.2 will further explain our "collection efficiencies," which will be an integral part of our analysis, plus a few caveats for how the simulations were run.

8.1.1 Overview of Terms, Methods, and Samples

To facilitate our description of analysis methods and simulated samples, we begin by defining a few terms we'll be using in our studies of how well-measured events are and where they occur:

- **Bulk** refers to the volume of the detectors themselves. We will look at several "bulk samples" in which we simulate energy deposits directly in the detector volume instead of modeling particles from external sources entering the volume (as is done in "calibration samples").

- **QS1** and **QS2** are shorthand for "charge side 1" (the top) and "charge side 2" (bottom) of the detectors, respectively[1]. QS1 mostly collects electrons and QS2 mostly collects holes, but these are not absolute.

- **True** (or **expected**) quantities are what the detectors would measure if they were perfect; these values are part of the output of SourceSim (or are calculated from them). These include the energies actually deposited in the detectors (i.e. the "recoil energy") or the ionization yields of recoils, for example. These quantities are what the final, "reconstruction" stage will be trying to reconstruct.

- **Collected** energies are the energies that are measured by the sensors on the detector faces and will be converted into pulses by the readout circuitry; these values are output by the DMC and are not available in real data. They are reported for each channel individually, though to compare with true energies we will often combine some of them (since we can't determine exactly how a given hit will divide its energies between adjacent channels in real data). For the phonon system, the collected energy comes directly from the collected phonons themselves. The charge system, though, operates by counting individual charges; to convert this count to an energy, we simply multiply the number of collected electrons and

---

[1] Hence the similar reconstructed quantities mentioned in Table 4.1.

holes by E_{eh} (the energy spent to create the charge pair). Collected energies will be indicated by "col" subscripts in equations.

- **Measured** or **reconstructed** quantities refer to the output of CDMSBats (which we will see in the next chapter; we include this here for comparison with "true" and "collected"), generally after final calibration. These quantities were given in Table 4.1 or will be derived from those shown there.

- The **collection efficiency** here is the ratio of charges or energies collected at the detector faces (the collected energies) to the amount of each that is expected; it would range from 0 (at worst) to 1 (at best) and can only be measured in simulations. It can be found event-by-event, but we will also construct average efficiencies to both quantify more generally how accurately the detector responds to energy deposits and determine calibration/correction factors for the collected energies. Note that real data uses calibration factors in the same way; only the source of the factors differ between real and simulated data.

- We say that events are **well-measured** when we get a reliable detector response for them. These are most associated with the central, "fiducial" region of the detector, where the charges and phonons of hits tend to be collected in relatively consistent amounts–generally showing up in a Gaussian on the high side of the collection efficiency distributions; see the next section for details.

- **Corrected** or **calibrated** energies are our best estimates of the true energies in simulated data. These are constructed from the DMC's collected energies by rescaling them by the average collection efficiency of a set of well-measured events (this is similar to how real data is calibrated, though in that case the correction factor is estimated from, e.g. the visible 356 keV peak from Ba-133). Note that most of the energies labeled "collected" in the following chapters are actually "corrected," but we use the first term in reference to the physics in the DMC instead of details of our analysis.

- **SimFiducial**, described previously in chapter 4, is a region in the detector where events are reliably well-measured–that is, reliably enough that we can determine calibration factors from them. This is only identifiable in simulations, where we identify it based on the true spatial coordinates of well-measured events.
- **LT Fiducial**, also described in chapter 4, should be similar to SimFiducial, but it is identified event-by-event based on several measured criteria output by CDMSBats. We note it here to associate it with SimFiducial, but it will be more relevant in the next chapter, as it is based on reconstructed quantities.

With our terms defined, we now briefly summarize how we will go about studying the detector performance. Ideally the entirety of the energies deposited in the SourceSim stage be collected and read out by the detectors in the DMC and ultimately reconstructed accurately by CDMSBats. However, there are multiple ways for charge and phonon energies to be lost along the way; we want to quantify these losses and identify how and/or where they occur. So in this and the following chapters we will:

- See (firstly) how much energy is collected for each of QS1, QS2, and phonons as a whole.
- Quantify the fraction of each kind of energy that we actually collect–i.e. determine the energy collection efficiency.
- Determine our SimFiducial region–i.e. identify a fiducial volume of the detector based on the hit locations of events that are reliably well-measured.
- Use the average collection efficiency in the fiducial region as a correction/calibration factor to convert the collected energies into corrected energies.
- Determine our energy resolution based on the spread of the collection efficiency distributions of well-measured events as a function of energy.
- Check the yields as calculated from the collected charge and phonon energies–and see if or how badly mismeasurements affect identifications of ERs and NRs.

- Process through the rest of the simulation and processing chain and try to identify how well-measured events could be identified in real data–that is, using only reconstructed quantities. In short, we want to establish a realistic LT Fiducial cut that matches the idealistic SimFiducial cut[2]. We will do this part in the next two chapters.

We now introduce the samples we'll be describing with these terms and to which we'll be applying these methods; these are also summarized in table 8.1. First we will look at a set of "bulk" samples of only simple ERs and NRs. Our current DMC allows us to place recoils with specified energies directly in the detector volumes (the "bulk") without running SourceSim at all–that is, bypassing it to start with the output we'd like it to have produced. Such source-agnostic simulations allow us to precisely control recoil types and deposited energies. From these we can identify collection efficiencies and resolutions for specific recoil types, establish the fiducial volume where events are well-measured, and see what processes might cause these simplest events to be mismeasured. We will start with a bulk 356 keV ER sample–essentially, the most idealized form of our favorite Ba-133 calibration peak–and expand on it from there. The first expansion will be another ER sample that simply expands out to more energies: 1 to 400 keV instead of a single delta function. We will then move to a bulk NR sample with the same energy range to see how splitting up the deposited energies between phonons and charges affects the results. After these three bulk samples we will return to more realistic simulations with external sources in the apparatus shown in Fig. 2.2: the calibration sources Ba-133 and Cf-252 again. From these we will see how the basic results from the bulk samples are affected by more complicated distributions of hit types, locations, and energies–especially in events with multiple hits, where all of these can vary at once.

We note one obscure but not-insignificant setting for our samples. Recall from section 6.3.1 that TESSim and FETSim can create pulses either by solving differential equations or by simply scaling up pre-made pulse templates (like those used in reconstruction) based on collected energies. The differential equations method is more precise, but it was not working reliably enough at the time of these studies, so all of our samples used the template method instead. This likely will make

---

[2] Or, in long, find some configuration/subset of data-selection criteria used in the real LT Analysis at Soudan and compare to our simulation-specific SimFiducial criteria.

Dataset	Description	Goal
Bulk 356 keV ERs	Simulated, single-energy ERs created directly and uniformly in a single, isolated detector	Check collection efficiencies and resolutions, identify SimFiducial, study electric-field effects
Bulk 1-400 keV ERs	Simulated ERs with a range of energies created directly and uniformly in a single, isolated detector	Check how previous results scale with energy, check effects of noise addition
Bulk 1-400 keV NRs	Simulated NRs with a range of energies created directly and uniformly in a single, isolated detector	Check how results change with a different recoil type
Ba-133 source	Simulation of the full Soudan experimental setup with the Ba-133 calibration source in the apparatus' electronics pipe; analyzing one detector	Compare single and multi-hit ER events, see how non-uniform energies and hit locations change results
Cf-252 source	Simulation of the full Soudan experimental setup with the Cf-252 calibration source in the electronics pipe; analyzing one detector, limited to interactions before 1 second	Compare single and multi-hit NR events, see how non-uniform energies and hit locations change results, check that ERs are consistent between sources
Real Ba-133 data	Real data from Soudan with the Ba-133 calibration source in the electronics pipe	Check how well simulations match real data and investigate differences
Real Cf-252 data	Real data from Soudan with the Cf-252 calibration source in the electronics pipe	Check how well simulations match real data and investigate differences

Table 8.1: This table lists the datasets we'll analyze to study how well our simulation chain performed. The left column shows the name of the sample (which is simply the source of the events), the middle describes the setup, and the right notes the specific aspects of each we want to check. Note firstly that "Bulk" here means simulating hits directly in the detector volumes (the "bulk") instead of modeling external sources. Note secondly that the simulated Cf-252 sample is limited to hits occurring within 1s of the primary for reasons described in chapter 7. Finally, note that we've listed the real-data samples here for completeness, though we won't be using them until the next chapter.

our results slightly more idealized than real data: less noisy, more easily reconstructed, smaller resolutions etc. This is not expected to have qualitative effects, but a study of the exact quantitative differences will have to wait for future studies.

8.1.2 Expected Features of Efficiency Distributions

We make one last stop before seeing the samples themselves: as the collection efficiency will be a key part of our determination of how well the detectors respond to events, here we summarize the behaviors we'll be seeing in our collection efficiency distributions (much of this based on the particle behaviors described in chapters 2 and 3). Note that we will be checking the efficiencies (and other quantities) individually for each of QS1, QS2, and the sum of the phonons. We provide detail here both on how the efficiency is calculated for each of these and what the results will look like–and why.

To describe the calculation, we represent the collection efficiency with ϵ, with subscripts for charges or phonons. For the charge system, ϵ_{charge} can be found straightforwardly as the ratio of collected and expected charges:

$$\epsilon_{charge} = \frac{N_{eh,col}}{N_{eh}} \tag{8.1}$$

where the denominator is defined in equation 3.2 and the numerator is measured; note that the electrons on QS1 and holes on QS2 are measured separately, giving us two measurements of the same quantity. The phonon system, meanwhile, cannot rely on simply counting because individual phonons can have a range of energies and many of them are not created in the initial hit (e.g. NTL phonons). We begin with the ratio of collected and expected phonon energies:

$$\epsilon_{phonon} = \frac{E_{Ph,col}}{E_{Ph}}$$

and substitute equation 3.9 into the denominator to get the final result:

$$\epsilon_{phonon} = \frac{E_{Ph,col}}{E_{recoil} + E_Q * \frac{eV_{bias}}{E_{eh}}}. \tag{8.2}$$

Recall for all these that E_{eh} is the electron-hole pair-creation energy (2.96 eV), V_{bias} is the voltage applied across the detector (4V for normal iZIPs), and e is the electron charge (conveniently with a magnitude of 1 in our units). To be clear, further, perfect collection efficiency would equal 1 while 0 would mean all energy was lost. In simulations we can identify efficiencies per-event, but–since well-measured events turn out to be relatively consistent–we'll be picking out single, average efficiencies for well-measured events that we associate with a given combination of recoil type and detector across all samples in our analysis. These averages will only be calculated using a subset of all events, however, due to the shape of the collection efficiencies.

The shape of the collection efficiency distributions for each of QS1, QS2, and phonons will all be essentially the same: a high, nearly-Gaussian peak just below 1 representing well-measured events, and a long tail towards 0 representing poorly-measured events; look ahead to Fig. 8.11 for an example of this shape in two of our samples. The Gaussian peaks–though they are below 1–represent our best-measured events, and so we will use the mean of just those peaks as calibration (or "correction" or "rescaling") factors to convert our collected energies into estimates of the true energies. The poorly-measured tails, meanwhile, will be cut–mostly–by SimFiducial (spatial criteria) in this chapter and LT Fiducial (measurement/reconstruction criteria) in the next.

The questions remain of why the "well-measured" peaks are below 1 and why the poorly-measured tails exist; refer back to table 3.1 for the following discussion. The bulk of the mismeasurements are sidewall and face events; because of this, SimFiducial–which will cut events based on extreme R and Z values (or, more explicitly, remove the detector regions with nonuniform electric fields; see Fig. 3.7)–will remove most of the collection efficiency tails. However, the tails will not be gone completely and the peaks will still be below 1:

- For charges on QS1 and QS2, these remaining issues will be due almost entirely to off-electrode effects. Even the best-measured events will have some charges that don't land exactly on the electrodes–and so are mismeasured–and only the worst-measured events far from the main peak will be removed by other cuts.

- Phonon efficiencies are also worsened by off-electrode effects (due to lost NTL phonons

> from the charges), and, further, ERs and NRs will be affected to different degrees. To make matters worse, both the lower efficiencies and the ER/NR difference are exacerbated here by a simulation artifact that was not discovered until late in the analysis. This is described further in Appendix C, but in short, this artifact caused the simulation at the time of these studies to stop tracking phonons before they had reflected enough times to deposit all their energy.

We note that we're going to see another, separate simulation artifact later when we look at the energies of phonons; this one will cause the resolutions of single-hit and multi-hit events to differ in a way they shouldn't. Appendix C again has more detail. Though these artifacts affect some of the quantitative values in this thesis, they do not significantly affect our conclusions; they also are not difficult to remove and have been fixed (or otherwise updated) for future work already.

We will highlight some of these features again as we proceed through our samples.

8.2 DMC Results for Bulk Samples

We begin by looking at the bulk samples–the top three entries of Table 8.1–to study the simplest interactions that can occur in the detectors. These bulk samples each are composed entirely of single-hit events (i.e each hits/event are independent of one another) of specified recoil type that are distributed uniformly throughout the detector volume. In this section we check the energies (and particles) that propagate from the original deposition points to the detector faces, where they are read out (for context, recall that this is only the first part of DetectorSim; the second part, DAQSim, will be discussed at the end of this chapter). We will move from the simplest case to the most complex–starting with a single energy and recoil type and expanding on each from there with each sample.

8.2.1 Idealized ER Samples: 356 keV Peak

Our most idealized simulation is a set of pure, single-hit ERs at exactly 356 keV, distributed uniformly in the volume of a single detector, as shown in Fig. 8.1. With minimal distractions in this sample, we will establish the energy collection efficiencies of simulated events (and use them to

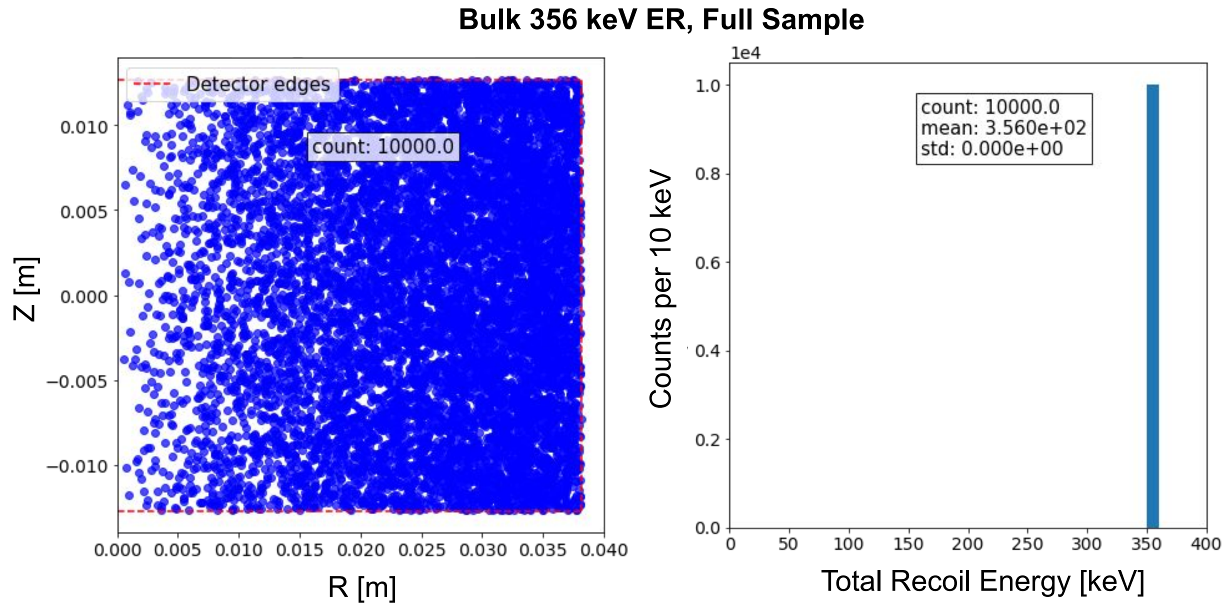

Figure 8.1: This figure shows the hit locations and deposited energies of the Bulk 356 keV ER sample. Note that all of these hits are independent from one another (that is, these are all single-hit "events", whereas a realistic source could have multiple hits per event) and we're considering only a single iZIP5 detector (not the full 15 from Soudan). Left: hit locations in the detector in Z vs. R; in our three idealized bulk samples, we specify to the DMC directly that the hits be uniformly-distributed (this would be more visually apparent in Z vs. R^2). Right: our simplest sample only has one energy for every one of its hits: 356 keV exactly–as if from the main peak in the Ba-133 spectrum.

calibrate the results), identify the detector volume where well-measured events are most common (SimFiducial), identify where energy might be lost, and get a first look at energy resolutions in simulations.

Fig 8.2 shows the charge energies collected on each detector face as well as the total phonon energy (that is, these are the energies that made it from the original hit locations to the sensors at the detector faces). We note two main aspects:

- The main peaks, representing events with maximal energy collection, are slightly below 356 keV (or 837 keV in the case of phonons, per equation 3.10) and relatively narrow compared to the full distribution. So, as expected, there is some non-unity collection efficiency we will have to calibrate for, due to the various energy losses described in chapters 2 and 3–which we will revisit later in this section.

- There are tails from the main peaks down to zero energy, representing events with poor energy collection. These are from events in the "non-fiducial" region of the detector–i.e. on the edges, where electric field nonuniformities and other effects often impede energy collection.

Our method of calibrating this sample is straightforward (and mostly mirrors what is done in real data). Since we know the exact true energy (356 keV), we can simply apply whatever multiplicative factor shifts the energies such that the main peak of best-measured events is centered there[3]–this multiplicative factor being simply the observed collection efficiency. While we expect this same calibration factor will work in the *DMC* stage for all future simulated ERs in iZIP5s (we leave open the possibility it will change for NRs in other detectors), note that we will not be using it in later processing stages, which do their own calibrations (they have to, since real data doesn't have a DMC stage to calibrate, as we do here).

In addition to setting such calibrations based on the peaks of the collected energy distributions, we also want to separate out the poorly-measured events in the long tails. In the DMC, we can do this by identifying a specific volume of the detector where events are reliably well-measured–that is, by establishing our SimFiducial region based on the locations of events with good collection efficiencies.

8.2.1.1 Identifying Detector Regions Where Single-Hit Events are Well-Measured: SimFiducial

As described previously, the peaks in Fig. 8.2, in addition to giving us efficiency and resolution estimates, represent well-measured events. Here we try to select a sub-sample of such events from the data by identifying a particular volume in the detector that has minimal mismeasurements–that is, our "SimFiducial" region; this should be similar to the "fiducial volume" marked in Fig. 3.7, as we expect to exclude the detector regions where the electric fields are non-uniform. Note, though, that because electrons, holes, and phonons each move differently, they likely won't all be collected

---

[3] Assuming a simple linear calibration suffices for all charges and phonons. In chapter 10 we will see this may not hold for real data–but until then we find it works well for simulated data.

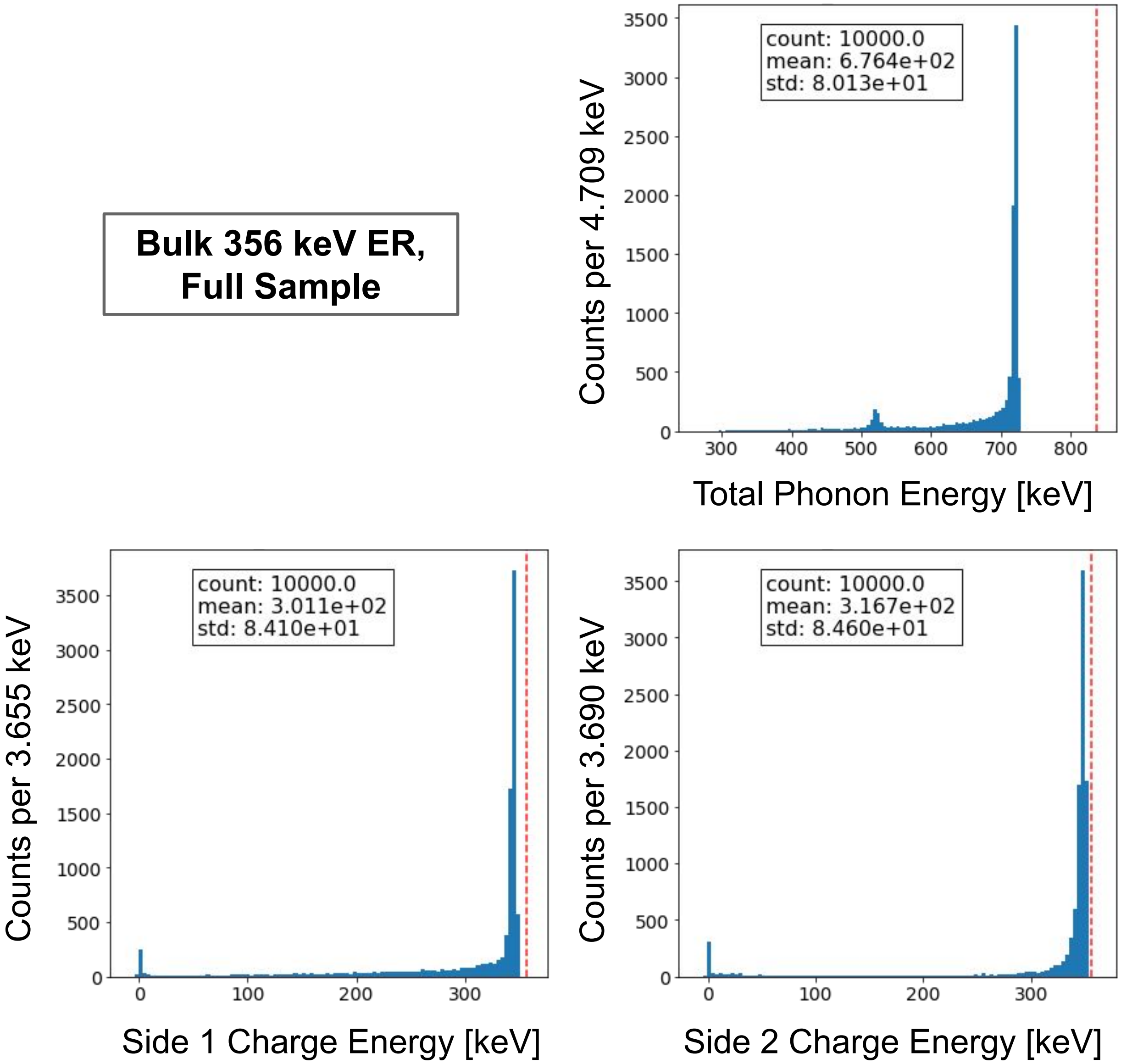

Figure 8.2: This figure shows the collected phonon and charge energies (sides 1 and 2 separately for charge) for the 356 keV ER sample shown in Fig 8.1. In each we see peaks of well-measured events and tails of poorly-measured events. From the peaks of these distributions we can estimate the detector's collection efficiencies and resolutions for charges and phonons. The top plot shows collected phonon energies, which, in this case, includes NTL phonons and recombination phonons (ERs do not produce prompt phonons). If all the energy is collected, we should observe 837 keV, which is marked with a red dashed line on the plot. Because the sensors do not collect all the energy from all the phonons, however, the main peak is seen at a lower energy closer to 700 keV; further below that is a long tail of more clearly-mismeasured events. The small peak near the middle is from edge events where one side had near-full collection efficiency while the other had near-zero. The bottom-left and bottom-right plots show collected charge energies for sides 1 and 2, respectively. Full energy collection here would mean 356 keV (marked in red), but again we see a main peak somewhere below that and a long mismeasurement tail.

with the same efficiencies from a given location–meaning a given event might be "well-measured" for one particle but not the others. The "fiducial region," then, will likely be different depending on which of QS1, QS2, and phonon measurements are used to identify it; we will check each and define SimFiducial based on whichever option is the most restrictive to give us confidence that all three are well-measured.

Fig. 8.3 shows how we construct SimFiducial using only the measured charge from QS1, which turns out to be the most restrictive option (unsurprising since electrons have the most lateral motion in the lattice). We first plot the collection efficiencies to see where in that distribution the well-measured events occur. Next we more quantitatively define "well-measured" events by setting a minimum collection efficiency cutoff at 5σ below the main energy peak. Then we plot the R_{hit} and Z_{hit} coordinates of the hits failing that cutoff and slice out a trapezoidal region that excludes most, if not all of them.

We note a few aspects of the resulting SimFiducial region.

- First, as noted, it is trapezoidal:
  - The slope of the radial cutoff is expected primarily due to how electrons and holes propagate through a germanium detector–this slope determined by the motion of electrons specifically, in this case. Recall from chapter 3 (see also Appendix A) that electrons follow "valleys" in the crystal (while holes do not). The outer slope of the SimFiducial trapezoid is essentially the angle of the electron valleys–because past that radius, freed electrons become much more likely to end up being caught on the detector sidewall instead of being collected at the top face.
  - The top and bottom cutoffs are inset from the detector faces to exclude face events–and the scalloped electric fields that handle them–as described in chapters 3 and 4.
- Second, the marked SimFiducial does not exclude all "poorly-measured" events. There are a handful that leak inside the top edge around radii of 20 mm. These are some of the worst-measured "off-electrode" events, as described in chapter 3 (refer to table 3.1) and we will

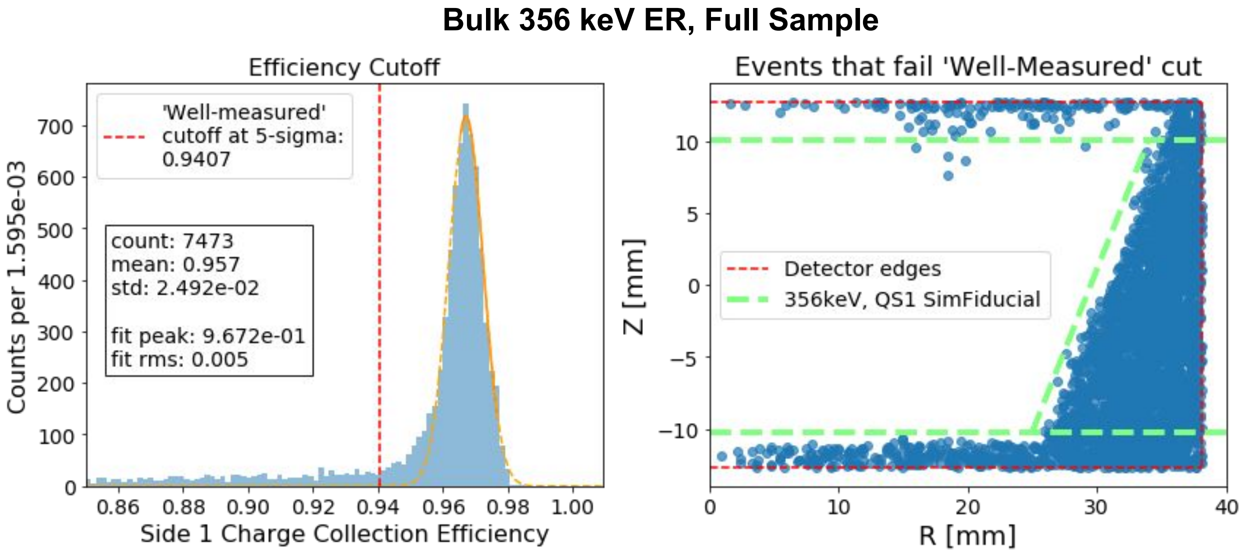

Figure 8.3: These plots show, for charge side 1 in the Bulk 356 keV ER sample, the cutoff in the collection efficiency distribution identifying "poorly-measured" events and the hit locations of such events, which are used to establish SimFiducial. Left: we start by fitting a Gaussian to the main peak of the efficiency distribution of all events (which is simply the data in Fig 8.2 divided by the expected energy of 356 keV) and setting a cutoff, somewhat arbitrarily, at 5σ below its mean. We consider all the events failing that 5σ cutoff to be "poorly-measured." Right: Those poorly-measured events are plotted in RZ, where we hope to see them outline a clean, "fiducial" region. Based on these events, we set our SimFiducial as the volume inside the green dashed lines. There are a few events leaking inside this region at high Z, which we will address shortly. Note as well that SimFiducial is defined using only single-hit events; multi-hit events, discussed later, will complicate both the use of SimFiducial and identifying well-measured events more generally.

discuss them more in the next section.

In Fig 8.4 we repeat the SimFiducial-establishing process for QS2 and phonons. The phonons show the same R/Z boundaries that electrons did since missing electrons means missing NTL phonons; the hole/QS2 shape is mostly just due to electric field non-uniformities. But there are also notably more off-electrode events around R=20mm here–for QS2 in particular. However, taking these as exceptions (to be discussed in the next section) and noting that the SimFiducial established using QS1 still excludes the high-radius mismeasurements (and most of the high- and low- Z mismeasurements), we will continue on using QS1's SimFiducial as *the* SimFiducial for all samples (we have constructed SimFiducial for each sample and found that they all agree with the one established here; as there is nothing new to see, we won't show the SimFiducial process for the following samples).

8.2.1.2 Studying Causes of Poor Energy Measurements

The previous few figures showed that not only do our collection efficiencies have long tails towards low energies, they also have peaks centered below 100%–the phonon peak notably lower than those for charges. As was discussed in section 8.1.2, we have two culprits in mind for these lower-than-expected efficiencies:

- Off-electrode effects (see Table 3.1) are pulling down the efficiency of all events; the clearly-mismeasured events at middle R values are simply the worst-affected. These account for the charge peaks being below 1.
- A simulation artifact caused the phonon efficiencies to be significantly lower than those for charges[4]. At the time of these studies, the simulation was inadvertently set to stop tracking phonons before they could reasonably have deposited all their energy (specifically by limiting the number of times they could be reflected for sake of simulation speed). This was only noticed after this analysis was done and has been fixed for future simulations, so we won't discuss this further here. See appendix C for more detail.

For the remainder of this discussion, we focus on how off-electrode effects impact both charge and phonon energy measurements.

To start, we can use the hit locations and total collected energies to verify the relationship between events with obvious off-electrode mismeasurements and electrode bends described in Chapter 3. Fig. 8.5 shows the locations of all hits in the detector, as viewed from the bottom, with the poorly-measured events that nevertheless passed the SimFiducial cut shown in red (and all other events in green). The poorly-measured events inside SimFiducial very clearly fall along a triangle

---

[4] We actually expect our simulations to have nearly 100% phonon efficiency–which is unphysical–because the main causes of phonon energy loss are not currently simulated. Even the observed efficiency in the high 80%'s is unphysical. What is meant by the "phonon collection efficiency" is somewhat ambiguous, however; see chapter 3, appendix C, and Ref. [17] for further detail.

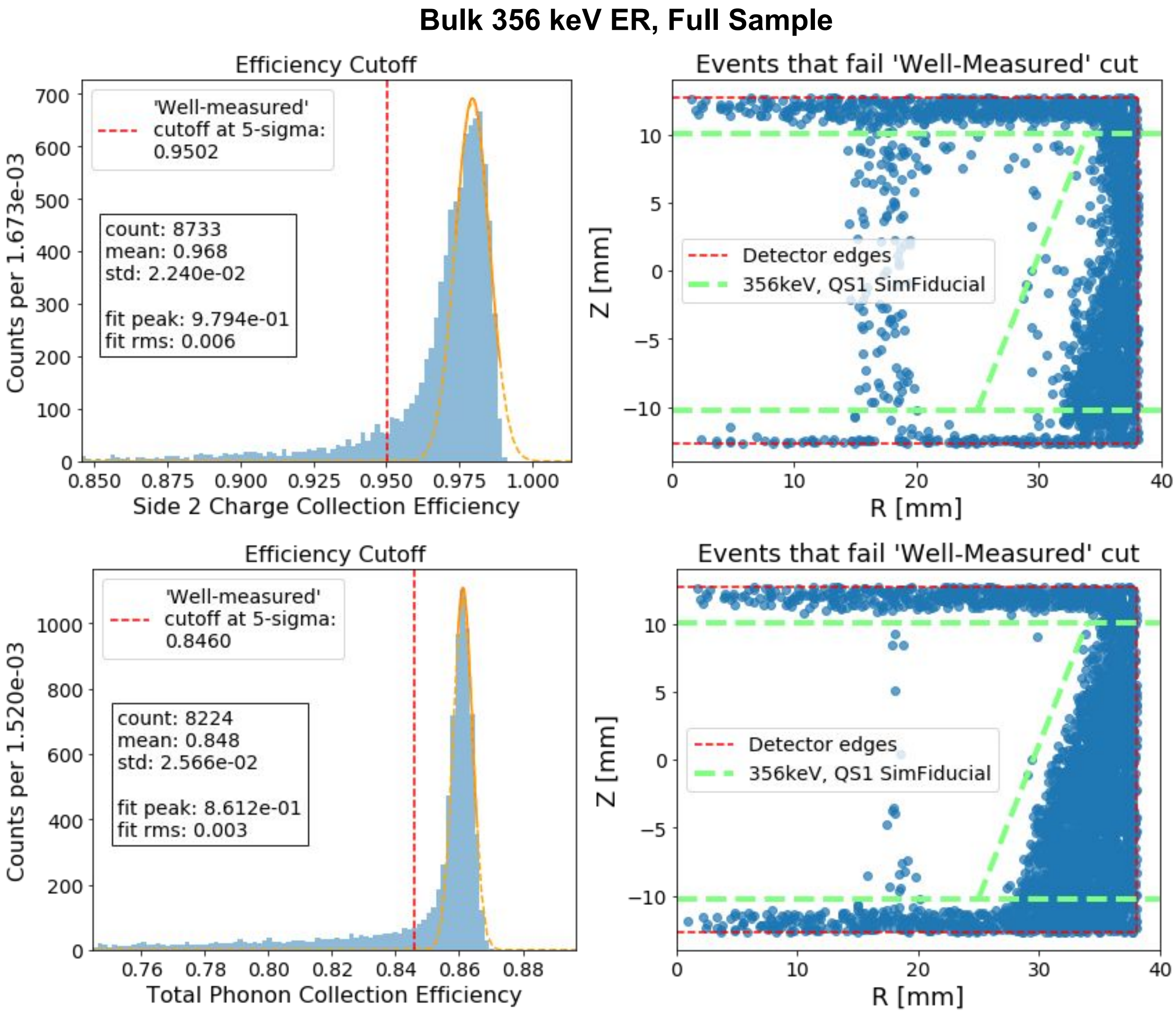

Figure 8.4: This figure shows the same information as in Fig 8.3, but now for QS2 and phonons–though with the QS1 SimFiducial still shown–to compare the fiducial regions for each. We see the QS1 SimFiducial still successfully excludes face and sidewall events, but there are many poorly-measured events towards the middle that we will explain in more detail in section 8.2.1.2. It is particularly clear for QS2 (and somewhat visible for phonons) that poorly-measured events favor leaking into SimFiducial between radii of about 15 mm to 20 mm. In any case, because the denser populations of edge events do not cross inside the boundaries we set for QS1, we will continue using those bounds as our SimFiducial.

and an additional clump near at high Y in the figure. These shapes in fact correspond to the electrode bends on the iZIP5–both the bends as they double-back on themselves and also where they connect to the output electronics.

These electrode bends correlate with energy mismeasurements for the reasons described in chapter 3–though we summarize again here. The electric fields around the electrode bends are slightly weaker than those elsewhere, meaning there is a higher likelihood that charges may speed through the fields and land off-electrode. In the real detector they may be either absorbed (and emit recombination phonons) or trapped there; in simulations the charges are simply "killed" there, meaning they are absorbed (as in the real detector) and no longer tracked. Whether killed or trapped off-electrode, the charges do not traverse the full voltage range they should, which causes us to lose both charge and phonon energy:

- Charge energy is lost because, per the Shockley-Ramo theorem, charges that don't reach Ramo fields equal to 1 don't induce a full signal (see section 3.3.1).
- Phonon energy is lost[5]–even though phonons themselves don't interact with the electrodes or fields–because charges that don't go through the full voltage drop also don't emit all the NTL phonons they are expected to.

It is important to note, however, that it is only *more likely* for hits near electrode bends to have charges landing off-electrode–that is, such events are simply the most egregious sign of off-electrode effects. *All* events, in fact, suffer from some proportion of charges landing off-electrode. This is demonstrated in figure 8.6, which shows a variation of the Bulk 356 keV ER sample in which we essentially replaced the lines of electrodes with solid, flat surfaces over the detector faces; this makes it impossible for charges that reach the detector faces to miss the electrodes–meaning there are no off-electrode effects. This corresponds with a perfectly uniform electric field inside the detector as well, so we'll refer to this sample as the "uniform-field" sample. As seen in the figure, this field/electrode change collapses the charge collection efficiencies[6] to 100%–though phonon

---

[5] That is, some of it is never created, in this case.

[6] Excepting face or edge events (where charges don't reach the faces they should) and Fano fluctuations (which

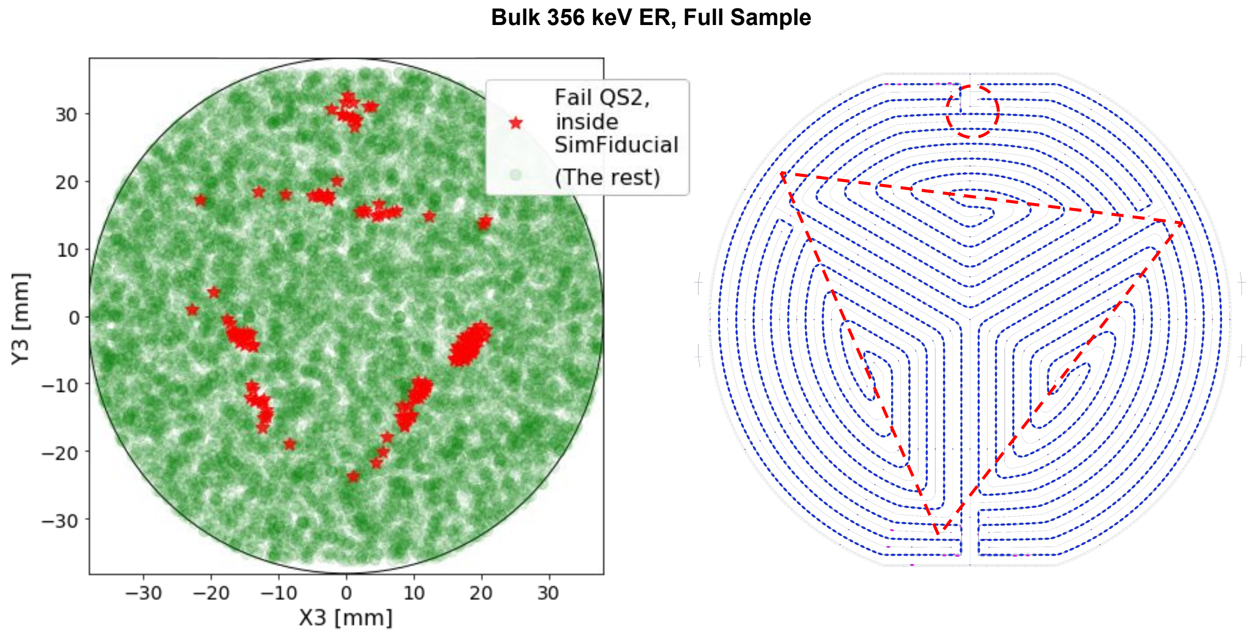

Figure 8.5: This figure shows the hit locations of events that were in SimFiducial but were poorly-measured on QS2–and their correlation to the iZIP5 electrode layout shown in Fig 3.9 (though note that side 2 is flipped compared to the top side). Left: The poorly-measured events in the top-right plot of Fig 8.4, plotted in X vs. Y here, in red, show a clear triangular pattern, plus a clump near the top. Right: The side-2 electrode (and interleaved QET) layout on the iZIP5, with a superimposed red triangle and oval highlighting locations where the electrodes bend the most.

efficiencies are still low (though about 1.2% higher) due to the previously-mentioned simulation artifact (we can estimate this artifact's inefficiency contribution here, but the number doesn't have physical significance).

Returning to the normal sample with the iZIP5 electrode layout: because the speeds of the electrons are somewhat moderated by the valleys they are restricted to, the off-electrode effects show up more strongly for holes and QS2 than for electrons and QS1. Fig. 8.7 shows how these differences manifest in the collection efficiencies as a function of Z_{hit}. While the electron collection efficiency is fairly stable all throughout (only slightly benefiting from hits closer to QS1), the hole collection efficiency more clearly is improved when hits occur near QS2 and hurt when near QS1. This is likely due to the holes from events near QS1 having more space to accelerate and so punch through the electric field of QS2 more easily (while electrons starting near QS2, again, are

---

always cause small variations in the "expected" energy).

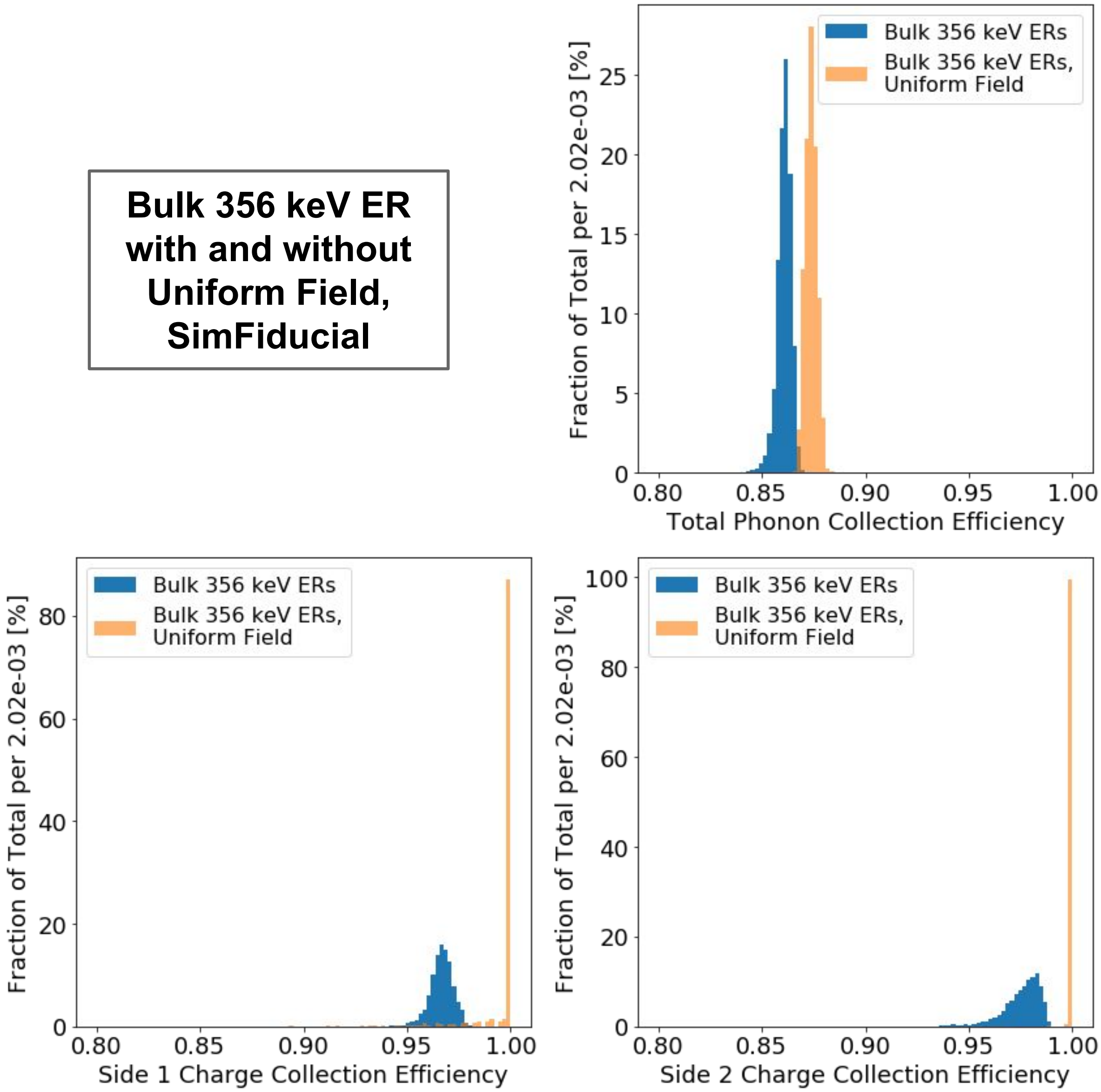

Figure 8.6: This figure shows the collection efficiencies in the Bulk 356 keV ER sample when the electrode lines are replaced by a continuous conductive sheet on each of the top and bottom of the detector–or, as implemented in the simulation, the electric fields are made perfectly uniform–and those for the normal sample for comparison. This shows that when charges cannot avoid being collected by the electrodes (if they reach the detector faces at all), the collection efficiencies of well-measured events reach 100% (small variations due to Fano fluctuations aside). The few events below that in the uniform-field sample happen to be close enough to the radial SimFiducial edge (which changes slightly from the previous sample due to the different electrodes and fields) in this sample to be edge events; QS1 is affected by the latter to a greater degree due to the valleys shifting electrons laterally towards the sidewalls. Phonons efficiencies are raised by about 1.2% with the change, but are still below 90% due to separate sources of inefficiency not addressed in this figure; see Appendix C.

slowed by interactions with the valleys).

We will not try to remove the obvious off-electrode events by carving out a slice of our identified SimFiducial, which otherwise works very well; after all, we cannot identify or remove such events in real data, and even in simulation, off-electrode effects impact more than just these most obvious events. These effects will simply be a slight drain on our energy distributions going forwards–meaning slightly lower peaks (and thus higher calibration constants), slightly wider peaks (i.e. slightly higher resolutions) and slightly longer tails towards 0 energy–most significantly for QS2 and anything calculated from it.

8.2.1.3 Results and Primary Contributions to Energy Resolution in Well-Measured Events

Fig 8.8 shows the collection efficiencies of events in our SimFiducial region; essentially by construction, these are mostly Gaussians with only slight tails towards lower efficiencies. We see that phonons have peak collection efficiencies near 86% while both charge sides are in the high 90%s (the tails and the peaks being below 100% are due to the off-electrode effects and simulation artifacts, as described previously). We use these peak collection efficiencies as calibration corrections; going forward, all collected energies that are shown are recalibrated by these values–though note that the tail of QS2 in particular makes calibration more difficult[7]. Here we check how accurately and precisely those corrected values match the expected values (i.e. the overall correctness and resolution).

Fig. 8.9 shows the differences between the true deposited energies and the (calibrated) collected energies in SimFiducial (it looks similar to Fig. 8.8 since there is only a single true energy involved). These distributions are centered at zero, but this is by design, since we set our calibrations to do this. More important will be if these same calibrations also center other samples at the correct energies. While we're here, though, we note initial resolution measurements of 2.9, 1.8, and 2.3 keV for the phonon, QS1, and QS2 measurements, respectively. We'll watch to see how these change across samples (with different energies or recoil types) or simulation stages (likely

---

[7] Unfortunately, choosing a tighter fit that puts the calibration factor right at the peak causes later calculated quantities–such as the yield–to be worse-calibrated. This is likely due to the Z-correlation shown in figure 8.7: where one charge side benefits, the other suffers.

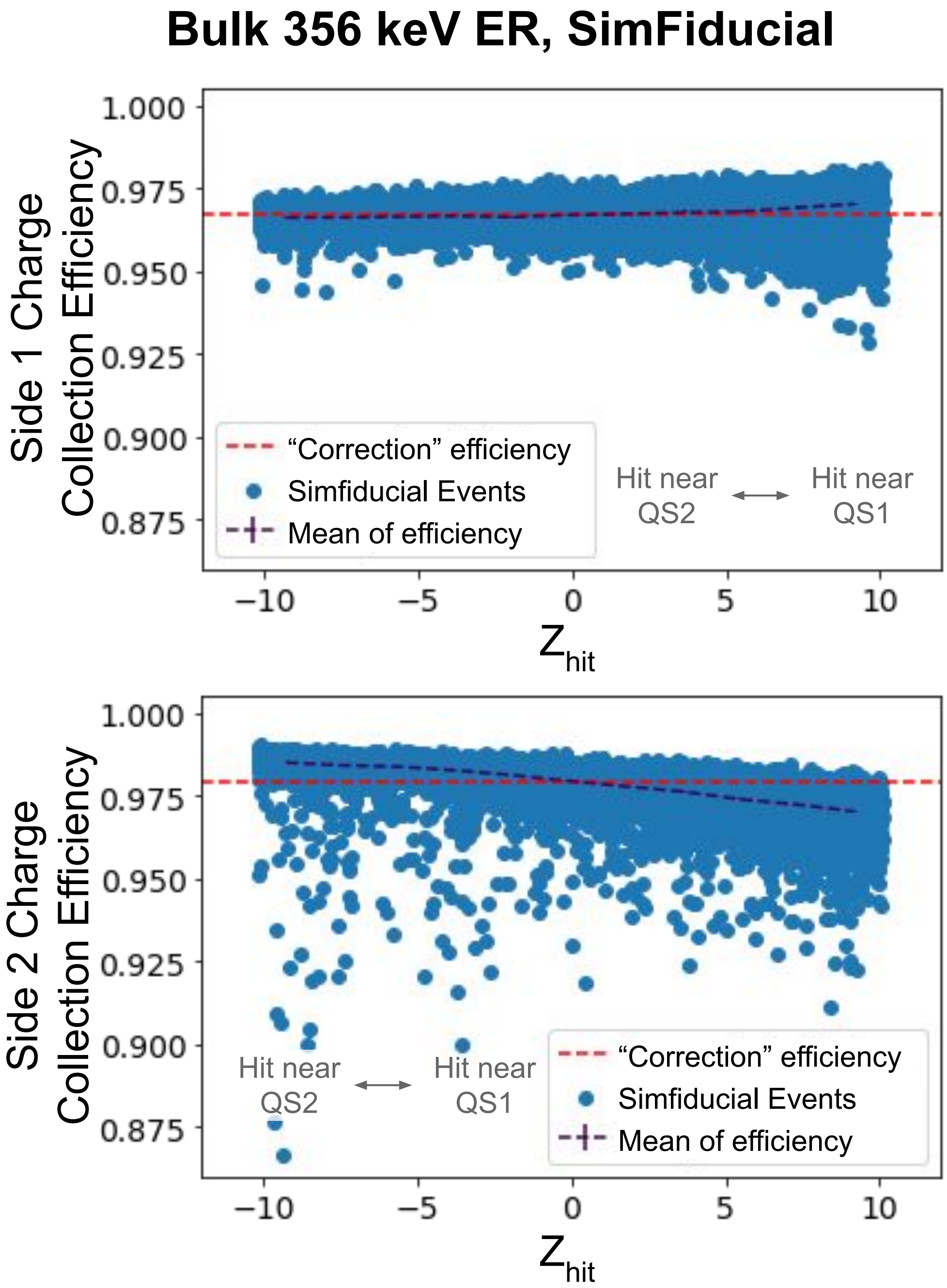

Figure 8.7: This figure shows, for the Bulk 356 keV ER sample, the collection efficiencies for QS1 and QS2 SimFiducial events as functions of the Z-coordinate of their original hits. The red-dashed lines mark the average, peak collection efficiencies for each. The upper plot shows the results for QS1 (which is mostly electrons), which show very little dependence on the Z location of the hit. The bottom plot shows QS2 (mostly holes) efficiencies, which more clearly are higher when the hits occur close to QS2 and lower when further away. Phonons (not shown) do not show any noticeable Z-dependence; since phonons are not measured by individual side, any missing NTLs on one are mitigated by the other.

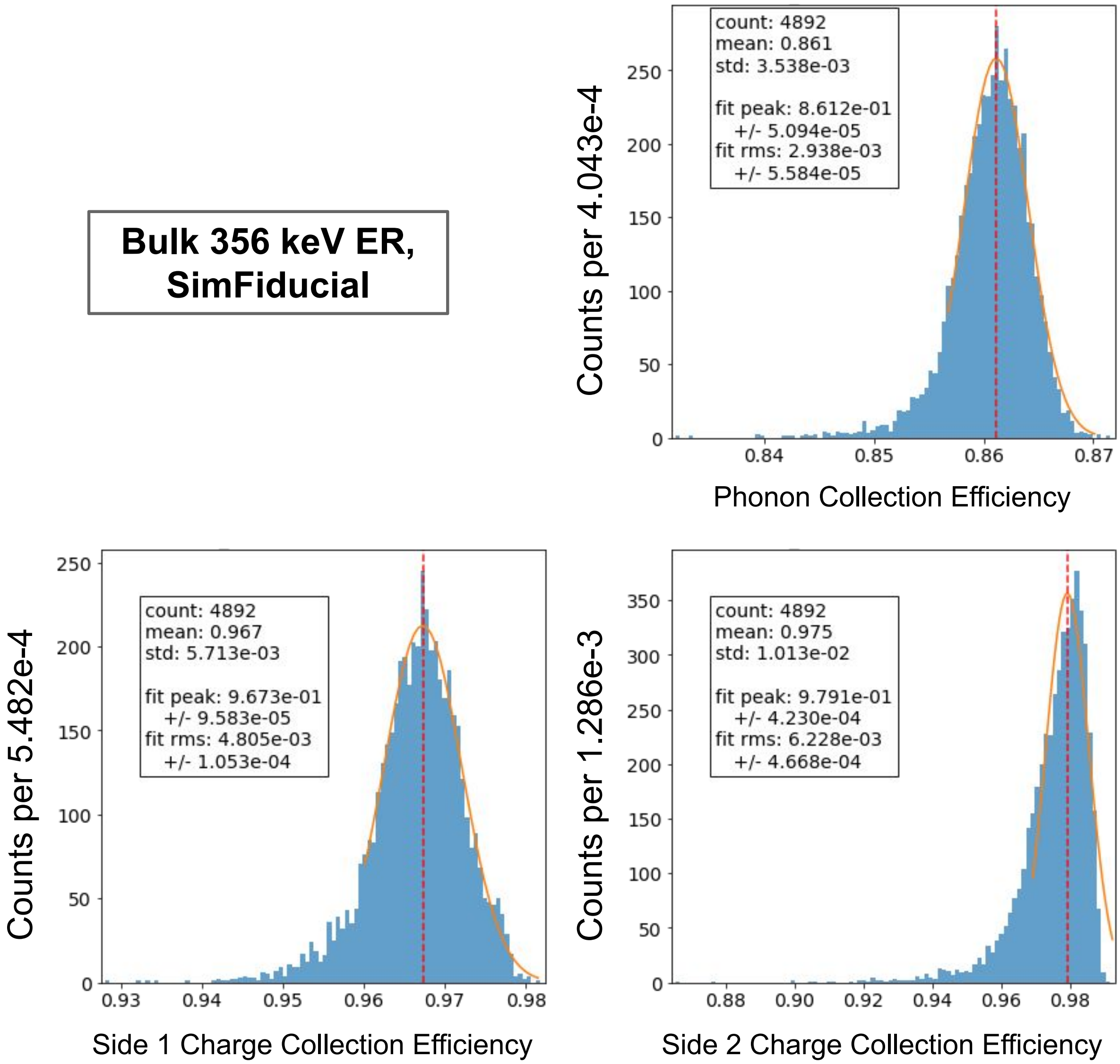

Figure 8.8: This figure shows the collection efficiencies for phonons and charges for events that hit within our identified SimFiducial region. In each we see that applying the SimFiducial cut reduces our data to mostly well-measured events. Top: Phonon efficiencies, showing peak efficiency value centered at 86.12%. This is likely high compared to real data, however; see Appendix C for details. Bottom-left: collection efficiency for (primarily) electrons hitting side 1 of the detector–peaking at 96.73%. Bottom-right: collection efficiency for (primarily) holes hitting side 2 of the detector–peaking at 97.91%. Comparing the bottom two plots, note that the QS2 results are centered slightly higher but have a more prominent tail towards lower efficiencies. This is in-line with the illustration in Fig. 3.10: holes do not spread out as much, so they are more likely to avoid the areas with the worst off-electrode effects–but when they don't, the effects are more dramatic.

increasing by the end)–even if the calibrations don't.

We will return to the Bulk 356 keV ER sample in the next chapter to see how it fares in the rest of the simulation chain; but for now, to summarize what it shows us about ERs in the DMC:

- The collected efficiency distributions for phonons, QS1, and QS2 all have main peaks below 100% (at 86.1%, 96.7% and 97.9%, respectively) and long tails towards 0.
- The poorly-measured events in the tail of those distributions are generally understood and can be excluded by identifying a SimFiducial volume.
- Off-electrode effects impact all events–decreasing efficiencies and increasing efficiency/energy resolutions.
- Our energy calibrations using the collection efficiencies work well for SimFiducial events and we see initial phonon, QS1, and QS2 energy resolutions of 2.9, 1.8, and 2.3 keV, respectively.

8.2.2 Idealized ER Sample: 1-400 keV Energy Range

Next we move to a slightly more complicated sample–where all events are still single-hit ERs, but now we give them a range of energies; with these we can study how or if the results of the previous sample change with recoil energy. We've chosen a minimum of 1 keV to avoid some volatility in our results[8] and a maximum of 400 keV as that is about the maximum energy for Ba-133 photons. These energies (and the uniform hit distribution of the sample) are shown in Fig 8.10.

As stated previously, we expect the collection efficiencies we identified and used for calibration in the previous sample should apply to other samples as well–other ERs in iZIP5s at least. Fig. 8.11 compares the collection efficiencies of the previous, single-energy sample to this energy-range sample and we do see good agreement, so we will continue on using the same energy calibrations in this chapter.

---

[8] For example, if noise or Fano fluctuations contribute a sizeable proportion of the energy (that is, for low-energy events), we might see efficiencies significantly greater than 1, which is not representative of the rest of the sample.

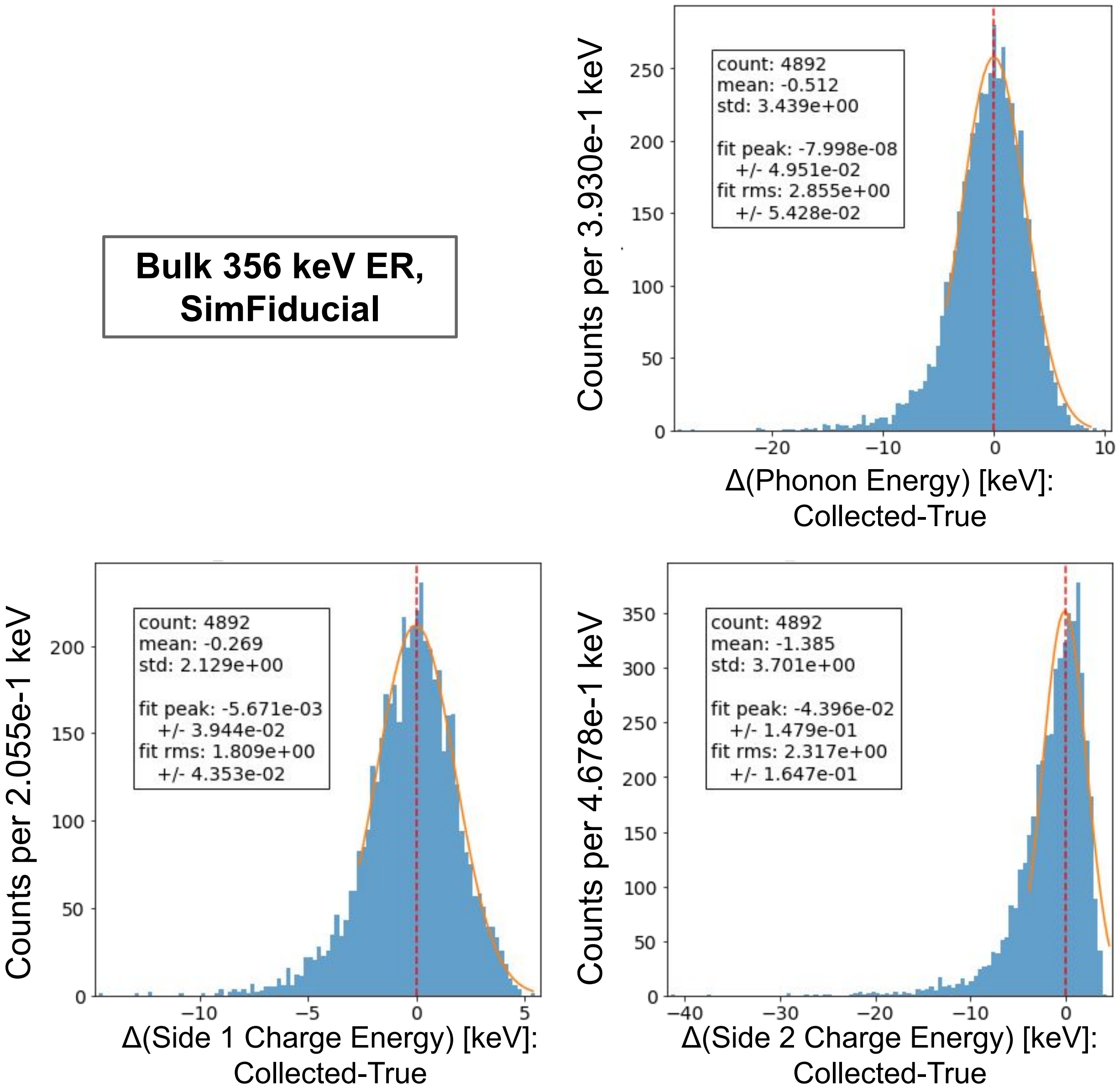

Figure 8.9: This figure shows the differences between collected (from CrystalSim) and "true" (from SourceSim) energies in our 356 keV ER sample. Note that "true" just refers to the deposited energies for charges, but includes both deposited and NTL energies for phonons. This distribution is helpful both because it demonstrates that we've understood the collected energies and applied efficiency calibrations correctly (i.e. these results are centered near zero) and because we can use the RMS of the distribution as an estimate of the measurement resolution. The collected energies are calibrated using the previously-shown collection efficiencies. Since there is only a single "true" energy, these are shaped essentially the same as the efficiency distributions in Fig 8.8.

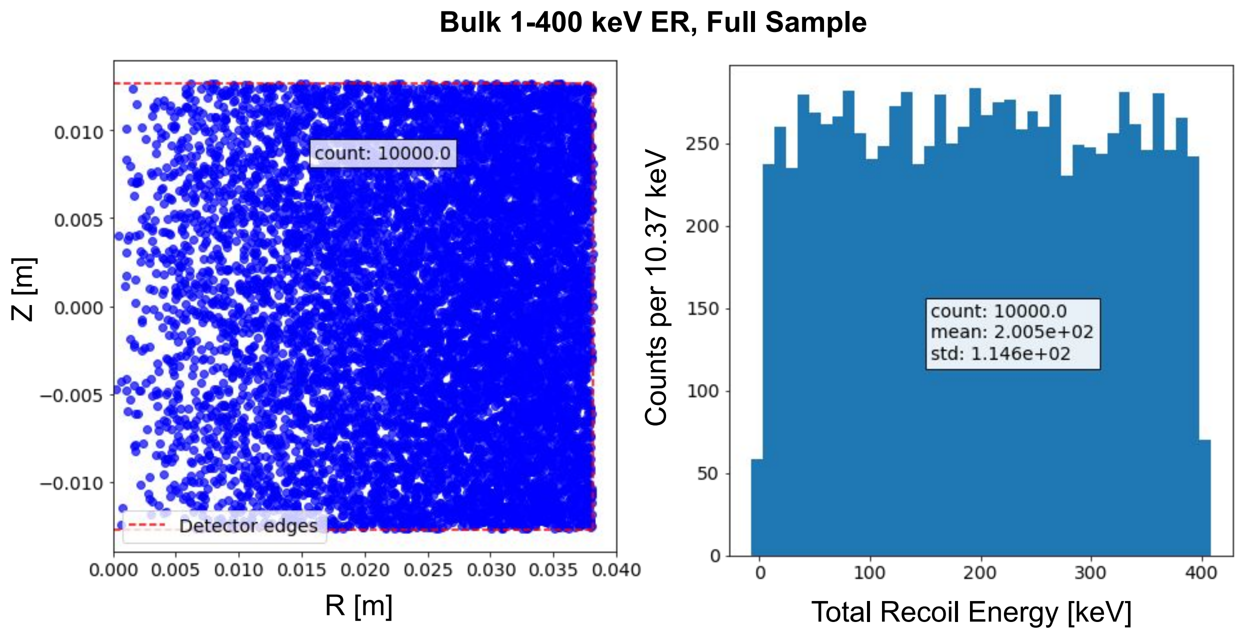

Figure 8.10: This figure shows the hit locations and deposited energies of a sample similar to the previous one (compare Fig. 8.1): ERs, but now with a range of deposited energy–from 1-400 keV–so we can check for any energy dependencies in our results.

Now that we have a sample with an energy range, we can check our results as a function of energy, as shown in Fig. 8.12. As expected, the primary change is an increasing resolution as the energy increases. Fig. 8.13, though, shows that the fractional resolution is mostly constant.

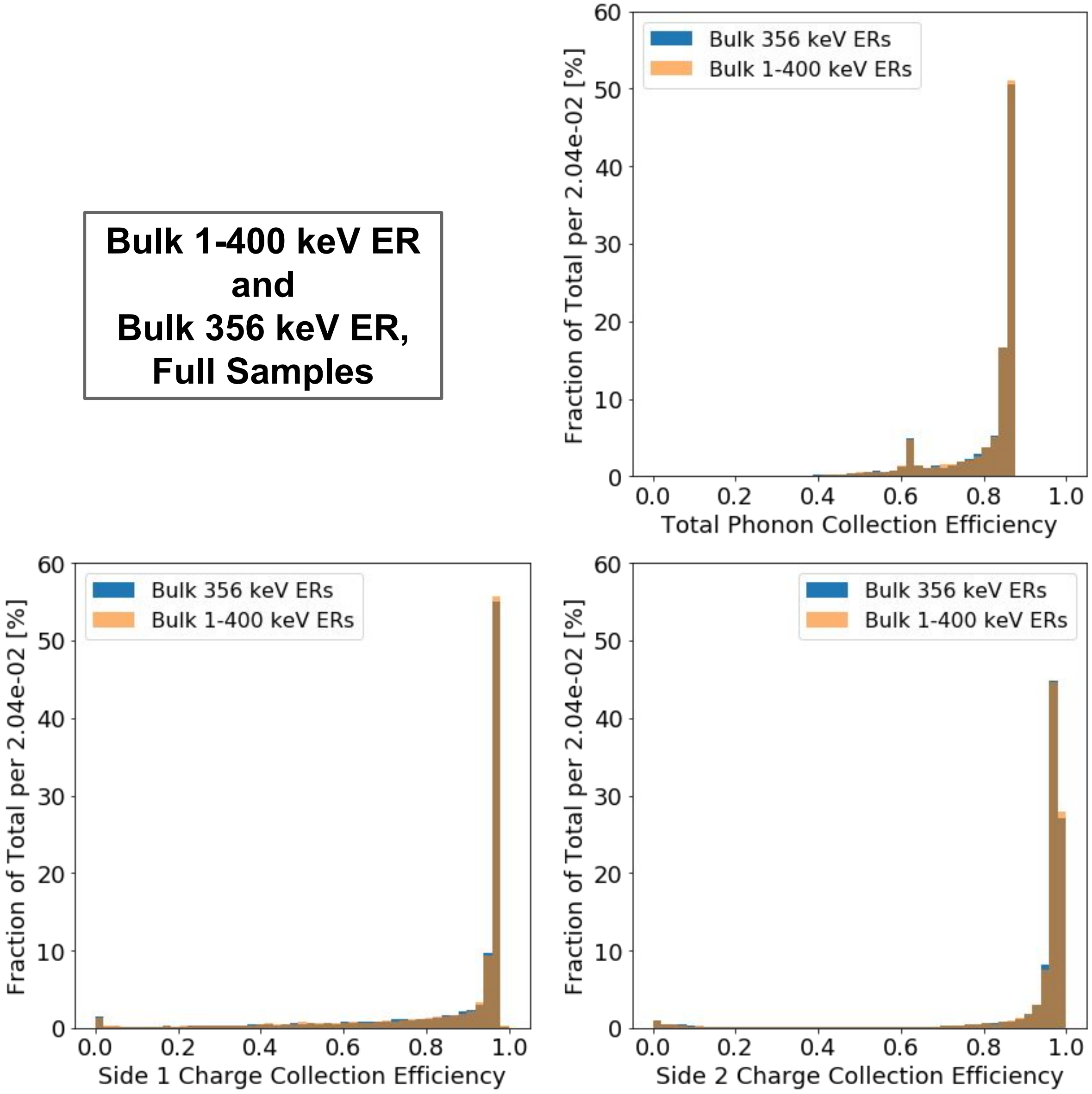

Figure 8.11: This figure shows the collection efficiencies for both our ER samples, which are overlaid for comparison. We do not see significant differences between the samples, meaning changing from a single recoil energy to a range of recoil energies does not significantly affect the collection efficiencies–and that we can use the same calibration/rescaling constants for both samples.

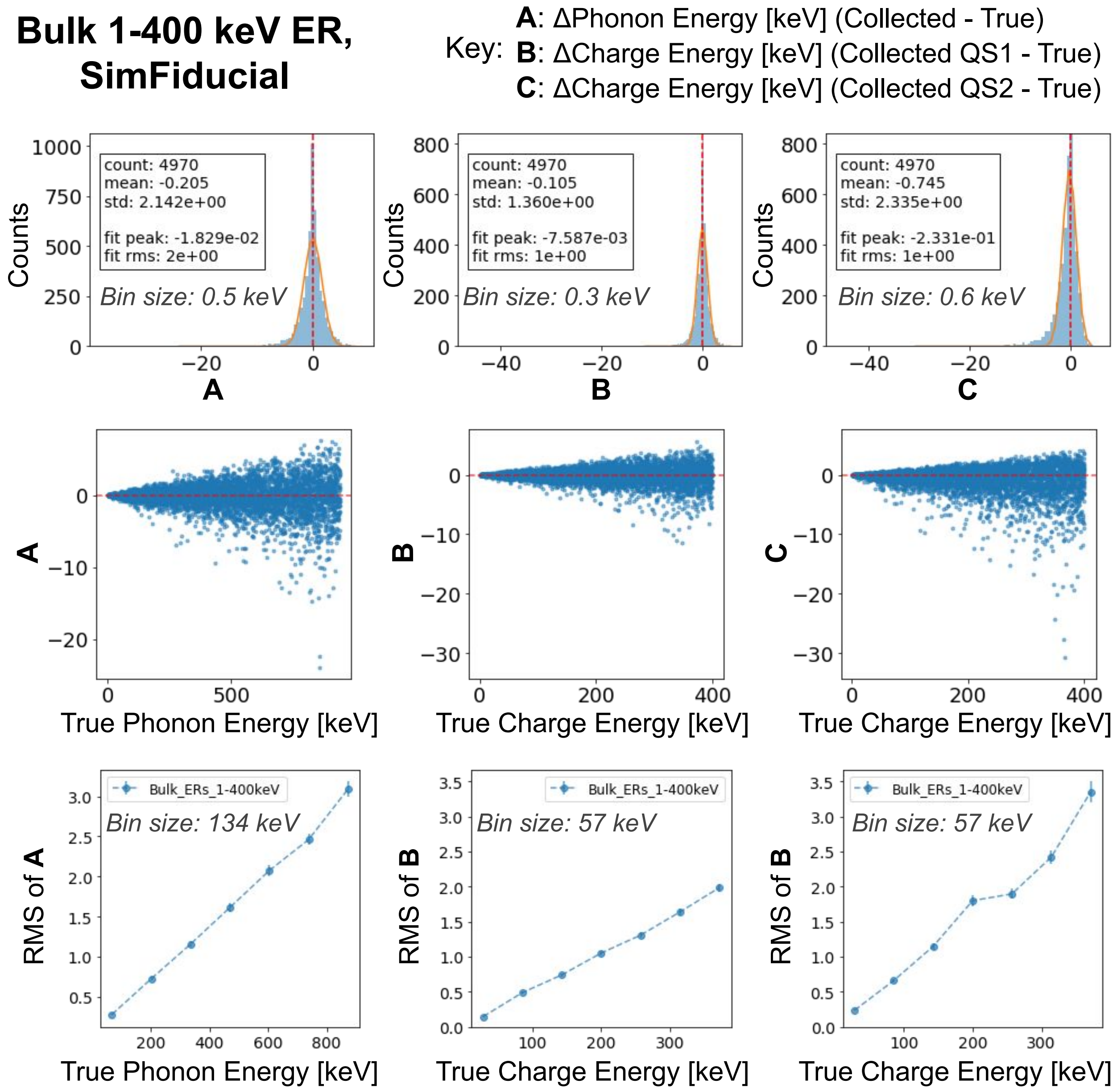

Figure 8.12: This figure shows three rows of plots (each row with phonons, QS1, and QS2) showing the difference between true and collected energy and the resolutions for the 1-400 keV ER sample. The top-row plots show that the differences between true and collected energies are centered at 0–the same as we saw in the previous sample (compare Fig 8.9), and further demonstrating that our calibrations work across an energy range. The bottom two rows in particular demonstrate how the previous ER results scale with energy. The middle row of plots show the energy differences increase as recoil energies increase, but this is expected. The bottom row of plots shows the resolution of the points in the middle plot, binned across the x-axis. The resolution, again, increases with deposited energy.

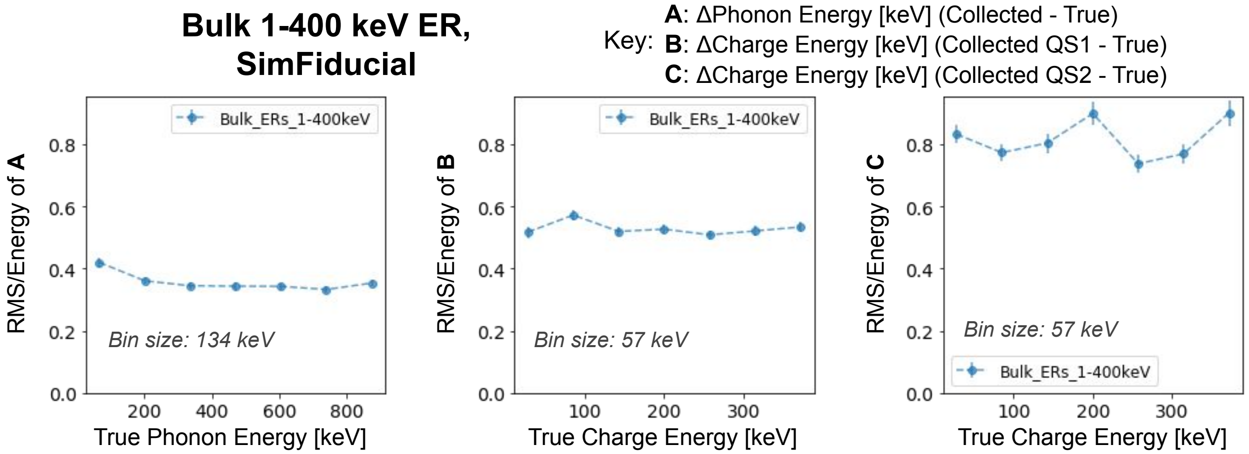

Figure 8.13: This figure shows the fractional resolution of phonons and charges for the 1-400 keV ER sample–the same data as the bottom row of Fig 8.12, but with the y-axis divided by recoil energy. This shows that the changes in resolution are due primarily to the changes in energy, as the fractional resolution as a function of energy is essentially flat across.

8.2.3 Idealized NR Sample and Comparisons to ER Sample: 1-400 keV Energy Range

We add another level of complexity with the next sample, here replacing ERs with NRs. This sample will in some ways be the same as the previous one–its energies and hit distributions will be qualitatively the same as those shown for the ERs in Fig. 8.10–except that now there is some non-unity ionization yield that is a function of recoil energy (see Fig. 3.2). That is, some energy in each deposit will create primary phonons, instead of all of it liberating charges, and this amount changes with recoil energy.

We find first of all that the phonon collection efficiencies have changed since the ER samples. As shown in Fig. 8.14, the NR sample's efficiency peak is slightly higher than that for the previous two ER samples. We explain this difference with off-electrode effects:

- Recall that charges that land off-electrode do not experience the full voltage drop and so do not emit all the NTL phonons they should–but there is no such drain on prompt phonons.
- Recall further that the difference between ERs and NRs is that the former have yields equal to 1 (i.e. no prompt phonons produced) while the latter's yields are lower (i.e. prompt phonons produced) but increase with recoil energy (see Fig. 3.2). That is, NRs produce

fewer charge pairs than ERs, but become more similar to ERs at higher energies.

- Low-energy NRs, then, will have higher phonon collection efficiencies because a smaller proportion of their energies will rely on charges that might miss electrodes. Higher-energy NRs, meanwhile, will have more charges subject to off-electrode effects and so have their efficiencies reduced to be more like those of ERs.
- Additionally, we believe the first simulation artifact mentioned in section 8.1.2 is worsening the difference between ERs and NRs here–not only by scaling up the difference along with the inefficiency, but also by favoring prompt phonons over NTL phonons. See details in Appendix C.

These effects are shown in Fig. 8.15, where the phonon collection efficiency of NRs clearly changes with the number of charge pairs created–becoming more like ERs as the yields converge (we've included a simple model as well to check our understanding; see figure caption). For now we will simply keep this efficiency difference in mind and recalibrate if/when needed, but we note that in real data such recalibration could only be done if we knew for certain a given event was an NR (and how much correction was actually needed).

The charge collection efficiencies, meanwhile, do not appear to change significantly, so we can continue calibrating charge energies using the Bulk ER results without issue.

Due to the higher phonon efficiencies, the NR sample's phonon energies–if we continue calibrating them using the efficiency value we found for ERs (as is done in real data, using Ba-133 photon events)–trend high compared to expectation and the ER sample, as shown in Fig. 8.16. Otherwise the charge energies and resolution trends behave as expected. Note that the total recoil energy is divided between phonon and charge energies in the case of NRs, so the NR data does not cover the full range of energies caused by ERs[9].

We leave the bulk samples for now with Fig. 8.17 showing the yields as determined by our collected energies (we'll check on these again in the next chapter with reconstructed energies); we

---

[9] One might expect NRs to reach higher phonon energies since they include prompt phonons, but this is outweighed by the ER sample's greater number of freed charges and subsequent higher number of NTL phonons

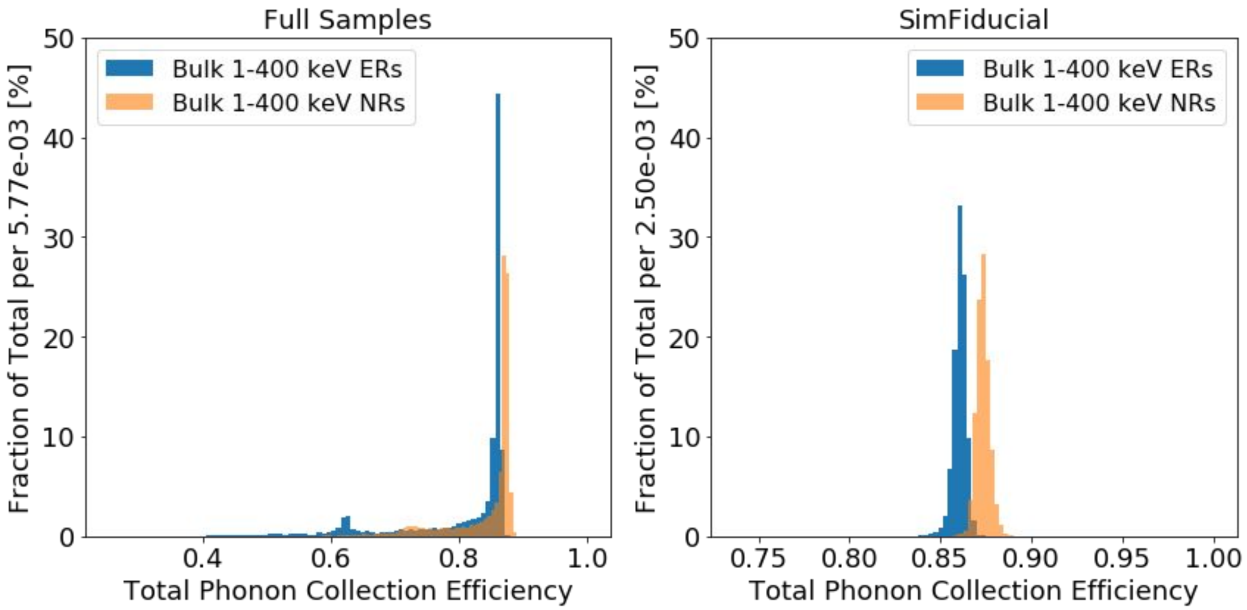

Figure 8.14: This figure shows the phonon collection efficiencies for the 1-400 keV NR and ER samples, with and without SimFiducial cuts. The NR sample's phonon efficiencies both as a whole and within just SimFiducial trend higher than those for the ER samples. This difference is likely due to off-electrode effects: only a part of the NR energy is allocated to charges–which negatively impact phonon collection efficiency if they don't emit all the NTL phonons they should–while the remaining energy in the prompt phonons is not affected. The charge collection efficiencies (not shown) do not noticeably change between recoil types.

see ERs and NRs largely where expected, but both are somewhat low–NRs more so due to the efficiency differences and simulation artifact mentioned previously. We attribute the low values for ERs and NRs primarily to off-electrode effects because, as a check, if we use only QS1 to represent charges in our calculations instead of Qsummean–thereby sidestepping the worst of the off-electrode effects on QS2–these differences are reduced by over 75%. It is likely a combination of the non-Gaussian shape of QS2's collected energies in particular (shown, e.g. in Fig. 8.8) and the Z-dependencies seen in Fig. 8.7 (the significance of this Z-dependence being that there is some correlation between events well-measured by side 1 but poorly-measured by side 2–and vice-versa).

At this point we've seen essentially everything we need from the Bulk samples in the DMC. We've identified our SimFiducial region and calibration factors and seen how they can be applied

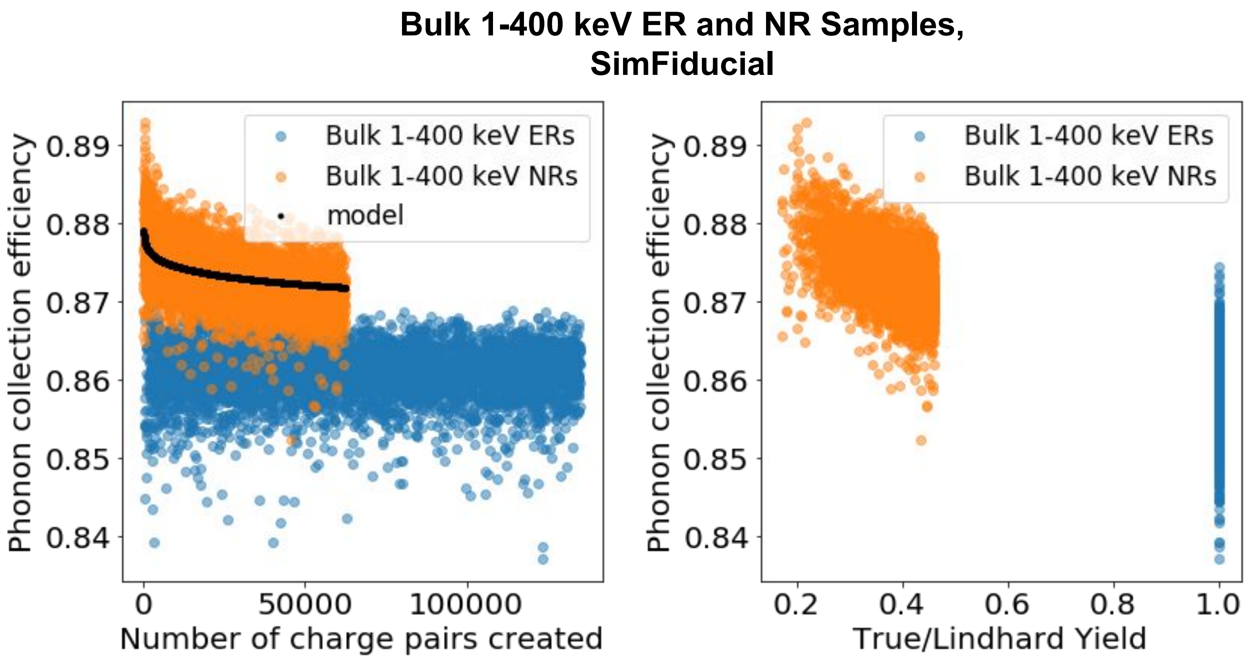

Figure 8.15: This plot shows how the phonon collection efficiency scales with the proportion of charge pairs created in a hit. The ER sample (blue) has essentially constant phonon collection efficiency (within some resolution) while the NR sample (orange) converges towards that value at higher energies, yields, and charge pair counts. Note that because these samples both simulated recoil energies of 1-400 keV, the NRs, which split up their energies between prompt phonons and charges, will never completely converge to the behavior of the ERs. In the left plot we have overlaid a simple model of the form $\epsilon_{NTL} * E_{NTL} + \epsilon_{(P+R)} * E_{(P+R)}$ where ϵ and E are efficiencies and energies of the relevant phonon subset, respectively (and "P+R" is short for "prompt+recombination"); this model describes the NR data well.

across recoil energies and recoil types–the one problem being phonons, which show different collection efficiencies between ERs and NRs. Both this and the other collection shortcomings we observe are reasonably attributable to off-electrode effects (and a removable simulation artifact for phonons). With the basics of the detector response understood, we next move to more realistic and complicated samples.

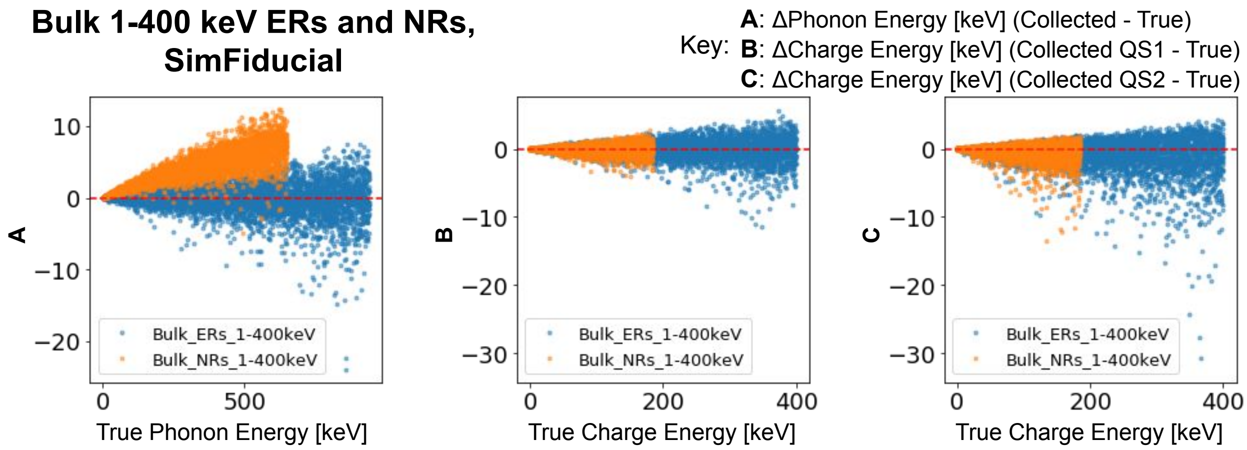

Figure 8.16: This figure shows the differences between collected and deposited energies as a function of energy for both ER (blue) and NR (orange) samples, to compare trends between recoil types. As shown in the leftmost plot (and as foreshadowed in the previous figure), only the phonons are clearly different between recoil types. We could recalibrate using the NR efficiencies to center the NR sample's phonon ΔE at 0, but we continue using ER calibrations because Ba-133 (which causes ERs) is the main calibration source for the real experiment. The cause of the difference in the phonons is likely off-electrode effects, as noted in the text.

8.3 DMC Results for Calibration Samples

We now move to full simulations of the calibration sources, starting with the simpler case of Ba-133 and then moving to Cf-252. The samples from the previous sections gave us an idea of how the detectors should respond to idealized, single-hit ERs and NRs; here we will see how they respond to more realistic, external sources that can have multiple hits, particles, etc. We first have two notes about these calibration samples, though:

- Firstly, these are different samples than the ones used in the previous chapter. These calibration samples were re-run both to take advantage of newer software versions and to focus on stages after SourceSim (the previous samples stored additional SourceSim information for sake of study that otherwise make the output files needlessly large and difficult to work with).

- Secondly, we limit the Cf-252 sample to simulate only the results of the fission neutron spectrum for computational convenience (using a Watt spectrum, specifically; see section

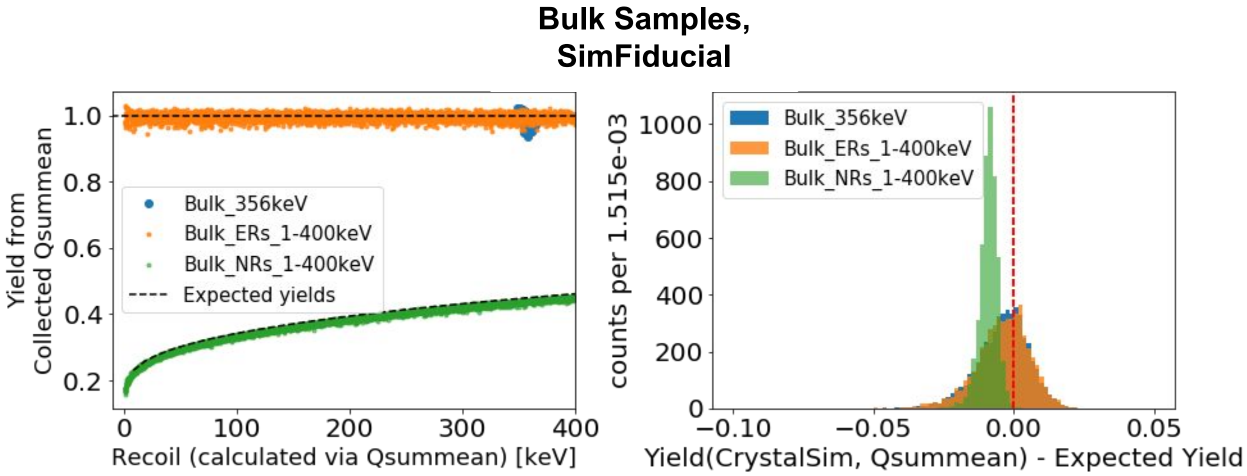

Figure 8.17: This figure shows the yields as constructed for our bulk samples in two forms to study the similarities and differences between the expected and measured values. Left: yield vs. deposited energy, both as calculated using qsummean. The ER samples are near 1 while the NR sample is around the expected curve. Right: Difference between measured yields and the expected yields. All three samples are a bit low, but mostly for explainable reasons: the NR sample has higher phonon collection efficiencies than the others and all three samples suffer from low trends in ionizing energy due to off-electrode effects (in QS2 in particular).

5.2.2). The fission gammas do not have particular energies we want to look for and the products of the alpha decay chain are almost entirely blocked; excluding these aspects of Cf-252 thus does not lose any of the information we're interested in (the NRs) but saves significant computational overhead. We mention this only because it is possible that this could cause differences (albeit small, inconsequential ones) when we compare simulated data to real data in chapter 10 (simulations may have a smaller ratio of ERs to NRs, for example; this is not too worrisome). See details in Appendix B

Looking ahead, we note that when we switch from SimFiducial to the LT Fiducial cuts (refer back to table 4.2) in the next chapter, these calibration samples will start to include a significant number of "semi-fiducial" mismeasured events (see table 3.1), where having multiple hits of different collection efficiencies causes problems. For now though, we only consider multi-hit events to be well-measured if all of their hits are within the previously-identified SimFiducial region, which precludes such mixed-collection-efficiency issues.

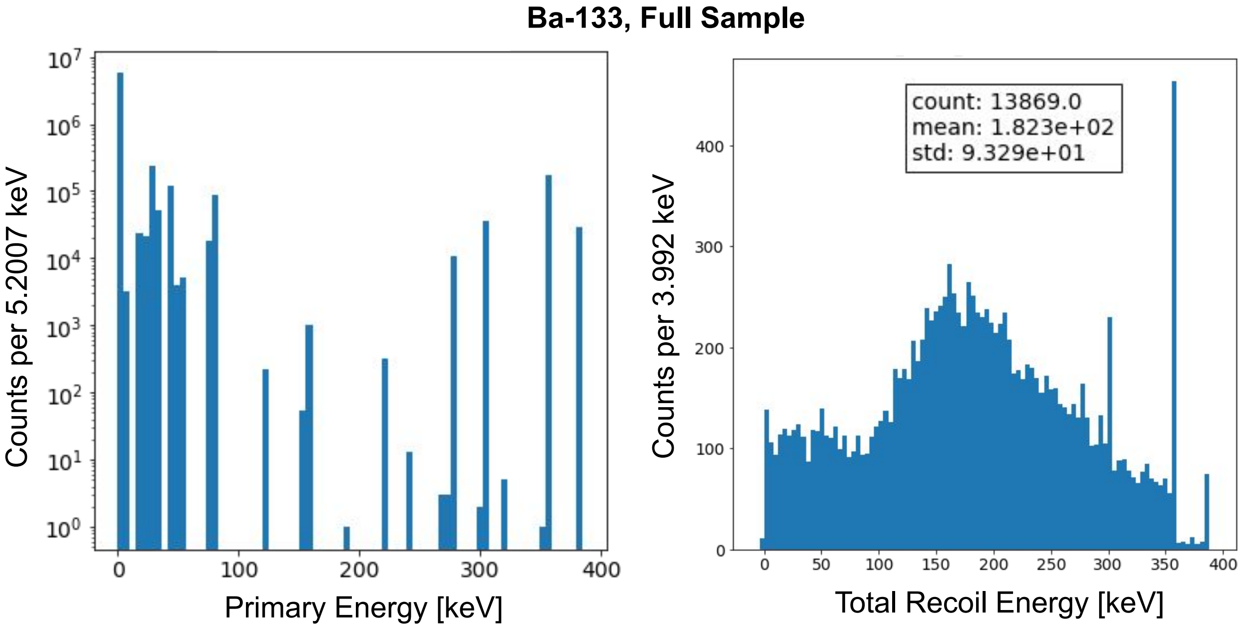

Figure 8.18: This figure shows the emitted and deposited energies for events from the simulated Ba-133 simulation. Shown at left are the primary energies released from the source–now external to the detectors, coming from the 'E-Stem' pipe shown in Fig. 2.5; these are all photons, with X-rays at the lowest energies and gammas up to nearly 400 keV. Particles from the source may not hit the detector we're watching at all or may deposit only part of their energy–either due to having lost some of it due to interactions with other apparatus components along the way or to simply bouncing off the detector instead of being fully absorbed. In any case, the final deposited energies will be more spread out towards lower energies, as shown in the figure on the right. We can still see full absorption of some of the highest-energy gammas, but the rest are largely lost in a sea of Compton-scattered energies.

8.3.1 Ba-133 Sample Results: Comparing Idealized ERs and Recoils Caused by Photons

While the Ba-133 contains only ERs, which are slightly simpler than NRs, it also introduces several complications compared to the Bulk ER samples. First and foremost, it introduces multi-hit events that will complicate our efforts to identify well-measured events. Second, being an external source emitting specific, discrete energies, the hits will not be uniformly-distributed either in energy or in space. These differences can be seen in Figs. 8.18 and 8.19. We note that the spatial non-uniformity will likely affect our QS2 results in particular, per Fig. 8.7.

Fig. 8.20 shows the collection efficiencies for both the Bulk ER 1-400 keV sample and the

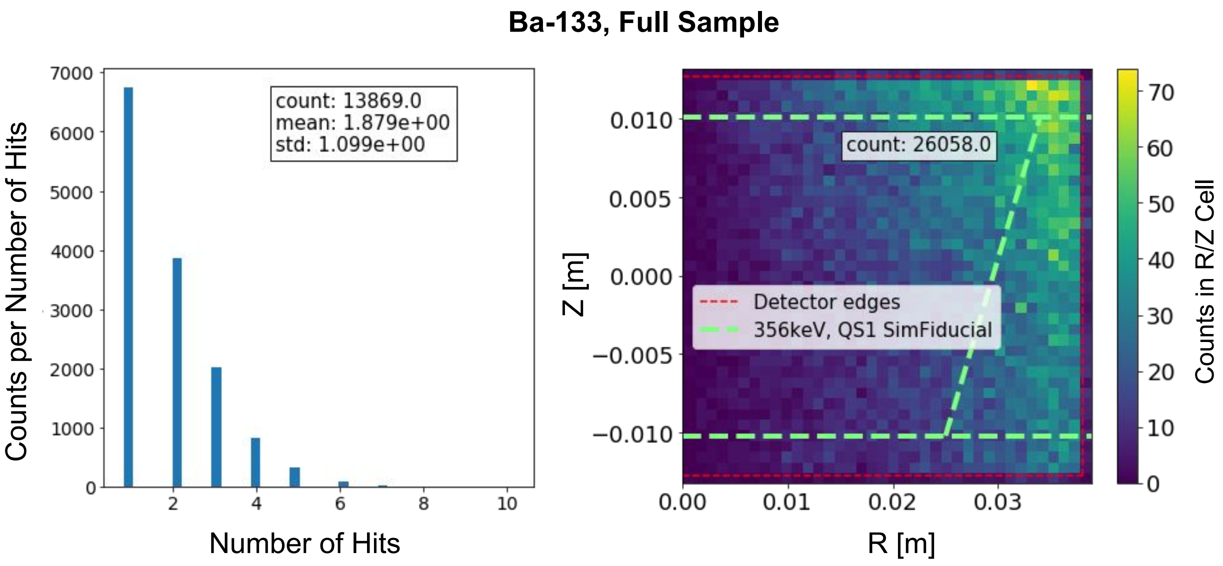

Figure 8.19: This figure shows both the distribution of the total number of hits in each event and their individual locations in the detector. The presence of multi-hit events will make these results more complicated than those for the previous samples. Note that the simulation has merged hits that occurred within 2mm of each other, so realistically there would be more than those shown here. Left: histogram of the number of hits in the detector in each event. The majority are single-hit events, representing either single particles that skim off the detector and leave or lower-energy particles that are captured. Right: heat plot of hit locations in the detector. Since here the source capsule is simulated in the electronics pipe– which was above and to the side of the detectors–hits are focused on the upper corner of the detector. Overlayed in green is the SimFiducial region we identified previously; this was defined for single-hit events, but here we consider multi-hit events to pass the SimFiducial cut if all hits are within this volume.

Ba-133 sample (without SimFiducial cuts), showing there is little difference between the two. The largest difference is in QS2 (which changes less than 1%, but nevertheless a statistically significant amount), which is affected the most by the nonuniform hit distribution in Ba-133; recall Fig. 8.7, which showed worse QS2 efficiencies for hits occurring closer to the top of the detector–which is favored here for an external source located above (if off to the side of) the detectors. This small difference in only one side is not enough to justify changing our calibrations, so we continue with those from the bulk samples.

To make the comparison between the Bulk ER sample and the Ba-133 sample more direct, we first cut down to only single-hit events. In theory this should make the two samples behave exactly

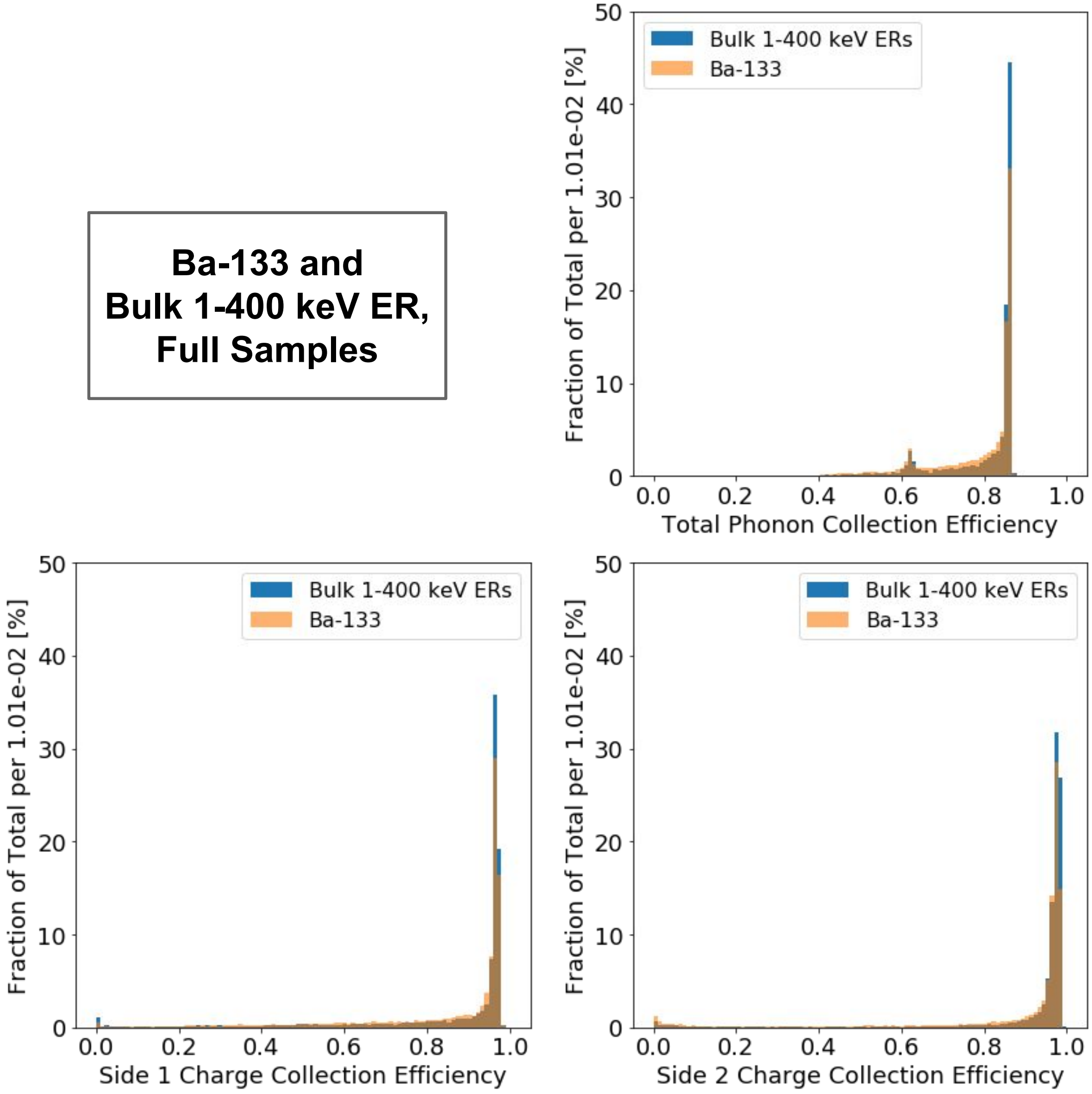

Figure 8.20: This figure compares the collection efficiencies for the 1-400 keV ER sample–which has only single-hit events– and the Ba-133 sample–which also has multi-hit events. The energies seen in QS2 (bottom-right) show the most clear difference, with the Ba-133 sample's main peak being more than 3σ lower, but this is likely due to the Z-dependence discussed in Fig 8.7.

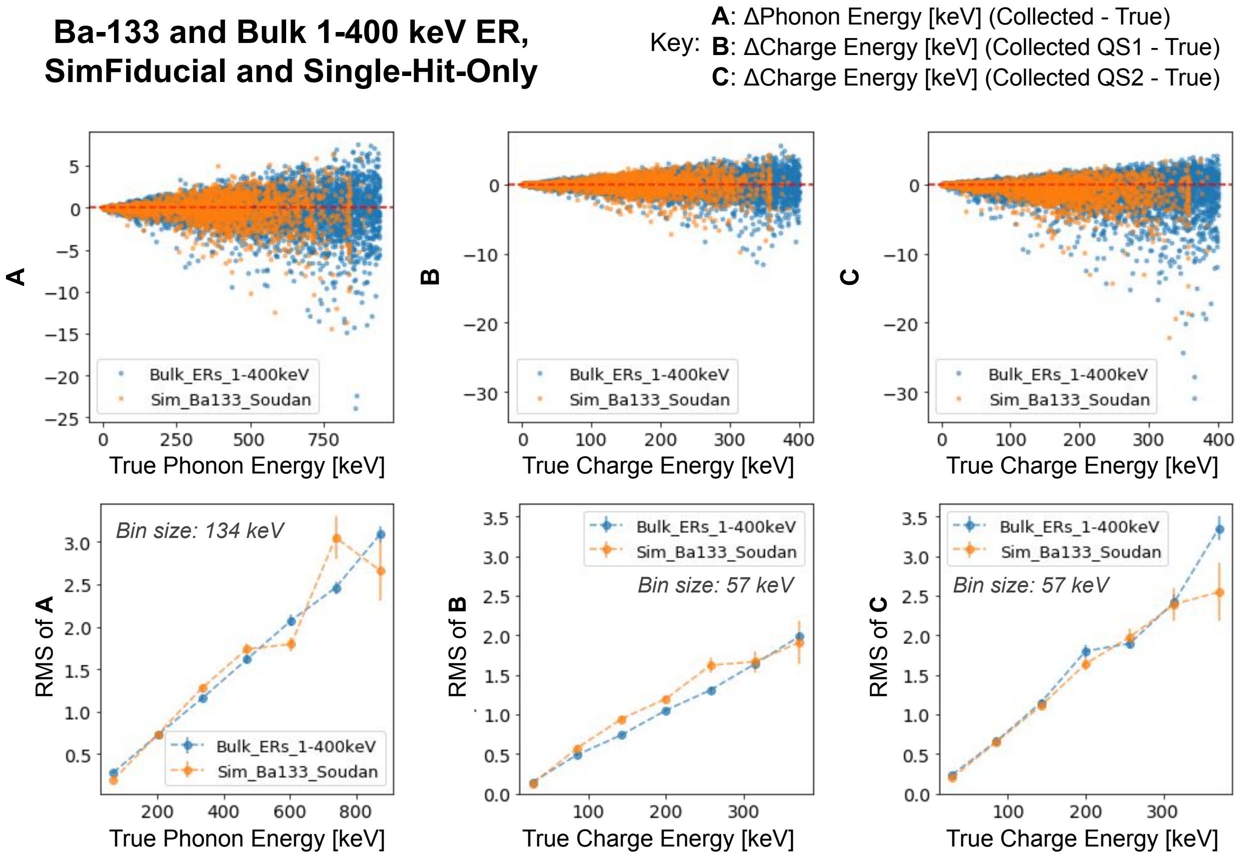

Figure 8.21: This figure compares the energy differences and resolutions as a function of energy for single-hit events for the Ba-133 and 1-400 keV ER samples. The top plots show that the differences between true and collected energies look essentially the same between samples, as expected, though we don't have similar statistics at every energy. The bottom plots show the energy resolutions as functions of energy; these largely agree, though perhaps Ba-133 trends high at middle energies.

the same, aside from the data not being uniformly distributed in energy or position. Fig. 8.21 compares the energy differences and resolutions as a function of expected phonon and charge energies for the two samples in the SimFiducial region; we see good agreement between the samples, within statistics.

We next add back in the multi-hit events for Ba-133 in Fig. 8.22; note that multi-hit events are considered to be within SimFiducial only if all of their individual hits are. While the energies still appear calibrated appropriately, the resolutions have dropped (i.e. gotten unexpectedly better)– most concerningly for the phonons. This turns out to be due to another simulation artifact affecting

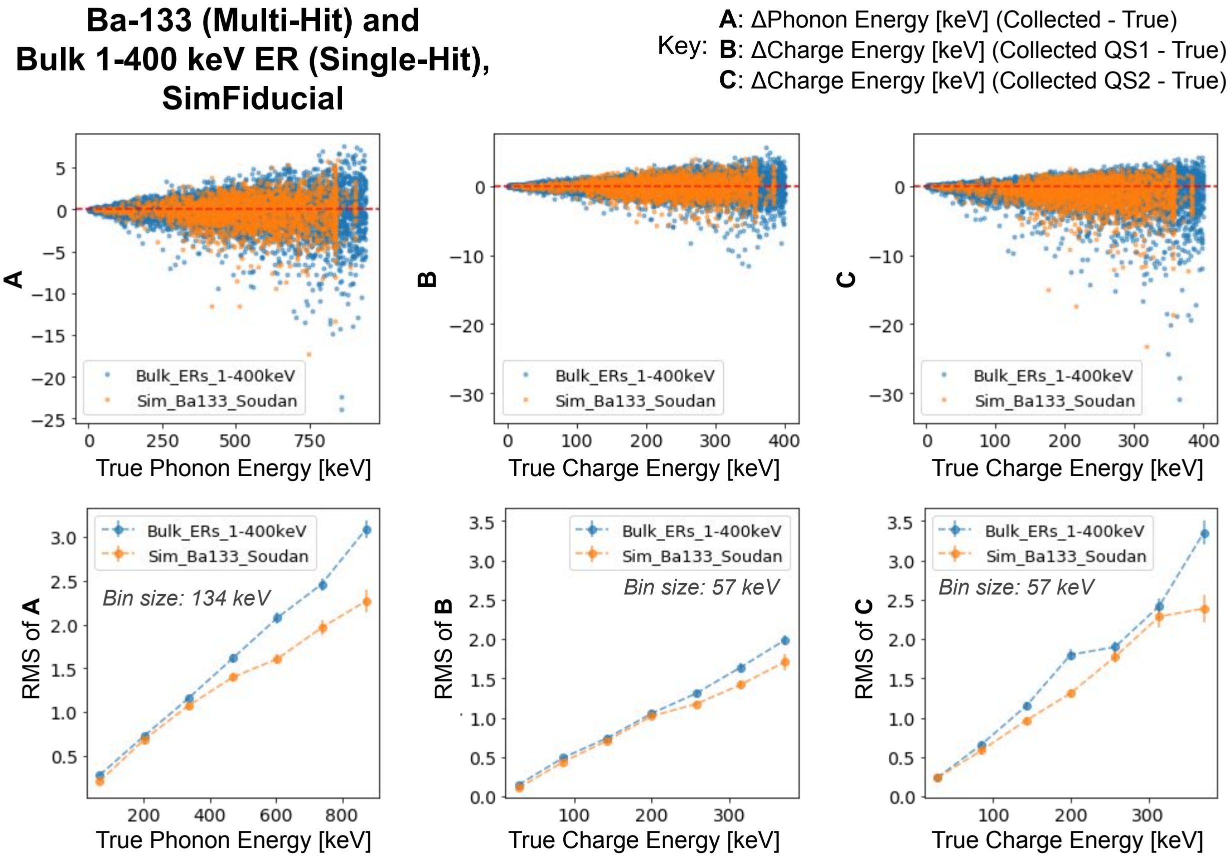

Figure 8.22: This figure compares the energy differences and resolutions as a function of energy between multi-hit events in Ba-133 and single-hit events in the 1-400 keV ER sample. Top: The differences between true and collected energies look essentially the same between samples, though we don't have similar statistics at every energy. Bottom: The resolutions for Ba-133 trend lower than those for the ER sample due to a simulation artifact noted in the main text.

the number of NTL phonons emitted per charge, however, which has been fixed since this analysis (this is different from the overall phonon efficiency artifact; see Appendix C).

8.3.2 Cf-252 Sample Results: Comparing Idealized NRs and Recoils Caused by Neutrons

As with the transition from the Bulk ERs to Ba-133, the transition from Bulk NRs to Cf-252 introduces multi-hit events and nonuniform hit and energy distributions due to having an external source. This source also will involve all of the complicated recoil types discussed in section 3.1.2, as shown in the previous chapter. In this section we will compare Cf-252 (that is, only the results of its fission neutrons) both to Ba-133 (for ERs) and the Bulk NR sample (NRs); we won't have

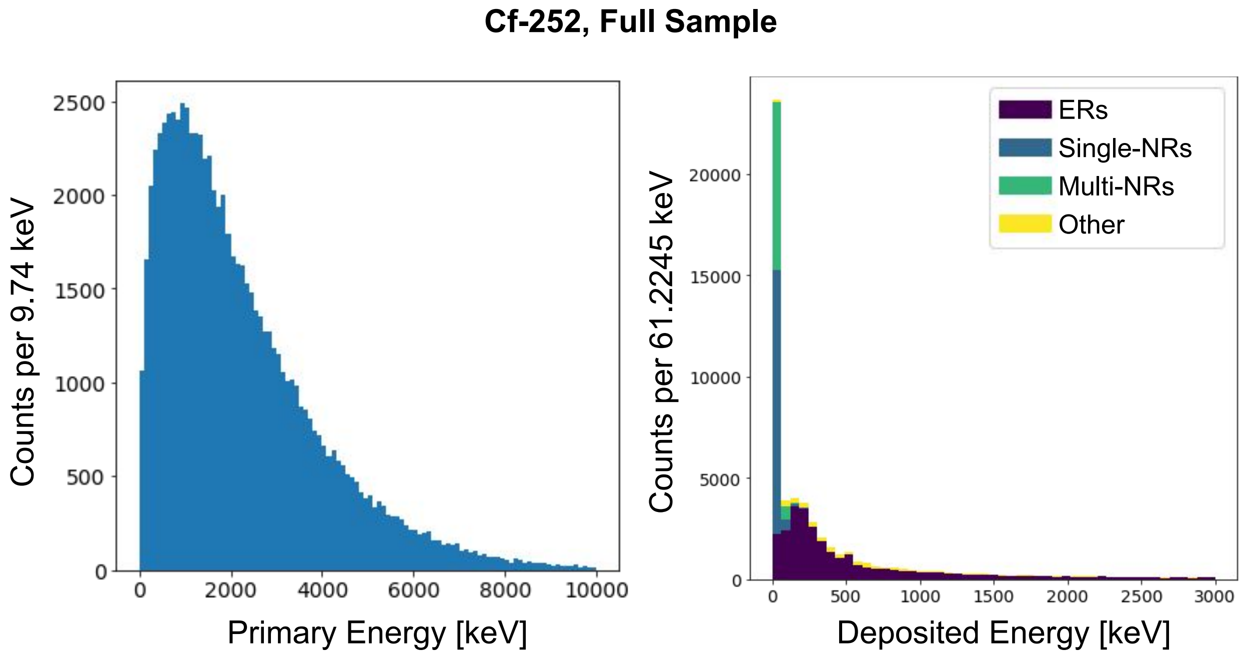

Figure 8.23: This figure shows the primary and deposited energies for our simulated Cf-252 simulation. Recall that this sample only simulates the prompt fission neutrons (real Cf-252 releases other particles, but we're only interested in these neutrons currently); shown at left are the energies of these neutrons as emitted from the source. Shown at right are the deposited energies, color-coded by recoil type. A lot of the initial energy is lost, so the final deposited spectrum is rather featureless: a low-energy peak with a tail towards higher energies, though there is an NR-specific peak that will be used later. Note that, despite the "Full Sample" label, we've removed all interactions after 1 second, for the reasons described in the chapter 7; this will be the case going forward as well.

as much to say about events with mixed ER and NR aspects here, since we don't have precedent from other samples. Starting with SourceSim results, Fig. 8.23 shows the emitted and deposited energies of the Cf-252 sample while Fig. 8.24 shows the hit distributions; we note the hits are are slightly biased towards high Z values–but not as strongly as those for Ba-133.

Since the Cf-252 sample includes both ER and NRs and multi-hit events, it is the first of our samples in this chapter that will include all the recoil types discussed in chapter 3. Fig. 8.25 shows the distribution of each recoil type and their expected yields (determined from their recoil types and energies) as a function of calculated recoil energy. Note that these are still using only SourceSim results; we see that even before detector mismeasurements are a factor, multi-NRs have

Cf-252, Full Sample

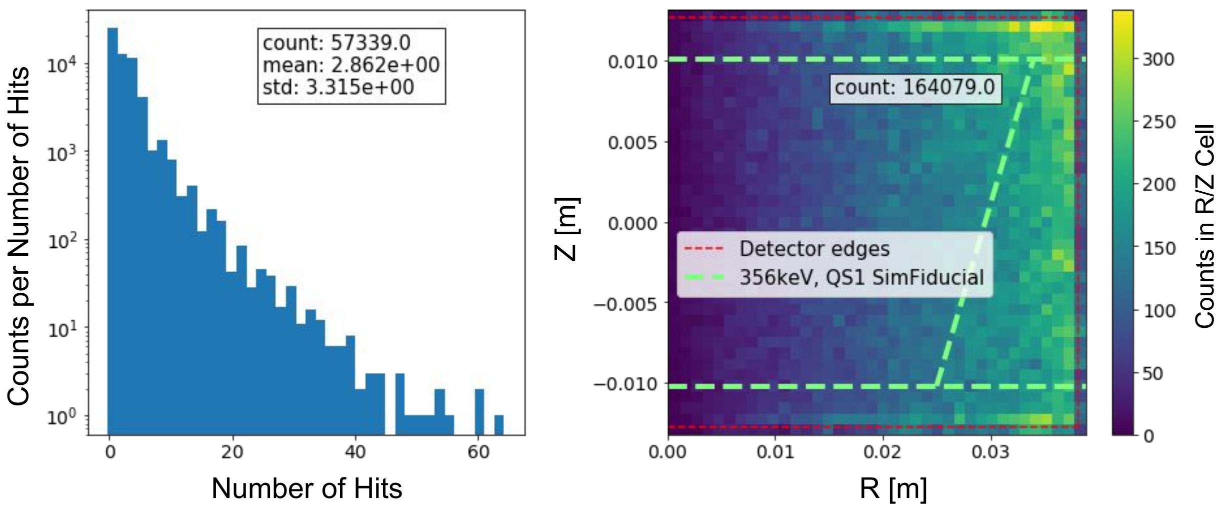

Figure 8.24: This figure shows the same information as Fig 8.19, now for the Cf-252 sample. Left: as with Ba-133, lower numbers of hits are more common, but Cf-252 does average a higher number of hits than Ba-133 (though recall, again, that hits that are very close to one another have been merged together). Right: heat plot of hit locations. Though it's still the outer edge that is favored, there is less obvious a trend in Z than there was in Ba-133. This is likely due to neutrons being able to bounce around so much and enter at more angles.

lower yields than single-NRs while the complicated "other" recoil types are between the normal ERs and NRs.

Moving now to the DMC, Fig. 8.26 shows the main collection efficiency differences we see between the past three samples. Recall that we saw higher phonon collection efficiencies in the Bulk NR sample than in the Bulk ER sample. Cf-252, having both ERs and NRs, has elements that match both, though the phonon efficiencies are slightly higher in the Cf-252 sample than the NR sample–likely because the former has more events at low recoil energies, where off-electrode effects are less impactful. Fig. 8.27 shows the relationship between phonon efficiency and recoil energy for both of the calibration samples and the Bulk NR sample for comparison (see also Fig. 8.15).

Figs. 8.28 and 8.29 compare single-hit and multi-hit ERs, respectively, for the Cf-252 and Ba-133 samples. Recall that while the two samples don't have the same distribution of recoil

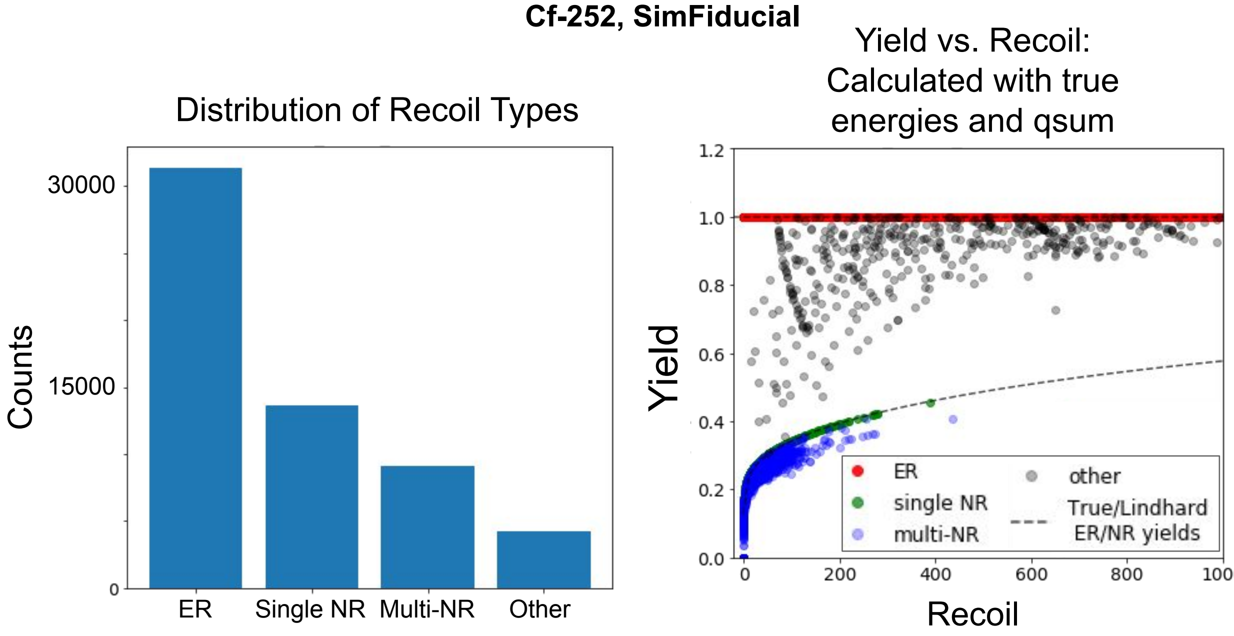

Figure 8.25: This figure shows a breakdown of the recoil types and associated yields we hope to be able to reconstruct at the end of the simulation chain for the Cf-252 sample. Left: This sample is the first one in this chapter that could involve all the recoil types covered in chapter 3, and here we see their distribution in the sample–"multi-NR" covering all the more complicated patterns. Right: the true yield as a function of recoil energy–as calculated from the true charge and recoil energies available in the simulation output. We hope to be able to reconstruct this later using the collected and processed energies from CDMSBats.

energies, the ERs at a given recoil energy should generally behave the same between the two. This is essentially what our simulation results show.

We now continue with a comparison of the NRs between the Cf-252 and Bulk NR samples. Fig. 8.30 compares the single-hit NR events of these samples. While the broad strokes are the same, The Cf-252 sample's preference for lower energies makes it difficult to get reasonable statistics and make comparisons at higher energies (above about 100 keV in phonon energy or 40 keV in charge energy).

Next, Fig. 8.31 compares multi-hit NR events in the Cf-252 sample to the necessarily-single-hit Bulk NR sample. Again there is general agreement, but again it becomes difficult to compare the samples at higher energies.

We end this section by looking at the yields calculated from the DMC results for our two

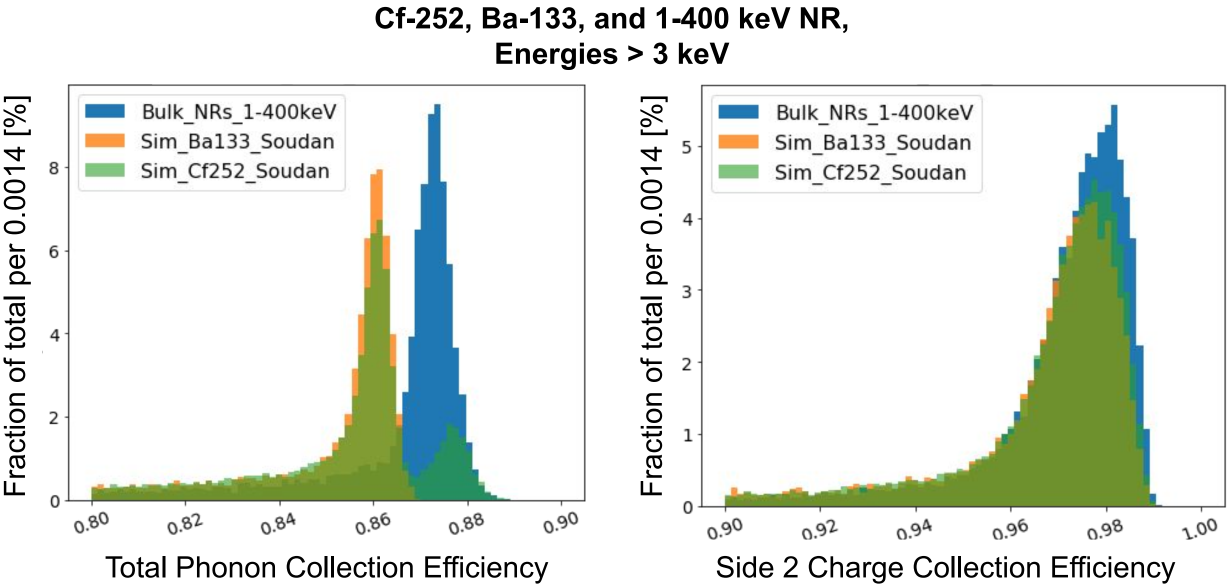

Figure 8.26: This figure shows the collection efficiencies for phonons and QS2 for three of our samples–here focusing on where the samples differ from one another. QS1 is not shown because the samples show good agreement there. We've also removed events with recoils below 3 keV, where noise and fluctuations cause extreme, non-representative efficiency measurements. Left: For phonons, we see the NR sample has a higher efficiency than the Ba-133 sample (similar to what we saw before for the ER and NR samples; see Fig. 8.14), and the Cf-252 sample has a peak the seems to correspond to each (since it has both ERs and NRs). Its NR peak appears to be higher than that for the NR sample, though, due to Cf-252 having more low-energy events and the associated efficiency dependence shown in Fig. 8.15. Right: For QS2 the differences are less dramatic; it appears to be only the slight shift due to the efficiency's dependence on Z.

calibration samples, shown in Fig. 8.32. Off-electrode effects again make all the yields low (as discussed in section 8.2.3) but otherwise both samples appear where we expect them:

- Ba-133's yields are centered at 1.
- Cf-252 recreates the structures seen in the previous chapter and in Fig. 8.25.
- The resolutions have generally increased–most clearly for ERs, since the NRs and multi-NRs run together.

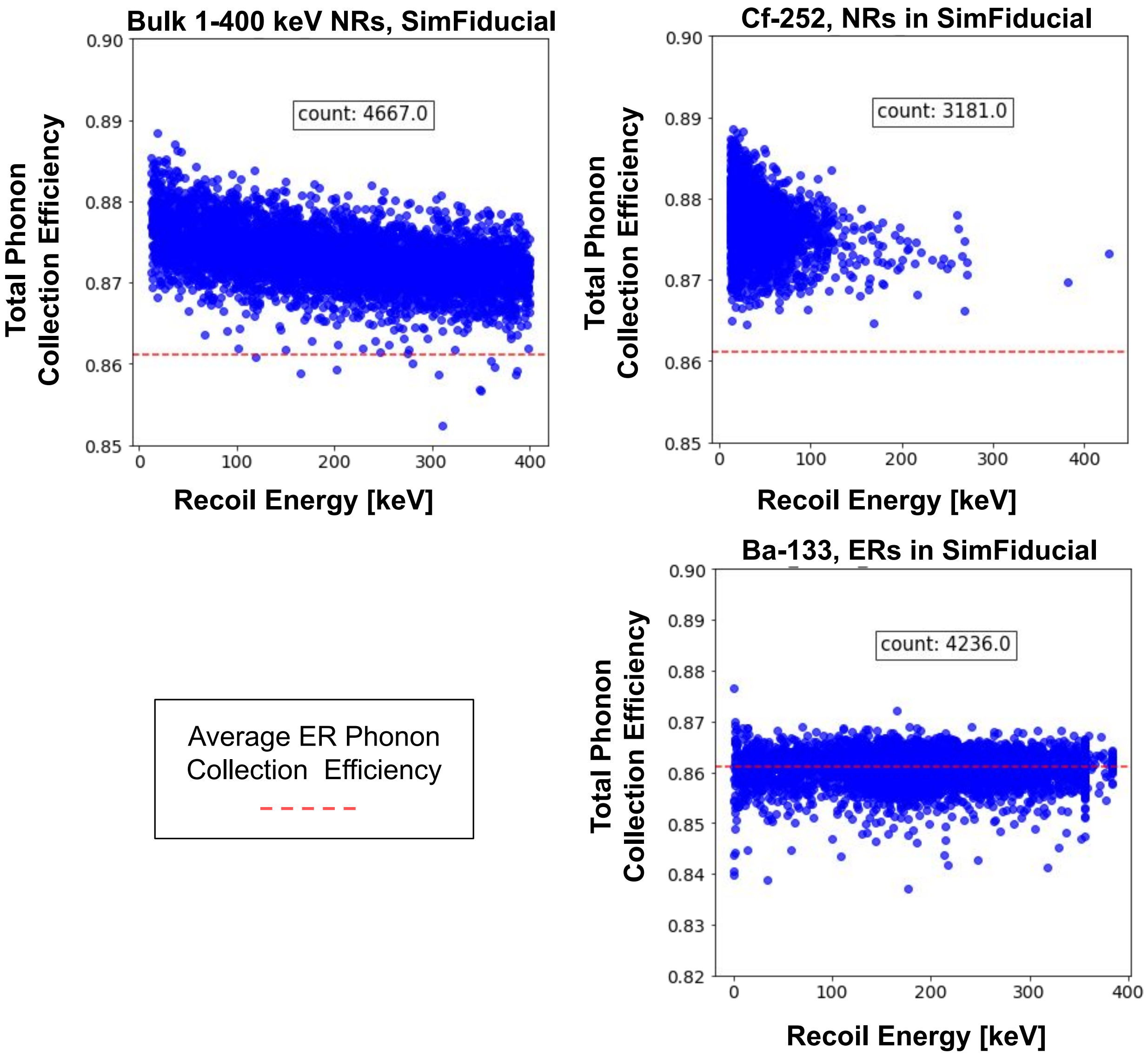

Figure 8.27: This figure shows the phonon collection efficiencies as functions of deposited energy for the Bulk NR sample, Cf sample, and Ba sample. These demonstrate that the NR phonon collection efficiencies–as seen in the Cf-252 and Bulk NR samples in the top two plots–have an energy dependency in our simulations while those for ERs–as from Ba-133 in bottom–do not. This correlates with the energy-dependency in the yield, suggesting that the efficiency loss is due to greater numbers of charges that are subject to off-electrode effects.

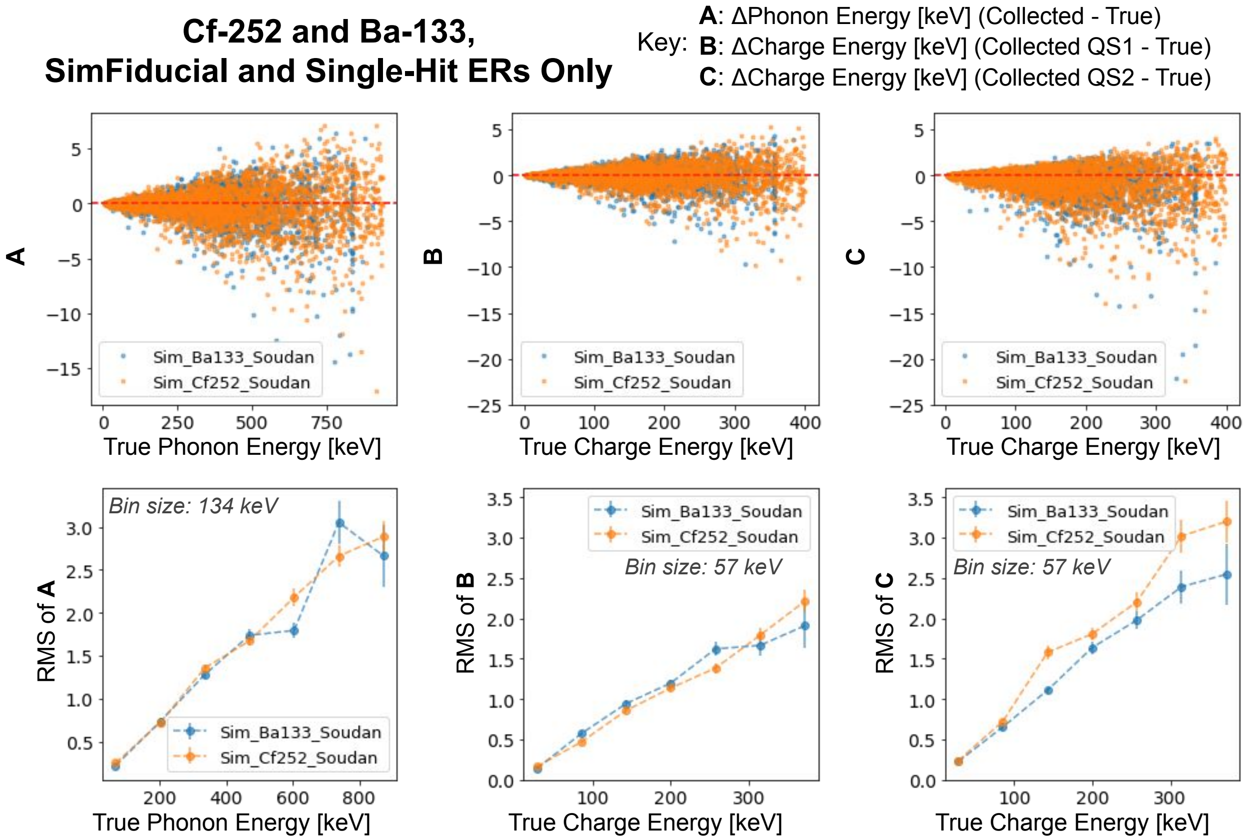

Cf-252 and Ba-133, SimFiducial and Single-Hit ERs Only

Key: **A**: ΔPhonon Energy [keV] (Collected - True)
B: ΔCharge Energy [keV] (Collected QS1 - True)
C: ΔCharge Energy [keV] (Collected QS2 - True)

Figure 8.28: This figure shows the ΔE and energy resolution as functions of recoil energy for single-hit ERs in simulated Cf-252 and Ba-133–all within SimFiducial– which lets us check that a given recoil type behaves the same across samples. Though we don't have good statistics for all energy sub-ranges, we see good agreement overall. Note that here we only show events with charge energies between 3 keV (a minimum to avoid proportionally-large low-energy fluctionations) and 400 keV (just over the maximum energy from Ba-133, and well above where WIMPs are likely to be).

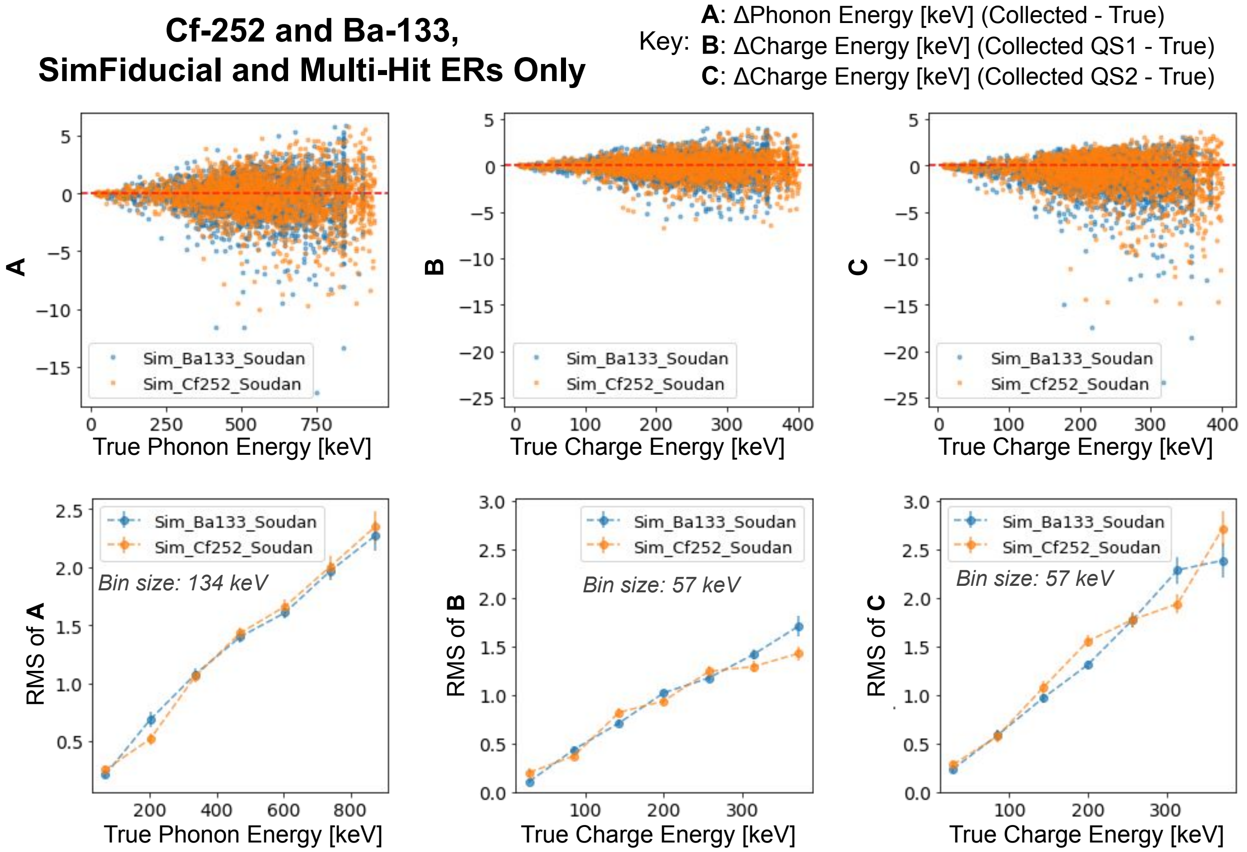

Figure 8.29: This figure shows the same information as the previous figure, but for multi-hit ERs instead of single-hit ERs. Though we don't have good statistics for all energy sub-ranges, we see good agreement overall.

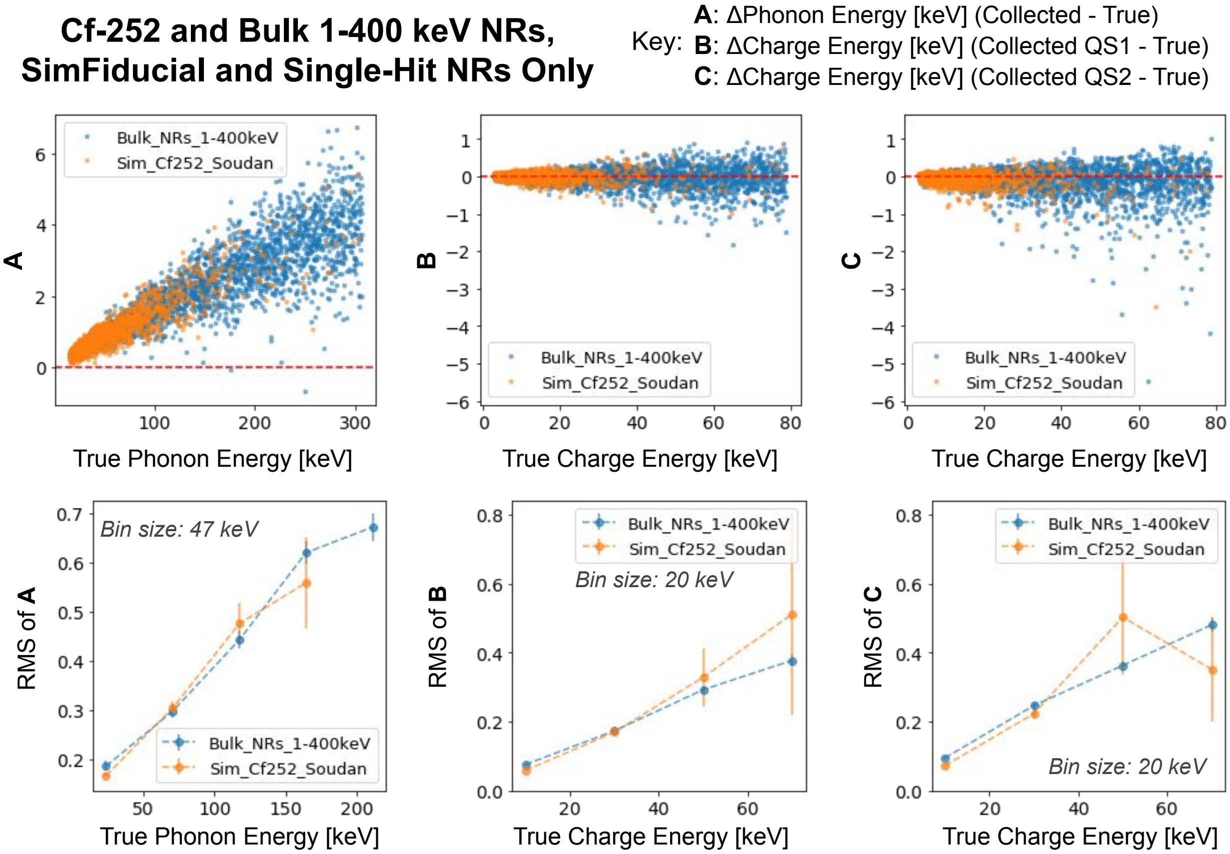

Figure 8.30: This figure shows ΔE and energy resolution as functions of true (or expected) energy for *single-hit* NRs in simulated Cf-252 and idealized NRs. The samples match well at low energies, as expected, but low statistics at high energies in the Cf-252 sample make it difficult to draw conclusions beyond that.

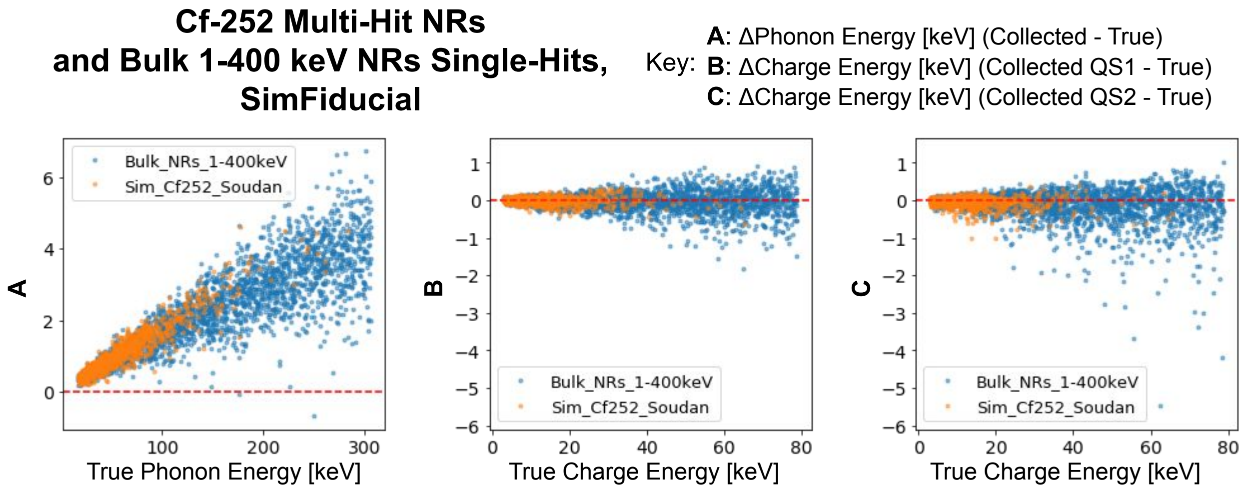

Figure 8.31: This figure shows ΔE as a function of true (or expected) energy for *multi-hit* NRs in simulated Cf-252 and idealized NRs. We show this to compare the behavior of ideal, single-hit NRs and Cf-252's multi-hit NRs. Due to low statistics and outliers, it's difficult to establish meaningful "resolution" values.

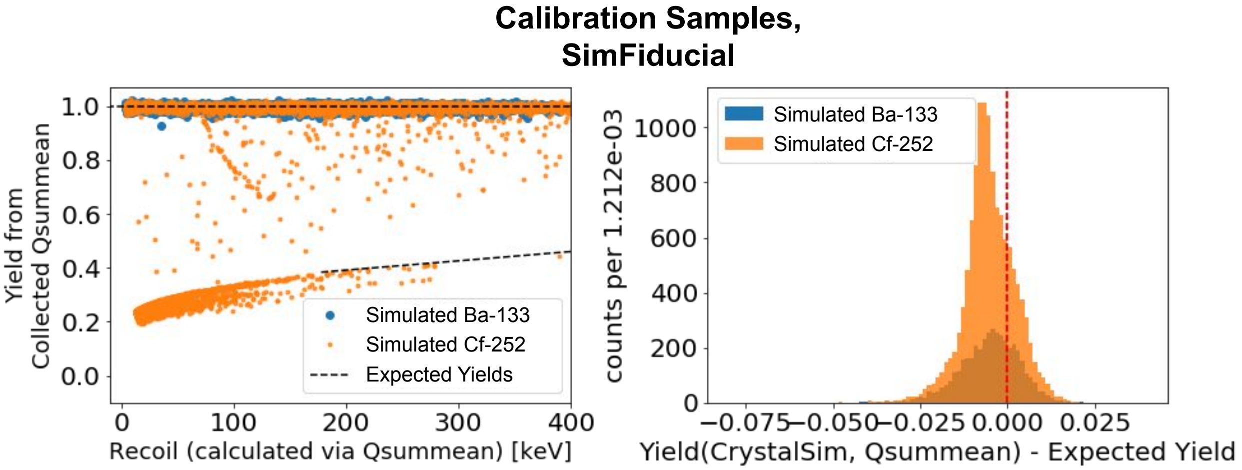

Figure 8.32: This figure shows the yields as constructed for our two calibration samples in two forms to study the similarities and differences between the expected and measured values. Left: yield vs. recoil energy, both as calculated using qsummean. ERs and NRs again both appear about where they are expected to. Comparing the Cf-252 data to Fig. 8.25, we see that the resolution at all energies has increased (most visibly for the ERs; the NRs change is smaller and obscured somewhat by multi-NRs at low energies); this is expected in the transition from the exact true energies to those subject to energy fluctuations and detector effects. We otherwise recognize the same features we've seen previously. Right: Difference between measured yields and the expected yields–the dashed red line highlighting 0. Both peaks are again slightly low, which is due to off-electrode effects.

Sample	Phonon Efficiency [%]	QS1 Efficiency [%]	QS2 Efficiency [%]
Bulk 356 keV ER	86.12 ± 0.01	96.73 ± 0.01	97.91 ± 0.04
Bulk 1-400 keV ER	86.11 ± 0.002	96.74 ± 0.003	97.85 ± 0.02
Bulk 1-400 keV NR	87.31 ± 0.003	$96.72 \pm .003$	97.85 ± 0.02
Ba-133: Single-Hit	86.11 ± 0.01	$96.75 \pm .02$	97.63 ± 0.03
Ba-133: Multi-Hit	86.10 ± 0.01	$96.70 \pm .01$	97.64 ± 0.02
Cf-252: Single-Hit ER	86.10 ± 0.01	$96.74 \pm .01$	97.73 ± 0.04
Cf-252: Multi-Hit ER	86.11 ± 0.004	$96.69 \pm .01$	97.75 ± 0.02
Cf-252: Single-Hit NR	87.68 ± 0.01	$96.73 \pm .01$	97.77 ± 0.03
Cf-252: Multi-Hit NR	87.76 ± 0.01	$96.69 \pm .01$	97.83 ± 0.03

Table 8.2: Summary of the simulated samples' peak phonon and charge collection efficiencies for events in the SimFiducial volume of the detector after the DMC stage. The phonons have the lowest efficiencies, but this may be due to simulation artifacts; refer to Appendix C for details. QS2 has the highest efficiency peaks, but recall it also has the longest tails to lower energies.

8.4 DMC Collection Efficiency Summary

Table 8.2 summarizes the peak collection efficiencies we observed for each simulated sample at the DMC stage in the SimFiducial region. Recall that we are using the efficiencies first established in the Bulk 356 keV ER sample to calibrate all the DMC energies in this chapter.

From the table we note:

- The phonons both have significantly lower collection efficiencies than charges and differ slightly between ERs and NRs. The former is primarily due to a fixable simulation artifact (see appendix C) and the latter is due to off-electrode effects, which affect NRs less since a smaller proportion of their energy goes into the charge system (though the difference is further exacerbated by the same simulation artifact).

- The QS2 collection efficiencies drop slightly for the calibration sources because more hits occur near the top side of the detectors–which exacerbates off-electrode effects on the bottom side.

In the next chapter we will see further changes to the energies and efficiencies shown here as we put events through reconstruction. First, though, we finish our description of the DetectorSim results by moving from the DMC to DAQSim.

8.5 DAQSim Results

The second part of DetectorSim, DAQSim, makes the DMC output more realistic. The DMC output is noiseless and has meaningful physical units. Unfortunately, the real output from the detectors is not like that: it always has some level of noise and is a digitized representation of circuit activity in unitless ADC counts. DAQSim handles these considerations, turning the DMC output into something that the reconstruction code, CDMSBats, can handle just as it would real data. While doing this for large numbers of events with myriad configurations is not computationally trivial, it is not conceptually very interesting for our purposes here. We show a few examples here for illustration, but will not discuss the results for each sample in detail, as quantitative comparisons are more meaningfully made after the next stage (reconstruction) is done.

Fig. 8.33 shows several example pulses before and after processing in DAQSim. The shapes do not significantly (visibly) change except in the case of digitization of extremely low-energy pulses. Note that every charge and phonon channel is handled individually. The pulse scaling into ADC units here is based on details of the real electronics–doing essentially whatever rescaling CDMSBats will do in reverse–and is also related to the collection efficiencies we identified in the DMC.

DAQSim also handles noise addition, which is done by sampling PSD functions (see chapter 4) of real noise recorded in the Soudan experiment. The results are illustrated in Fig. 8.34.

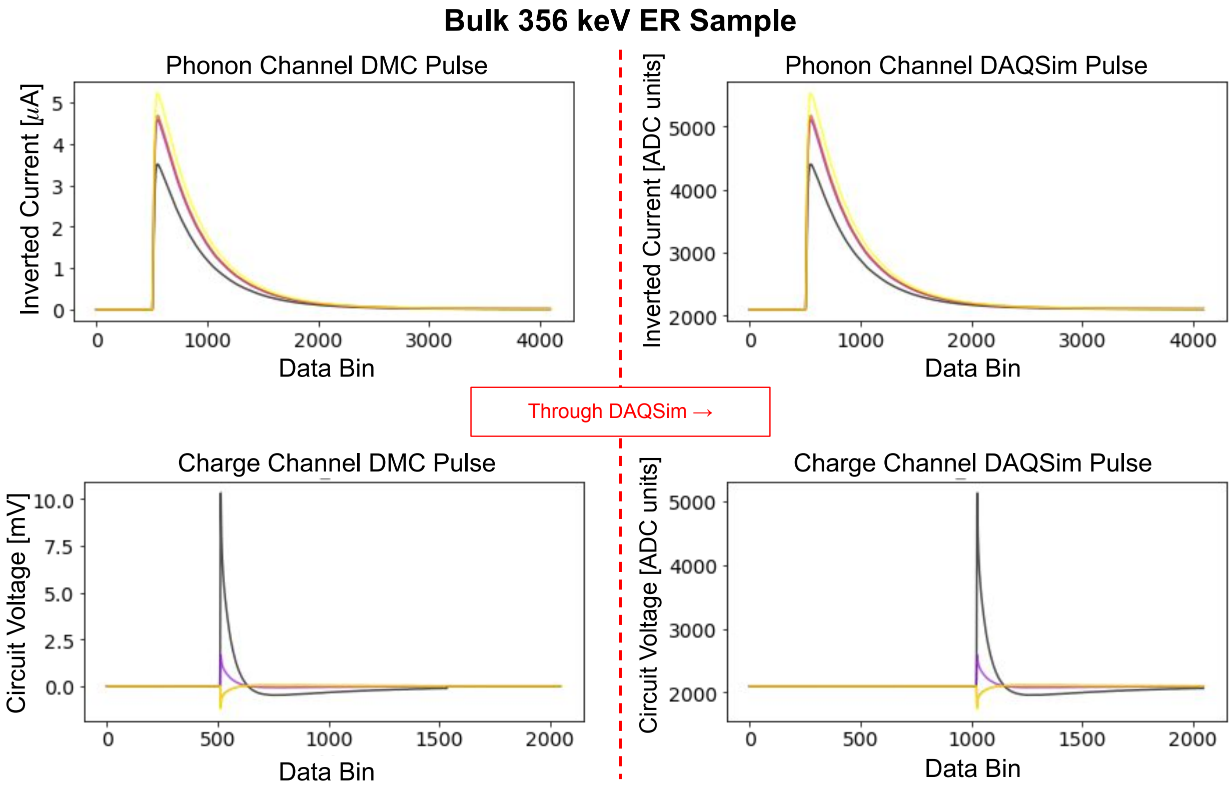

Figure 8.33: This figure shows example pulses from the 356 keV ER sample both as they come out of the DMC and as the final product of DAQSim. The pulses out of the DMC are generally in real units (millivolts or microamps), but DAQSim scales them to be in the more arbitrary units used by the real DAQ's analog-digital-converter–that is, "ADC units". Aside from the digitization (which is too small to see here), the pulse shapes should not change. DAQSim's role is mostly rescaling/calibrating to ADC units so that CDMSBats–which will be operated essentially like normal, as if on real data–can properly convert from ADC units to real units again.

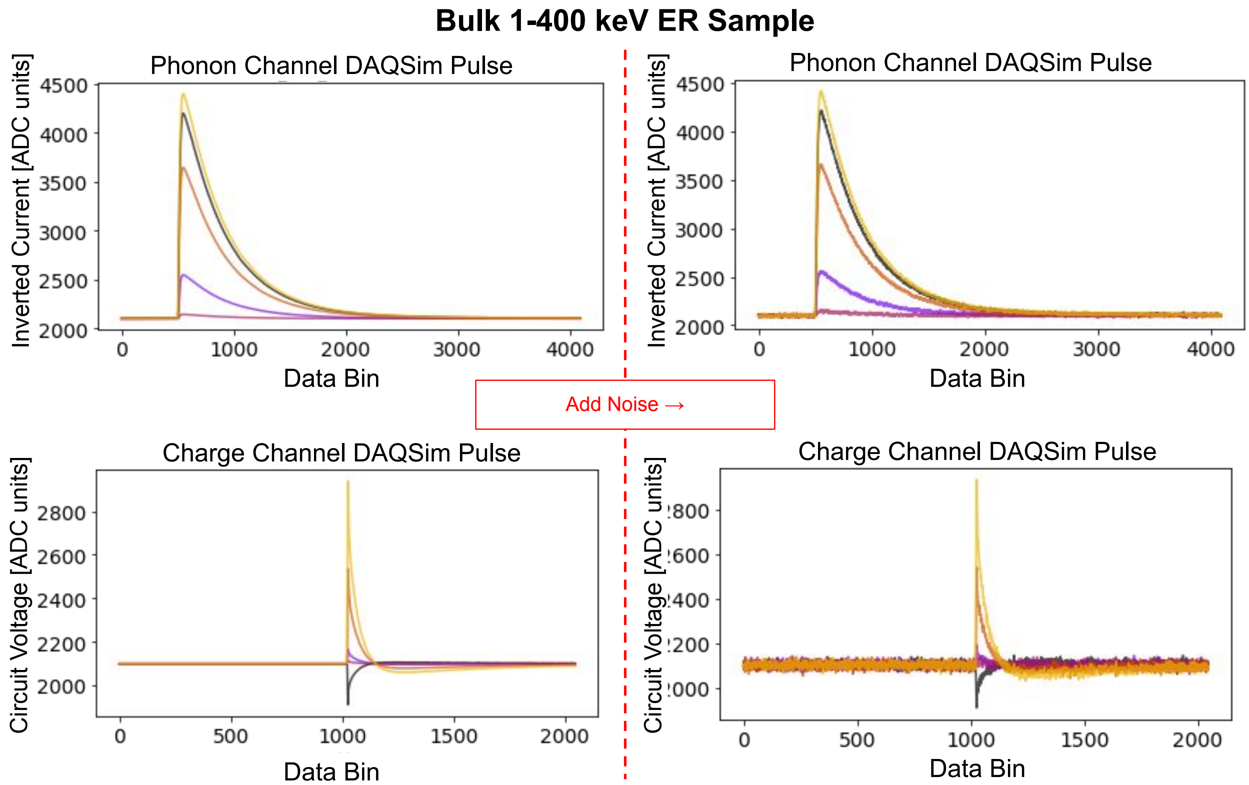

Figure 8.34: This figure shows example pulses with and without noise added. We show this for completeness in tracking our results from DetectorSim to Reconstruction. This noise addition happens in DAQSim and can be turned off, which is useful for studies.

9. RECONSTRUCTION RESULTS

In the previous chapter we studied the simulation results up to the point of detector readout. In this chapter we proceed through the final "reconstruction" stage, in which we apply the optimal filter (see chapter 4) and produce results that will be directly comparable to real data in the next chapter.

As we move to reconstructed data, we're going to switch from SimFiducial to LT Fiducial (see section 4.3.2). While SimFiducial largely selects the events we want, it relies on precise spatial information only available in simulations; LT Fiducial, meanwhile, uses only measured quantities that would exist in the real experiment. We ultimately want LT Fiducial to match SimFiducial–and we'll see that it does in broad strokes, but there is room for improvement–and a particular vulnerability to drastically-mismeasured "semi-fiducial" events.

Otherwise, we are most interested in tracking the energy resolutions and yields of events as they go through reconstruction–though we will also have to spend time studying "semi-fiducial" events, as noted in the previous chapter, since these cause significant mismeasurements. This chapter will look at the same five simulated samples discussed in the previous chapter in the same order, though somewhat more quickly because we find for the most part (i.e. excluding semi-fiducial events) that DAQSim and CDMSBats do not greatly change the results from the DMC (as will be seen in Fig. 9.3, for example). It is expected that they worsen the energy and yield resolutions slightly, but these effects turn out to be negligible (at least, when they are given clean, ideal template pulses from the DMC to start with; more realistic DMC pulses would likely increase CDMSBats' resolution as it tries to reconstruct pulses that don't look like its own templates). For this reason, we will not go into the same level of detail we did for every sample in the previous chapter–instead focusing on what changes we see (see Appendix D for some of the plots not included here). These changes will be due primarily to the switch to LT Fiducial (described next, in section 9.1) and noise addition (described in section 9.2).

9.1 Identifying Well-Measured Reconstructed Events: LT Fiducial

We begin by replacing the SimFiducial cut with LT Fiducial (refer back to its requirements in section 4.3.2) as we move from collected to reconstructed quantities. Recall that SimFiducial requires precise knowledge of hit locations–information that is only available for simulated data. LT Fiducial, meanwhile, uses only information output by CDMSBats, meaning it can be more evenly applied to both real and simulated data (though real data has additional quality cuts that don't apply to simulated data; refer to Table 4.2 for more details).

While LT Fiducial will not have the exact spatial boundaries that SimFiducial did, its cuts were designed to select roughly the same set of events, as we expect events being well-measured to correlate with position. As we are still considering simulated samples, we are able to verify this. Fig 9.1 shows both passing and failing events for LT Fiducial along with SimFiducial for comparison; though the boundaries for each are not quite at the same place, the same trapezoidal shape is preserved.

The differences warrant some discussion, though:

- LT Fiducial has a tighter radial allowance for well-measured events than SimFiducial. This is due to LT Fiducial requiring there be minimal energy in the outer channels (which is the simplest way to avoid edge events in real data) while SimFiducial allows energy in both inner and outer channels.
- Meanwhile the LT Fiducial Z-boundaries, based primarily on charge asymmetry measurements, are slightly looser; the poorly-measured events stop about at the SimFiducial Z-boundaries, but (supposedly) well-measured events extend significantly beyond those.

These differences suggest the official charge asymmetry cut could be made more restrictive[1] (as we don't want face events even if they appear to pass the LT Fiducial criteria) and the outer-channel energy restriction loosened (which need not significantly increase the number of edge events) to

---

[1] Though this depends somewhat on our energy resolutions, which simulations don't have quite right; see next chapter.

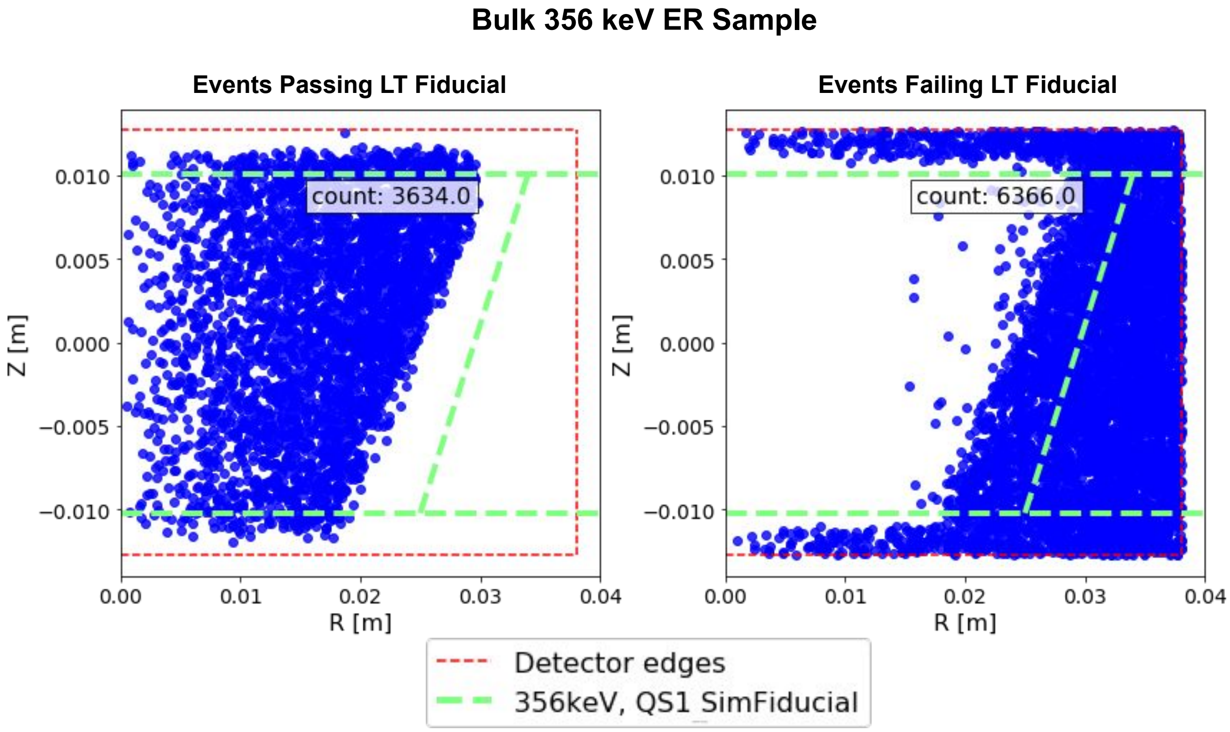

Figure 9.1: This figure shows hit locations for events in the 356 keV ER sample that passed and failed the "LT Fiducial" cut–with the SimFiducial region overlaid to compare the two cuts. Because the cut is based entirely on CDMSBats quantities–that is, quantities that we would have for real data–it can't be informed by exact hit locations. The general shape it outlines is similar to that of SimFiducial, however, which is encouraging.

make LT Fiducial more like SimFiducial. However, we will leave those details to the consideration of future analyses–not modify it here; we'll see in section 9.3.1 that the worst-mismeasured events might be best-handled by an additional cut for multi-hit events anyways.

To summarize, we hoped to see LT Fiducial select the same events as SimFiducial, and it largely does–for this sample of single-hit events. We will see later in section 9.3.1 though, that LTFiducial has also quietly introduced a new vulnerability to certain multi-hit mismeasurements in which some hits are well-measured while others aren't.

9.2 Results From Idealized ER and NR Samples

We start again with the simplest, "Bulk" samples, now comparing the reconstructed energies to the true deposited energies. Again, for brevity we will mostly only show what changes or otherwise new information we see at this stage for each sample; these will mostly be minor resolution changes and a look at the final measured yields for the samples (the calibration samples afterwards will have some some more dramatic effects due to multi-hit events).

Before continuing, we note that DAQSim and CDMSBats have their own built-in calibration procedures–and the details of the former depend on the latter–but we do a final calibration ourselves anyways and so will gloss over the details of the processing-stage-specific calibrations. There are multiple output quantities from CDMSBats (some listed back in Table 4.1, for instance), and exactly which one is calibrated depends on the goals of the analysis and/or the sample used. For our study, we calibrated the CDMSBats phonon measurements as a whole ($ptNF$) and the charge channels individually (all four of them)–each with a single multiplicative scaling factor–such that the difference between them and the corresponding corrected energies from the DMC were minimized. As with the DMC calibrations, we did this for just the Bulk 356 keV ER sample and applied its calibrations to the other simulations, as the Bulk 356 was the simplest to use and using the others did not significantly change the results anyways.

9.2.1 Resolution Effects

First we check how much the resolutions have increased by the end of reconstruction; in this section we will look for changes due to the reconstruction process itself, variations in energy, noise, and/or recoil types. Regarding noise: note that real data always has noise, but to study other effects in simulations we will only include noise for one sample here, which will be noted; the others in this chapter will be noiseless by default (noise will be added back in to the simulated calibration source samples for the next chapter, where we compare to real data).

Fig. 9.2, first, shows the differences between the final reconstructed energies and the true energies deposited originally for the Bulk 356 keV sample (so all the "true" energies are 356 keV exactly). Compare to Fig. 8.9; after processing through DAQSim and CDMSBats we expect similar, if slightly less-precise results, and that is what we have here. The differences are still close to zero and the resolutions (which now include the detector resolutions of the previous chapter along with effects due to DAQSim, reconstruction, and event selection) have only slightly worsened, as expected:

- The phonon and QS1 resolutions have each increased by less than 4%.
- The QS2 resolution, ostensibly, increased by about 18% between Figs. 8.9 and 9.2, but that change is due to event-selection differences between SimFiducial and LT Fiducial, not the reconstruction process (see the summary table 9.1 at the end of this chapter). Much of that, furthermore, is just due to ambiguity in the peak width due to off-electrode effects causing the non-Gaussian shape.

Switching to the 1-400 keV ER sample, Fig 9.3 shows how the energy resolutions change as a function of energy–broken down by simulation stage. We see that for all energies the largest contribution to the final resolutions is from the DMC (or earlier processes); this is encouraging, as we expect the detector response to be the most significant factor and reconstruction and event selection to contribute very little. Otherwise, the resolution still increases with energy, as seen previously.

Next we specifically consider noise, which may be added to simulated data in DAQSim (see section 6.3.2) and is expected to worsen the resolutions (most significantly at low energies). To study the impact on the resolution here, we add noise to the same Bulk 1-400 keV ER sample we're using already. Figs. 9.4 and 9.5 show how noise addition contributes to the resolutions of each simulation stage by comparing the sample processed with and without noise. We see that while including noise increases the resolution introduced by DAQSim and CDMSBats a great deal proportionally at low energies, it does not significantly affect the final reconstructed results, which are still dominated by DMC resolution. For the rest of this chapter we will return to noiseless samples so we can more closely study the differences caused by recoil types or calibration source details.

Finally we check that different recoil types behave similarly in Fig 9.6, which compares the final, reconstructed energy resolutions for the Bulk ER and NR 1-400 keV samples (returning to noiseless samples); we see good agreement for most of their overlapping energy ranges.

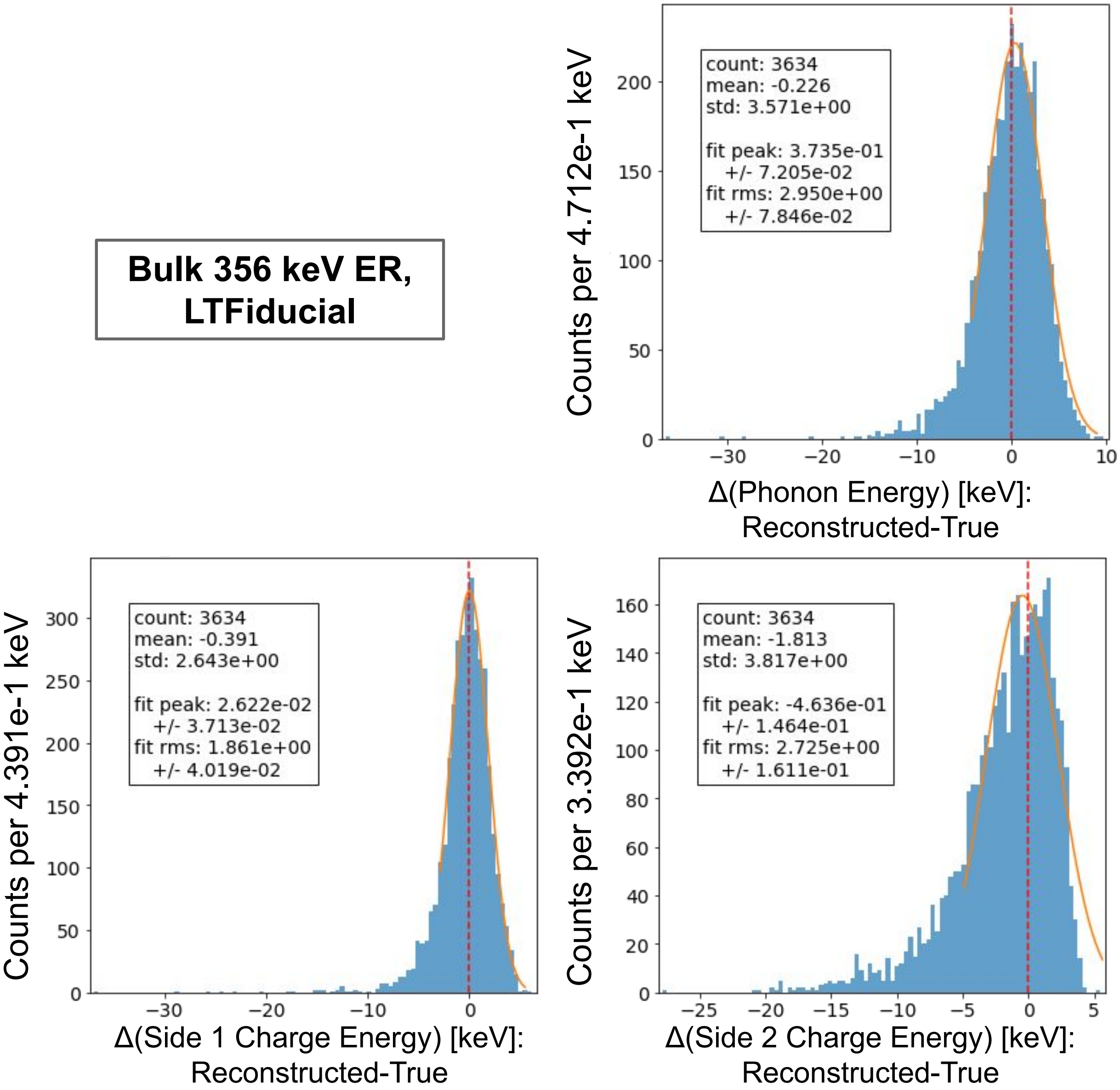

Figure 9.2: This figure shows differences between the true deposited energies from SourceSim and the final reconstructed energies from CDMSBats for the 356 keV ER sample, using the LT Fiducial cuts, as a check how well our final measurements match the original energies. We note the RMS values have increased slightly compared to had using SimFiducial, but otherwise these the final results match the inputs well.

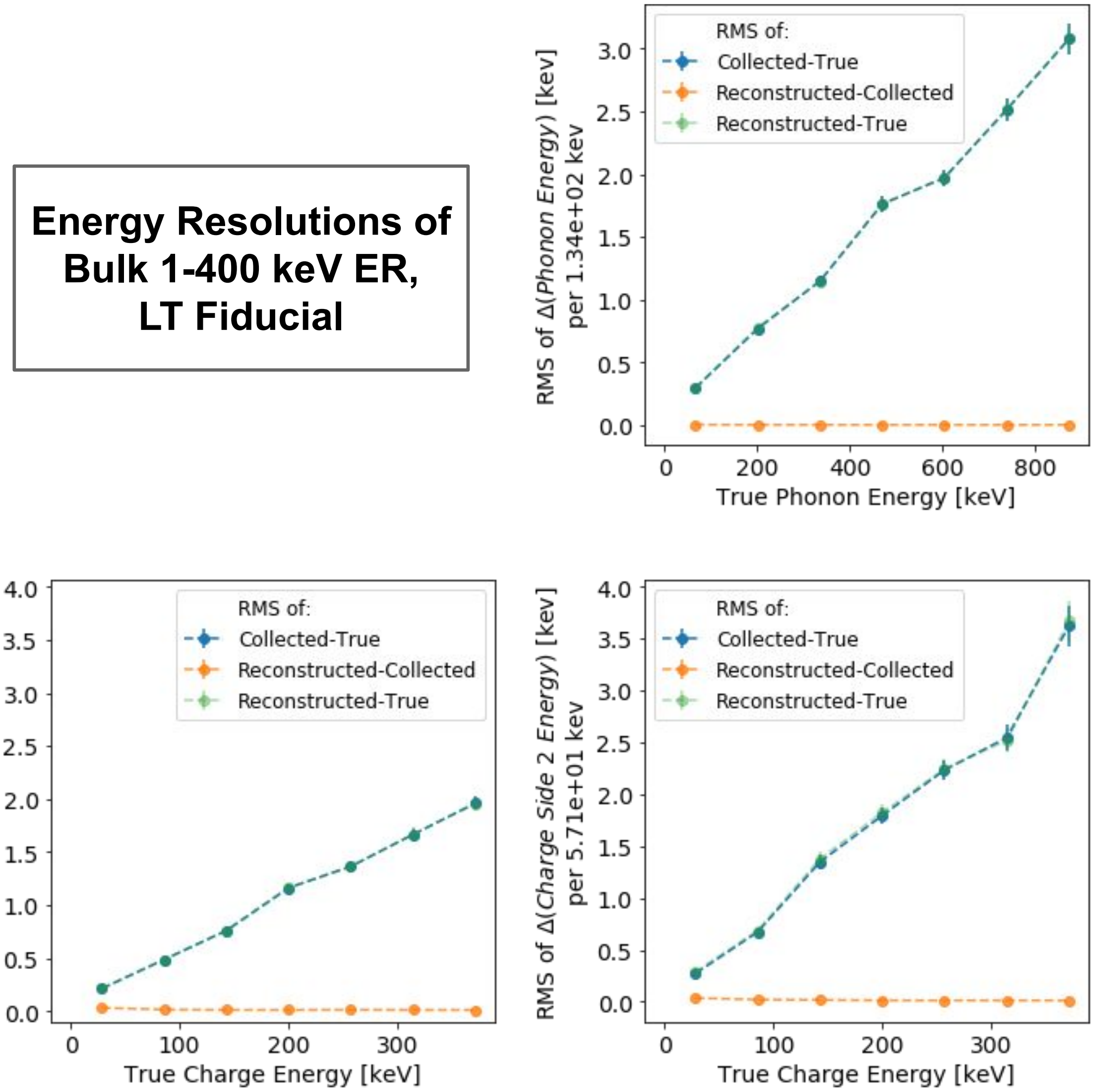

Figure 9.3: This figure shows a breakdown of resolution contributions by simulation stage in the 1-400 keV ER sample. The resolution between true energies and the final, processed energies is almost entirely due to effects in the DMC. The "Reconstructed-Collected" line shows that the resolution contribution from DAQSim and CDMSBats itself is essentially negligible.

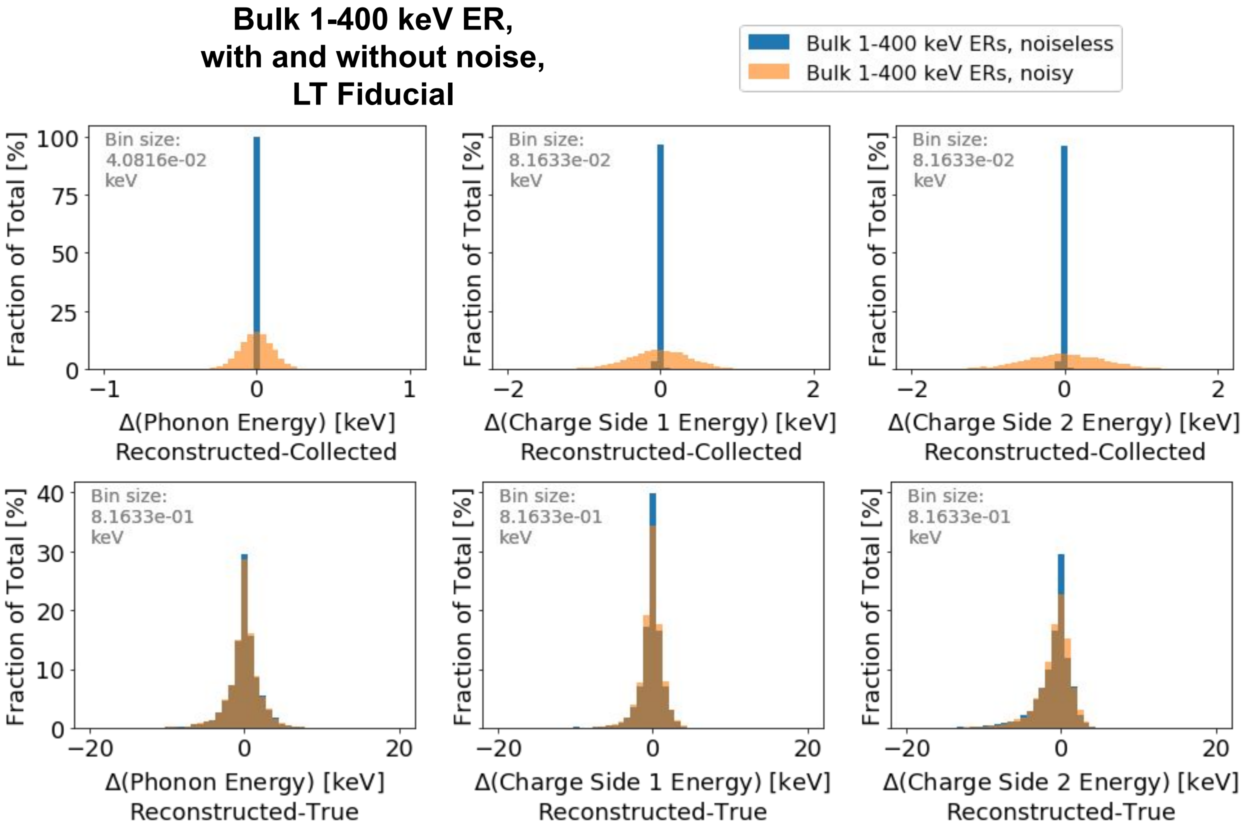

Figure 9.4: This figure shows energy differences between simulation stages for the 1-400 keV ER sample with and without noise, which lets us estimate the contribution noise adds to the final energy resolution. The top row of plots shows the energy differences between the final processed energies and the collected energies–showing essentially the resolution contribution in DAQSim and CDMSBats. Adding noise in DAQSim clearly contributes a much larger spread in energies, proportionally. The final differences between processed and true energies shown in the bottom row, however, show that there is not actually much of a change overall by the end of the simulation chain.

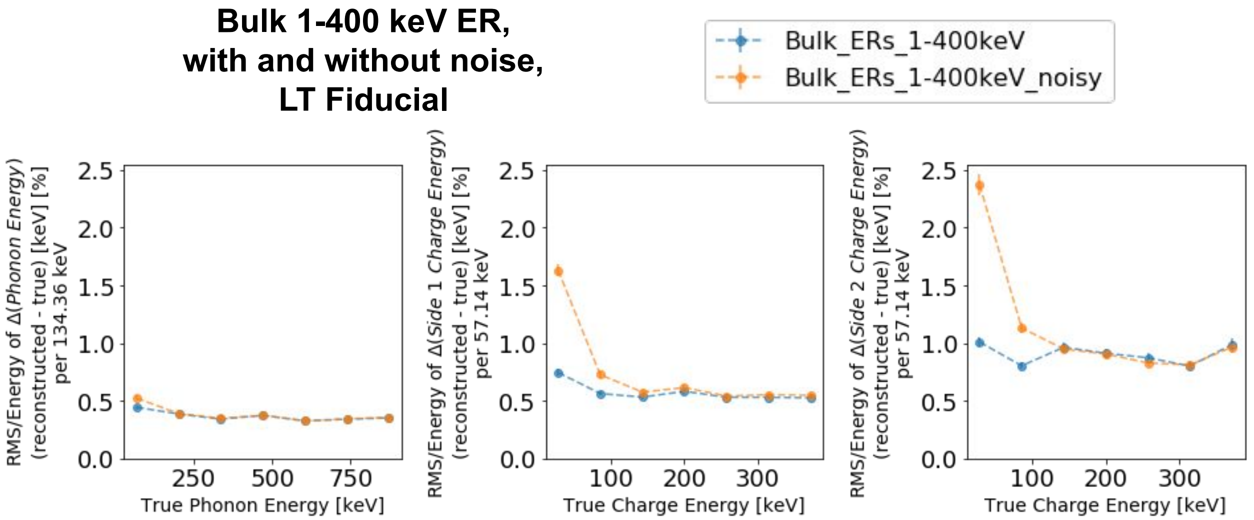

Figure 9.5: This figure shows the final fractional resolutions for the 1-400 keV ER sample both with and without noise, showing how the noise contribution to resolution scales with energy. As expected, adding noise is significant only for lower energies.

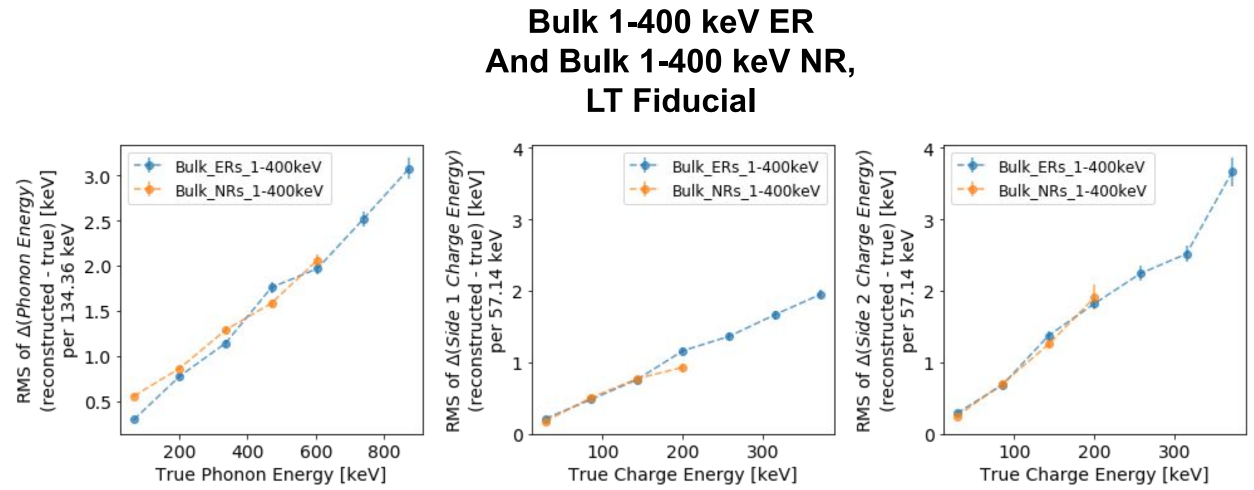

Figure 9.6: This figure shows the final (i.e. from the reconstruction stage–though note we've gone back to noiseless samples) energy resolutions for processed energies in the 1-400 keV ER and NR samples to compare the resolutions as a function of energy between recoil types. Aside from low-energy phonons, the samples agree within uncertainties.

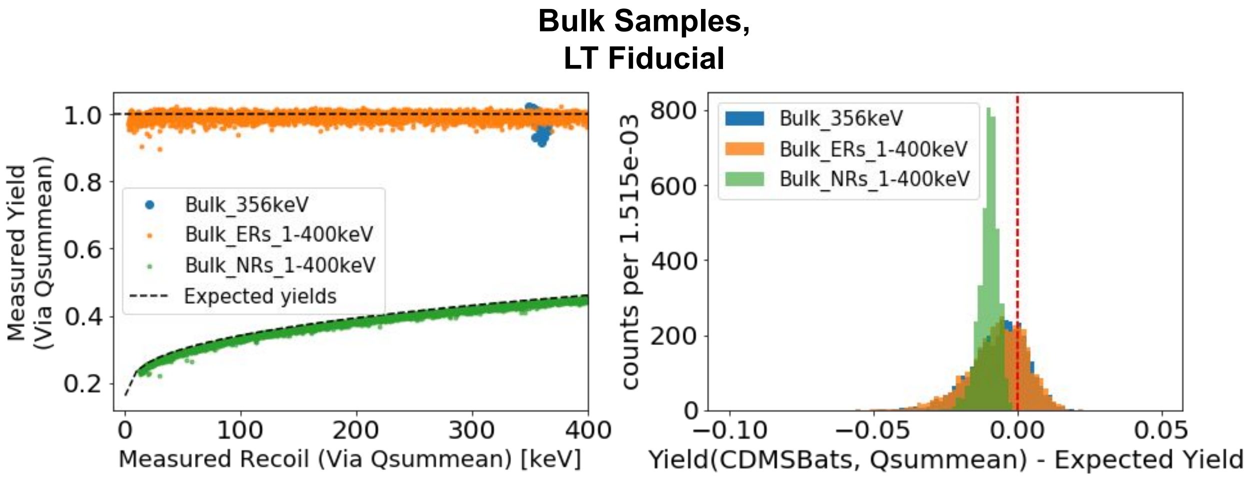

Figure 9.7: This figure shows the reconstructed/calculated yields for our ER and NR samples in two forms to study the similarities and differences between the expected and measured values; compare Fig. 8.17 which showed the same results as calculated with DMC quantities. Left: Measured yield vs. deposited energy. The ER samples are near 1 while the NR sample is around the expected curve. Right: Difference between measured yields and the expected yields. All three samples are a bit low, but mostly for explainable reasons: the NR sample is still being calibrated with ER phonon collection efficiencies and all three samples suffer from low trends in ionizing energy due to charges missing electrodes.

9.2.2 Measured Yields

Rounding out our study of the Bulk samples are the yields shown in Fig 9.7. In broad strokes, the final calculated yields match our expectations from the Lindhard model (and the DMC/SimFiducial results in Fig. 8.17) well: ERs centered at 1 and NRs following a curve below that. All three samples have a mean which is slightly below the expected yields, but it is not significantly worse than what was seen for the DMC/SimFiducial results in the previous chapter, so we again point to off-electrode effect as explanation; refer to the discussion in section 8.2.3.

To summarize our Bulk samples after running through the final, reconstruction sage of the simulation chain and switching from SimFiducial to LT Fiducial:

- With LT Fiducial, events with more extreme Z-values are allowed, but events are also largely restricted to lower R-values. LT Fiducial could benefit by tuning these cuts to be more like SimFiducial, with fewer questionable face events (removing some of the collection efficiency Z-dependency–for QS2 in particular–as well) and more high-radius events that aren't edge events.

- Energy resolutions have increased negligibly since the DMC output–the most significant changes only occurring at low energies when noise is added.
- The final measured yields mostly match the expected yields, but are low due to the same off-electrode effects seen in the previous chapter.

9.3 Results From Ba-133 and Cf-252 Samples

We now return to our two calibration source simulations to see how particles from external sources and multi-hit events affect our reconstructed/LT Fiducial results. In this section, we want to see how well these calibration sources have been reconstructed–the yields in particular. Single-hit events in theory shouldn't look much different than the Bulk samples (except possibly due to different Z-distributions and related effects); we'll see, though, that having multi-hit events that aren't limited to SimFiducial introduces a new way for events to be mismeasured, in the form of "semi-fiducial" events, wherein some hits of an event are well-measured while others are not (refer back to table 3.1). Note that these samples are again noiseless, though we will add noise to them in the next chapter.

9.3.1 Ba-133 Results

The results of reconstruction in the Ba-133 simulation largely look very similar to those seen out of the earlier DMC stage, as were shown in Figs. 8.21 and 8.22 (as such, we won't show all the results here; some are included in Appendix D). What's new are semi-fiducial events and a slight shift in yield.

We first look at the final, reconstructed yields for the Ba-133 sample, shown in Fig 9.8 (along with the Bulk 1-400 keV ER sample for comparison). While the majority of events have yields near 1, as expected, there is one strange outlier near 0.6. This is our first "semi-fiducial" event.

Recall that semi-fiducial events are a form of mismeasurement unique to multi-hit events in LT Fiducial in which some hits within an event are well-measured and others aren't–generally because

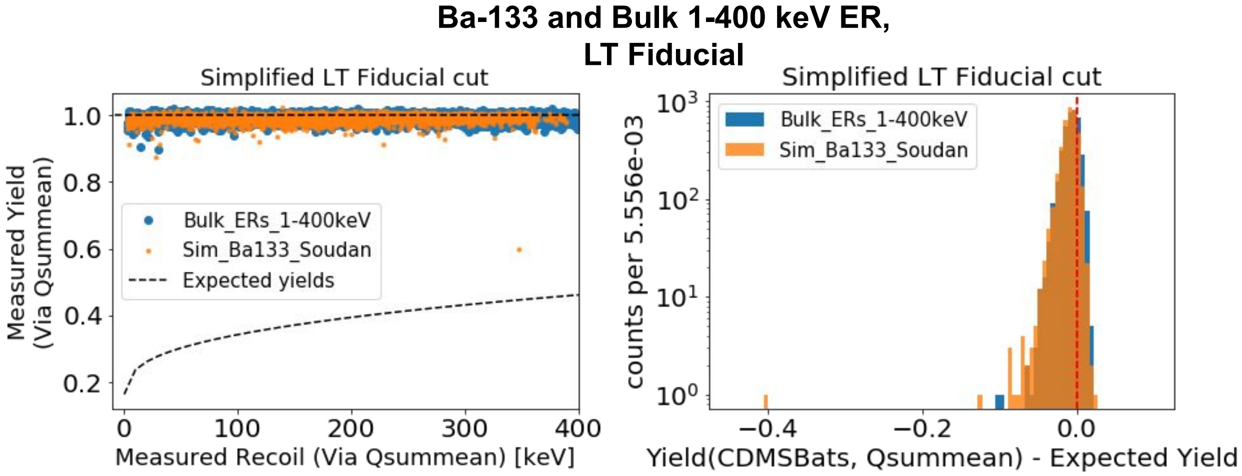

Figure 9.8: This figure shows two plots of the final measured yields (calculated using $qsummean$) for simulated Ba-133 and the Bulk ER sample to check where and how they differ. Left: Both samples have yields around 1, as expected for ERs. Note the single semi-fiducial event with a yield around 0.6. Right: The Ba sample is centered a little lower than the Bulk ER sample due to the Z-distribution of its hits (i.e. worse off-electrode effects for QS2).

some are inside SimFiducial while the others aren't. We see this is the case here in Fig. 9.9, which shows the three hit locations and energies of this event. The event deposited 356 keV total across three hits of 10, 195, and 151 keV, but the 151 keV hit occurred right at the top detector face; the electrons and holes it frees are immediately trapped together and their charge contributions cancel out–meaning the measured charge energies for both QS1 and QS2 are missing that 151 keV (the phonon system is missing energy as well, since the trapped charges don't emit the expected NTL phonons). Because the two charge sides are mismeasured by the same amount (i.e. they are still symmetric) and the two bulk hits provide significant inner-channel energies, the event as a whole passes LT Fiducial–despite the missing energy. It happens to show up particularly low in the yield because the phonons happen to be less mismeasured than the charges are.

The semi-fiducial outlier aside, the Ba-133 and Bulk ER samples agree fairly well, though the Ba-133 yields are centered slightly lower, its tail is a little longer, and its resolution is a bit smaller. The low mean and tail we attribute to Ba-133 having a lower average QS2 collection efficiency (due to the Z_{hit} dependence shown in Fig. 8.7–due, in turn to off-electrode effects); the

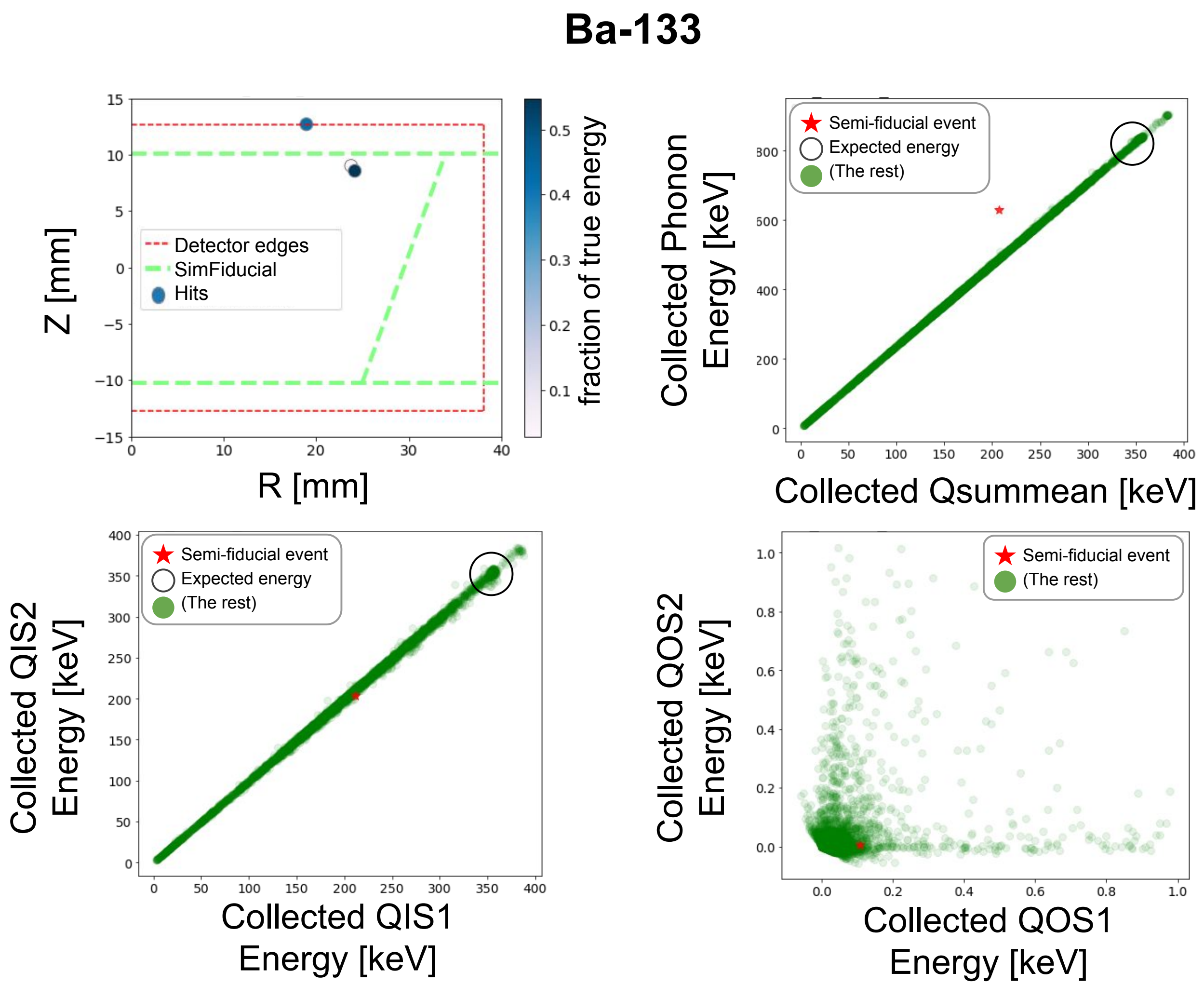

Figure 9.9: This figure shows four views of the single semi-fiducial event in the Ba-133 sample. As shown in the top-left plot, two hits of this event deposit energy in the SimFiducial region and are well-measured (though note we haven't applied the SimFiducial restriction; we only show it as a reminder of where events tend to be well-measured), but one hit in the same event is right at the detector face, where all of its electrons and holes are immediately trapped and their charge contributions cancel out. The top-right plot shows how both charge readings and phonon readings (due to missing NTL phonons) suffer from this. The bottom two plots, however, show that the charge measurements are still symmetric (left) and restricted to inner channels (right), so the criteria of LT Fiducial are nevertheless satisfied.

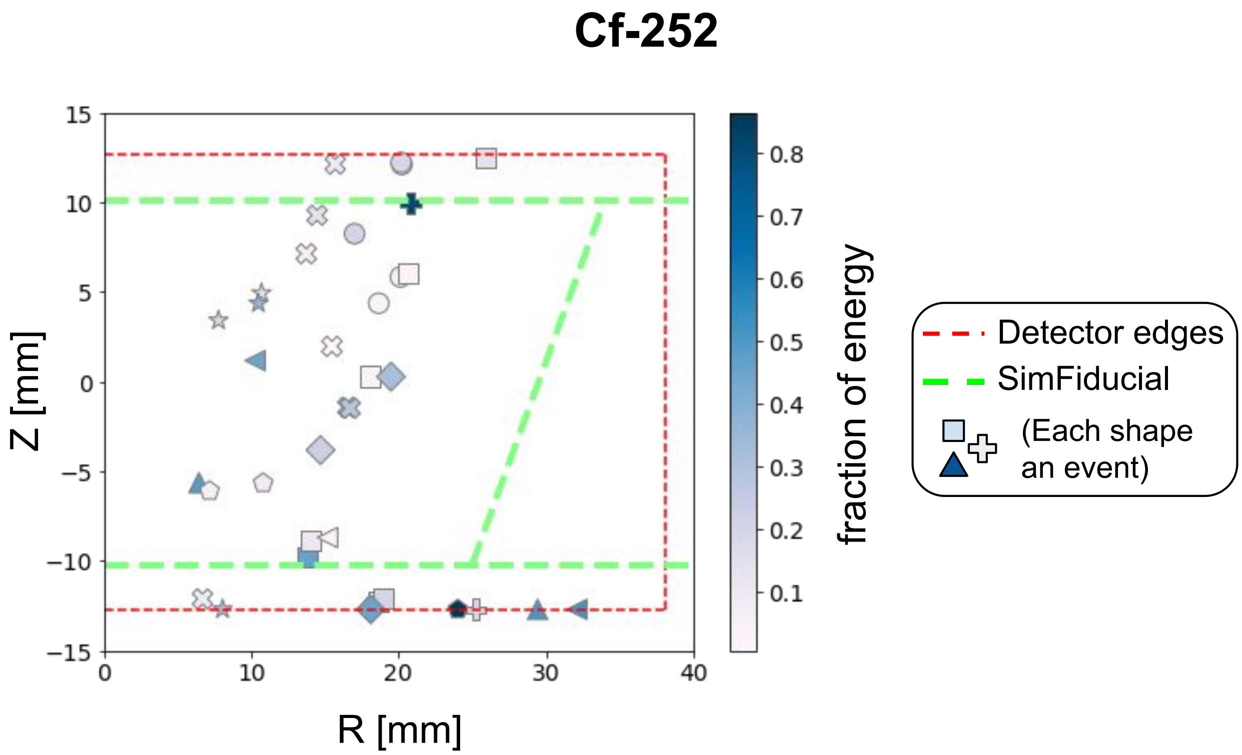

Figure 9.10: This figure shows the same multi-hit LT Fiducial failure mode as in Fig 9.8, but here showing hit distributions for several such events in the Cf-252 sample. We note that this plot has more events than Fig 9.9, partially because the Cf-252 sample has more events than the Ba-133 sample and partially because Cf-252 events average a higher number of hits than those for Ba-133, thus making this form of mismeasurement more likely.

resolution we attribute to simulation artifacts (effect shown in Fig. 8.22 and discussed in appendix C), respectively.

9.3.2 Cf-252 Results

Moving to the Cf-252 sample, the main difference to note since proceeding from DMC to reconstruction and from SimFiducial and LT Fiducial is again the presence of semi-fiducial events. Due to both a larger sample size and higher number of hits per event (due to the neutrons, which may knock out many photons through their multiple interactions; refer back to Fig. 8.24), we see more semi-fiducial events here than we did for Ba-133. Fig 9.10 shows all the hit locations for each of these events (which are all ERs)–and we confirm that they all have significant energies deposited both inside SimFiducial and right at the detector faces.

Fig 9.11 shows the yields for the Cf-252 sample, color-coded by recoil type[2]. The semi-fiducial ER events very clearly stand out–several of them looking very similar to NRs; in fact, past recoil energies of 400 keV, all the events that would be identified as NRs are actually semi-fiducial ERs. The other events with low yield measurements (more than 0.2 below the true yields) all have significant energy deposits outside SimFiducial as well. We are otherwise pleased to see ERs largely centered at 1, NRs following the Lindhard Yield curve below that, multi-NRs with yields no greater than those for single NRs, and the more complicated events with both ER and NR effects showing up in the middle–as was expected based on the original deposited energies in Fig. 8.25. We note that all these yields are again centered slightly lower than they should be (based on the true deposited energies), but they are not notably lower than those for the Bulk samples out of the DMC, so we again point to the causes described in section 9.2.

9.4 Summary

We've now concluded the final stage of the simulation chain; our samples are fully simulated and processed. To conclude both this chapter and the full description of our samples, we will summarize the measurement challenges specific to the reconstruction stage covered in this chapter and also look back at the contributions to the final resolutions of well-measured events across the full simulation chain. In the next chapter, we will compare the final results of the calibration source simulations to real data.

9.4.1 Mismeasured Events

Mismeasurements at the reconstruction stage often mean problems with pulse shapes–that is, deviations from the template shapes that the OF is trying to match. These could be due to pulse saturation, pileup events, or (in the case of real data) glitches of various kinds–but our simulations do not suffer from most of these[3]. In this chapter, though, we instead identified a way for events to

---

[2] The recoil type list here is slightly simplified from the full list covered in Chs. 3 and 7; the information required for complete and precise identification takes up significant computing resources that are not feasible to apply to all samples.

[3] Saturation is handled by cuts (as it is in real data), pileups can't happen when events are simulated individually, and glitches aren't simulated. Our particular samples have also excluded most pulse pathologies by using TESSim and FETSim templates, as was noted at the end of section 8.1.1.

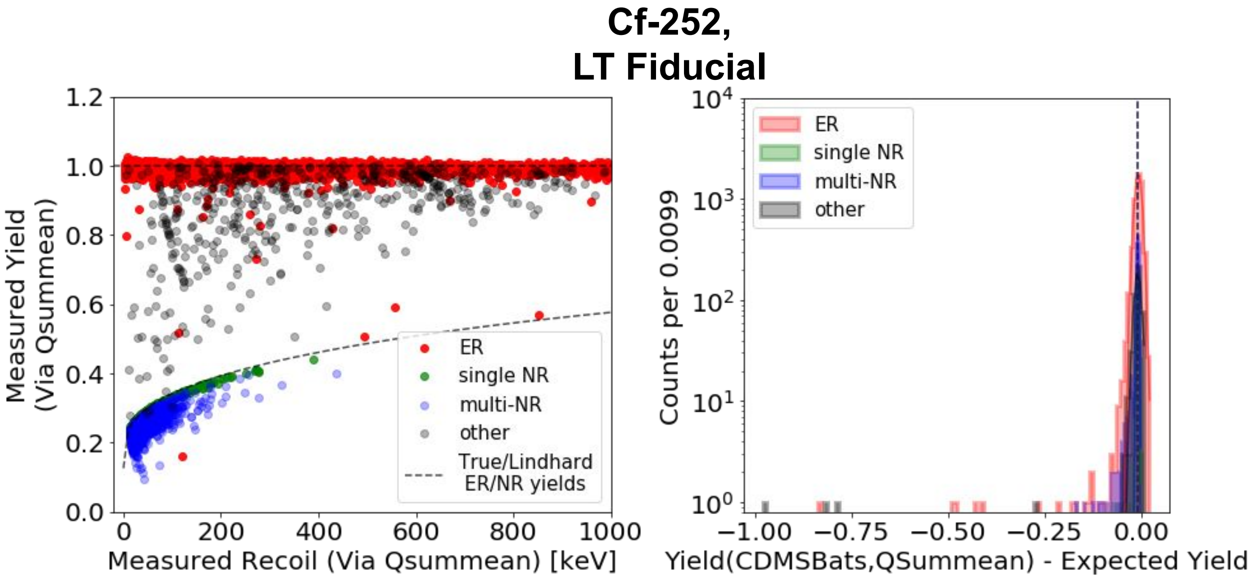

Figure 9.11: This figure shows two plots of the final measured yields for simulated Cf-252, color-coded by recoil type. At left is the yield as a function of measured recoil energy, in which we see simple ERs and NRs mostly along the expected lines, though they have some low mismeasurements–ERs in particular. The more complicated recoil types again show up between and below the simple recoils. The histogram of yield differences on the right shows that the worst mismeasurements are from ERs and "other," more complicated recoils, though most of them are centered near zero.

be mismeasured during reconstruction even if the pulses are well-formed: "semi-fiducial" events, in which the problem stems from the spatial distribution of hits in an event (and our LT Fiducial criteria) rather than a failure in reconstruction itself.

Because these are simulations, we can see that semi-fiducial events have hits both inside and outside the fiducial region–but there is currently no reliable way to identify such a problem in real data, where there is no exact position information. In real Cf-252 data, the lowest-yield ER events of Fig. 9.11 would simply be identified as NRs. This would be more of a problem for calibration source data than WIMP-search data–since the latter doesn't have as many high-energy particles that could interact multiple times in a single detector (and WIMPs themselves interact too rarely to have more than one hit). Nevertheless, future studies of these events in simulations will hopefully determine a way to identify them in all real data.

	Contribution to Resolution [keV]		
Readout & Cut	DMC-True	CDMSBats-DMC	CDMSBats-True
QS1 SimFiducial	1.81 ± 0.04	1.25 ± 0.02 ($\times 10^{-2}$)	1.81 ± 0.05
QS1 LT Fiducial	1.86 ± 0.04	1.25 ± 0.02 ($\times 10^{-2}$)	1.86 ± 0.04
QS2 SimFiducial	2.32 ± 0.17	$1.32 \pm .03$ ($\times 10^{-2}$)	2.31 ± 0.17
QS2 LT Fiducial	2.73 ± 0.16	$1.32 \pm .03(\times 10^{-2})$	2.73 ± 0.16
Phonons SimFiducial	2.86 ± 0.05	$1.76 \pm .02(\times 10^{-3})$	2.85 ± 0.05
Phonons LT Fiducial	2.95 ± 0.08	$1.76 \pm .02(\times 10^{-3})$	2.95 ± 0.08

Table 9.1: This table summarizes the resolution contributions from our three main simulation stages for the 356 keV ER sample–broken down by cut and readout. Each column reports the RMS of the energy differences between the two stages listed at the top. We see that the largest contributions to the total resolution ("CDMSBats-True" column) are from the detector measurements ("DMC-True" columnn) and that the reconstruction algorithms add very little ("CDMSBats-DMC" column).

9.4.2 Summary of the Contributions to the Energy Resolution

Now that we've reached the end of the simulation chain, we can look back at which stages contributed the most to the final energy resolutions of well-measured events. This is summarized for the Bulk 356 keV sample (to focus just on the simulation machinery instead of physics effects) in Table 9.1. We see, again, that essentially all of the resolution comes from the DMC. We otherwise note that the LT Fiducial cut has larger resolutions than SimFiducial did; we believe this is generally due to LT Fiducial allowing in more face events, which would be even more of a concern for the sample with multi-hit, semi-fiducial events.

10. COMPARING DATA FROM REAL AND SIMULATED CALIBRATION SOURCES

In this chapter we compare our simulated data for calibration sources to that for real data, now that the former has been through all the same processing as the latter. We've seen already that simulations can produce the appropriate energies (e.g. the 356 keV peak in Ba-133), but here we will see how well the energy resolutions and measured yields match those of real data. We'll do this in two broad passes–first a general, more qualitative look, then a more specific one focusing mostly on the differences seen in the more-complicated NRs. Keep in mind meanwhile, however, that the goal of Cf-252 calibrations–from which we get those more-complicated NRs–is to see what WIMP-like single-NRs should be like in data.

Note that in this chapter we're using the same simulated calibration source samples as in the previous two chapters, but now we've added noise. We largely skipped noise in the previous chapters in order to focus on how the machinery of each simulation stage contributed to the overall resolutions, but it is more appropriate to include it when comparing to real data–which obviously cannot be noiseless.

10.1 Qualitative Comparisons

We begin with a broad look at the Ba-133 and Cf-252 samples to see what large-scale differences there may be. Recall that the simulated data has been cut down to events passing the LT Fiducial criteria and note that the real data has additional cuts of its own (LT Fiducial criteria plus others that cover hardware failures, excessive environmental backgrounds, etc); refer back to Table 4.2 and its references.

10.1.1 Ba-133 Photon Source

Fig. 10.1 shows the reconstructed phonon and charge energies of the real and simulated Ba-133 samples (though note that we have calibrated both samples separately so the 356 keV peaks in each of $ptNF$, $qi1OF$, and $qi2OF$ appear in the correct place[1]). We see general agreement, but

---

[1] More specifically, the simulated data is calibrated the same as it was in the previous chapter–that is, using channel calibrations that minimize the difference between collected and reconstructed data. The real data is calibrated by

two main differences:

- The resolutions of the simulated sample are better (smaller) than those for the real sample. This is not new (see, e.g. Ref. [34]; this is typical for many experiments) but nevertheless something we still want to improve on for future simulations and will discuss more later.

- The Compton peaks are higher in the simulated sample. It is suspected, though, that these particular simulated samples were run with a sub-optimal physics configuration[2] that might account for the difference. We will not discuss this further here; while it's not ideal, it shouldn't affect our conclusions.

Next we take a closer look at the resolutions around the 356 keV peak. Fig. 10.2 zooms-in on the charge and phonon peaks for both Ba-133 samples and also the Bulk 356 keV sample, to get a sense of this single peak's behavior. We see that for both phonons and charges, the simulated resolutions–summarized in Table 10.1–are less than half as wide as the real resolutions, as quantified by the RMS of Gaussian fits to the peaks. We have three potential causes (not mutually-exclusive) in mind:

- There are several potential sources of energy loss that are not simulated. Some of these were mentioned in section 3.3.3; otherwise see refs. [17] and [40] for more. Adding in these more realistic opportunities for energy loss would likely increase our simulated resolutions.

- Second, recall there are two options for modeling pulses in the DMC: either getting shapes from templates (like those used in reconstruction) or by solving differential equations informed by the actual hardware and physics[3]. These samples used the former option–the templates–which may have resulted in "too-perfect" pulses that are reconstructed too easily. Switching to an ODE solver (which is already coded but still needs tuning and validation) would likely make them more realistic.

---

rescaling its energies (charge channels individually, but phonon channels all together in $ptNF$) such that its peaks at 303, 356, and 384 keV are in the right place (we will do something similar for Cf-252). Doing the same for simulated data has negligible effect.

[2] Different electromagnetic physics lists, in Geant4 terms. See options 0 and 4 in Ref. [77].

[3] Refer back to section 6.3.1 for a broader DMC description.

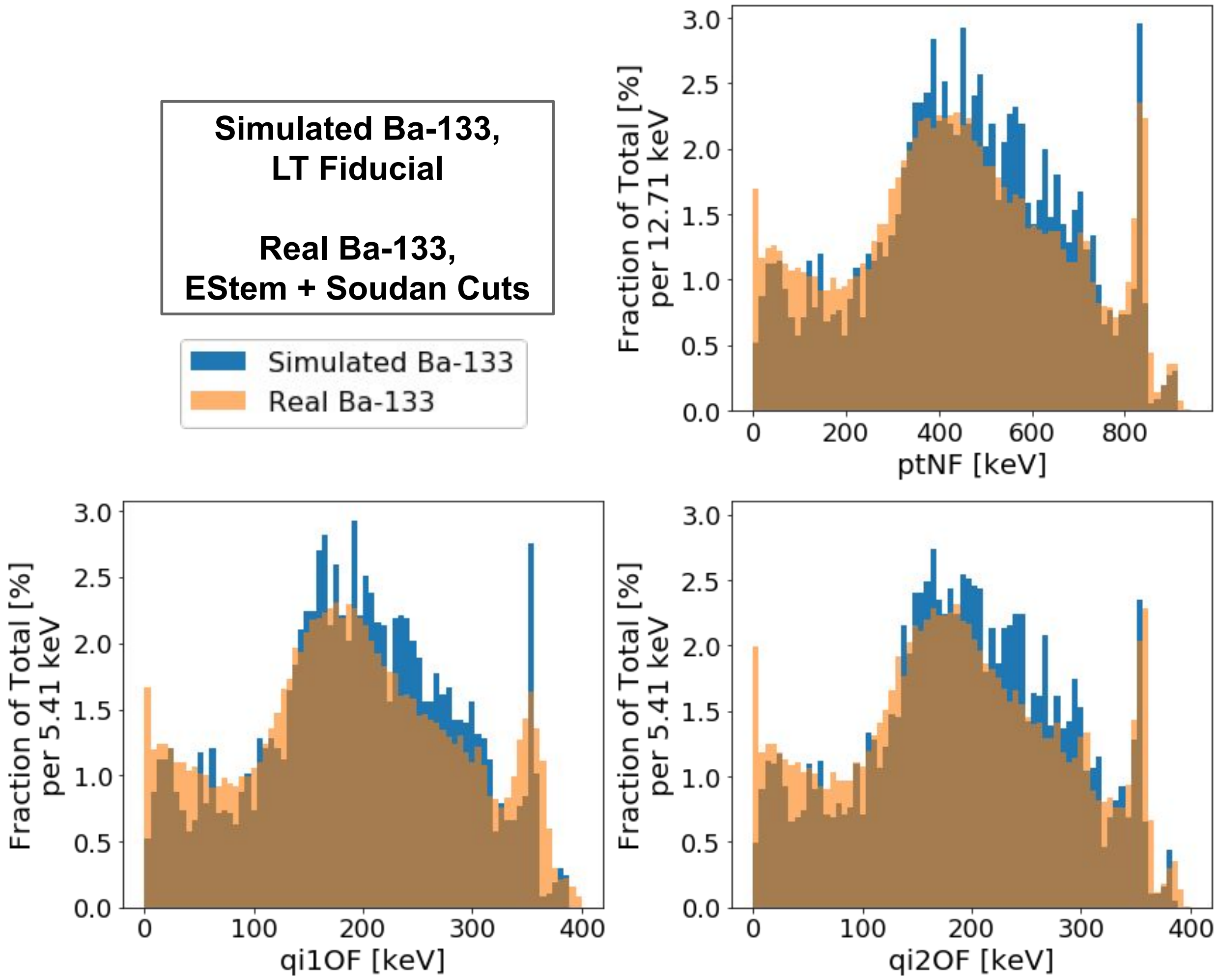

Figure 10.1: This figure shows the phonon and charge energies for both real Ba-133 data and our simulation. They match in broad strokes: the same calibration and Compton peaks are visible in both. However, the real data has larger resolution overall, has fewer events in the Compton peak, and trends slightly towards lower energies.

- Third–counterpoint to the previous option–it's possible that the real data's resolution is too high due to CDMSBats overlooking useful information in the pulses it reconstructs. Variations of reconstruction used in other running modes[27] are already able to reach better resolutions by combining multiple pulse templates in reconstruction to better-match real pulses; it may be that reconstruction of iZIP data would benefit by doing something similar. Future, more realistic simulations will help determine if this is the case.

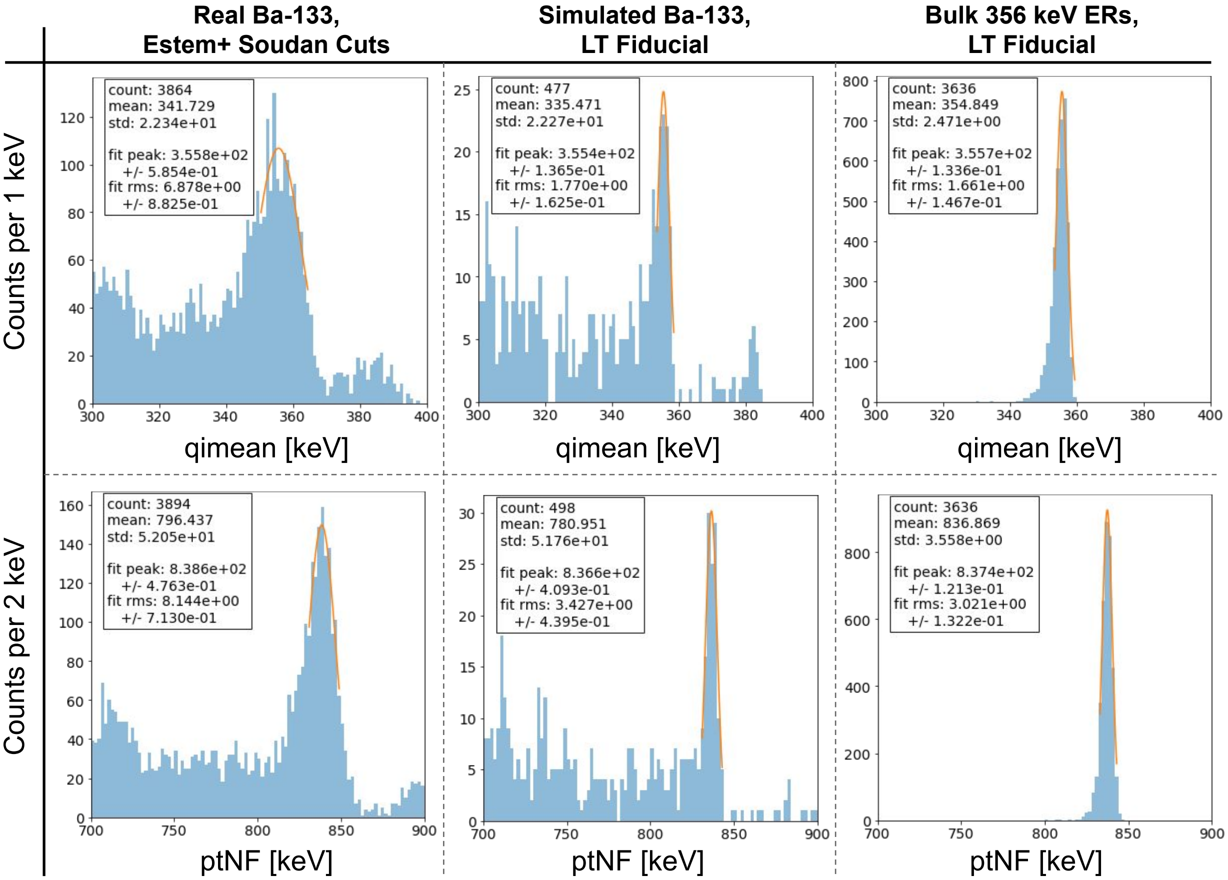

Figure 10.2: This figure shows the same data from Fig 10.1 and data from the simulated 356 keV ER sample as well–here focusing on the 356 keV peak itself (or the 837 keV peak for phonons, which includes NTL energies). The energy resolution (as given by the RMS of Gaussian fits to the peaks) in simulations are less than half those for real data. Potential causes for this and the Compton peak differences seen in the previous figure are discussed in the text.

"356 keV" Peak Resolutions		
	ptNF [keV]	qimean [keV]
Real Ba-133	8.1 ± 0.7	6.9 ± 0.9
Simulated Ba-133	3.4 ± 0.4	1.8 ± 0.2
Simulated Bulk 356 keV	3.0 ± 0.1	1.7 ± 0.1

Table 10.1: This table summarizes the resolutions of the 356 keV peak (or 837 keV peak for phonons) from Fig 10.2. We see the simulated samples have significantly lower resolutions than the real data does.

In Fig. 10.3 we have proceeded to the measured yields (as constructed with $ptNF$ and $qimean$) as a function of measured recoil energy (calculated via the same). Both the real and simulated data are centered generally about 1, as expected, but again the simulated data has notably smaller resolution. The mean of the simulated data is also slightly low–again due to the effects first noted in section 8.2.3–but nearly constant. The real data's mean, on the other hand, trends high at lower recoil energies (ignoring the very lowest energies, where calculations are volatile due to noise) and then crosses low for energies past about 200 keV. This trend in the real data suggests some additional, energy-based calibration may have been warranted, but we won't re-implement such a thing here.

10.1.2 Cf-252 Neutron Source

Cf-252 does not have an expected, reliable, easily-distinguishable energy peak (like 356 keV in Ba-133)[4] that we can use for calibration or resolution-checking. To calibrate this real data, we make due with the broad peak around 200 keV in the charge energies (with which we don't associate any particular, singular physical process)–rescaling the real charge channels to match those peaks and then rescaling $ptNF$ such the the ER yields are centered at 1. Fig 10.4 shows the resulting reconstructed recoil energies–in which we see that the $ptNF$ peak around 500 keV matches up between real and simulated data–confirming that our calibration worked well. While

---

[4] In theory we could use the 511 keV annihilation peak noted in Fig. 7.6, but it does not stand out consistently enough.

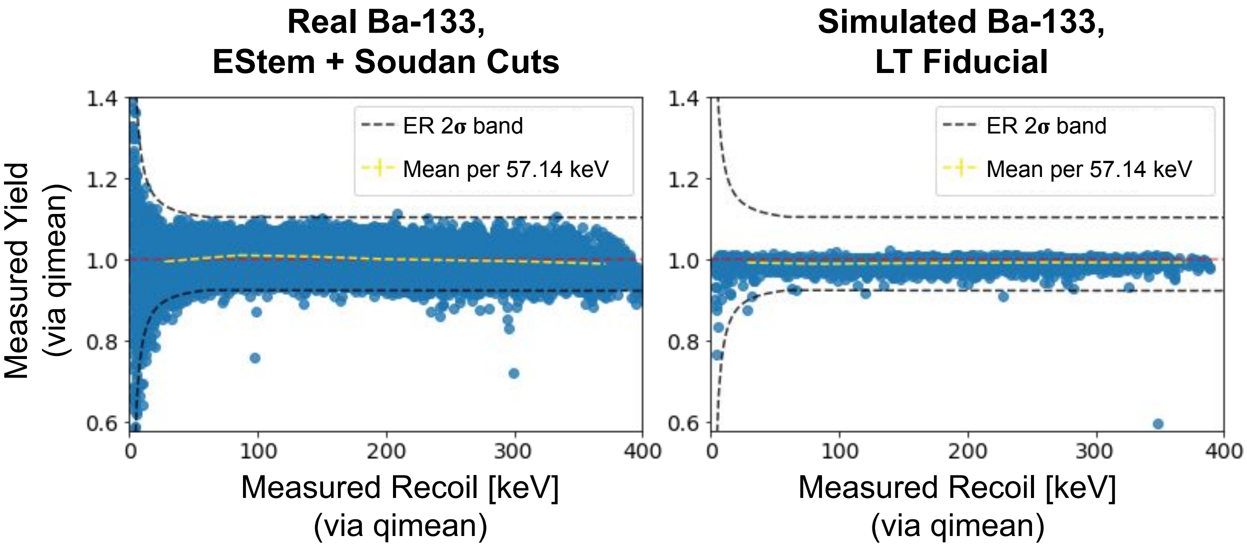

Figure 10.3: This figure shows the measured yields as a function of measured recoil energy for simulated and real Ba-133 data (left and right, respectively). The black dashed lines show 2σ from the means as identified in a previous Soudan analysis [25], the red dashed lines show the expected value of 1, and the yellow dashed line shows the mean of the data. The yields are clustered around 1, as they should be for ERs, though further calibration could center them better and there is variation across the energy bins. The lower resolutions in simulated data are visible here as well.

we don't have any particular peaks we want to check, we do note that the real data seems to trend lower than the simulated data. This may be due to the sub-optimal physics configuration we noted when discussing Ba-133's Compton peak, or possibly from photons that are not simulated[5].

More interesting to us are the yields, shown for the ER band region in Fig 10.5. These look similar to the Ba-133 yields of Fig. 10.3: both samples centered generally around 1, simulated data with a lower resolution and slightly low-but-constant mean yield, and real data with a mean yield trending from high to low as the energy increases. We do see some more outlying events below the main ER bands that weren't present in the Ba samples, though (see Fig. 5.10 for the full distribution). These lower-yield events are expected to be from events involving neutron interactions in the detector (e.g. quasielastics, neutron captures, and inelastics, per chapters 3 or 7), which we

---

[5] Recall these would include prompt fission photons, prompt alpha decay photons, and some combination of subsequent effects in an aged source. As noted in section 8.3 and Appendix B, though, most of those are blocked and/or not useful. If they do come through in the real sample, our simulation results would simply have a smaller ratio of ERs to NRs, but this is not something we use here anyways.

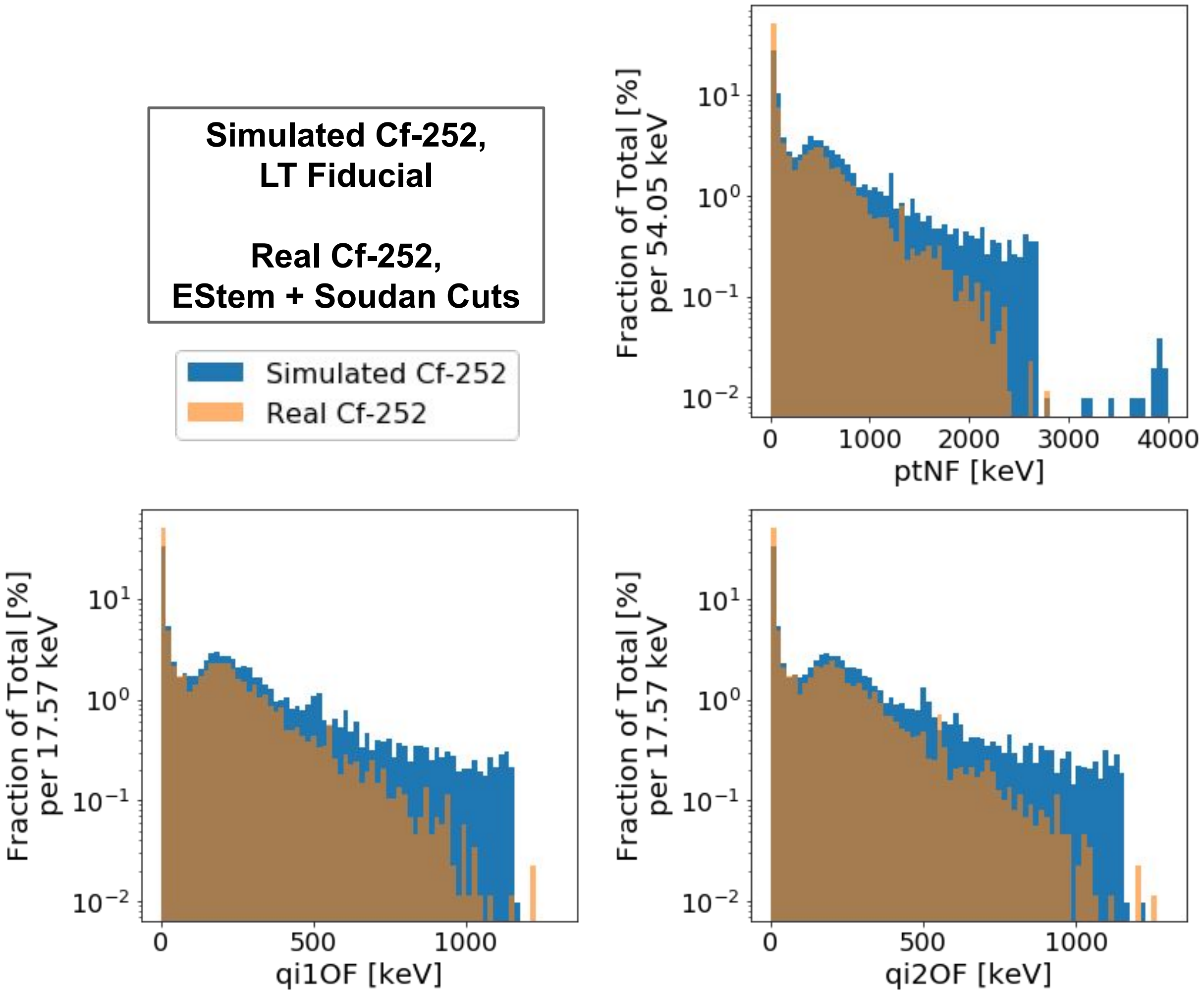

Figure 10.4: This figure shows phonon and charge energies for both real Cf-252 data and our simulation. The same features are present in each, but the real data trends towards lower-energy events than the simulated data, which is discussed in the text. Note the y-axis is log-scaled so the higher-energy bins are visible.

could have removed in the simulated data here (since we know exactly what kind of recoil each event is) but did not, since we can't do the same for the real data.

Next, Fig. 10.6 shows the NR yield band for the Cf-252 samples. Again the broad strokes match (between expectations, real data, and simulated data) but the simulated data averages a bit low, as seen previously. Note that the simulated data also has clear single-hit and multi-hit sections–which is likely also the case for real data, though we can't color-code real events to verify.

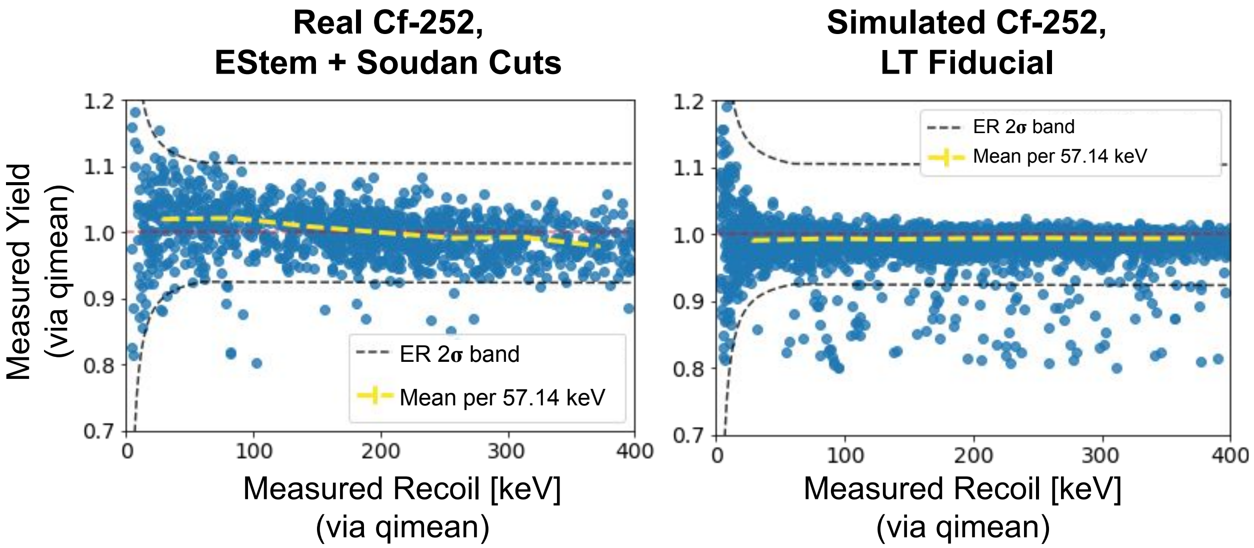

Figure 10.5: This figure shows the ER band of the yields for real and simulated Cf-252 data. Note that we've simply selected events with yields above 0.8, as we can't verify the true recoil types for real data. The yields are clustered around 1, as they should be for ERs, though further calibration could center them better and there is variation across the energy bins. Note that the red and black dashed lines are the same as those shown in Fig 10.3.

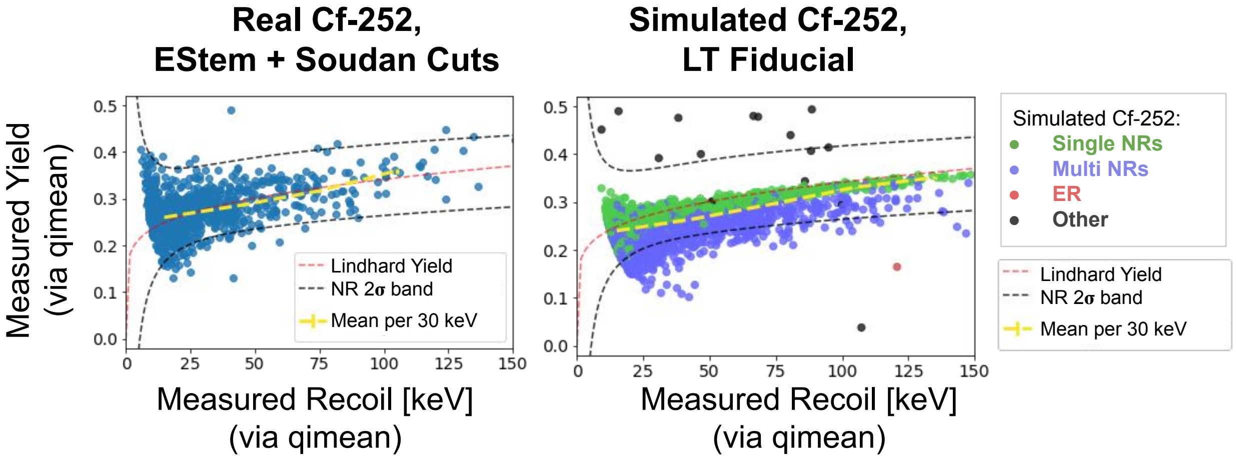

Figure 10.6: This figure shows the NR band of yields for real and simulated Cf-252 data, the latter now color-coded by recoil type; here we show all events with yields below 0.5. The red and black dashed lines again indicate the expected values and 2σ from the means, now for the NR band; the yellow line again shows the mean of the data. The simulated data is consistently low, which we saw for ERs as well, but the lower collection efficiencies of NRs contribute as well. Otherwise we note that multi-NRs (blue) are consistently measured lower than single NRs.

In short, the simulated and real data match generally, but there are specific differences (in means and resolutions) that we want to try to account for.

10.2 Identifying and Accounting For Mean and RMS Differences in the Yield

In this section we focus on the differences between the real and simulated data and try to determine what physical or simulation-specific processes might be causing them.

10.2.1 Means, RMSs, and Resolutions

We begin with Fig. 10.7, which shows the means and RMSs of the ER yields as a function of recoil energy for all four calibration source samples (Ba-133 and Cf-252, real and simulated). Note that we mean to distinguish here between the "RMS" as a mathematical concept and the "resolution" as a physics/measurement concept. As seen in the previous sections, the simulated yields are fairly constant but low while the real means have some energy dependence. We have described some reasons the simulated means might be low–and we will try to mitigate these in the next section–but we do not plan on trying to match the energy-dependent behavior, which may just indicate the need for more detailed calibration procedures in the real data.

The ER yield resolutions, meanwhile, do show similar trends between real and simulated data–all four samples showing asymptotically-decreasing resolution as recoil energies increase, as expected. The simulations are consistently lower than the real data, though. Fig. 10.8 shows the differences (in quadrature) between the real and simulated samples, for both Ba-133 and Cf-252. We find that the differences are essentially constant across energies (diverging the most at the lowest energies, where measurements are the most volatile–especially for charge) and essentially the same between the two calibration sources. Given this, we note the average difference of 0.0305 for use later.

Moving to the NR band of Cf-252, Fig. 10.9 again shows the real and simulated means and RMSs. As before, we see the simulations are lower in both–but perhaps not unreasonably so (as we'll see in the next section).

In Fig. 10.10 we briefly look at how multi-NR events contribute to the yields we observe in

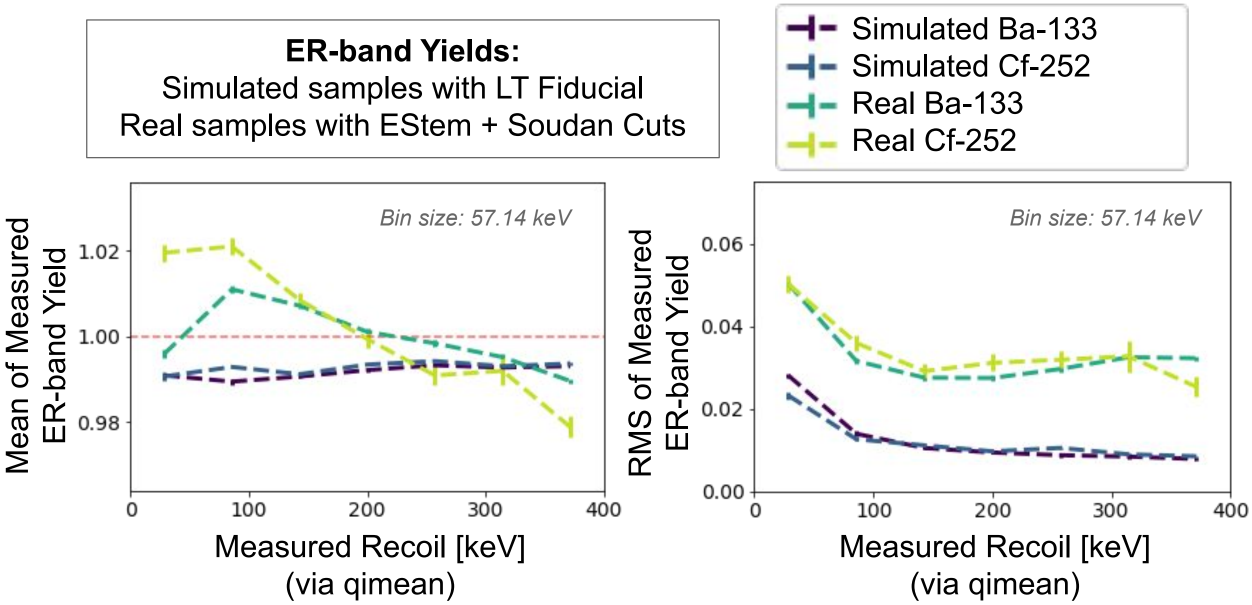

Figure 10.7: This figure shows the means and resolutions of the ER yields for real and simulated Ba-133 and Cf-252; these were previously shown in Figs 10.3,10.5, and 10.6, but we summarize here. The plot on the left shows the yield means for the four samples. The real data has a downward trend not present in simulated data, suggesting the former may need some additional calibration. The simulated data, meanwhile, is flat across but consistently low for reasons discussed previously. The plot to the right shows the RMSs of the yields, in which we see real and simulated data have the same energy dependence, but a different offset–simulations being consistently low.

the simulation. As seen in previous plots (e.g. Fig. 10.6), the multi-NRs have yields below the normal NRs, thus causing the overall NR band–which in real data cannot be broken into single-NR and multi-NR components to see this–to trend below the expected Lindhard Yield. However, they drive up the overall RMS–both because they themselves have greater resolution than single-NRs, and also because they are simply offset slightly (but not far enough to be separately distinguished); in the energy range of Fig. 10.10, for example, the single-NRs have an RMS of 0.014 while the full sample has an RMS of 0.023. Multi-NRs make up about half of all NRs throughout the energy range we're considering (though we don't have such a measurement from real data for comparison) so these effects should be relevant at all energies. To be clear, this occurs even without any particular mismeasurements or shortcomings in the simulation or experimental setup (our inability to distinguish individual hits occurring at the same time aside). For both real and

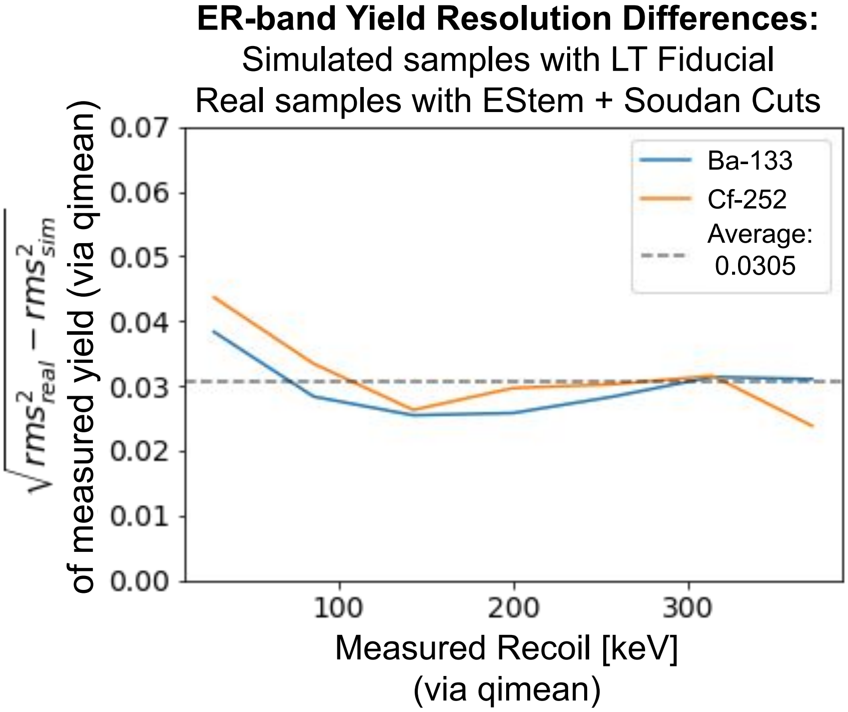

Figure 10.8: This figure shows the differences in quadrature between the ER band resolutions of real and simulated Ba and Cf data (from the right side of Fig 10.7) to estimate what resolution contributions are "missing" from the simulated sample. We see that the difference is energy-independent–diverging the most at the lowest energies where measurements are the most volatile.

simulated data, then, we should expect an NR band with a mean that trends systematically below the Lindhard Yield but with an *apparent* resolution that is deceptively high[6].

Fig. 10.11 shows the yield means and resolutions as a function of recoil energy again, now with the contributions from single-hit and multi-hit events in simulations shown separately. We see the single-hit events are consistently closest to the realistic means, but also the furthest from the RMS of the real data.

In the next section we will try to account for some of these differences, but first we want to highlight a notable consequence of the differences we've seen here. Recall that ultimately we want to be able to detect WIMPs, which would interact as single-NRs. Fig. 10.6 demonstrated how

---

[6] We first got a hint of this back in Fig. 7.7, where the NR band appeared to have resolution that the ER band didn't–that is, there appeared to be many mismeasured NRs. But Fig. 7.8 showed that those were actually all multi-NR events showing up where they were supposed to be.

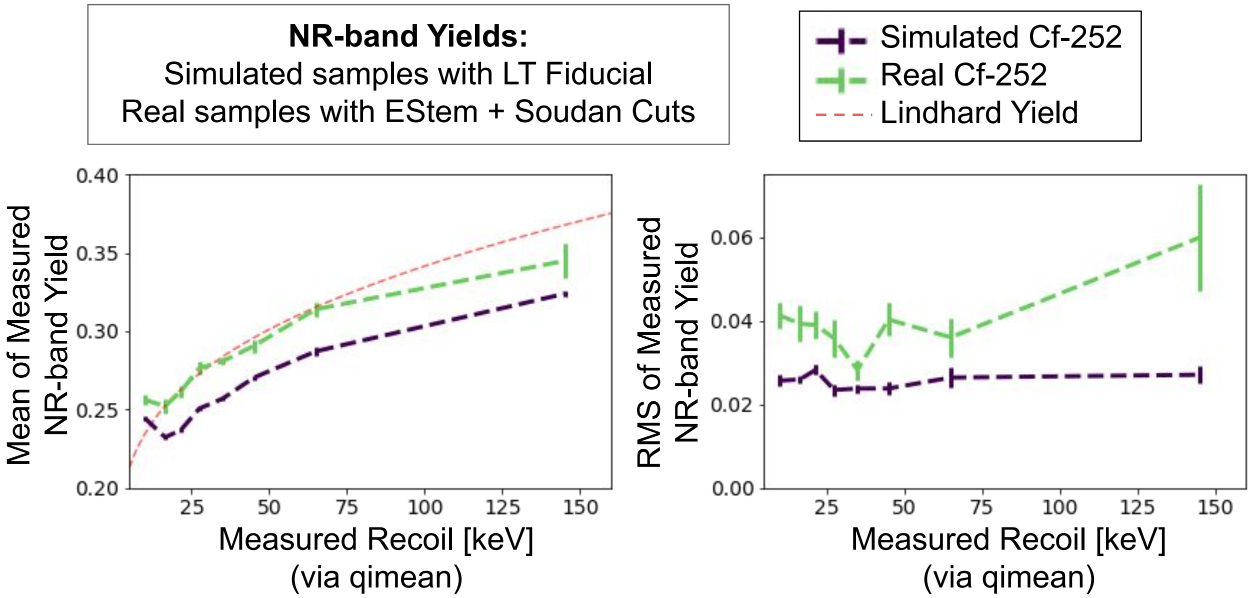

Figure 10.9: This figure shows the means and RMSs of the NR bands in Cf-252 for real and simulated data. The left plot shows the means, which–as in the ER band– start above the expected value but cross below it; the simulated data is again consistently low. The plot to the right shows the RMS, which doesn't show a clear trend for either sample, but once again the simulation is lower–i.e. has a better resolution.

single-NRs and multi-NRs are not easily separable in real data as they might be for simulated data. Fig. 10.11 shows that not only do multi-NRs have a different mean yield than single NRs, they also have a larger resolution. The combination of an offset mean and wider resolution will cause the overall NR band (i.e. band of NR events themselves) to have a significantly wider resolution than the single-hit, WIMP-like events we are looking for. That is, even if we haven't fully matched the NR resolution of real data, we have good reason to believe that the real-data RMS is not actually the experiment's *WIMP* resolution–especially if the third option for resolution differences in section 10.1.1 turns out to be correct.

10.2.2 Study of Cf-252 Nuclear Recoil Band Differences

Here we try to account for the differences between real and simulated data seen in the previous subsection. To do this we will re-analyze our data with four changes:

- *Rescale the simulated phonon energies.* Recall that:

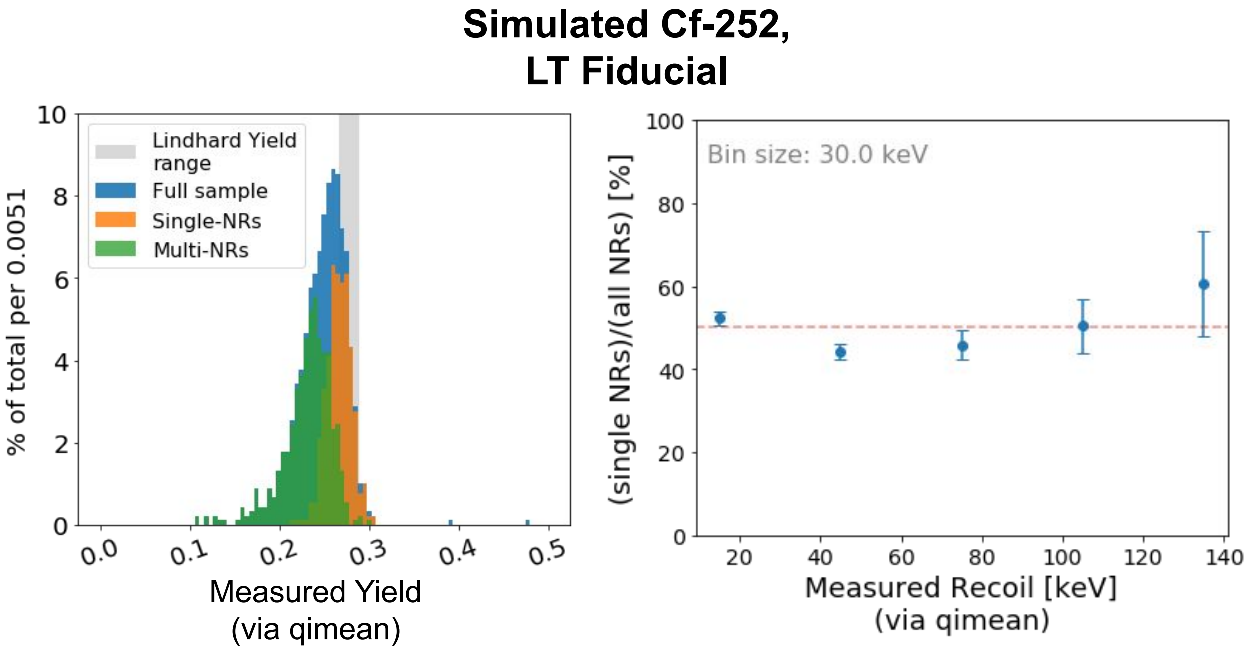

Figure 10.10: This figure shows the contribution to the measured yield from each recoil type in the Cf-252 simulation. The left plot histograms the yields for recoils between 25 and 40 keV–and yields below 0.5, to focus on NRs. As in Fig 10.6, the single-hit NRs (orange) are close to the expected Lindhard yield (grey), but multi-hit NRs (green) pull down the total (blue). The plot on the right shows the fraction of NRs that are single hit as a function of recoil energy. Because it hovers around 50% full the full range considered, this indicates the multi-hits pull down the overall yields for all the data.

- For simulated data, our reconstructed energies are calibrated to match the DMC's corrected energies–which were themselves calibrated using the collection efficiencies found in the Bulk 356 keV ER sample.
- But we saw the phonon energies in the NR sample had different efficiencies due to ERs and NRs allocating different proportions of their energy into the charge system, which loses some of it to off-electrode effects.

This difference made our corrected/calibrated NR phonon energies "too high" and the resulting yields "too low." So rescaling by the actual phonon collection efficiency (using the orange NR peak instead of the blue ER peak in Fig. 8.14 as our energy correction factor) will boost the final yields (though in theory the same should be done for the real data–except we

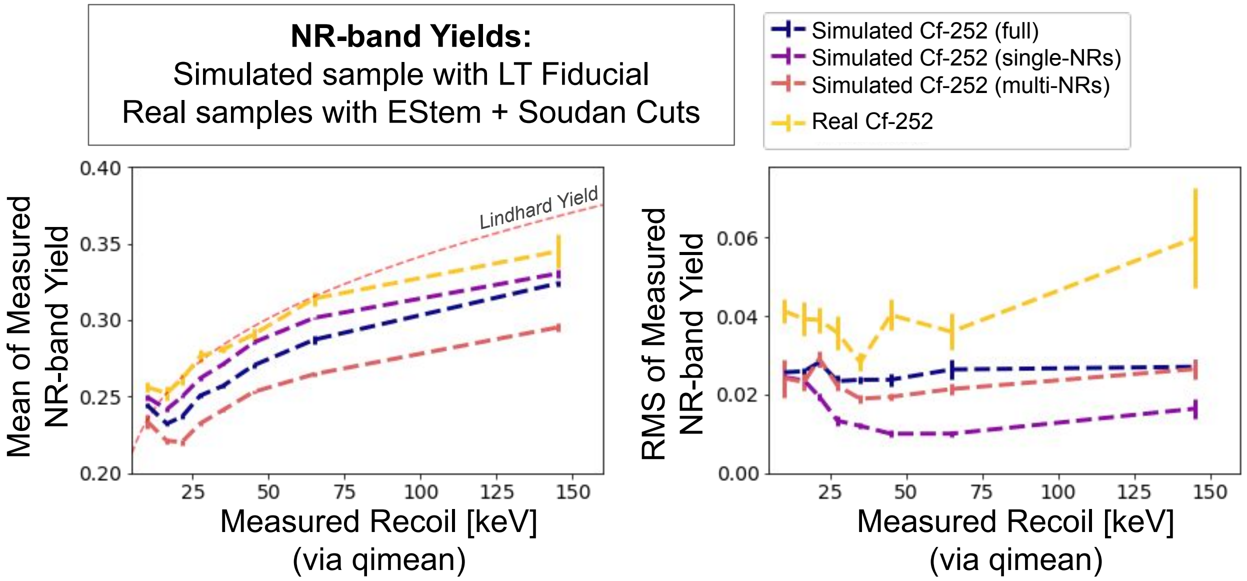

Figure 10.11: This figure shows the same data as Fig 10.9, but now splits up the simulated data by hit count. As in the previous figures, the single-hit NR yields are the most similar to both the real and expected (i.e. Lindhard) values, though they do have very low resolutions. The multi-hit NRs, meanwhile, have mean measured yields that are far from the Lindhard values and slightly more reasonable resolutions–though still not as high as those in real data.

don't know how much the off-electrode effects affect real phonon collection efficiencies). This is essentially operating under the assumption that ERs and NRs shouldn't actually have significant calibration differences.

- *Use only QS1.* Recall that off-electrode effects reduce all our charge collection, but affect holes and QS2 the most–especially for hits closer to QS1. We've so far been using $qsummean$ or $qimean$ as our charge energy measurements, but switching now to use only QS1 measurements may avoid much of the Z-dependent off-electrode trouble on QS2 (at the cost of increasing resolutions slightly).
- *Recalibrate real data.* Short of introducing a complicated energy dependency, we can recalibrate Cf-252 specifically by focusing on just the lower recoil energies (where most of our interest lies anyways) to avoid the full variation seen in the yield means. To do this we just rescale the $ptNF$ so the average of low-energy ER yields (for events with recoil energies

below about 150 keV) are centered at 1–instead of using the full recoil energy range.

- *Artificially increase the simulated RMS.* We found an average ER RMS difference between real and simulated data in Fig. 10.8. We'll add this "missing" variation into the NRs to see if that accounts for the difference here as well.

Fig. 10.12 shows the same yield means as were shown in Fig. 10.11 after applying the above changes (the first three of them, that is; we'll look at the RMSs in a moment). These updates have made the real and simulated yield means much more similar. Not only are the full simulated yield means now only slightly lower than the real data, the single-hit yields are above both, and the multi-hit yields are below both, as expected. The simulation's single-hit yields now track the Lindhard Yield expectations well (until the higher energies where statistics start running thin and we can't make substantive comparisons) but the mean yields of both real and simulated data trend below that due to the influence of the multi-hits–again, as expected.

Lastly, we apply the fourth change mentioned above to the NR yield RMSs in Fig. 10.13 to see if the RMS "missing" for ERs also accounts for the differences in the NRs. We find that by adding the ER RMS difference we found back in Fig. 10.8 to the NRs, the real and simulated resolutions (single- and multi-hit all together) become consistent within statistics. While this doesn't identify what, exactly, is missing that should be contributing to the simulated RMS values (though we have some ideas–e.g. the switch to ODEs from templates in FETSim and TESSim, as mentioned previously), this does show that whatever is missing is likely independent of recoil type and likely nothing large.

10.3 Summary of Comparisons Between Real and Simulated Events

We found in this chapter that our simulated calibration sources matched the data for the real calibration sources in broad strokes, but there are several differences and potential opportunities for improvement:

- Simulated data has lower RMSs than the real data–for both energy and yield. However, the ER and NR yield RMSs differ between the real and simulated data by the same amount, sug-

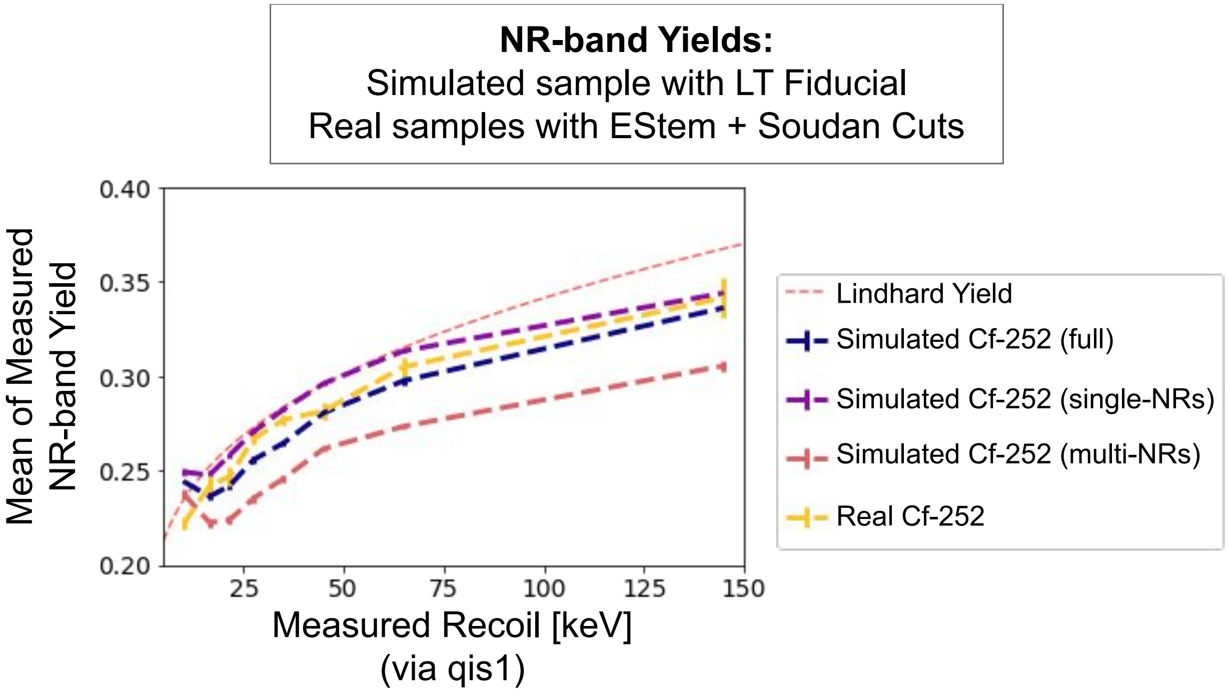

Figure 10.12: This figure shows the same data as the left plot of Fig. 10.11, but now with the changes described in the text (the first three, that is). We show it to check that we've understood what effects may be causing differences between real and simulated data. We see now that simulated single-hit events have mean yields above the real data, multi-hits are below, and so the total averages much closer to the real data. Though the simulation is still slightly low, this suggests we've got a good handle on the causes of the discrepancies (artifacts in simulation and nonlinear calibrations in real data).

gesting both might benefit from some single (currently unidentified) change to simulations or reconstruction–though we expect NRs have more at play (see third item below).

- The mean of the yields trend lower in simulations than in real data. As first noted in section 8.2.3, this is due primarily to off-electrode effects[7], which drain all our energies and yields–hurting the NRs in particular due to the different phonon efficiencies between ERs and NRs. There is currently no measurement of how much either recoil type is affected in real data, but since our current results might be getting inflated by a simulation artifact (see Appendix C), fixing that is a good next-step towards making simulations match real data and determining

---

[7] The energy-dependency in the mean of real data yields could be thought of as another reason, but that suggests a more detailed calibration of real data, not an improvement needed immediately in the simulation.

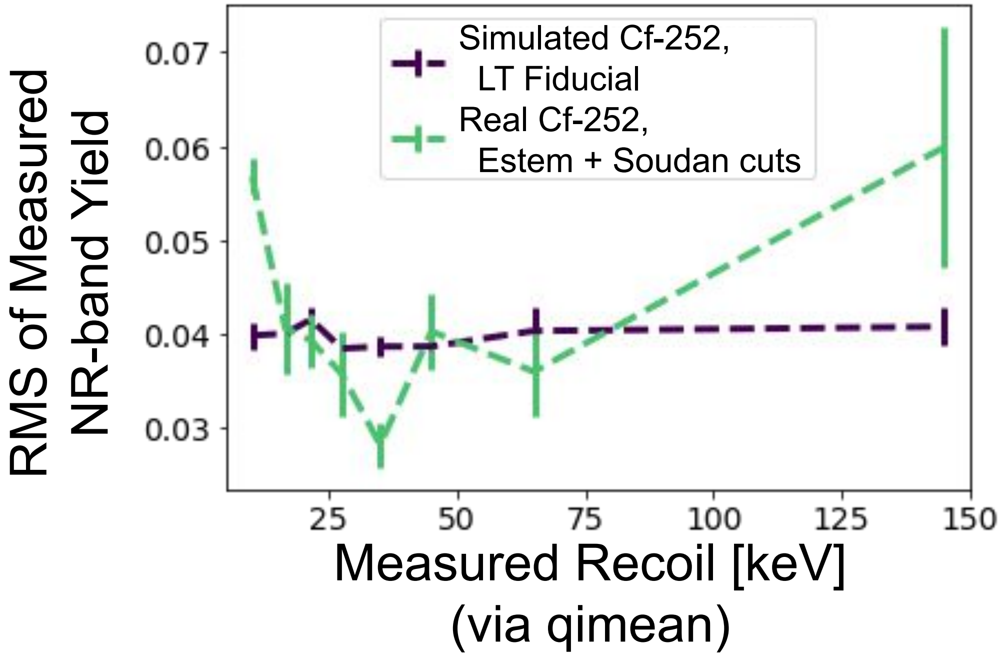

Figure 10.13: This figure shows the same data as the right plot of Fig. 10.9, but now we've added in the value found in Fig 10.8–the resolution difference between simulated and real ERs–as described in the text. Adding the "missing" ER resolutions makes the NR resolutions match well. This suggests that whatever is missing in the simulation is not recoil-type-specific.

what more important differences there may be.

- Our simulation showed that multi-NRs–which make up about 50% of all NR (single- and multi-) events–are causing (as seen in in Fig. 10.11):
  - The yield means for Cf-252's NR events to be lower than the expected Lindhard yield–i.e. lower than what is expected for WIMP-like (i.e. single-NR) events.
  - The yield RMSs for neutrons overall to be higher than those for WIMP-like events. This is not just because multi-NRs themselves have a higher resolution, but also because of their offset mean (so multi-NRs and single-NRs all together appear as an extra-wide NR band).

It's unclear how we'd specifically account for this in real data since no measurement of the multi-NR fraction has been made for it, but comparisons between the *apparent* real-data NR band of events and the Lindhard yield will be incorrect if the multi-NRs are overlooked. In particular, the true resolution of WIMP-like single-NRs will not be the same as the resolution of the observed NR band.

- If we had real data analysis tools that could identify or remove multi-hit events, we could more easily distinguish between ERs, NRs, and multi-NRs and determine the degree to which mismeasurements occur.

While there is room to improve, then, our simulations have performed well and we've learned a lot about our data. With our studies completed, we next move to our final conclusions and potential next steps for simulation developers and analyzers.

11. CONCLUSIONS

The search for dark matter is difficult–"dark matter" is, after all, so-called because it is not easily seen. Here we have described how the CDMS experiment is designed to tackle this problem, how we have constructed simulations to help us understand the experiment, and how well real and simulated experiment data match–and what we can learn from that. We conclude by summarizing our main findings and what steps future scientists can take from here.

Though simulated data did not match all expectations perfectly, we already have identified from simulations several factors that should be taken into account when analyzing real data (like the WIMP-search data in Fig. 1.7 or the calibration data in Fig. 5.10):

- As first seen in Chapter 7, there are multiple ways for well-measured events to look like something other than simple ERs or NRs (i.e. even before considering energy losses in the detectors or circuits themselves). We saw several recoil types that have aspects of both ERs and NRs–and multi-NR events that should have lower yields than normal NRs. While these types of events may look like noise or mismeasurements in the final data, they belong to specific, potentially well-measured recoil patterns that we can identify in simulations. As there is not currently a robust way to identify these specific multi-hit recoil types in real data, we can only encourage future analyzers to not assume all backgrounds outside the ER and NR bands are mismeasurements.

- Multi-NRs in particular are a concern because they can trend close enough to the normal NRs that the distinction is unclear; since they otherwise should be measured below the Lindhard Yield, they will make all NRs appear to trend low, which is easily misinterpreted.

- Off-electrode effects cause energy loss for both charges and phonons; this may both affect ERs and NRs differently and have some hit-location Z-dependence. Though events near electrode bends are worst-affected by this, all events suffer some amount, leading to lower means and wider resolutions. The change in mean energy may be calibrated out on average for all events–though for phonons this calibration differs between ERs and NRs–but the increase in resolution is less easily overcome. We note, though, that these effects seen in our results may be larger than they are in reality, due to a simulation artifact; it's not clear how to measure their magnitude for real data, however.

- There is a failure mode for the LT Fiducial cuts[1] in the form of the "semi-fiducial" events first seen in chapter 9.The most concerning instances of these that we've seen (e.g. in Fig. 9.11) are ERs that look like NRs. Now that we've been able to identify a cause of such events–i.e. both well-measured and poorly-measured hits within a given event–in simulation, we can next work to find a way to identify and exclude them in real data.[2]
- The observed RMS for NR events is not the same as the resolution of WIMP-like events. Multi-NRs are both slightly offset from and have a higher resolution than single-NRs. This means that the NR band determined from Cf-252 calibrations is not quite representative of the WIMP-like signals we're looking for; taking the RMS of the former as the resolution of the latter will lead to allowing in more backgrounds than necessary (because if we make the band too wide it collects more junk) and underestimating the WIMP efficiency (because if the true distibution has lower RMS, we'll have unknowingly captured more of it in the wider-RMS band).

Ultimately we wanted to see if the known effects we put into our simulations could produce data that matched real data. In chapter 10 we saw good qualitative agreement between the two (for measured energies and yields), though they do not perfectly match. We note specifically:

- The means of the simulated yields for ERs are both lower than expectation and constant in a way that the yields of real data are not. We believe the former is due to the Z-dependence and non-Gaussian energy measurements (of QS2 in particular) due to off-electrode effects;

---

[1] Technically it's a larger problem for any analysis that can't separate out multiple hits occurring in quick succession.

[2] To be clear, this is not a problem that would cause us to mismeasure WIMPS themselves, since they are unlikely to interact multiple times. We are more concerned about non-WIMPs that erroneously look like WIMPs.

the latter suggests additional calibration is needed for real data–since ER yields should not change with recoil energy.

- The means of the simulated yields for NRs are also low; we expect them to be below the Lindhard Yield due to multi-NRs, but the simulation artifact worsening off-electrode effect differences between ERs and NRs makes them additionally, erroneously lower.
- The resolutions of the simulated yields are significantly smaller than those for real data. It is not clear why this is, but the differences appear to be independent of recoil type or recoil energy, which suggests something that affects both ERs and NRs at once. Future studies will have to determine if this is due to something missing from the DMC or something suboptimal in CDMSBats (we suspect it could be doing better than trying to match a single pulse template to all real pulses, for example).

Based on our results, we have several suggestions and future steps in mind–mostly for improving the current simulations, but some for better understanding or cleaning up real data generally[3]:

- *Try a more complete Cf-252 fission simulation.* For our final samples we only simulated the prompt fission neutron spectrum; while we determined that the alternate alpha decay spectrum was ignorable, we weren't able to check the output spectra of fission fragments, as they aren't simulated. Implementing and running a more complete simulation including those fragments (and subsequent radiations) would be good for validating whether or not later fission effects are relevant to our results–though we currently do not think they are important.
- *Switch from DMC pulse templates to ODE solvers in TESSim and FETSim.* As noted in chapters 6 and 8, for the samples used in our analysis the DMC created its pulses for each channel using the same templates CDMSBats uses in the optimal filter–meaning the match between the two is artificially good. Switching to ODEs in the DMC will make its pulses

---

[3] Some of these have already been taken since these studies. Note as well that this list is non-exhaustive; there will always be more ways the simulations can be improved than the few included here.

more realistic (i.e. more nuanced–and likely with more potential mismeasurements or other pathologies to study) and so likely increase the simulated energy and yield resolutions. On the other hand, current studies suggest more realistic pulse simulations may also provide better energy measurement resolution–*if* we allow for more intricate pulse reconstruction algorithms than relying on a single template; accounting for this would lower the resolutions of both simulated and real data.

- *Fix problematic phonon simulation parameters.* These are described more in Appendix C, but to summarize, some of the simplifications implemented to make phonon simulation more computationally reasonable (in terms of time and memory) affect the results. For example, limits on the number of times phonons can bounce affect their collection efficiencies (further affecting ERs and NR to different degrees) while downsampling limits their statistics and, in turn, resolutions.

- *Add in more real-world effects.* We will not discuss all the possibilities, but there are some effects and processes missing in the simulation that may play measurable roles in the results. These include factors such as charge trapping in the crystal, energy loss in the QETs, cross-channel noise, and ambient temperature dependencies.

- *Tune LT Fiducial to better match SimFiducial.* Though LT Fiducial largely selected well-measured events, it could include more well-measured events at high radii and fewer suspicious events close to detector faces–especially given the potential for semi-fiducial events.

- *Measure the magnitude of off-electrode effects.* These hurt our collection efficiencies and vary by hit location–and their impact has not been measured for real data. We note, though, that the next generation of iZIPs to be used at SNOLAB have improved electrode layouts that will reduce these effects.

- *Find a way to handle multi-hit events.* We need some way to measure, reject, or otherwise account for these because left alone they will obscure the distinctions between ER and NR events. Multi-NRs in particular further cause the apparent NR yield band of Cf-252 to be both systematically low (and normal NRs–like from WIMPs–to appear unusually high by comparison) and too wide (in a way that WIMPs wouldn't be).

In conclusion: our simulations work well, we have leads on how we can improve both them and the related analyses (with several efforts under way already), and we've already learned useful information about the behavior of our detectors from them. Dark matter will be difficult to find, but with an ultrasensitive experiment and well-understood simulations to help interpret the data, CDMS is well-equipped to search for it.

REFERENCES

[1] Planck Collaboration. “Planck 2018 results - VI. Cosmological parameters”. In: *A&A* 641 (2020), A6. DOI: `10.1051/0004-6361/201833910`. URL: `https://doi.org/10.1051/0004-6361/201833910`.

[2] *SuperCDMS | Super Cryogenic Dark Matter Search*. `https://supercdms.slac.stanford.edu/`. 2023. URL: `https://supercdms.slac.stanford.edu/`.

[3] R. Agnese et al. “Projected sensitivity of the SuperCDMS SNOLAB experiment”. In: *Phys. Rev. D* 95 (8 Apr. 2017), p. 082002. DOI: `10.1103/PhysRevD.95.082002`. URL: `https://link.aps.org/doi/10.1103/PhysRevD.95.082002`.

[4] Gianfranco Bertone, Dan Hooper, and Joseph Silk. “Particle dark matter: evidence, candidates and constraints”. In: *Physics Reports* 405.5 (2005), pp. 279–390. ISSN: 0370-1573. DOI: `https://doi.org/10.1016/j.physrep.2004.08.031`. URL: `https://www.sciencedirect.com/science/article/pii/S0370157304003515`.

[5] Jonathan L. Feng. “Dark Matter Candidates from Particle Physics and Methods of Detection”. In: *Annual Review of Astronomy and Astrophysics* 48.1 (2010), pp. 495–545. DOI: `10.1146/annurev-astro-082708-101659`. URL: `https://doi.org/10.1146/annurev-astro-082708-101659`.

[6] Fritz Zwicky. “Die Rotverschiebung von extragalaktischen Nebeln. (German)”. In: *Helvetica Physica Acta* 6 (1933), pp. 110–127.

[7] Vera C. Rubin and W. Kent Ford. “Rotation of the Andromeda Nebula from a Spectroscopic Survey of Emission Regions”. In: *Astrophysical Journal* 159 (1970).

[8] Edvige Corbelli and Paolo Salucci. “The extended rotation curve and the dark matter halo of M33”. In: *Monthly Notices of the Royal Astronomical Society* 311.2 (Jan. 2000), pp. 441–447. ISSN: 0035-8711. DOI: `10.1046/j.1365-8711.2000.03075.x`. eprint:

`https://academic.oup.com/mnras/article-pdf/311/2/441/2881340/311-2-441.pdf`. URL: `https://doi.org/10.1046/j.1365-8711.2000.03075.x`.

[9] Douglas Clowe et al. “A Direct Empirical Proof of the Existence of Dark Matter”. In: *Astrophysical Journal* 648.2 (2006), pp. 109–113.

[10] C. Alcock et al. “The MACHO Project: Microlensing Results from 5.7 Years of Large Magellanic Cloud Observations”. In: *The Astrophysical Journal* 542.1 (Oct. 2000), p. 281. DOI: `10.1086/309512`. URL: `https://dx.doi.org/10.1086/309512`.

[11] Tisserand, P. et al. “Limits on the Macho content of the Galactic Halo from the EROS-2 Survey of the Magellanic Clouds”. In: *A&A* 469.2 (2007), pp. 387–404. DOI: `10.1051/0004-6361:20066017`. URL: `https://doi.org/10.1051/0004-6361:20066017`.

[12] Lam Hui. “Wave Dark Matter”. In: *Annual Review of Astronomy and Astrophysics* 59.1 (2021), pp. 247–289. DOI: `10.1146/annurev-astro-120920-010024`. eprint: `https://doi.org/10.1146/annurev-astro-120920-010024`. URL: `https://doi.org/10.1146/annurev-astro-120920-010024`.

[13] C. Bhm, P. Fayet, and J. Silk. “Light and heavy dark matter particles”. In: *Phys. Rev. D* 69 (10 May 2004), p. 101302. DOI: `10.1103/PhysRevD.69.101302`. URL: `https://link.aps.org/doi/10.1103/PhysRevD.69.101302`.

[14] Gerard Jungman, Marc Kamionkowski, and Kim Griest. “Supersymmetric dark matter”. In: *Physics Reports* 267.5 (1996), pp. 195–373. ISSN: 0370-1573. DOI: `https://doi.org/10.1016/0370-1573(95)00058-5`. URL: `https://www.sciencedirect.com/science/article/pii/0370157395000585`.

[15] Howard Baer et al. “Dark matter production in the early Universe: Beyond the thermal WIMP paradigm”. In: *Physics Reports* 555 (2015), pp. 1–60. ISSN: 0370-1573. DOI: `https:`

//doi.org/10.1016/j.physrep.2014.10.002. URL: https://www.sciencedirect.com/science/article/pii/S0370157314003925.

[16] George R Blumenthal et al. “Formation of galaxies and large-scale structure with cold dark matter”. In: *Nature* 311.5986 (1984), pp. 517–525.

[17] Matt Christopher Pyle. “Optimizing the Design and Analysis Of Cryogenic Semiconductor Dark Matter Detectors For Maximum Sensitivity”. PhD thesis. Stanford University, 2012.

[18] Gary Steigman and Michael S. Turner. “Cosmological constraints on the properties of weakly interacting massive particles”. In: *Nuclear Physics B* 253 (1985), pp. 375–386. ISSN: 0550-3213. DOI: https://doi.org/10.1016/0550-3213(85)90537-1. URL: https://www.sciencedirect.com/science/article/pii/0550321385905371.

[19] Timothy Cohen et al. “γ-ray Constraints on Decaying Dark Matter and Implications for IceCube”. In: *Phys. Rev. Lett.* 119 (2 July 2017), p. 021102. DOI: 10.1103/PhysRevLett.119.021102. URL: https://link.aps.org/doi/10.1103/PhysRevLett.119.021102.

[20] E. Komatsu et al. “Five-Year Wilkinson Microwave Anisotropy Probe Observations: Cosmological Interpretation”. In: *The Astrophysical Journal Supplement Series* 180.2 (Feb. 2009), p. 330. DOI: 10.1088/0067-0049/180/2/330. URL: https://dx.doi.org/10.1088/0067-0049/180/2/330.

[21] Antonio Boveia and Caterina Doglioni. “Dark Matter Searches at Colliders”. In: *Annual Review of Nuclear and Particle Science* 68.1 (2018), pp. 429–459. DOI: 10.1146/annurev-nucl-101917-021008. eprint: https://doi.org/10.1146/annurev-nucl-101917-021008. URL: https://doi.org/10.1146/annurev-nucl-101917-021008.

[22] Jennifer M. Gaskins. “A review of indirect searches for particle dark matter”. In: *Contemporary Physics* 57.4 (2016), pp. 496–525. DOI: 10.1080/00107514.2016.1175160.

eprint: `https://doi.org/10.1080/00107514.2016.1175160`. URL: `https://doi.org/10.1080/00107514.2016.1175160`.

[23] D. et al Abrams. “Exclusion limits on the WIMP-nucleon cross section from the Cryogenic Dark Matter Search”. In: *Phys. Rev. D* 66 (12 Dec. 2002), p. 122003. DOI: `10.1103/PhysRevD.66.122003`. URL: `https://link.aps.org/doi/10.1103/PhysRevD.66.122003`.

[24] R. Agnese et al. “Improved WIMP-search reach of the CDMS II germanium data”. In: *Phys. Rev. D* 92 (2015).

[25] R. Agnese et al. “Results from the Super Cryogenic Dark Matter Search Experiment at Soudan”. In: *Phys. Rev. Lett.* 120 (2018).

[26] SuperCDMS Collaboration. *A Strategy for Low-Mass Dark Matter Searches with Cryogenic Detectors in the SuperCDMS SNOLAB Facility*. 2022. arXiv: `2203.08463 [physics.ins-det]`.

[27] R. Agnese et al. “Low-mass dark matter search with CDMSlite”. In: *Physical Review D* 97 (2018).

[28] R. Agnese et al. “Search for Low-Mass WIMPs with SuperCDMS”. In: *Phys. Rev. Lett.* 112 (2014).

[29] J. Allison et al. “Recent developments in Geant4”. In: *Nuclear Instruments and Methods in Physics Research Section A: Accelerators, Spectrometers, Detectors and Associated Equipment* 835 (2016), pp. 186–225. ISSN: 0168-9002. DOI: `https://doi.org/10.1016/j.nima.2016.06.125`. URL: `https://www.sciencedirect.com/science/article/pii/S0168900216306957`.

[30] J. Allison et al. “Geant4 developments and applications”. In: *IEEE Transactions on Nuclear Science* 53.1 (2006), pp. 270–278. DOI: `10.1109/TNS.2006.869826`.

[31] S. Agostinelli et al. "Geant4a simulation toolkit". In: *Nuclear Instruments and Methods in Physics Research Section A: Accelerators, Spectrometers, Detectors and Associated Equipment* 506.3 (2003), pp. 250–303. ISSN: 0168-9002. DOI: `https://doi.org/10.1016/S0168-9002(03)01368-8`. URL: `https://www.sciencedirect.com/science/article/pii/S0168900203013688`.

[32] M.H. Kelsey et al. "G4CMP: Condensed matter physics simulation using the Geant4 toolkit". In: *Nuclear Instruments and Methods in Physics Research Section A: Accelerators, Spectrometers, Detectors and Associated Equipment* 1055 (2023), p. 168473. ISSN: 0168-9002. DOI: `https://doi.org/10.1016/j.nima.2023.168473`. URL: `https://www.sciencedirect.com/science/article/pii/S0168900223004631`.

[33] Martin E. Huber. *Closing In On Dark Matter*. UCD Mini-STEM School. Feb. 2013.

[34] Jorge Morales. "Simulation Of The Charge Measurements For The SuperCDMS Soudan Experiment". PhD thesis. Texas A&M University, 2020.

[35] Adam J. Anderson. "A Search for Light Weakly-Interacting Massive Particles with SuperCDMS and Applications to Neutrino Physics". PhD thesis. Massachusetts Institute of Technology, 2015.

[36] Jeffrey Peter Filippini. "A Search for WIMP Dark Matter Using the First Five-Tower Run of the Cryogenic Dark Matter Search". PhD thesis. University of California at Berkeley, 2008.

[37] D.-M. Mei and A. Hime. "Muon-induced background study for underground laboratories". In: *Phys. Rev. D* 73 (5 Mar. 2006), p. 053004. DOI: `10.1103/PhysRevD.73.053004`. URL: `https://link.aps.org/doi/10.1103/PhysRevD.73.053004`.

[38] Ciaran A. J. O'Hare. "Dark matter astrophysical uncertainties and the neutrino floor". In: *Phys. Rev. D* 94 (6 Sept. 2016), p. 063527. DOI: `10.1103/PhysRevD.94.063527`. URL: `https://link.aps.org/doi/10.1103/PhysRevD.94.063527`.

[39] Scott Hertel. "Advancing the Search for Dark Matter: from CDMS II to SuperCDMS". PhD thesis. Massachusetts Institute Of Technology, 2012.

[40] Kyle Michael Sundqvist. "Carrier Transport and Related Effects in Detectors of the Cryogenic Dark Matter Search". PhD thesis. University of California, Berkeley, 2012.

[41] R.H. Pehl et al. "Accurate determination of the ionization energy in semiconductor detectors". In: *Nuclear Instruments and Methods* 59.1 (1968), pp. 45–55. ISSN: 0029-554X. DOI: `https://doi.org/10.1016/0029-554X(68)90342-X`. URL: `https://www.sciencedirect.com/science/article/pii/0029554X6890342X`.

[42] U. Fano. "Ionization Yield of Radiations. II. The Fluctuations of the Number of Ions". In: *Phys. Rev.* 72 (1 July 1947), pp. 26–29. DOI: `10.1103/PhysRev.72.26`. URL: `https://link.aps.org/doi/10.1103/PhysRev.72.26`.

[43] P. N. Luke. "Voltage-assisted calorimetric ionization detector". In: *Journal of Applied Physics* 64 (1988), pp. 6858–6860.

[44] Jens Lindhard et al. "Integral equations governing radiation effects". In: *Mat. Fys. Medd. Dan. Vid. Selsk* 33.10 (1963), pp. 1–42.

[45] J.D. Lewin and P.F. Smith. "Review of mathematics, numerical factors, and corrections for dark matter experiments based on elastic nuclear recoil". In: *Astroparticle Physics* 6.1 (1996), pp. 87–112. ISSN: 0927-6505. DOI: `https://doi.org/10.1016/S0927-6505(96)00047-3`. URL: `https://www.sciencedirect.com/science/article/pii/S0927650596000473`.

[46] R.H. Pratt et al. "Compton scattering revisited". In: *Radiation Physics and Chemistry* 79.2 (2010). Special Issue on Future Directions in Atomic and Condensed Matter Research and Applications, pp. 124–131. ISSN: 0969-806X. DOI: `https://doi.org/10.1016/j.radphyschem.2009.04.035`. URL: `https://www.sciencedirect.com/science/article/pii/S0969806X09003491`.

[47] K.M. Sundqvist and B. Sadoulet. "Detectors of the Cryogenic Dark Matter Search: Charge Transport and Phonon Emission in Ge100Crystals at 40 mK". In: *J Low Temp Phys* (151 2008), pp. 443–447. URL: `https://doi.org/10.1007/s10909-007-9666-5`.

[48] S.W. et al Leman. “Comparison of CDMS [100] and [111] Oriented Germanium Detectors”. In: *J Low Temp Phys* (167 2012), pp. 1106–1111. URL: `https://doi.org/10.1007/s10909-011-0427-0`.

[49] B. Cabrera et al. “Oblique propagation of electrons in crystals of germanium and silicon at sub-Kelvin temperature in low electric fields”. In: (2010). arXiv: `1004.1233 [astro-ph.IM]`.

[50] J. Singleton. *Band theory and electronic properties of solids*. Oxford University Press, 2001.

[51] G. A. Northrop and J. P. Wolfe. “Ballistic Phonon Imaging in Solids—A New Look at Phonon Focusing”. In: *Phys. Rev. Lett.* 43 (19 Nov. 1979), pp. 1424–1427. DOI: `10.1103/PhysRevLett.43.1424`. URL: `https://link.aps.org/doi/10.1103/PhysRevLett.43.1424`.

[52] G. Wang. “Phonon emission in germanium and silicon by electrons and holes in applied electric field at low temperature”. In: *Journal of Applied Physics* 107.9 (2010), p. 094504. DOI: `10.1063/1.3354095`. eprint: `https://doi.org/10.1063/1.3354095`. URL: `https://doi.org/10.1063/1.3354095`.

[53] KM Sundqvist et al. “Transport and two-species capture of electrons and holes in ultrapure germanium at millikelvin temperature”. In: *Journal of Low Temperature Physics* 176 (2014), pp. 188–193.

[54] R.D. Westbrook. “Hole traps in germanium crystals”. In: *Nuclear Instruments and Methods* 108.2 (1973), pp. 335–338. ISSN: 0029-554X. DOI: `https://doi.org/10.1016/0029-554X(73)90609-5`. URL: `https://www.sciencedirect.com/science/article/pii/0029554X73906095`.

[55] W. Shockley. “Currents to Conductors Induced by a Moving Point Charge”. In: *Journal of Applied Physics* 9.10 (1938), pp. 635–636. DOI: `10.1063/1.1710367`. eprint: `https://doi.org/10.1063/1.1710367`. URL: `https://doi.org/10.1063/1.1710367`.

[56] S. Ramo. “Currents Induced by Electron Motion”. In: *Proceedings of the IRE* 27.9 (1939), pp. 584–585. DOI: `10.1109/JRPROC.1939.228757`.

[57] Joel Sander. “Results from The Cryogenic Dark Matter Search Using a Chi Squared Analysis”. PhD thesis. University of California at Santa Barbara, 2007.

[58] Sunil Golwala. “Exclusion Limits on the WIMP-Nucleon Elastic-Scattering Cross Section from the Cryogenic Dark Matter Search”. PhD thesis. University of California at Berkeley, 2000.

[59] Mark David Pepin. “Low-Mass Dark Matter Search Results and Radiogenic Backgrounds for the Cryogenic Dark Matter Search”. PhD thesis. University of Minnesota, 2016.

[60] Yu. Khazov, A. Rodionov, and F. G. Kondev. In: *Nucl. Data Sheets* 112 (2011), p. 855.

[61] P. Auger. “The Auger effect”. In: *Surface Science* 48.1 (1975), pp. 1–8. ISSN: 0039-6028. DOI: `https://doi.org/10.1016/0039-6028(75)90306-4`. URL: `https://www.sciencedirect.com/science/article/pii/0039602875903064`.

[62] T Åberg. “Unified Theory of Auger Electron Emission”. In: *Physica Scripta* 1992.T41 (Jan. 1992), p. 71. DOI: `10.1088/0031-8949/1992/T41/013`. URL: `https://dx.doi.org/10.1088/0031-8949/1992/T41/013`.

[63] Brookhaven National Laboratory. *National Nuclear Data Center*. `https://www.nndc.bnl.gov/`. 2022. URL: `https://www.nndc.bnl.gov/`.

[64] M.J. Martin. In: *Nucl. Data Sheets* 122 (2014), p. 377.

[65] S. Cox et al. “Delayed Neutrons from the Spontaneous Fission of Cf^{252}”. In: *Phys. Rev.* 112 (3 Nov. 1958), pp. 960–963. DOI: `10.1103/PhysRev.112.960`. URL: `https://link.aps.org/doi/10.1103/PhysRev.112.960`.

[66] W Mannhart. “Evaluation of the Cf-252 fission neutron spectrum between 0 MeV and 20 MeV”. In: *Properties of Neutron Sources*. 1987, pp. 158–171.

[67] F. H. Fröhner. “Evaluation of "^{252}Cf" Prompt Fission Neutron Data from 0 to 20 MeV by Watt Spectrum Fit”. In: *Nuclear Science and Engineering* 106.3 (1990), pp. 345–352. DOI: `10.13182/NSE89-177`. eprint: `https://doi.org/10.13182/NSE89-177`. URL: `https://doi.org/10.13182/NSE89-177`.

[68] Raymond A. Bunker III. “A Low-threshold Analysis of Data from the Cryogenic Dark Matter Search Experiment”. PhD thesis. University of California at Santa Barbara, 2011.

[69] F C Maienschein et al. “Gamma Rays Associated With Fission”. In: (Oct. 1958). DOI: `10.2172/4325517`. URL: `https://www.osti.gov/biblio/4325517`.

[70] R.J Gehrke et al. “The gamma-ray spectrum of 252Cf and the information contained within it”. In: *Nuclear Instruments and Methods in Physics Research Section B: Beam Interactions with Materials and Atoms* 213 (2004), pp. 10–21.

[71] N. J. Roberts. “Photon Spectra In NPL Standard Radionuclide Neutron Fields”. In: *Radiation Protection Dosimetry* 180.1-4 (Aug. 2018), pp. 62–65.

[72] F. et al Abe. “Observation of Top Quark Production in $\overline{p}p$ Collisions with the Collider Detector at Fermilab”. In: *Phys. Rev. Lett.* 74 (14 Apr. 1995), pp. 2626–2631. DOI: `10.1103/PhysRevLett.74.2626`. URL: `https://link.aps.org/doi/10.1103/PhysRevLett.74.2626`.

[73] S. Chatrchyan et al. “Observation of a new boson at a mass of 125 GeV with the CMS experiment at the LHC”. In: *Physics Letters B* 716.1 (2012), pp. 30–61. ISSN: 0370-2693. DOI: `https://doi.org/10.1016/j.physletb.2012.08.021`. URL: `https://www.sciencedirect.com/science/article/pii/S0370269312008581`.

[74] *Physics Reference Manual*. 10.7. Geant4. URL: `https://geant4-userdoc.web.cern.ch/UsersGuides/PhysicsReferenceManual/BackupVersions/V10.7/html/index.html`.

[75] *Physics Simulation Packages*. Lawrence Livermore National Laboratory. URL: `https://nuclear.llnl.gov/simulation/`.

[76] David G Madland and J Rayford Nix. “Prompt fission neutron spectra and average prompt neutron multiplicities”. In: *NEANDC Specialists Meeting On Yields and Decay Data Of Fission Product Nuclides*. 1983, p. 427.

[77] *Guide for Physics Lists*. 10.7. Geant4. URL: `https://geant4-userdoc.web.cern.ch/UsersGuides/PhysicsListGuide/BackupVersions/V10.7/html/index.html`.

[78] C. Kittel. *Introduction to Solid State Physics*. 8th ed. Wiley, 2005.

[79] H. W. Schmitt, W. E. Kiker, and C. W. Williams. “Precision Measurements of Correlated Energies and Velocities of ^{252}Cf Fission Fragments”. In: *Phys. Rev.* 137 (4B Feb. 1965), B837–B847. DOI: `10.1103/PhysRev.137.B837`. URL: `https://link.aps.org/doi/10.1103/PhysRev.137.B837`.

[80] Jonathan Corbett. “Neutron Calibration System for the Cryogenic Underground Test Facility (CUTE)”. Queen’s University, 2021.

APPENDIX A

MOTION OF ELECTRONS AND HOLES IN IZIP5S

As noted in section 3.2.1, electrons and holes move differently from one another in the germanium crystal lattice of the iZIP5s (and differently than how they'd move outside of this specific crystal). We provide further qualitative explanation here, but for more detail, refer to chapter 4 of Ref. [39], chapter 2 of Ref. [40], or to your favorite solid-state physics textbook.

We first provide a few informal definitions:

- The "valence band" of–in our case–a semiconductor is the set of states (i.e. energies) that electrons settle into around an atom when there are no external influences (including heat). Electrons in the valence band stay close to their given atoms at all times.

- The "conduction band" is the set of electron states at energies just above the valence band. It takes energy to move electrons from the valence band to the conduction band[1] (for germanium, 2.96 eV). Electrons in the conduction band can move between atoms–i.e. through the detector crystal–easily.

- The "Brillouin zone" of a crystal, in loose terms, is a representation of important or favored directions a particle might travel in a crystal.

Electrical conductivity requires having electrons free to move between atoms in the conduction band; the holes they leave behind in the lattice upon ionization may be thought of as positively-charged particles that can move between atoms as well, though in the valence band. And details of the crystal shape–i.e. the Brillouin zone–determine how electrons and holes might move between bands energetically and through the crystal spatially.

In a CDMS context, particles deposit energy in the iZIP5 detectors via ERs or NRs, as described in the main text. The ionizing energy kicks electrons from the valence band to the con-

---

[1] For materials, like semiconductors, where the bands do not overlap.

duction band, leaving holes behind in the valence band. With those electrons and holes free to move, the bias voltage over the iZIP5 (see section 3.2.2) splits them up–causing electrons to drift towards one detector face and holes to drift towards the other (generally). But the internal structure of the crystal–i.e. the corresponding Brillouin zone of germanium–makes some lateral motion energetically favorable.

Fig. A.1 shows the Brillouin zone (the same one shown in Fig. 3.6) and the valence and conduction bands of our germanium detector crystals–and how the interactions of each lead to the motion of electrons and holes described in the main text–in which electrons favor angled "valleys" and holes do not[2]. The left side of the figure shows the Brillouin zone for germanium with several important directions marked; for our purposes, note the Γ in the very center of the zone and the L in the center of the hexagon at the edge of the zone (note that the L equally refers to all the hexagons at the edges, as the zone is rotationally symmetric). The right side of the figure, next, shows the energy bands in germanium–specifically showing energy as a function of *direction*; the valence band is towards the bottom, colored grey, and the conduction band is above that, with a small gap between the two. Note again that the directions corresponding to Γ and L have been marked (red and blue, respectively). Electrons that have made it into the conduction band will try to settle back down into the lowest part of that band (at L) while holes settle at the top of the valence band (at Γ)–as those are the most energetically-favorable positions for each. Electrons, then, favor moving in the L direction–that is, through the hexagons of the Brillouin zone–while holes favor no particular direction at all–i.e. the middle of the zone. The only additional modification here is again our bias voltage, which makes electrons drift upwards (through the upper four hexagons) and holes drift downwards (ballistically), as was shown in Fig. 3.1.

---

[2] Again, we only summarize here. See the references listed previously or those in the figure caption for more detail.

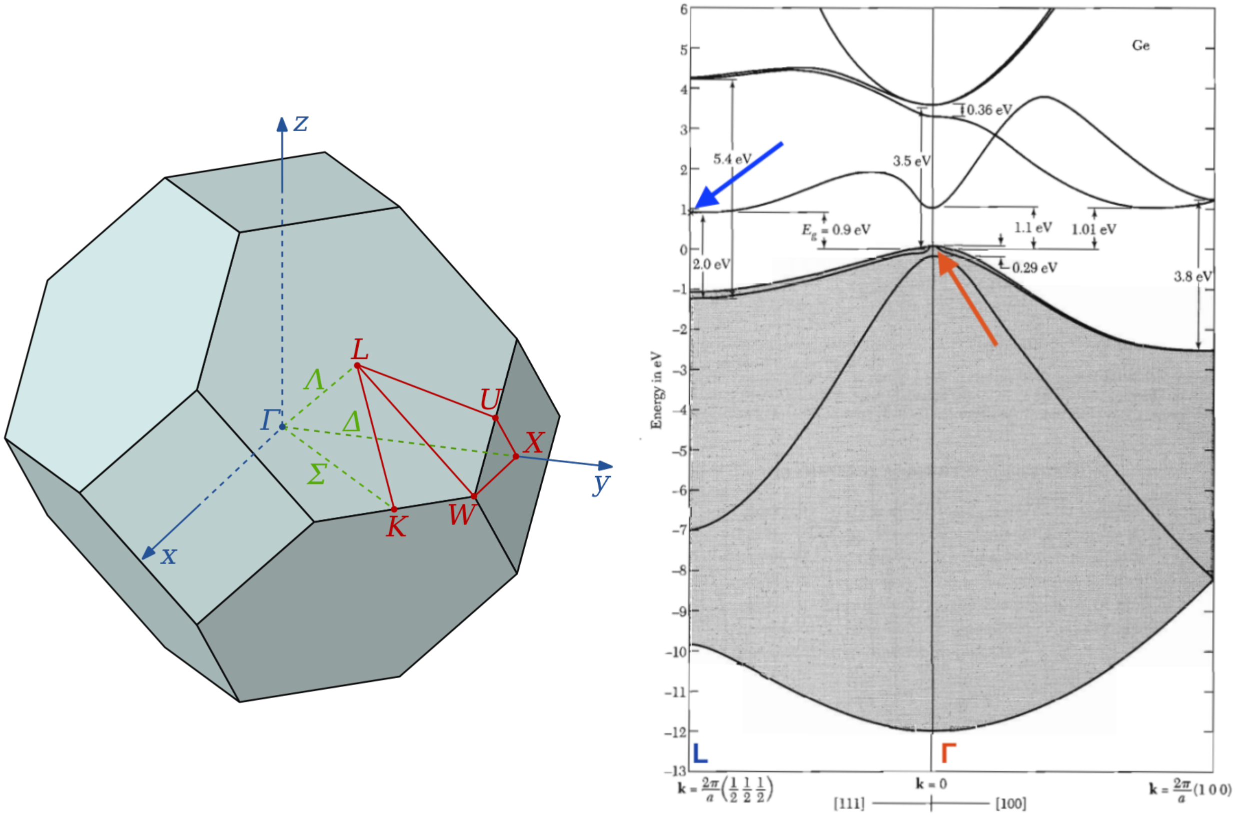

Figure A.1: Some solid-state physics considerations that determine how charges move in our detectors. Left: First Brillouin zone of a face-centered cubic, like our Ge-71 detector crystals (in other words, a representation of important directions particles could travel in our detectors). Right: Ge-71 band structure (y-axis is energy, x-axis is direction)–valence band below in grey, conduction band above; original figure from Ref. [78], colored annotations from Ref. [34]. Free electrons want to drop from the conduction band to the valence band, so they gather at the lowest point, marked with the blue "L", which corresponds to the eight hexagons of the Brillouin zone. Holes want to go up to the conduction band from the valence band, so they favor the highest point, at the orange "Γ," corresponding to no particular direction. The applied electric field in our iZIPs then makes the electrons favor their four upward options while the holes travel downwards.

APPENDIX B

CF-252 SIMULATION DETAILS

A real Cf-252 source does much more than emit the fission neutron spectra we're interested in–and our simulations don't model all these other spectra or their changes over time completely[1]. We do not expect these to have significant impact on our results, as it's mostly the photon spectra–which don't have any particular features that interest us–whose changes are not fully modeled but might have been visible. For completeness, though, in this appendix we will:

- Look briefly at some of the shortcomings of the Cf-252 simulation shown in chapter 7–expanding in particular on the topics mentioned in section 7.2.2 in section B.1.
- Comment on the results of some of the less important spectra in SourceSim for completeness in section B.2

B.1 Shortcomings and Caveats

Though we are most interested in the prompt neutron spectra of Cf-252 itself (shown in Fig. 5.6), not only does a real-world source emit other prompt particle spectra, it also changes those spectra over time; a real "Cf-252" source will gradually build up other isotopes (or begin with contaminants) that emit something other than the expected prompt spectra. This introduces a few additional considerations for us in simulations; below we consider what decay/particle emission timescales are relevant to us, the particles missing from our fission simulation in chapter 7, how the outgoing spectra should be changing over time, and possible contaminants.

B.1.1 Particle Emission Timescales

Section 7.2 described why we focused on energy deposits happening within one second of decays for Cf-252; here we describe when the decays themselves happen (with no time cuts). We

---

[1] That is, the Cf-252 simulation has shortcomings in ways that the Ba-133 simulation–for example–does not.

are most interested in the prompt spectra emitted during the initial Cf-252 decay, but the full source simulation has many other decays and output spectra. As shown in figure B.1–which shows only decays in the "Cf-252" source capsule itself–we can somewhat arbitrarily identify three time scales for the full Cf-252 (and daughters or later progeny) decay timing (as we did in the main text):

- The earliest timescale, below one second and representing the "prompt" particles emitted in the initial Cf-252 decays, is what we are most interested in.

- The latest time scale, 10 years after the original decay and where many of the alpha decay products begin to show up (some leaking into the middle timescale, but only at extreme statistics), is ignorable. There won't be significant numbers of these decays until tens or hundreds of years after we run the experiment (and almost none of them will emit more neutrons–our interest).

- Lastly, the middle timescale, between one second and ten years, is comprised of energy deposits due to de-exciting atoms in the Cf-252 container (some stainless steel and polycarbonate). Atoms around the source capsule that were excited by neutrons in the "prompt" time period may, at this later time, release their energy as photons or electrons that could potentially cause more hits themselves; but we ignore these because what rare few may actually reach the detectors are themselves simulated separately.

So the one-second cut we established in section 7.2.4 accomplishes what we wanted: it leaves us only the original fission events–and the only significant source of neutrons.

B.1.2 Missing Fission Fragments

Our next consideration is the behavior of the fission products remaining in the source capsule after the prompt neutrons (and photons) are emitted–that is, the fission fragments and the particles they emit. Providing a full account of the results of Cf-252 fission is difficult for two reasons:

- First, the set of possible daughter nuclei is large and varied. The distribution of possible masses for these daughter nuclei is shown in Fig. B.2, which shows a range of possibilities

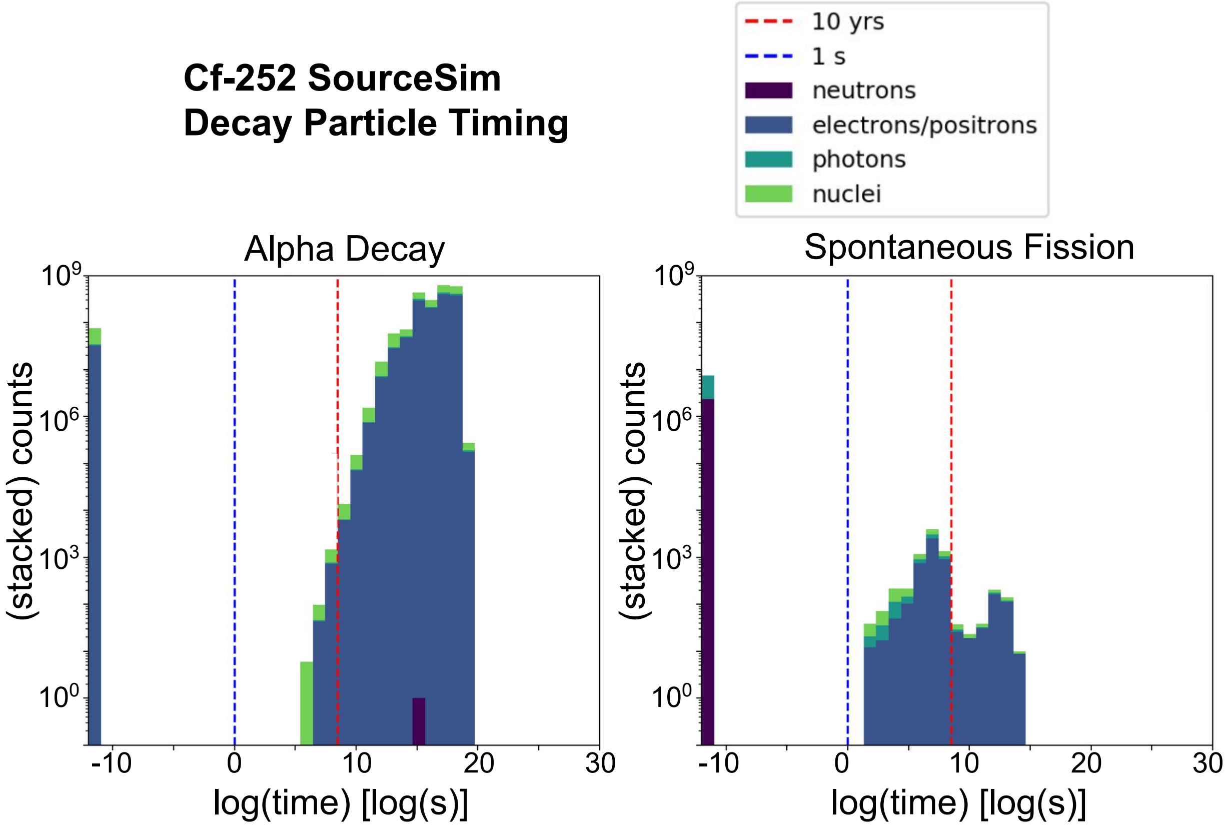

Figure B.1: This figure shows the decay times of particles in our Cf-252 simulation (i.e. the times when the given decay products we might detect are produced), due to either alpha decay (left) or spontaneous fission (right); these are decays inside the source capsule itself, specifically. Based on this data we determine a cutoff for events we want to consider in our analysis. We somewhat arbitrarily identify three time regions: the far left region, before one second, covers the initial decay and is the most important to us; the middle region contains some alpha-chain products and de-excitations from nuclei excited by the earlier particles; and the rightmost region, after 10 years, is mostly the more long-lived segments of the alpha chain, plus some lingering de-excitations from fission. If the simulation modeled fission daughters (see B.1.2), there might be more entries in the middle and right segments of both plots.

nearly 100 AMU (atomic mass units, or, loosely, the number of protons and neutrons) wide[2]. Each one of these will have its own set of isotopes, excited states, and subsequent decay patterns.

- Second, our current simulations do not include fission fragments *at all*. The developers of the fission simulation code we use (a package from LLNL, as noted in the main text) were focused primarily on the overall neutron and photon spectra, not specific processes producing specific daughters (LLNL created this functionality separately, but it is not included the Geant4 code we use[3]).

Fig. B.3 illustrates a fission decay and which physical components are included or missing from the simulations. Here we briefly look at what that means for our results, though–in short–we don't expect the effects to be significant.

Without doing a full study of all the possible fission daughters, we can still generalize and claim that their subsequent decays are unlikely to affect the "prompt" fission neutron spectrum from Cf-252 that we're interested in in simulations. This is because the fission daughters tend to be neutron-rich and undergo beta decay (see Ref. [63]'s Chart of Nuclides for good visualization of this). It's possible for some of them to emit "delayed" neutrons after beta decays, but these are much more rare than the prompt neutrons[65]. Missing the fission fragments in simulations, then, shouldn't cause our neutron results to deviate too much from a real source.

The non-neutron sources from fission fragments, on the other hand, will change over time. As noted above, the fission fragments will usually undergo beta decays and emit a number of different beta particles and photons. Our simulated sources will not reflect these accurately without the fission fragments–but we are not much interested in these spectra. We don't look for any particular energies or even ratios of ERs to NRs, so while these factors may change, they don't affect our conclusions.

---

[2] Note that it favors unequal masses instead of a split into two fragments of equal size[79].

[3] See `https://geant4.kek.jp/lxr/source/processes/hadronic/models/radioactive_decay/include/G4SFDecay.hh`, which is still current as of Geant4 version 11.1.2.

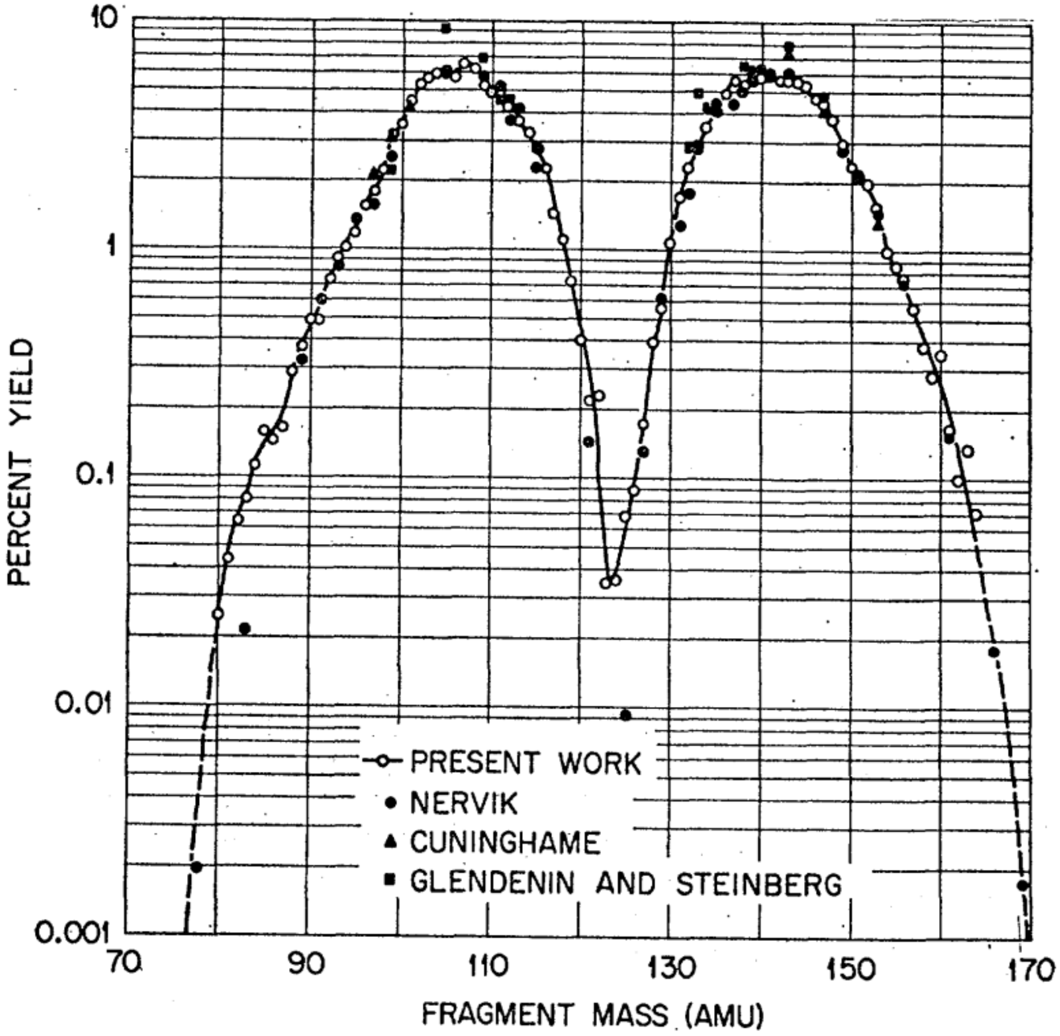

Figure B.2: This figure shows the distribution of fission daughter nuclear masses for Cf-252, from Ref. [79]. Generally spontaneous fission produces two daughter nuclei with distinctly unequal masses instead of an even split, and this can cover quite a range of elements and isotopes–each one representing a different next-step in the "complete" decay chain for Cf-252. We are missing all of this from our Cf-252 simulation and a full study of the impacts has not been done–but we do not expect this to affect the results we're interested in (i.e. the prompt fission neutrons).

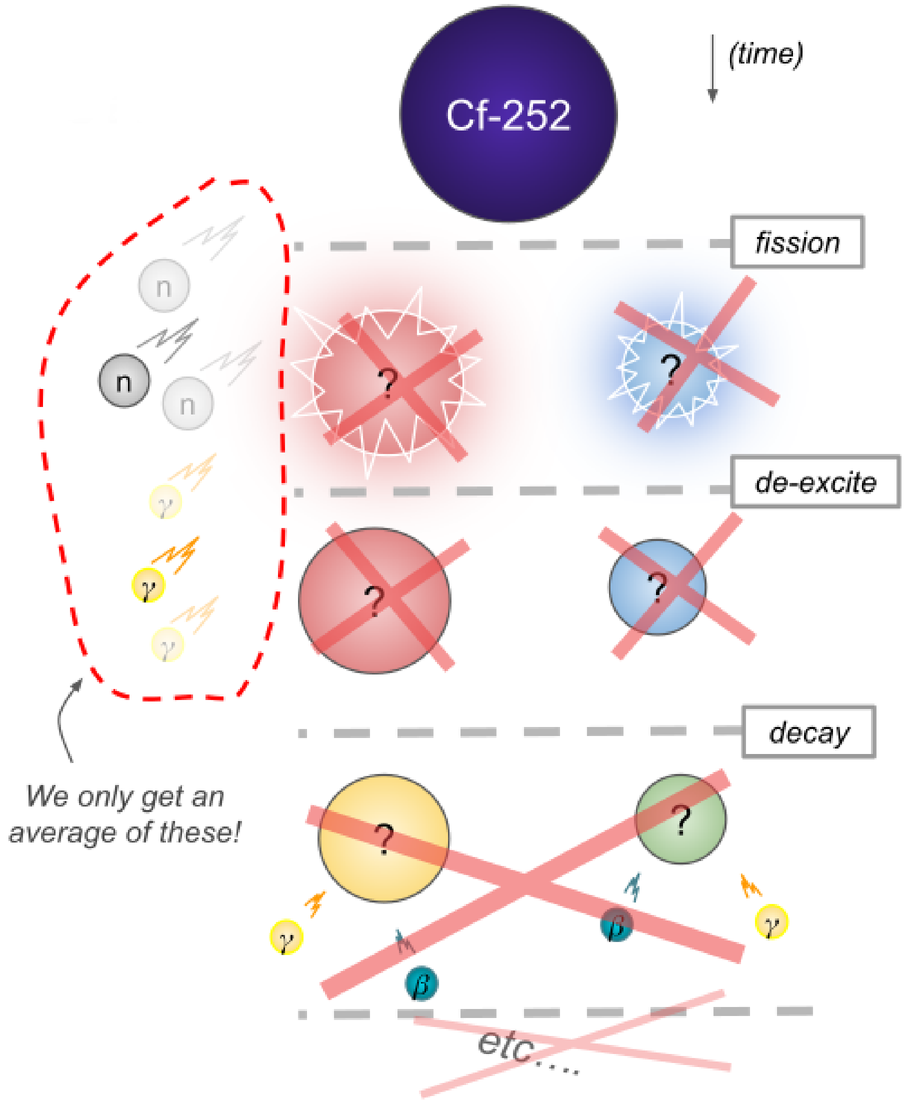

Figure B.3: This figure is an illustration of which particles are produced or neglected in the Cf-252 spontaneous fission simulation. The simulation was made to model the initial decay's average photon and neutron spectra, so not much else is included.

To summarize: our simulated data is missing fission fragments and that will cause our simulated results to have different particles incident on the detectors than real data. However, since the neutron spectrum–our focus–is not significantly affected, these missing fragments should not be a problem. The photon spectra may change–in both the numbers of photons and their energies–but we are not interested in those.

B.1.3 Evolution of the Source

The problem of missing fission fragments contributes to a slightly larger problem: our simulated Cf-252 source does not look like a real, aged Cf-252 source (see section 5.2.3). Missing fission fragments aside, this problem is also due to the timing of nuclear decays:

- In our simulation, the Cf-252 source is a collection of Cf-252 nuclei (exclusively) that all decay at a time designated 0.
- A real source, on the other hand, does not wait for us to watch and does not all decay at once; at any given time it will have some combination of Cf-252 atoms and daughter nuclei–or contaminants.

In short, the mixture of Cf-252 and its daughters will never be quite correct in simulations because we don't simulate the decay timing realistically.

The effects this difference will have on our simulations are essentially the same as what we described for the missing fission fragments:

- Neutrons, our main focus, are fine. Their spectrum essentially doesnt change over time because they are only produced by the initial Cf-252 fission (there exist other potential fission branches further down the alpha decay chain, but they are rare and gated behind the long Cm-248 half-life). Perhaps contaminants could affect this (see following section), but these have not been significant enough to initiate study by CDMS, as far as we're aware.
- The spectra for electrons and alpha particles are probably inaccurate, but that is acceptable since they will not make it from the source capsule to the detector anyways.

- The photon spectrum is also likely inaccurate, but we do not know exactly how. Fig. B.4 shows how the photon spectrum changes between a real two-year-old Cf-252 source and a 42-year-old source (qualitatively, for our purposes); our source, though, was only about 10 years old, and so would likely have emitted a spectrum somewhere in-between. While the differences in the figure appear drastic, most (though not all) of the photons will be blocked and–again–we're not looking for specific energies from those that do reach the detectors. So while the simulation could be made to better handle photons, the potential differences here are not a major concern for us.

B.1.4 Potential Contaminants

Another aspect missing from simulations is contaminants in the original source. A realistic source is likely to have some isotopes of the given elements that were not intended to be present–not to mention other elements that could settle out of the environment (e.g. elements from the decay of radon, as mentioned in chapter 2); some such contaminants contribute to the differences seen in Fig. B.4. While our simulations are missing such contributions, however, we are, again, not looking for specific energies from Cf-252: we use it to see what NRs look like over a range of energies. So while real data will have some contaminant effects and the simulation (currently) won't, the specific energy differences introduced are not important to our current study.

B.2 Non-Fission-Neutron Spectra

For completeness we check that the output spectra of the fission photons and alpha decay chain match expectations. We do not use these spectra, but we can verify that the decay simulation is working as expected.

Fig. B.5, shows the simulated photon energies produced in spontaneous fission and the model producing them (equation 7.1). We don't see any significant differences so we will not discuss this further.

The full alpha decay chain is complicated and uninteresting to us, but we can check that the overall energies emitted are appropriate. Fig. B.6 shows the energies of both the outgoing photons

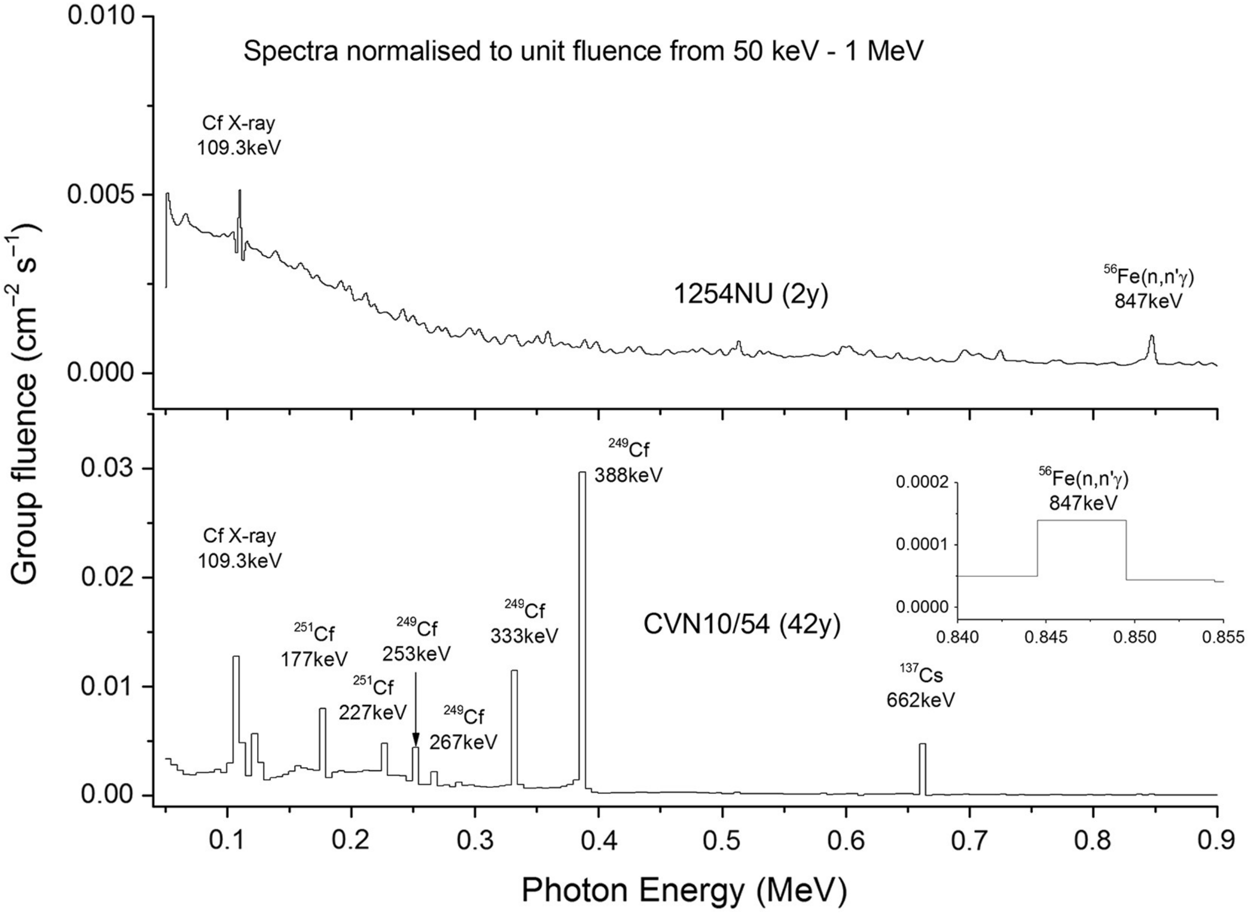

Figure B.4: Differences between the photon spectra of new (2-year old, top) and old (42-year old, bottom) Cf-252 sources–from Ref. [71]–which our simulations largely do not contain. Certain peaks come to stand out over time as the more likely results of the wide-ranging Cf-252 decay chains accumulate. Currently our simulations will not show these changes because they don't keep track of all the decay daughters, meaning our photon spectra may not be accurate; however, since we're more interested in neutrons, which are less commonly produced by the missing decay products, such changes are ignored in our studies.

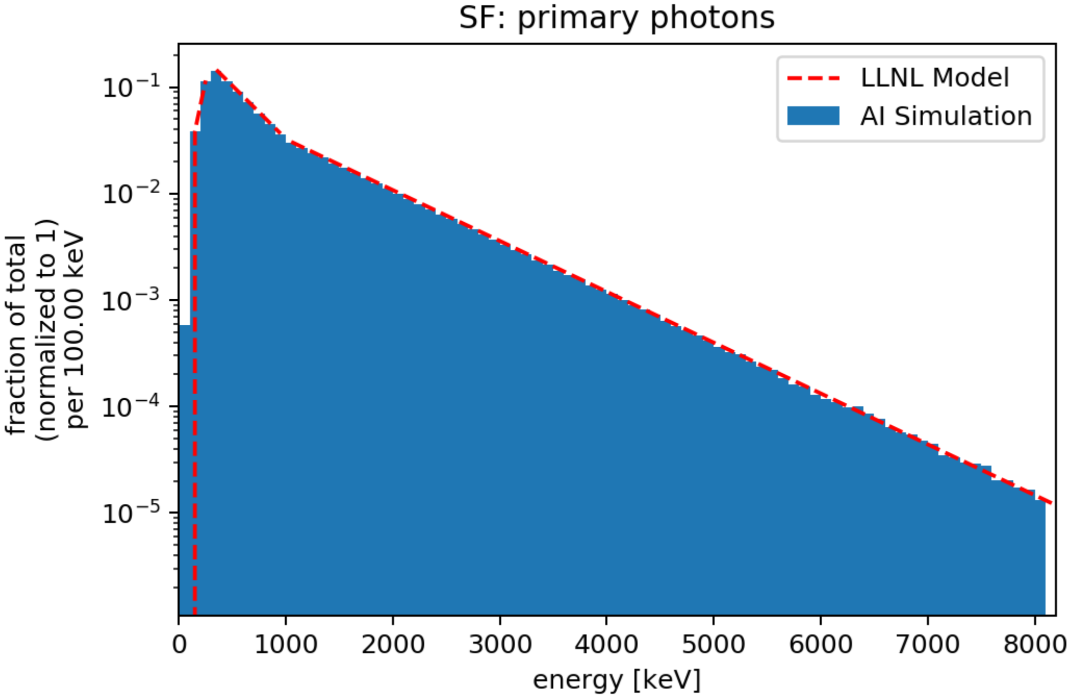

Figure B.5: This figure shows the simulation's output photon spectra from Cf-252 decays, with LLNL's piecewise function overlaid. We see that the simulation behaves as expected.

and electrons together and the alpha particles. A higher-energy alpha would leave the nucleus in a lower-energy excitation state (which would emit lower-energy photons and electrons) and vice-versa. As expected, then, we see a symmetry in the figure between each alpha line and each photon/electron line.

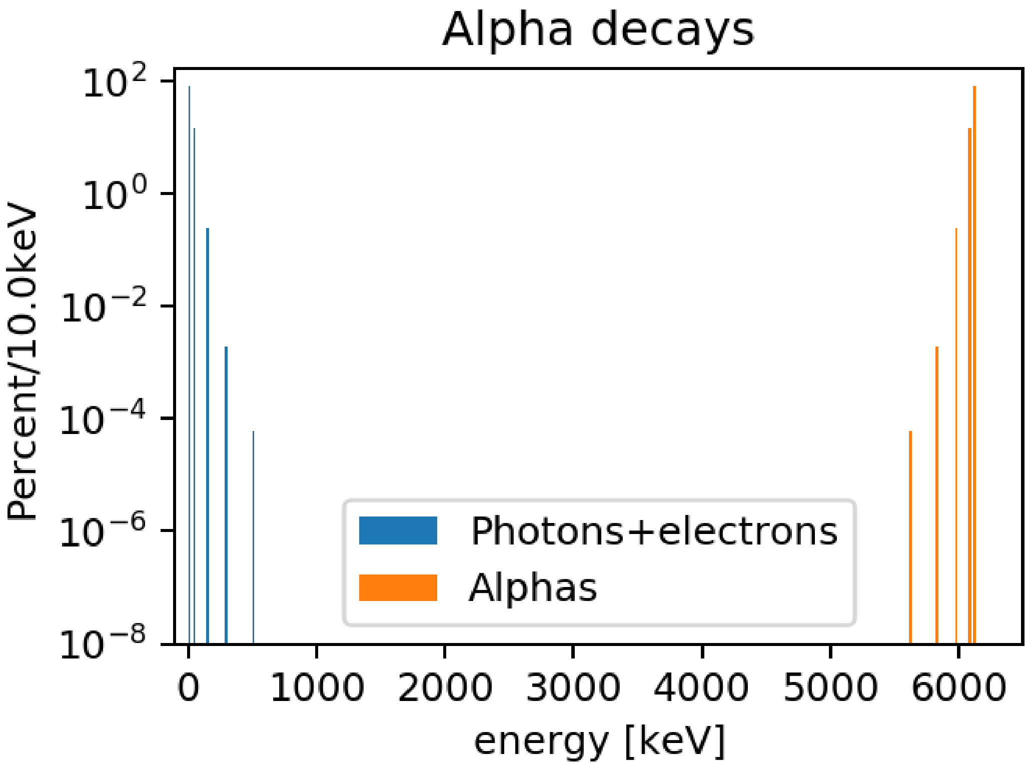

Figure B.6: This figure shows the energies of particles emitted in alpha decays of the Cf-252 source: both individual alpha particles and the summation of photons and electrons in each event. As expected, we see higher-energy alphas with corresponding lower-energy photon/electron lines, and vice-versa. Recall we won't see this in our detectors; this is simply validating the simulation's performance.

APPENDIX C

DMC SHORTCOMINGS AND SHORTCUTS

There are several points of note in the simulation where phonons are not treated realistically. In theory mis-estimations of the collection efficiencies (phonon or otherwise) could simply be calibrated out[1], but other quantities can be affected as well (e.g. resolutions) and we want to check how much they are impacted[2]. In section C.1 we discuss how the phonon collection efficiency differs between real and simulated data while sections C.2 and C.3 cover two parameters used to speed up simulations that had unintended effects–and that weren't recognized or fixed in time for the results presented here.

C.1 Expected Phonon Efficiencies Vs. Simulated Phonon Efficiencies

As was noted in sections 3.2.4 and 3.3.3, there are several sources of real phonon energy loss that we do not simulate: while our simulated results show a collection efficiency at 87% (see Fig. 8.4), real data suggests phonon collection efficiencies should be closer to 30% [80]. However, our simulations do not specifically simulate every process that is accounted-for in that latter estimation; in other words, those different percentages are not actually measuring the same thing. To elaborate, here we identify three categorical components to phonon efficiencies (see Ref. [17], which goes into more detail than just these three):

1. *Phonons traveling through the detector to reach the QETs.* If phonons reflect and decay/downconvert too many times, they may reach energies that are too low to create quasiparticles in the QETs ("thermalization"[3]); in this case their energy is eventually sapped out by the cryogenics.[3]

---

[1] For example, the Bulk 356 keV ER sample's collection efficiencies in Fig. 8.8 could have been centered at any values. We would calibrate our energies by wherever those efficiency peaks happened to be–whatever caused the energy estimates to be centered at 356 keV.

[2] And having similar calibrations between real and simulated data would be generally convenient as well.

[3] The phonons may still be more energetic than the thermal bath, but for our purposes that distinction is not useful.

[3] It's also possible that phonons will land directly on the tungsten TES and heat them up directly. They don't need

2. *Quasiparticles traveling through the aluminum fins to reach the tungsten wires and heat them up*. Energy might be lost here if quasiparticles instead get stuck around impurities. There may be other mechanisms as well, but these need further study.

3. *The conversion of heat in the tungsten into a change in current* (as illustrated in Fig. 3.13). If some of this heat is instead released into the germanium crystal again, it might be lost with the other thermalized phonons.

The simulations shown in this thesis, however, only simulate the first of these and some aspects of the second, with everything else assumed to have 100% efficiency–and since we do not think a total of 87% is accurate, all three of these categories need further study[4].

Given that we don't simulate several of the real phonon inefficiencies, we actually expect the simulated phonon collection efficiencies to be similar to those for the charges–that is, nearly 100%, and hurt only slightly by off-electrode effects (missing NTL phonons in this case). Instead, though, we have peak phonon collection efficiencies under 90%, as shown in chapter 8. This–and related resolution effects–are due to simulation details that were meant to simply speed up the simulation but ended up affecting our results as well. The two parameters at fault here are called "MaxBounces" and "MaxLuke".

C.2 "MaxBounces" Cuts Off Phonon Energies

"MaxBounces" is the main culprit causing our simulated phonon energy losses–such that their efficiencies are lower than those for charges, at least. MaxBounces is a simple numerical limit on the number of times a phonon can reflect (or "bounce") off detector surfaces before it is removed from the simulation; this was intended as a proxy for the fraction of phonons that downconvert enough to thermalize. At the time of our studies, MaxBounces was simply set too low; phonons were being killed before they had undergone a realistic number of bounces (and thus had the appro-

---

as much energy as is required for absorption on the aluminum fins of the QET, but the tungsten itself takes up much less surface area on the detector, so absorptions here are less common.

[4] Ref. [17] estimates item 1 above to lose about 6% of the phonon energies, but other current simulations work estimates this loss to be closer to a single percent or so. Other in-progress studies suggest the third item should be around 67%. More work is needed to confirm these.

priate chance of being absorbed on a QET)–which sped up simulation performance, but negatively impacts our efficiencies. Fig. C.1 illustrates this effect: two samples with a MaxBounces value of 100–the default for our samples–have efficiencies in the 80%'s while another set of samples with MaxBounces set to 400 have efficiencies in the high 90%'s, similar to the simulated charge efficiencies[5]. Other in-progress studies show that phonons with no MaxBounces limit will simply bounce until they are finally absorbed by the QETs–that is, with a collection efficiency of 100% (or 97% due to NTL phonons lost from off-electrode effects), which itself may not be realistic. For simulations in the immediate future MaxBounces has simply been set much higher to avoid the worst of the effects seen here, but a representation of thermalization is currently being constructed to replace it altogether; this will likely take the form of a minimum energy below which phonons are killed instead of relying on an arbitrarily-set number of bounces.

Note that Fig. C.1 also shows different efficiencies between ERs and NRs, which was seen in the main text as well (e.g. Fig. 8.15); we believe these differences between recoil types are due to off-electrode effects–not MaxBounces per se–but changing MaxBounces changes the efficiencies of both and likely changes the difference between them as well. It may further increase that difference by favoring the collection efficiencies of prompt phonons over those of NTL phonons–due to another simulation detail. When phonons undergo anharmonic decay (that is, splitting up into smaller phonons), the new phonons have their bounce counter reset; this means the energies of high-energy prompt phonons, which can experience multiple decays and bounce-counter-resets, may have more chances to be absorbed (though this has not been studied specifically).

C.3 "MaxLuke" Limits Phonon Statistics and Resolutions

"MaxLuke" also affected our phonon results, causing the resolution differences between the samples shown in figure 8.22. MaxLuke is simply a limit on the number of NTL phonons that can be created due to a single hit; above that number, additional energies are simply added back into previously-created phonons. This "downsampling" means the simulation can essentially just re-weight a small number of phonons (keeping the total energy the same) instead of spending the

---

[5] The resolutions become more narrow as well, though it's not clearly visible in the figure.

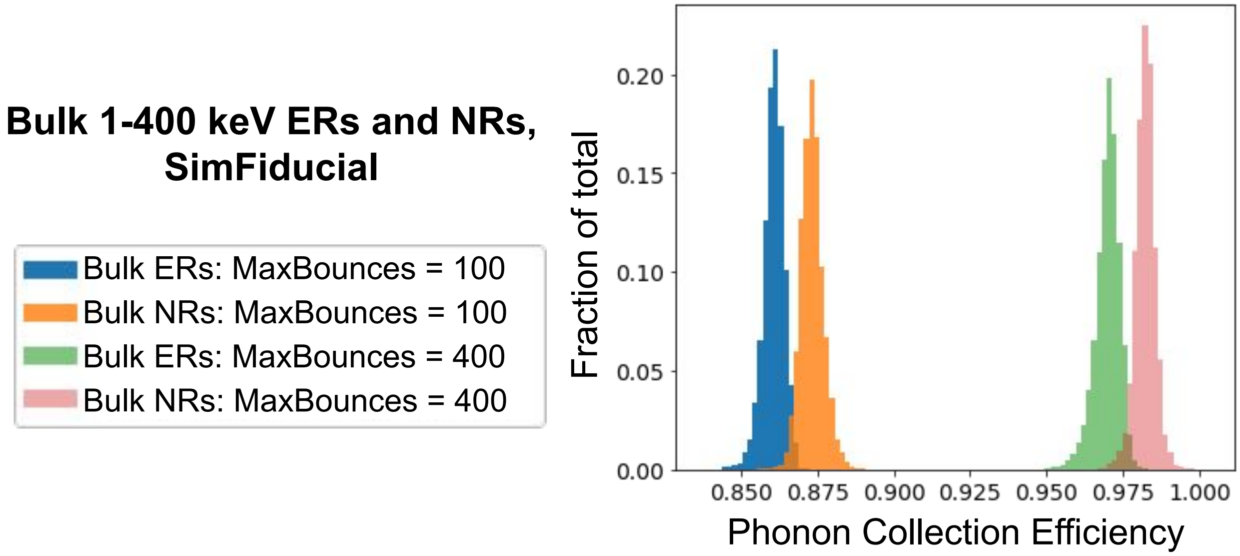

Figure C.1: This figure shows how the simulated phonon collection efficiencies (that is, fraction of the phonon energy that is collected on the QETs) change with the MaxBounces parameter. Our default MaxBounces parameter at the time of these studies (100 bounces) put our phonon efficiencies below 90% (blue and orange peaks in this figure), but raising that parameter value by a factor of 4 caused the efficiencies to jump up by about 10% (green and pink peaks); other studies (not shown here) show it asymptoting to about the same efficiency as charges, capped around 97% due to off-electrode effects. Recall, though, there are more phonon collection effects that are not implemented in the version of the simulations used here.

resources to track a large number–but this comes at the cost of lower statistics. At the time of these studies, the resolution of our phonon energy measurements was still statistics-dominated, scaling with $1/\sqrt{N}$, where N is the number of phonons. This meant multi-hit events would have smaller resolutions than single-hit events because even if MaxLuke cut off too many phonons from a single hit, multi-hit events could easily have a factor of 2 or more phonons to make up for that loss–not that multi-hit events couldn't also benefit from less aggressive downsampling. Fig. C.2 shows results from several samples across which only MaxLuke changes, demonstrating how increasing MaxLuke causes single- and multi-hit events to converge on more similar, lower phonon energy resolutions (while charges themselves are not much affected). For future samples MaxLuke has been raised.

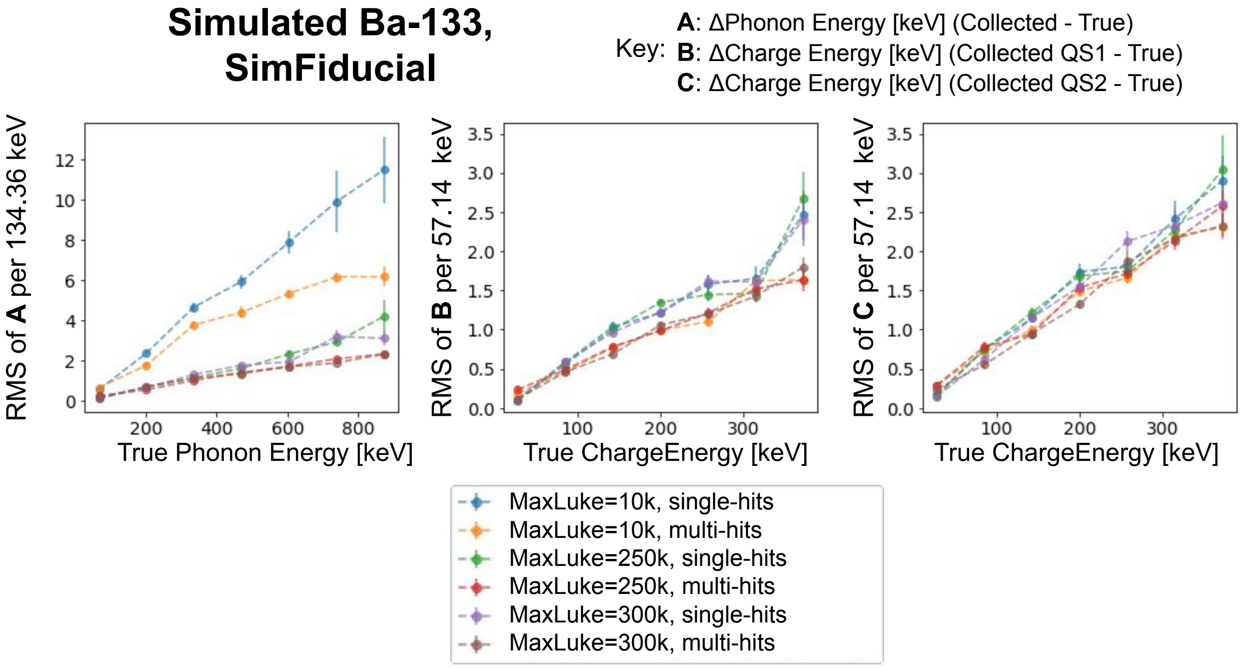

Figure C.2: This figure shows how the simulated energy resolutions change due to the MaxLuke downsampling parameter, which determines how many individual NTL phonons the simulation creates (as opposed to adding weights to existing NTL phonons, to save computation time). In the leftmost plot, for phonons, we see the lowest-downsampling, single-hit events (blue) have nearly twice the resolution of multi-hit events (orange). Using less severe downsampling reduces the resolutions and the difference between single and multi-hit events (compare the blue and orange lines with the most downsampling to the purple and brown lines with the least). The middle plot shows slight differences in the QS1 resolution between single- and multi-hit events (perhaps due to statistics, but we have not investigated this), but it is unaffected by MaxLuke. QS2 on the right shows no obvious differences or changes.

APPENDIX D

ADDITIONAL RESULTS FROM CHAPTERS 8 AND 9

In this appendix we show some figures that were made in the course of our studies in chapters 8 and 9. These do not provide significantly more insight into the samples, but we include them here for completeness.

D.1 Uniform-Field Sample

The plots in this section are for the uniform-field variant of the Bulk 356 keV sample introduced in section 8.2.1.2–in which the electrodes are effectively replaced with flat sheets that charge carriers cannot miss (if they reach the top or bottom detector faces, that is).

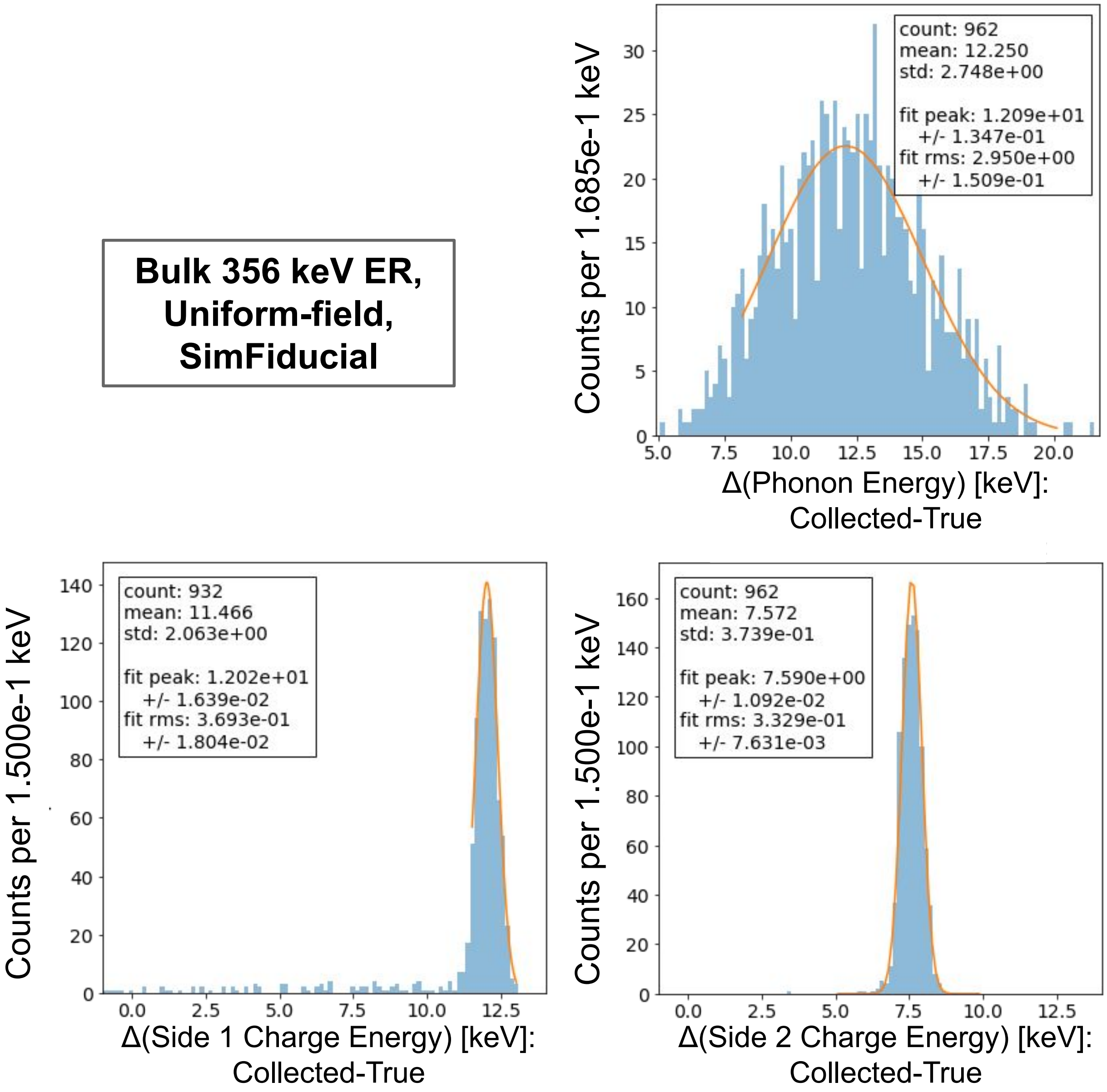

Figure D.1: This figure shows the differences between (calibrated) collected and deposited energies for phonons, QS1, and QS2 in the uniform-field sample–which effectively removes the possibility of charges missing electrodes; that is, every charge that reaches the detector faces will be collected with a Ramo field value of 1 (see section 3.3.1). Comparing to fig 8.9, we see the averages are no longer centered at zero, as we're still using calibrations that "correct" for off-electrode effects. The collected energies (i.e. the efficiencies) have gone up for both charges (by about 3% for QS1 and 2% for QS2) and phonons (1.2%, since charges crossing the full voltage means more NTL phonons). The charge resolution has also decreased by about 1.8 keV (and the lower-energy tails due to off-electrode effects are gone); the phonon resolution does not change significantly.

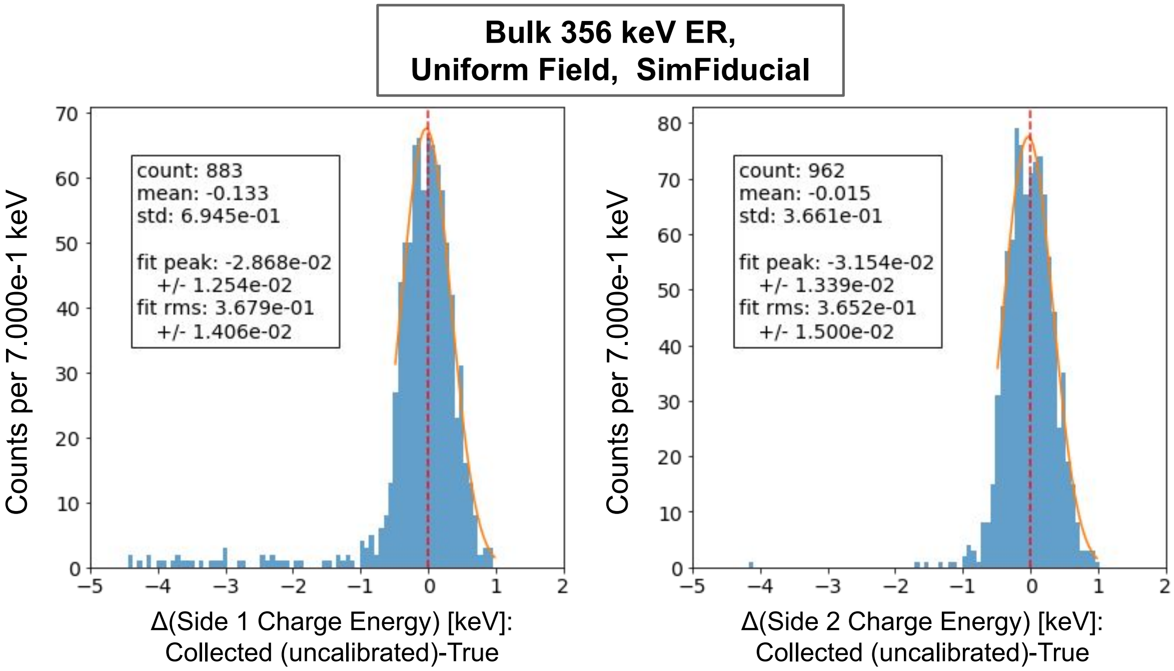

Figure D.2: This figure shows the differences between collected and deposited energies for QS1 and QS2 in the uniform-field sample–as we did in Fig. D.1–but without any calibration of the collected energies. Not only are the two very similar, at this point the only thing causing collected charge energies to not equal true energies is Fano fluctuations, so we can read off their contribution to the resolution here as 0.37 keV (0.1% of the true energy of 356 keV). Phonons still have other effects present preventing us from reading off the Fano contribution here (see Appendix C) and so are not shown.

D.2 Ba-133 Details

These plots show more details of the simulated Ba-133 sample (without noise added) shown in sections 8.3.1 and 9.3.1. Figs. D.3-D.5 provide more detail for SimFiducial events of figure 8.20. Fig. D.6 shows reconstructed results, as might have been in section 9.3.1, but doesn't have much more to show since the DMC results of section 8.3.1.

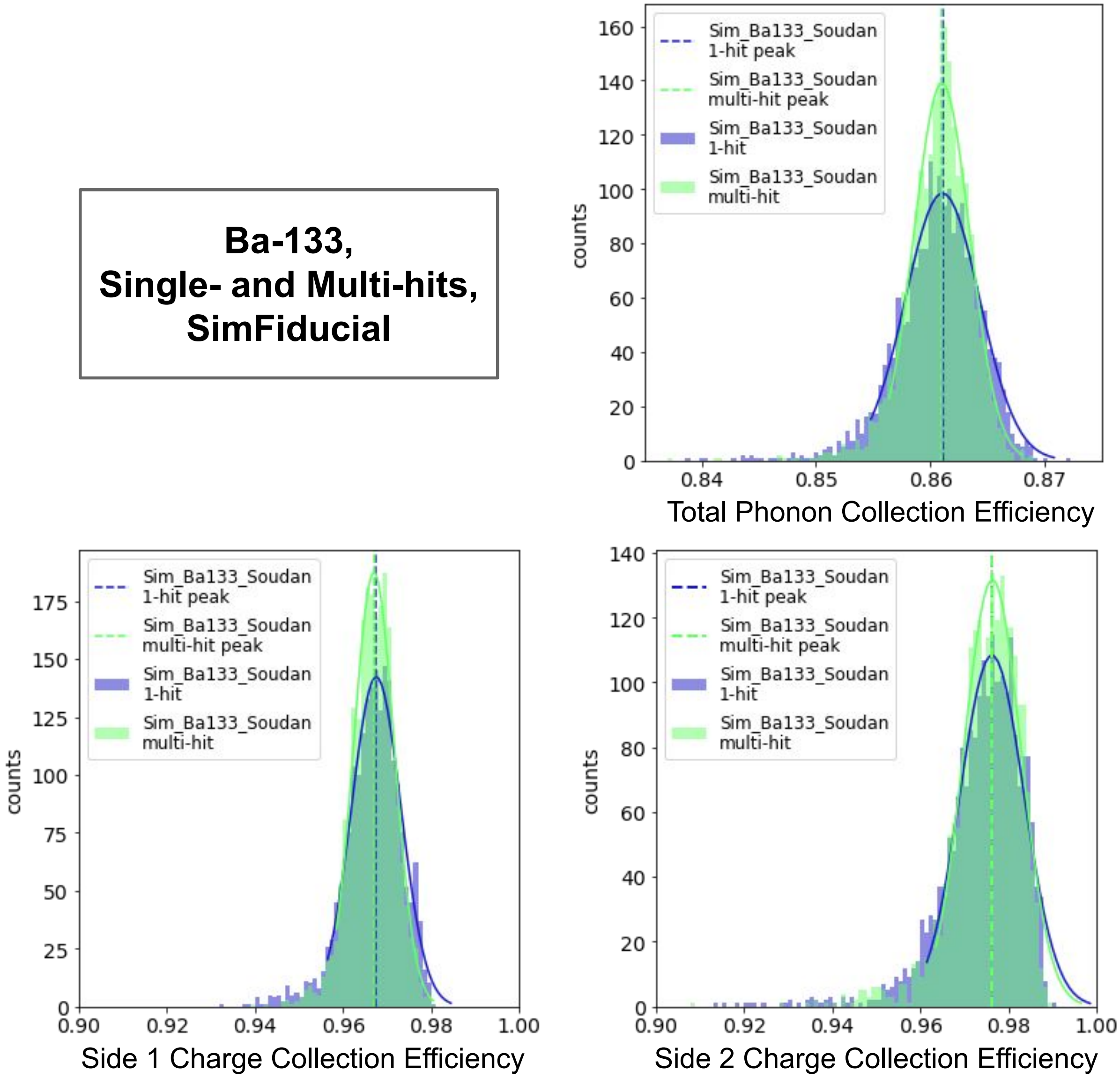

Figure D.3: This figure shows the collection efficiencies in SimFiducial for both single- and multi-hit events in the Ba-133 simulation, to see if hit counts significantly affect how energies are collected. Compare to the Bulk 356 keV sample of Fig. 8.8. While the peak locations generally agree, the RMS values for multi-hit events are consistently lower than those for single-hit events. We suspect this is due to NTL phonon downsampling in the simulation (see Appendix C) limiting the single-hit phonon statistics to a statistic-dominated regime where the RMS scales with $N^{-0.5}$. That is, the "true" resolution is likely lower, and the multi-hit events approach it asymptotically.

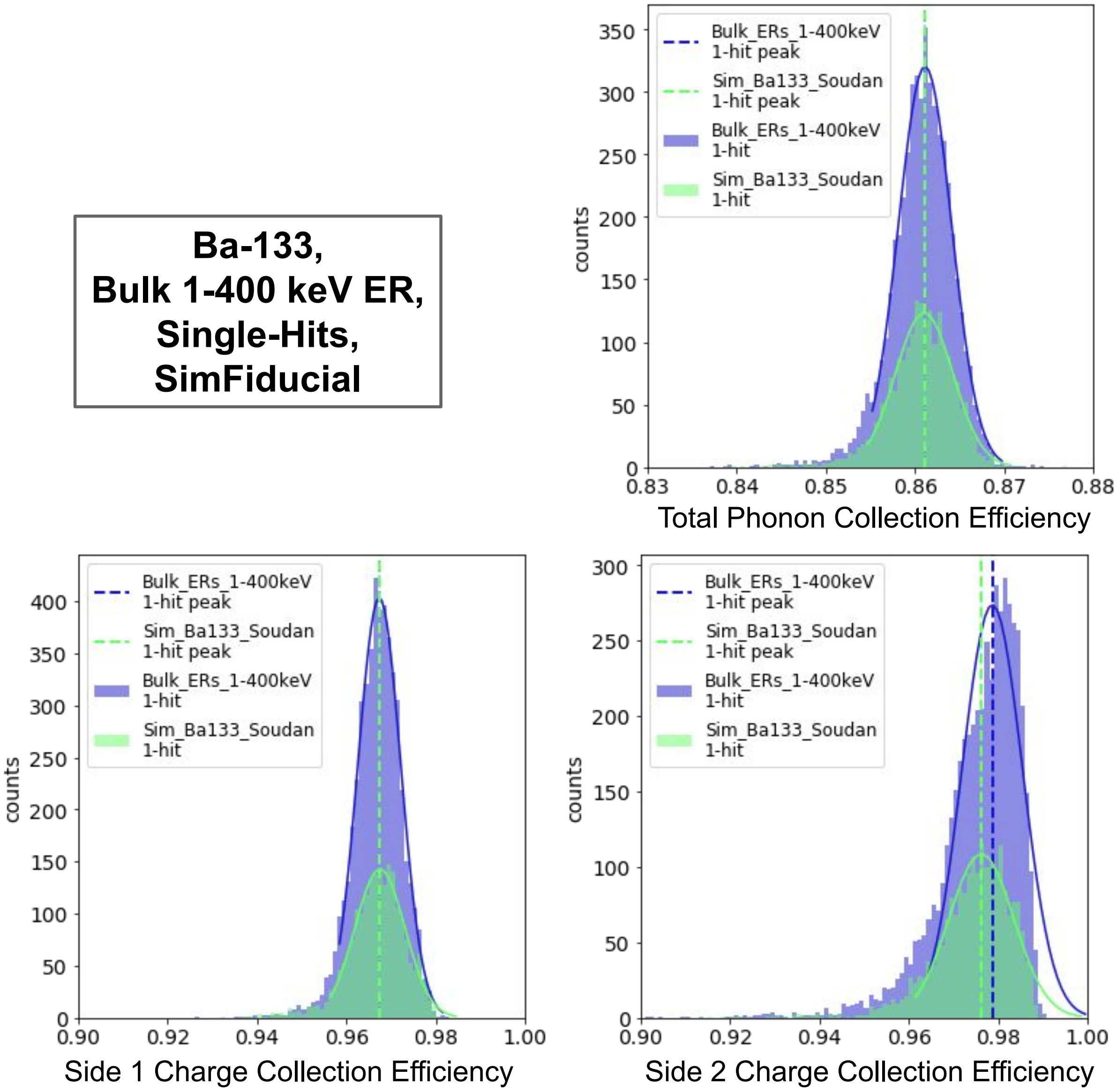

Figure D.4: This figure shows the collection efficiencies for single-hit events in both the 1-400 keV ER sample and the Ba-133 sample (both in SimFiducial); compare previous figure. We show this to check that these distributions are the same–excepting possibly effects due to different energy and hit location distributions. Indeed the only notable difference we see here is in QS2, which is due to the Z-dependence we've discussed previously (see Fig. 8.7).

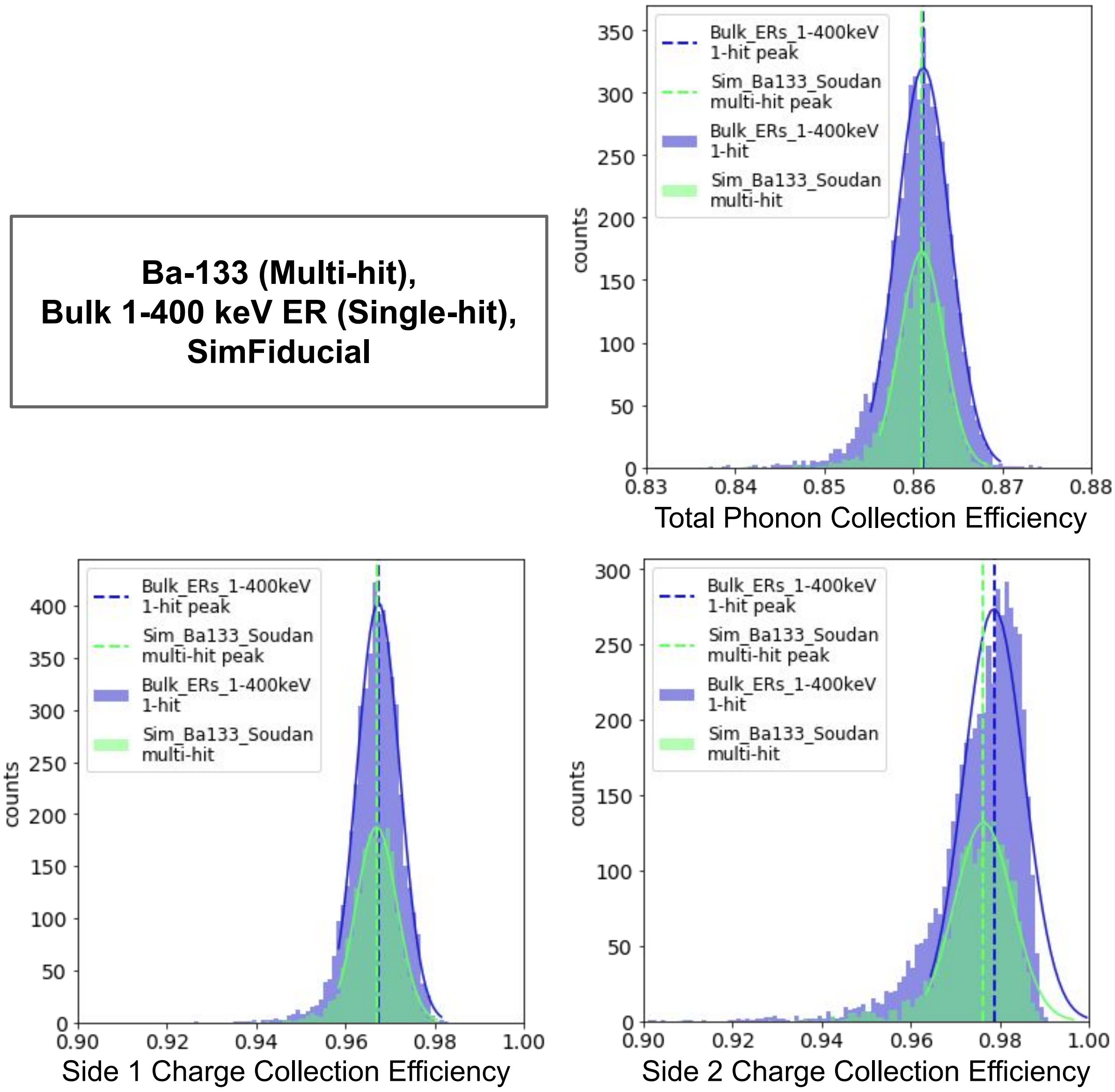

Figure D.5: This figure shows the collection efficiencies for multi-hit events in the Ba-133 sample compared to the necessarily single-hit events from the 1-400 keV ER sample (compare previous two figures). The comparison is less direct than it was for the previous figure, but we want to see here if having multi-hit events introduces any new effects. Again the QS2 peak is low, but the phonon resolution for Ba-133 might trend low as well due to "maxLuke", as described in Appendix C.

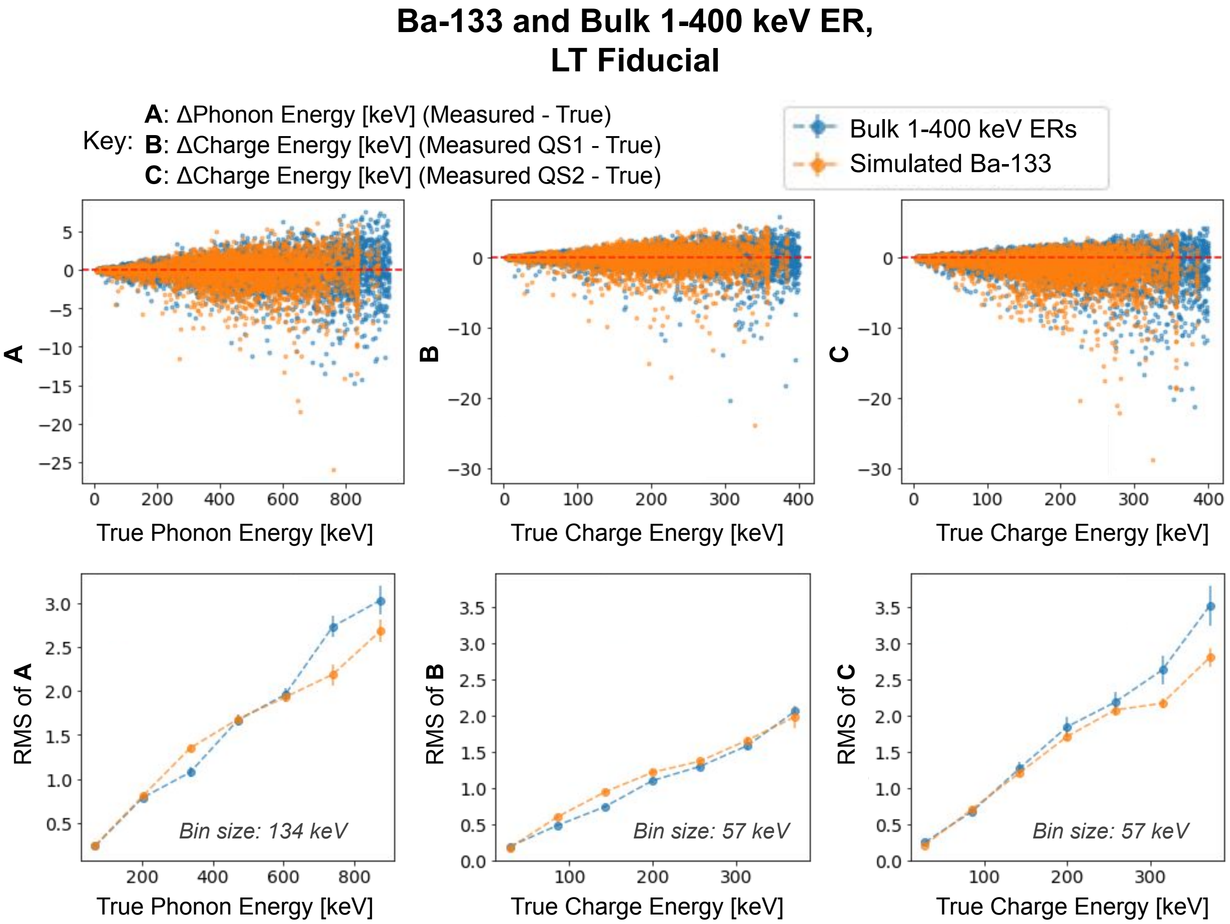

Figure D.6: This figure shows the energy differences and resolutions for all LT Fiducial events (except the one semi-fiducial event noted in section 9.3.1) the Ba-133 and Bulk ER samples after the full simulation chain (i.e. after reconstruction). There is little new to see here comparing to the DMC results in Figs. 8.21 and 8.22.

D.3 Cf-252 Details

These plot show details of the simulated Cf-252 sample (again without noise added) shown in sections 8.3.2 and 9.3.2. Figs. D.7-D.9 show more details of the collection efficiencies shown in Fig. 8.26. Fig. D.10 shows final reconstructed results that might have been in section 9.3.2, but again there is little new to see since the DMC results.

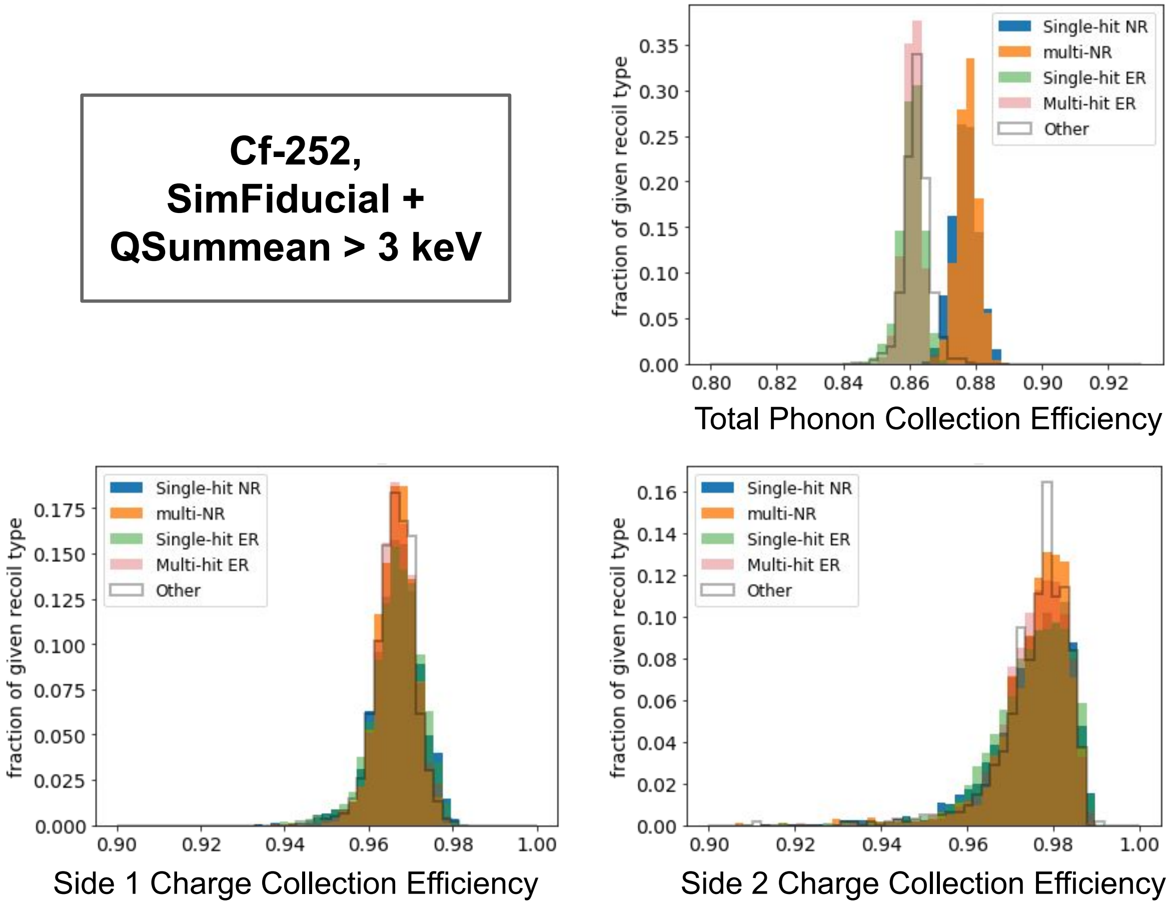

Figure D.7: This figure shows the SimFiducial collection efficiencies for several sets of events in our Cf-252 sample: single-hit and multi-hit ERs and NRs (or "other" events with aspects of both ERs and NRs) for each of phonons, QS1, and QS2 (compare with Fig. 8.26, which shows three samples with different recoil types). We show this to see broadly if/how the distributions of each differ from one another. QS2 might be a bit messy due to the usual charges missing electrodes, but otherwise the most interesting feature here is in the phonon distribution, which is double-peaked. The two peaks essentially represent ERs and NRs, but the "other" events (that have both ER and NR effects) align mostly with the ERs.

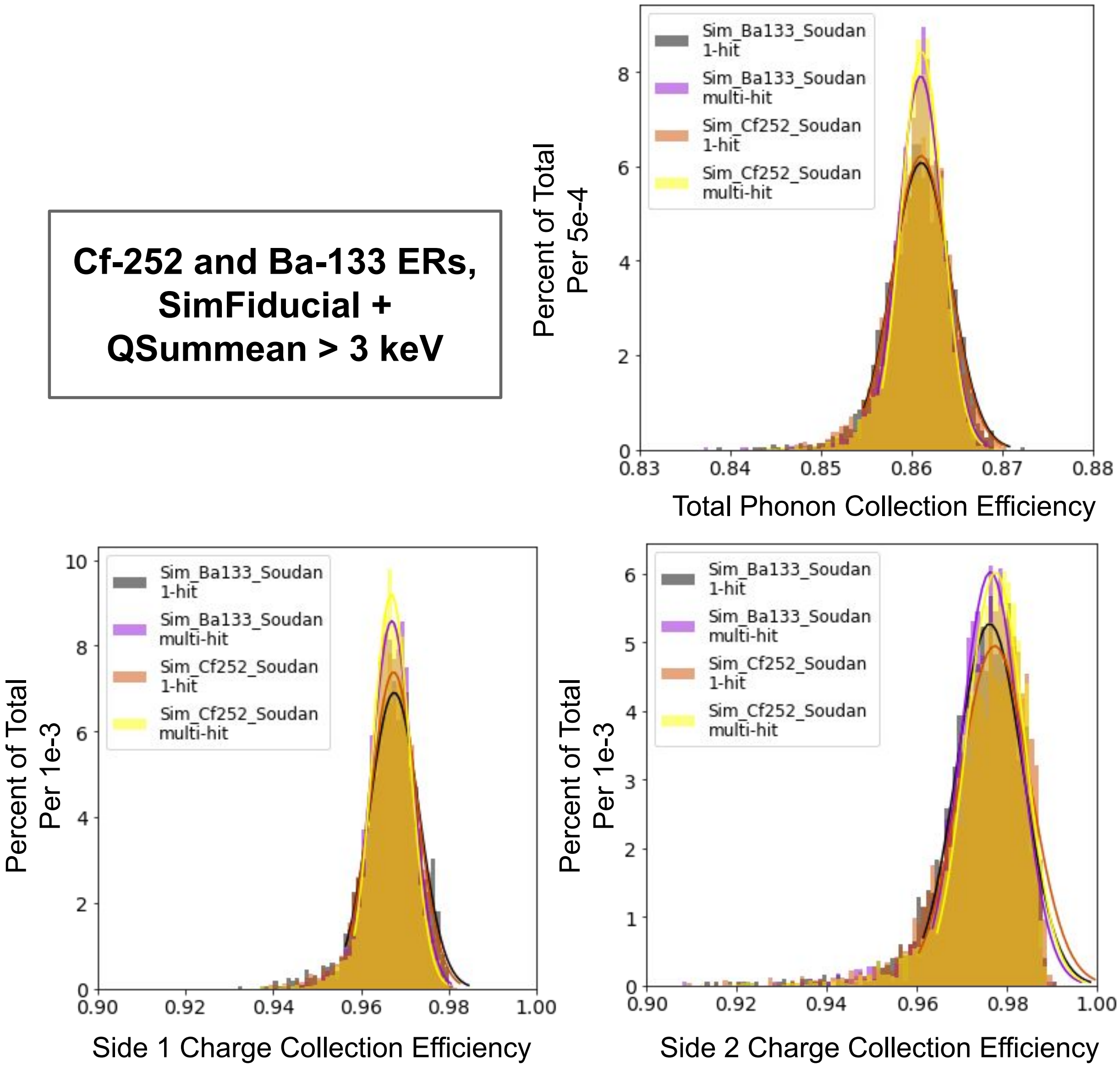

Figure D.8: This figure shows the collection efficiencies for single-hit and multi-hit ERs in the Cf-252 and Ba-133 samples (Fig. D.3 showed the same information for only Ba-133). This is to check, broadly, if anything changes with sample or hit counts. QS2 is a little messy due to off-electrode effects, but otherwise everything matches up nicely.

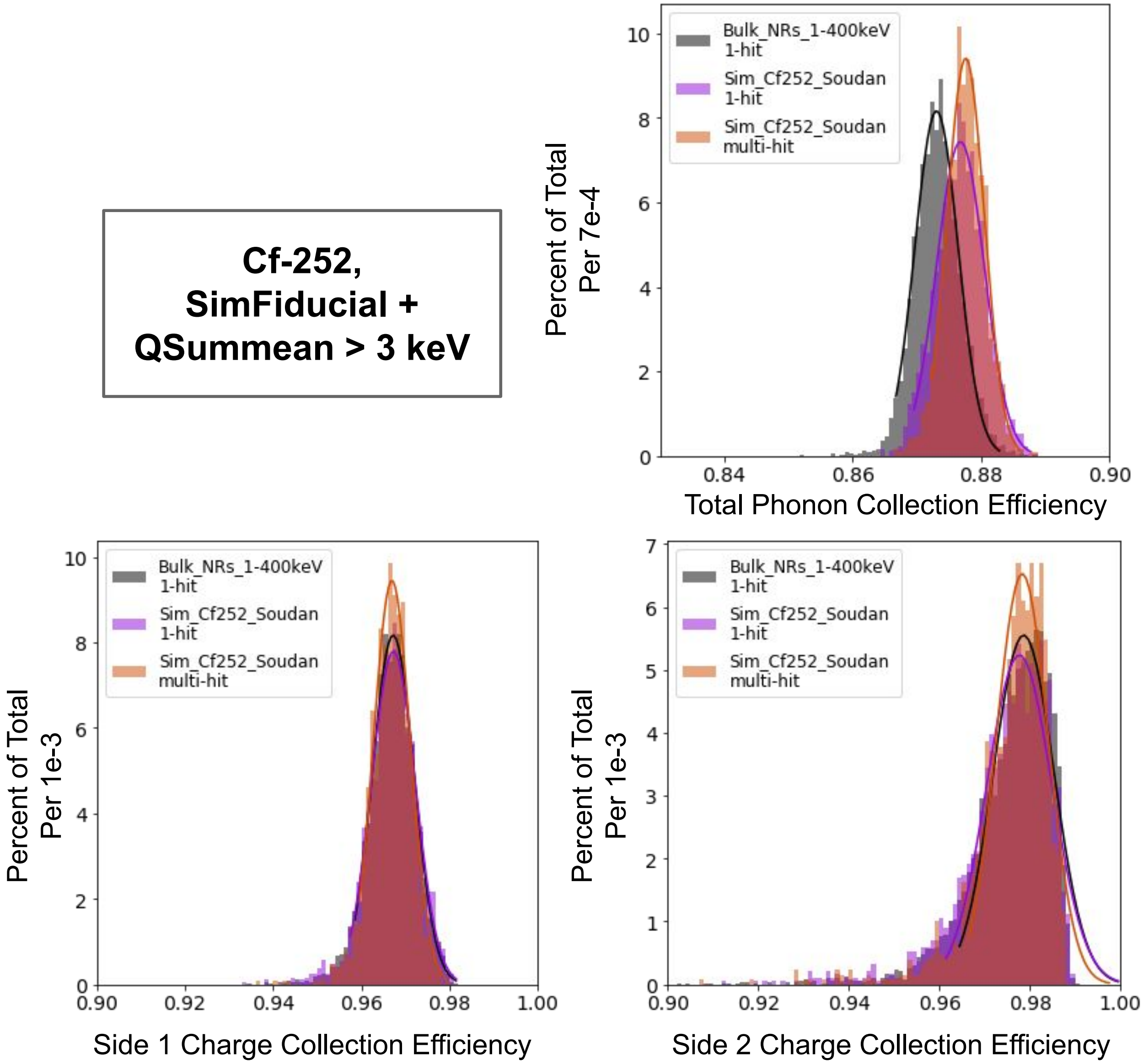

Figure D.9: This figure shows the collection efficiencies for NRs in the Cf-252 and idealized NR samples to check for hit-count dependencies. Single-hit Cf-252 NRs are centered higher than the idealized NRs because lower-energy NRs (which Cf-252 has more of) have better efficiencies (refer to Fig. 8.15).

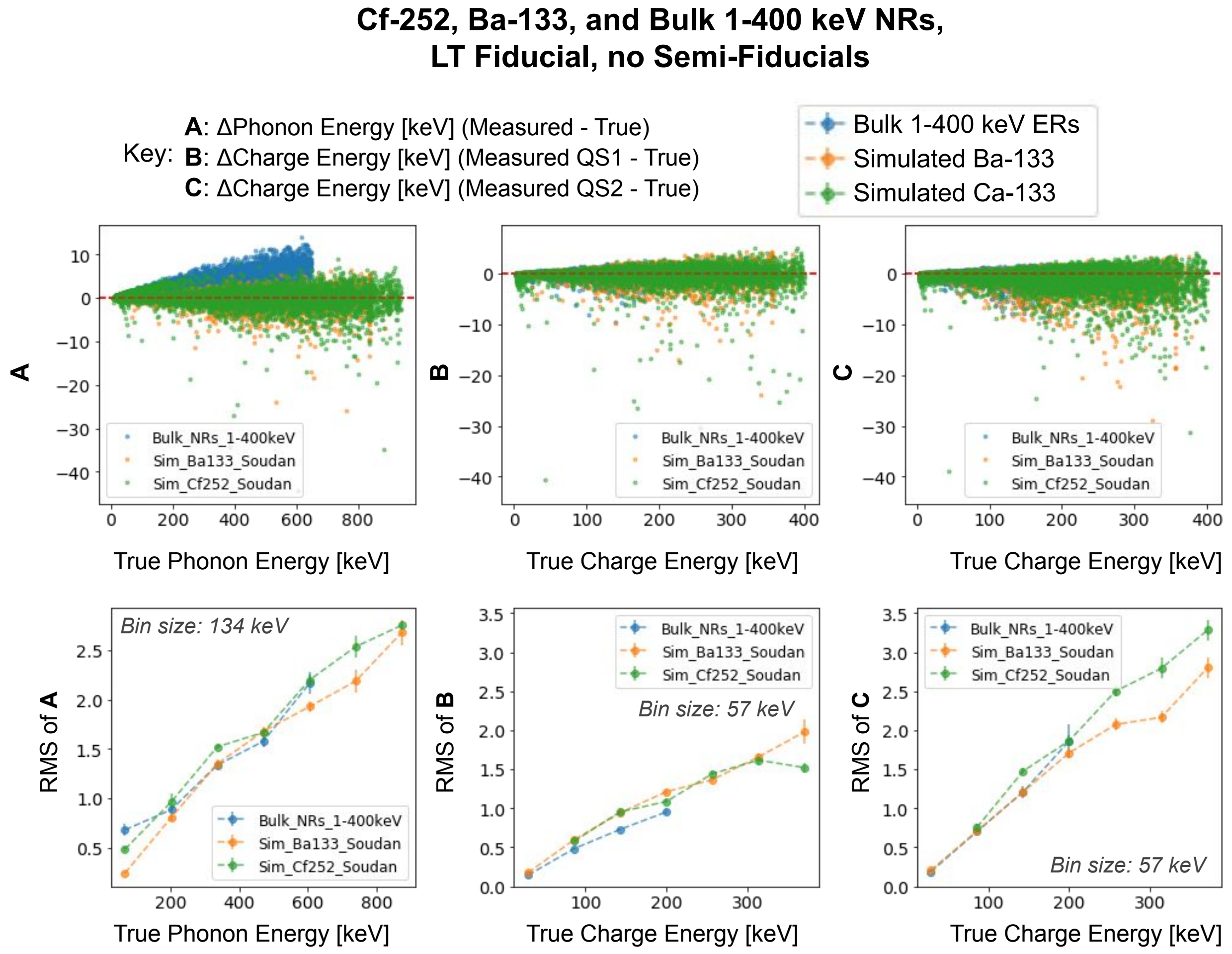

Figure D.10: Shown here are the energy differences and resolutions for the Ba-133, Cf-252, and Bulk NR samples after the full simulation chain (i.e. after reconstruction). Compare Figs. 8.28-8.30. We show this as a description of the "end results" for several samples, but there is little new to see here since the earlier DMC results; we note that Ba-133 trends low in QS2 resolution, which is likely due to off-electrode effects (recall the Ba-133 favors QS1 a bit more significantly, which worsens QS2 results).